University of Sheffield

Doctoral Thesis

Growth of GaAsBi pin diodes using MBE

Author:
Thomas Rockett

Supervisor:
Prof. John David

A thesis submitted in fulfillment of the requirements
for the degree of Doctor of Philosophy

in the

Semiconductor Materials and Devices Group
Department of Electronic and Electrical Engineering

April 26, 2019

Declaration of Authorship

I, Thomas ROCKETT, declare that this thesis titled, "Growth of GaAsBi pin diodes using MBE" and the work presented in it are my own. I confirm that:

- This work was done wholly or mainly while in candidature for a research degree at this University.
- Where any part of this thesis has previously been submitted for a degree or any other qualification at this University or any other institution, this has been clearly stated.
- Where I have consulted the published work of others, this is always clearly attributed.
- Where I have quoted from the work of others, the source is always given. With the exception of such quotations, this thesis is entirely my own work.
- I have acknowledged all main sources of help.
- Where the thesis is based on work done by myself jointly with others, I have made clear exactly what was done by others and what I have contributed myself.

Signed:

Date:

UNIVERSITY OF SHEFFIELD

Abstract

Faculty of Engineering
Department of Electronic and Electrical Engineering

Doctor of Philosophy

Growth of GaAsBi pin diodes using MBE

by Thomas ROCKETT

The incorporation of bismuth into GaAs induces a large decrease in the band gap energy per unit strain. This band engineering ability makes GaAsBi a promising material for near-infrared optoelectronic devices based on GaAs substrates including LEDs and solar cells.

The bismuth incorporation into GaAs and the resulting optoelectronic properties of the epilayers are dependent on the growth temperature and the fluxes of all three constituent atoms. In addition, the propensity of the bismuth atoms to segregate out of the bulk and form into droplets on the wafer surface has restricted the development of GaAsBi optoelectronic devices thus far.

In this work, a systematic series of GaAsBi bulk pin diodes was grown using molecular beam epitaxy using different growth temperatures and bismuth fluxes. This series allows the influence of the growth conditions on the device properties to be independently studied. The devices grown at higher temperatures show lower bismuth contents, evidence of epilayer inhomogeneity using, brighter luminescence, and lower dark currents. The FWHM of the emitted PL is proportional to the bismuth content of the layer and independent of the growth conditions.

GaAsBi multiple quantum well structures studied by other authors have had degraded performance due to strain relaxation. In this work, a series of GaAsBi multiple quantum well structures with different numbers of wells was grown and compared to a complementary set grown previously in Sheffield. The devices grown in this work had a lower strain per period of the MQW and exhibit improved electroluminescence performance for the devices with large numbers of wells.

The electroluminescence of the brightest device was compared to a strain-balanced InGaAs/GaAsP device with a similar structure. The GaAsBi device has weaker electroluminscence than the InGaAs device, however, there are significant current spreading issues which obfuscate a proper comparison. The possibility of using GaAsBi based quantum well LEDs as a broadband light source for optical coherence tomography due to the large FWHM displayed by the LEDs is discussed.

List of publications

Journal papers

1. **T. B. O. Rockett**, R. D. Richards, Y. Gu, F. Harun, Y. Liu, Z. Zhou, J.P. R. David, *Influence of growth conditions on the structural and opto-electronic quality of GaAsBi*, Journal of Crystal Growth **477**, 139-143 (2017)
2. L. Gelczuk, J. Kopaczek, **T. B. O. Rockett**, R. D. Richards, R. Kudrawiec, *Deep-level defects in n-type GaAsBi alloys grown by molecular beam epitaxy at low temperature and their influence on optical properties*, Scientic Reports **7**, 12824, (2017)
3. R. D. Richards, **T. B. O. Rockett**, M. R. Nawawi, F. Harun, A. Mellor, T. Wilson, C. Christou, S. Chen, J. P. R. David, *Light-biased IV characteristics of a GaAsBi/GaAs multiple quantum well pin diode at low temperature*, Semiconductor Science and Technology **33**, 094008 (2018)
4. **T. B. O. Rockett**, R. D. Richards, Y. Liu, F. Harun, Z. Zhou, Y. Gu, J. R. Willmott, J. P. R. David, *Electroluminescence study of GaAsBi multiple quantum wells with varying well number*, Submitted to Journal of Applied Physics, under review

Oral and poster presentations

1. Z. Zhou, R. D. Richards, **T. B. O. Rockett**, F. Bastiman, J. P. R. David. *Investigation of bismuth incorporation into GaAs based on growth conditions*, UK Semiconductors, Sheffield UK, 1st July 2015
2. R. D. Richards, C. J. Hunter, F. Bastiman, Z. Zhou, F. Harun, **T. B. O. Rockett**, J. P. R. David, *GaAsBi LEDs emitting at 1200nm*, UK Semiconductors, Sheffield UK, 1st July 2015
3. F. Harun, **T. B. O. Rockett**, A. R. Mohmad, R. D. Richards, Z. Zhou, F. Bastiman, J. P. R. David, *Polarised photoluminescence study of GaAsBi grown by molecular beam epitaxy*, UK Semiconductors, Sheffield UK, 1st July 2015
4. Z. Zhou, R. D. Richards, **T. B. O. Rockett**, F. Bastiman, J. P. R. David, *Investigation of the mechanism of bismuth incorporation into GaAs*, 6th International Workshop on Bismuth Containing Semiconductors, Madison, Wisconsin, USA, 21st July 2015
5. **T. B. O. Rockett**, F. Harun, A. R. Mohmad, R. D. Richards, F. Bastiman, B. Y. Majlis, J. P. R. David, *Investigation of ordering in GaAsBi through photoluminescence polarisation effects*, 6th International Workshop on Bismuth Containing Semiconductors, Madison, Wisconsin, USA, 21st July 2015
6. R. D. Richards, **T. B. O. Rockett**, Z. Zhou, Y. Liu, J. P. R. David, *GaAsBi work at the University of Sheffield*, UK MBE User Group Meeting, Cambridge, UK, 18th March 2016
7. **T. B. O. Rockett**, R. D. Richards, F. Harun, Y. Gu, Z. Zhou, J. P. R. David, *Optimising the structural and optical quality of GaAsBi*, UK Semiconductors, Sheffield, UK, 6th July 2016

8. Z. Zhou, R. D. Richards, Y. Gu, **T. B. O. Rockett**, F. Harun, Y. Liu, J. S. Cheong, A. Baharuddin, J. P. R. David, *Investigation of photo-multiplication in GaAsBi diodes*, 7th International Workshop on Bismuth Containing Semiconductors, Shanghai, China, 25th July 2016
9. **T. B. O. Rockett**, R. D. Richards, F. Harun, Y. Gu, Z. Zhou, J. P. R. David, *Optimising the opto-electronic properties of GaAsBi*, 7th International Workshop on Bismuth Containing Semiconductors, Shanghai, China, 25th July 2016
10. **T. B. O. Rockett**, R. D. Richards, F. Harun, Y. Gu, Z. Zhou, J. P. R. David, *Optimising the opto-electronic properties of GaAsBi by tuning growth conditions*, 19th International Conference on Molecular Beam Epitaxy, Montpellier, France, 6th September 2016
11. **T. B. O. Rockett**, R. D. Richards, Y. Gu, F. Harun, Y. Liu, Z. Zhou, J. P. R. David, *Opto-electronic measurements of GaAsBi PIN diodes*, Semiconductors and Integrated Opto-Electronics, Cardiff, UK, 18th April 2017
12. R. D. Richards, **T. B. O. Rockett**, Y. Liu, J. P. R. David, *Bismides in the basement update*, UK MBE User Group Meeting, Edinburgh, UK, 21st April 2017
13. R. D. Richards, **T. B. O. Rockett**, Y. Liu, F. Harun, J. S. Roberts, J. P. R. David, *Making progress in photovoltaics: Can dilute bismides fill the 1 eV band gap gap?*, Wroclaw University of Science and Technology, Wroclaw, Poland, 11th May 2017
14. R. D. Richards, **T. B. O. Rockett**, Y. Liu, F. Harun, J. P. R. David, *Hole trapping in GaAsBi/GaAs MQWs: Lessons from dilute nitrides*, UK Semiconductors, Sheffield, UK, 12th July 2017
15. **T. B. O. Rockett**, R. D. Richards, Y. Gu, F. Harun, Y. Liu, Z. Zhou, J. P. R. David, *Electroluminescence and current-voltage measurements of GaAsBi PIN diodes*, 8th International Workshop on Bismuth Containing Semiconductors, Marburg, Germany, 25th July 2017
16. Z. Zhou, R. D. Richards, Y. Liu, **T. B. O. Rockett**, F. Harun, J. P. R. David, *The investigation of photo-multiplication in GaAsBi diodes*, 8th International Workshop on Bismuth Containing Semiconductors, Marburg, Germany, 25th July 2017
17. Y. Liu, R. D. Richards, N. Bailey, **T. B. O. Rockett**, M. R. Nawawi, J. P. R. David *Update on Sheffield bismides activity*, UK MBE User Group Meeting, Nottingham, UK, 13th April 2018
18. Y. Liu, R. D. Richards, **T. B. O. Rockett**, F. Harun, Y. Gu, J. P. R. David, *Electroluminescence study of GaAsBi devices of different growth conditions*, UK Semiconductors, Sheffield, UK, 4th July 2018
19. **T. B. O. Rockett**, R. D. Richards, Y. Liu, F. Harun, Z. Zhou, Y. Gu, J. P. R. David, *GaAsBi/GaAs multiple quantum wells with up to 120 periods*, 9h International Workshop on Bismuth Containing Semiconductors, Kyoto, Japan, 18th July 2018

Acknowledgements

To the technical staff at the University of Sheffield, my supervisor, colleagues, family, and friends. . . thank you for your support!

Contents

Declaration of Authorship **iii**

Abstract **v**

Acknowledgements **ix**

1 Review of semiconductor physics **1**
- 1.1 Binary III-V semiconductors and homoepitaxy 1
  - 1.1.1 Band gap dependence on temperature 2
  - 1.1.2 Homoepitaxy 2
- 1.2 III-V alloys, heteroepitaxy, and strain 2
  - 1.2.1 Ternary III-V alloys 3
  - 1.2.2 Band gap of GaAsBi 3
  - 1.2.3 Localised states in GaAsBi 5
  - 1.2.4 Lattice mismatch and strain relaxation 5
  - 1.2.5 Band gap of GaAs based ternary III-V alloys as a function of mismatch strain 6
- 1.3 Doping of semiconductors and related devices 7
  - 1.3.1 PN junction 8
  - 1.3.2 PIN junction 9
- 1.4 Light emitting diodes 10
- 1.5 Near-infrared broadband light sources & optical coherence tomography 11
  - 1.5.1 State of the art broadband light sources 12
  - 1.5.2 Output power requirements for an OCT light source 12
  - 1.5.3 Applicability of GaAsBi to broadband light sources 12
- 1.6 Summary 13

2 Molecular Beam Epitaxy **17**
- 2.1 Introduction 17
- 2.2 Operating principles 17
  - 2.2.1 Effusion cell design and operation 18
    - Source purity 18
    - Crucible design 18
    - Effusion cell design considerations for specific elements 19
    - Shutter transients 20
    - Beam fluxes 21
  - 2.2.2 Wafer heating and temperature calibration 22
    - Wafer heating 22
    - Thermocouples 23
    - Infrared thermometry 23
    - Band-edge thermometry 24
    - RHEED as a tool for wafer temperature calibration 24
  - 2.2.3 Growth of GaAs with MBE 28

Interaction of atoms on substrate 28
Growth modes 29
Defects in GaAs 30
2.2.4 Vacuum system 30
Requirements of the vacuum system 30
Mass spectrometry 32
Design of vacuum system 34
Vacuum pumps 36
Vacuum gauges 38
2.3 Comparison of MBE with competitor growth techniques 38
2.3.1 Advantages and disadvantages of the MBE-STM used in this work 39
2.4 Reflection high energy electron diffraction 40
2.4.1 Operating principles 40
2.4.2 Surface reconstructions 41
2.4.3 Theory 41
2.4.4 Practical use of RHEED in MBE 42
2.4.5 Group III flux measurement using RHEED 42
2.4.6 Group V flux measurement using RHEED 44
2.4.7 Camera system and image processing 45
2.5 Summary 45

3 Characterisation techniques **51**
3.1 X-ray diffraction 51
3.1.1 Operating principles 51
3.1.2 Theory – bulk homoepitaxial and heteroepitaxial layers 51
3.1.3 Theory – superlattices and multiple-quantum wells 54
3.1.4 Production of X-rays and design of diffractometer 54
3.1.5 Measurement procedure 56
3.1.6 Effect of strain relaxation on XRD pattern 56
3.1.7 Lattice constant of GaBi 57
3.1.8 Summary 57
3.2 Nomarski microscopy 57
3.2.1 Theory and equipment design 57
3.3 Photoluminescence spectroscopy 58
3.3.1 Operating principles 58
3.3.2 Theory 58
3.3.3 Equipment design 62
3.3.4 Measurement procedure and practical considerations 63
3.3.5 Summary 64
3.4 Fabrication of contacts using photolithography 64
3.5 Current-voltage 66
3.5.1 IV characteristics of diodes 66
3.6 Electroluminescence 66
3.7 Summary 67

4 Growth of GaAsBi pin diodes with different conditions **71**
4.1 Introduction 71
4.2 Review of GaAsBi growth investigations 71
4.2.1 Early reports of GaAsBi growth 71

- 4.2.2 Growth of GaAsBi at low temperatures using a stoichiometric arsenic flux . . . 72
- 4.2.3 Growth rate dependence of bismuth incorporation . . . 72
- 4.2.4 Growth temperature dependent limit to bismuth incorporation 72
- 4.2.5 Theoretical growth models of GaAsBi . . . 73
- 4.2.6 Growth of GaAsBi with high bismuth content . . . 73
- 4.2.7 PL intensity improvement with bismuth incorporation . . . 73
- 4.2.8 GaAsBi growth studies . . . 73
- 4.2.9 Deep-level transient spectroscopy studies into GaAsBi defects . 74
- 4.2.10 Previous studies into GaAsBi diodes . . . 74
- 4.3 Growth of GaAsBi using MBE . . . 75
  - 4.3.1 Preparation for growth . . . 75
  - 4.3.2 Bismuth flux calibration . . . 75
  - 4.3.3 Silicon and beryllium flux calibration . . . 76
- 4.4 List of devices . . . 76
- 4.5 Growth . . . 78
  - 4.5.1 Growth of GaAs n-type and p-type layers . . . 78
  - 4.5.2 Growth of GaAsBi i-region . . . 79
- 4.6 Nomarski microscopy . . . 80
- 4.7 X-ray diffraction . . . 83
  - 4.7.1 XRD dependence on bismuth BEP . . . 83
  - 4.7.2 XRD dependence on growth temperature . . . 84
  - 4.7.3 Bismuth content inhomogeneity . . . 85
  - 4.7.4 XRD fitting parameters for devices . . . 88
- 4.8 Photoluminescence spectroscopy . . . 88
  - 4.8.1 PL dependence on bismuth BEP . . . 88
  - 4.8.2 PL dependence on growth temperature . . . 90
  - 4.8.3 Bismuth content of layers as calculated using PL and XRD . . . 91
  - 4.8.4 Integrated PL as a function of bismuth content . . . 92
  - 4.8.5 Spectral width of PL as a function of bismuth content . . . 94
- 4.9 Current–voltage . . . 95
- 4.10 Conclusion . . . 97

5 Growth and electroluminescence characterisation of GaAsBi/GaAs multiple quantum wells 101
- 5.1 Introduction . . . 101
- 5.2 Review of previous GaAsBi MQWs . . . 101
  - 5.2.1 Growth studies . . . 101
  - 5.2.2 Optoelectronic studies and devices . . . 102
  - 5.2.3 Review of series C GaAsBi/GaAs MQWs . . . 102
    - Growth and structural investigation . . . 102
    - Optoelectronic studies . . . 102
    - GaAsBi based bulk LEDs . . . 103
- 5.3 List of devices . . . 103
- 5.4 Growth of MQW series G . . . 106
- 5.5 Nomarski microscopy . . . 107
- 5.6 X-ray diffraction . . . 113
  - 5.6.1 XRD fitting parameters for devices . . . 116
- 5.7 Photoluminescence spectroscopy . . . 117
- 5.8 Quantum well modelling and comparison with PL . . . 120
  - 5.8.1 Band offsets . . . 120

- 5.8.2 Effective mass approximation 121
- 5.8.3 Solution of Schrödinger equation using custom software 121
- 5.8.4 Bound state energies in device G2 122
- 5.9 Current – voltage 126
- 5.10 Electroluminescence 127
  - 5.10.1 EL of all GaAsBi/GaAs MQWs using constant current 127
  - 5.10.2 Comparison of both series of GaAsBi MQW devices and the implications for GaAsBi MQW photovoltaics 129
  - 5.10.3 EL microscopy 131
  - 5.10.4 Current dependent EL of device G40 133
  - 5.10.5 Comparison of GaAsBi EL with InGaAs MQW 135
  - 5.10.6 Suitability of dilute bismides as an OCT light source 137
- 5.11 Conclusions 138

6 Summary, conclusions, and future work **145**
- 6.1 Summary 145
- 6.2 Conclusions 145
- 6.3 Future work 146

List of Figures

1.1 Unit cell showing the zinc blende crystal structure of GaAs. The red and green circles represent Ga and As atoms respectively. The blue lines represent bonds 1

1.2 The GaAs $(001) - \beta(2 \times 4)$ surface reconstruction. (top) Top view, (bottom) side view. The red and green circles represent Ga and As atoms, respectively. The size of the atoms indicates which plane the atom is in. Adapted from [4] 2

1.3 Lattice constant plotted against band gap for III-V semiconductors. Binary alloys are displayed as blue points, with ternary alloys as solid (direct bandgap) or dashed (indirect bandgap) lines. The alloys GaAsN and GaAsBi are plotted in magenta and red respectively. The group IV elements Si and Ge are included for completeness. Data from [2], except GaAsN [14] and GaAsBi [10] 3

1.4 Band offsets and band gap of GaAsBi relative to the valence band maximum of GaAs as a function of bismuth content 4

1.5 Matthews-Blakeslee critical thickness as a function of the lattice mismatch strain 6

1.6 Magnitude of lattice mismatch strain relative to a GaAs substrate, plotted against band gap for GaAs based III-V semiconductors. Note that GaAsN is tensile-strained on GaAs while the other alloys are all compressively strained on GaAs. 7

1.7 Pn junction at zero bias. The filled circles represent electrons, and the open circles represent holes. 9

1.8 Simulated output spectrum (solid line) from GaAsBi quantum well based LED emitting at 1050 nm based on the sum of three component spectra (dashed lines), which could be from three different quantum wells or from a single quantum well with three radiative transitions. . 13

2.1 Beam flux measurement of Ga cell operating at 970 °C, showing a shutter transient. The cell was opened at 9 minutes and closed at 31 minutes. Data measured using the MBE-STM machine. 21

2.2 Vapour pressures of the elements used in this work, as a function of temperature. Sources: Al, Ga, In, Be [22]. As [23]. Bi [24]. Si [25] 22

2.3 RHEED pattern of GaAs c(4x4) reconstruction. Kikuchi lines are also visible in this figure 25

2.4 RHEED pattern of GaAs (2x4) reconstruction, showing the 4x pattern . 25

2.5 RHEED pattern of GaAs (001) surface before removal of surface oxide 26

2.6 RHEED pattern of GaAs (001) surface after removal of surface oxide . 26

2.7 Relationship between heater current and wafer surface temperature for GaAs n+ (001). The dashed line is a quadratic fit to the data, and the error bars are the uncertainty in the current from the limited resolution of the power supply (±0.005 A) 27

2.8 Calculated impurity concentration in GaAs thin films, as a function of the vacuum system background pressure. The sticking coefficient S is varied from $10^{-}8$ to 1, and the Ga flux corresponds to a typical growth rate of 0.6 ML/s. 32
2.9 Output of mass spectrometer attached to the growth chamber of the MBE system. These data were taken before a growth run, such that the growth chamber had not been opened to the entry chamber for over 12 hours. 33
2.10 Diagram of the MBE-STM used in this work. Each of the two main chambers should also have a vacuum monitoring gauge (more than one gauge is preferable, for redundancy) - these are not shown for simplicity. The effusion cells, RHEED system, cryo-panel, substrate stage, and wafer transfer mechanism are also not shown here. The black boxes represent vacuum gate-valves, with green indicating the valve is open, and red indicating the valve is closed. Note that the MBE machine in this work does not have a wafer preparation chamber, and that the entry lock chamber connects directly to the growth chamber via a gate valve 34
2.11 Diagram of the RHEED system. The angle θ is exaggerated in this image for clarity 41
2.12 Illustration of the diffuse scattering of the electron beam, and its influence on the RHEED signal intensity, during the growth of a single monolayer 43
2.13 Typical RHEED intensity oscillations during MBE growth of GaAs, gathered using custom software package with USB webcam 44

3.1 Diagram of the diffraction of X-rays from the (004) plane of a perfect crystal 52
3.2 Lattice constants of the substrate (a$_s$) and epilayer (a$_l$) when the alloys are free-standing and after deposition. Note that the out-of-plane lattice constant (c) is distorted to accommodate the strain. The zincblende unit cell structure of the semiconductors studied in this work is approximated by a square for simplicity 53
3.3 Example of XRD simulated data: a bulk GaAsBi layer (blue), and a 5 period GaAsBi/GaAs MQW (orange). The two scans are vertically offset for clarity. 54
3.4 Diagram of XRD measurement. The collimating mirror and monochromator are not shown for clarity 56
3.5 Arrangement of optical elements in a Nomarski microscope 58
3.6 Diagram of relevant excitation and recombination processes in a direct band gap semiconductor: a) radiative excitation and relaxation to band edge, b) radiative recombination, c) recombination via defect level, d) recombination via dopant states (these transitions can result in the emission of a photon, and the dopant energy levels are much closer to the conduction and valence bands, but this is not shown for clarity), e) CHCC Auger recombination, f) CHSH Auger recombination. The teal arrows denote transitions, and the black lines denote the conduction and valence bands. 59
3.7 Diagram of the photoluminescence equipment 62
3.8 Microscope image of front contact mesa structures on surface of wafer 65

4.1 Microscope image of bismuth droplets on a GaAs substrate, for the purpose of determining the bismuth flux 76
4.2 Graphical representation of the growth conditions for the GaAsBi bulk devices grown in this work. The size of the circles corresponds to the bismuth content (in %) of the devices as measured by XRD, which is also shown inside each circle in text. 77
4.3 Diagram of the device structure for the bulk GaAsBi pin diodes. The p++ layer at the top of the stack is not shown here 78
4.4 Time taken for the RHEED pattern to change to a bismuth terminated reconstruction after opening the bismuth shutter, depending on the substrate temperature 79
4.5 Time taken for the RHEED pattern to change to a bismuth terminated reconstruction after opening the bismuth shutter, depending on the bismuth BEP 80
4.6 Nomarski image of STG-38 (1.37% Bi) at 10x magnification 81
4.7 Nomarski image of STG-3D (1.31% Bi) at 10x magnification 81
4.8 Nomarski image of STG-34 (3.25% Bi) at 10x magnification 82
4.9 Nomarski image of STG-3B (4.12% Bi) at 10x magnification 82
4.10 Density of droplet-like defects in Nomarski images of GaAsBi pin diodes, as a function of bismuth content 83
4.11 XRD spectra of GaAsBi bulk devices grown with different bismuth BEPs. The legend describes the bismuth BEP in units of 10^{-7} mbar, and the scans are offset relative to the substrate peak for clarity 84
4.12 XRD spectra of GaAsBi bulk devices grown at different temperatures. The legend describes the growth temperature of each device in °C, and the scans are offset relative to the substrate peak for clarity. The red arrows highlight regions where the model agrees poorly with the data, caused by a varying bismuth content across the layer 85
4.13 XRD spectra of pair of devices with 1.3% bismuth, (top) STG-38 (grown at 405 °C) and (bottom) STG-3D (grown at 375 °C). The red arrow shows the region of the spectrum where the single layer model fails to fit the data. 86
4.14 Bismuth incorporation profiles in the GaAsBi layer of the device grown at 405 °C (STG-38), as calculated using single layer (red line) and bilayer (blue line) XRD simulations. The growth direction is to the right. 87
4.15 PL spectra of devices grown with different bismuth BEPs. The legend describes the bismuth BEP in units of 10^{-7} mbar 89
4.16 PL spectra of devices grown at different temperatures. The legend describes the growth temperature in °C. Note that the devices were measured using neutral density filters and scaled to take this into account. Therefore, the noise floor is different for several of the spectra. . 90
4.17 Bismuth content calculated using XRD and PL, as a function of the bismuth BEP 91
4.18 Bismuth content calculated using XRD and PL, as a function of the growth temperature 92
4.19 Integrated photoluminescence as a function of bismuth content for both series of GaAsBi pin diodes with the device that is part of both series marked in both colours. The devices plotted in red were all grown at 375 °C with varying Bi BEPs, while the devices plotted in blue were grown at different temperatures with the same Bi BEP. The dashed lines are fits to the data. 93

4.20 Dependence of PL FWHM on bismuth content, calculated using Gaussian fitting of the PL data . . . 94
4.21 Dark current density as a function of bias voltage for GaAsBi pin diodes. Not all of the devices are plotted for clarity. The legend denotes the bismuth content and growth temperature of each device . . . 96
4.22 Reverse saturation current density of GaAsBi diodes calculated from the Shockley diode equation and the forward bias data, as a function of the Bi content. The annotations denote the growth temperatures of the diodes, with the devices plotted in red all grown at the same temperature (375 °C). The device grown at 365 °C is not plotted here as it has an anomalously low Bi content compared to the other devices 97

5.1 Nominal growth structure of series C GaAsBi/GaAs MQWs grown by Richards et al. For the structure of the i-region, see table 5.1 . . . 104
5.2 Nominal growth structure of series G GaAsBi/GaAs MQWs grown for this work. The top p++ layer is not shown in this diagram . . . 105
5.3 Magnitude of the average strain plotted against the total thickness of the MQW stack, for GaAsBi/GaAs MQWs. The solid black line is the Matthews-Blakeslee critical thickness which corresponds to the mobilisation of already present dislocations. The dashed black line corresponds to the point at which the strain energy is large enough to generate new dislocations [47]. . . . 106
5.4 Nomarski image of G2, at 10x magnification . . . 108
5.5 Nomarski image of G5, at 10x magnification . . . 108
5.6 Nomarski image of G15, at 10x magnification . . . 109
5.7 Nomarski image of G30, at 10x magnification . . . 109
5.8 Nomarski image of G40, at 10x magnification . . . 110
5.9 Nomarski image of G80, at 10x magnification . . . 110
5.10 Nomarski image of G120, at 10x magnification . . . 111
5.11 Nomarski image of G120 segmented using Otsu's method, showing the droplet-like defects as white features against a black background . 112
5.12 Density of droplet-like defects in the Nomarski images as a function of the number of quantum wells, calculated using image processing . . 113
5.13 XRD scans and simulations of the GaAsBi/GaAs MQW devices . . . 114
5.14 Possible Bi incorporation profiles. In all four cases shown here the MQW period and the average bismuth content per period is the same, meaning that the 0-order satellite peak should occur at the same angle in XRD measurements . . . 115
5.15 Normalised PL spectra of a single quantum well GaAsBi test structure using 120 W/cm2 excitation at 532 nm . . . 117
5.16 PL spectra of the GaAsBi devices using 120 W/cm2 excitation at 532 nm118
5.17 Relationship between number of quantum wells and the PL peak intensity for the GaAsBi MQW devices. The points are connected with the black line to guide the eye. The point shown for G120 is from the middle of the wafer . . . 119
5.18 Diagram showing the band structure (black) for one of the GaAsBi quantum wells in device G2 using the structural parameters from XRD simulations ($L = 7.95$ nm, x= 4.29%). The bound state energies are shown for electrons (green), light holes (red), and heavy holes (blue).122

5.19 Contour plot of the dependence of the ground state transition energy in a GaAsBi/GaAs QW on the well width and bismuth content. The contour labels denote the transition energy. The red circle indicates the measured well width and bismuth content for G2 from the XRD simulation (L = 7.95 nm, x= 4.29%, see table 5.2). The black line is the contour corresponding to the measured ground state transition energy of G2 from PL (see 5.3), which has been highlighted for clarity. 124
5.20 Comparison of PL peak energy and ground state transition energy for series of GaAsBi/GaAs MQWs. The error bars for the PL data assume an accuracy of ± 3 nm for determining the peak energy from the relatively broad PL emission 125
5.21 Dark currents as a function of bias for the GaAsBi/GaAs MQWs grown in this work 126
5.22 EL spectra of series G devices, GaAsBi/GaAs MQWs grown in this work, using 20 A/cm^2 128
5.23 EL spectra of series C GaAsBi/GaAs MQWs grown by Richards et al. for comparison [20], using 20 A/cm^2 129
5.24 Integrated EL as a function of strain-thickness product for series G (blue circles) and series C (red circles), using 20 A/cm^2 130
5.25 Collage of microscope images showing EL of GaAsBi/GaAs MQW devices using 20 A/cm^2. The shadow of the top contact probe tip is visible in the bottom middle of each device, and its effect on the EL intensity is neglected. The shadow of the gold contact shows up as the black "eyeball" inside the circular mesa. Device G30 is not considered for this analysis due to its anomalously low EL intensity relative to the other devices 132
5.26 Current dependent EL measurements of G40 134
5.27 Current dependent radiant intensity of G40 EL emission 135
5.28 Spectra of three near-infrared LEDs operating at 8 A/cm^2: a strain balanced InGaAs/GaAsP 65 MQW device, a 95 nm bulk GaAsBi device grown in chapter 4, and the brightest of the GaAsBi/GaAs MQWs grown in this chapter (G40). Note that the noise floor of the InGaAs device appears more intense than it is in reality, since a neutral density filter was used to attenuate its emission 136

List of Tables

4.1 List of devices grown for this work 77
4.2 Bismuth content and thickness of the devices studied in this work, from XRD simulations assuming a single uniform layer of GaAsBi . . . 88

5.1 Summary of devices grown in this work (series G) and devices grown by R. Richards [20] (series C), which are used as a comparison. The number in the device names indicates the number of wells in the MQW stack 104
5.2 Summary of the XRD fitting parameters calculated using RADS Mercury 116
5.3 Summary of the PL data for the GaAsBi/GaAs MQWs 119
5.4 Effective masses used for calculating bound state energy levels in the GaAsBi/GaAs quantum wells, relative to the electron mass [6, 11] . . . 121

List of Abbreviations

Al	Aluminium
As	Arsenic
Be	Beryllium
Bi	Bismuth
In	Indium
N	Nitrogen
P	Phosphorus
Si	Silicon
Sb	Antimony

BEP	Beam equivalent pressure
EL	Electroluminescence
FEL	Fast entry lock
MBE	Molecular beam epitaxy
MQW	Multiple-quantum well
PL	Photoluminescence
RHEED	Reflection high energy electron diffraction
STM	Scanning tunnelling microscope
x	Commonly used to denote fractional composition of ternary III-V alloys
XRD	X-ray diffraction

Chapter 1

Review of semiconductor physics

1.1 Binary III-V semiconductors and homoepitaxy

Gallium arsenide is a binary III-V semiconductor alloy with a direct band gap of 1.42 eV at room temperature, and a lattice constant of 0.565325 nm [1, 2]. GaAs crystallises in the zinc-blende structure as shown in figure 1.1 and is one of the most widely studied and mature semiconductor materials [3]. GaAs is also relatively easy to grow in MBE, due to it possessing a large temperature window for epitaxial growth and a relatively low surface oxide removal temperature. This makes GaAs an excellent choice as a host material for dilute bismides from a growth point of view. The growth of GaAs using MBE will be described in section 2.2.3.

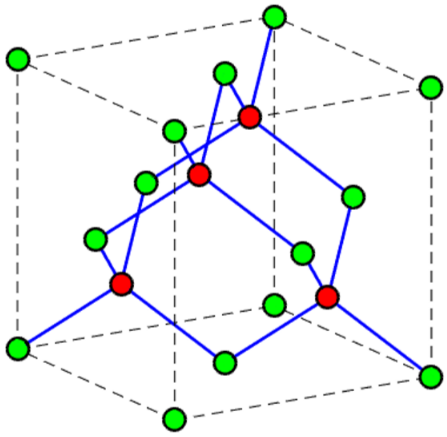

FIGURE 1.1: Unit cell showing the zinc blende crystal structure of GaAs. The red and green circles represent Ga and As atoms respectively. The blue lines represent bonds

Each GaAs unit cell contains four gallium atoms, with each being bonded to four arsenic atoms. The zinc blende structure shown in figure 1.1 is only found in the bulk of the crystal and not at the surface, as it is energetically unfavourable for the lattice to terminate with unsatisfied "dangling" bonds. At the crystal surface the atoms form into a reconstruction to minimise the surface free energy. This reconstruction is periodic, and its structure depends on the surface temperature and incident molecular beam fluxes.

The surface reconstruction is referred to as $(n \times m)$ where n and m are integers that refer to the periodicity of the reconstruction in the plane of the surface relative to the lattice constant, in the $[\bar{1}10]$ and $[110]$ crystal directions respectively. The surface reconstruction can be identified and studied using RHEED, which will be explained in greater detail in section 2.4. As an example, the $(001) - \beta(2 \times 4)$ reconstruction of GaAs is shown in figure 1.2.

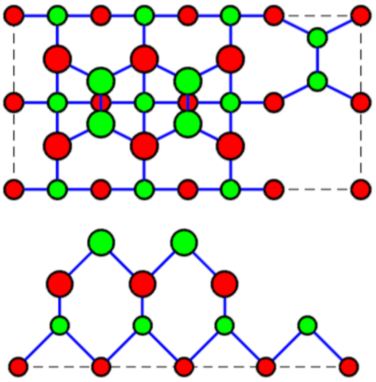

FIGURE 1.2: The GaAs $(001) - \beta(2 \times 4)$ surface reconstruction. (top) Top view, (bottom) side view. The red and green circles represent Ga and As atoms, respectively. The size of the atoms indicates which plane the atom is in. Adapted from [4]

1.1.1 Band gap dependence on temperature

If the temperature of a semiconductor is changed, thermal expansion causes the lattice parameter to vary. This changes the size of the Brillouin zone in reciprocal space, and hence the band gap varies with temperature. This has important consequences as the emission and absorption wavelengths of semiconductor devices will vary with temperature. Devices often have to be aggressively cooled to maintain stable performance, such as InGaAsP/InP 1300-1550 nm telecommunications lasers [6]. The change of the band gap with temperature can be modelled using the empirical model of Varshni, see equation 1.1 [5].

$$E_g(T) = E_0 - \frac{\alpha T^2}{\beta + T} \tag{1.1}$$

Here E_0 is the band gap at absolute zero, and α and β are fitting coefficients. The band gap of most III-V semiconductor alloys tends to decrease with increasing temperature. Note that heating the device is not usually considered a viable method for producing a device with longer wavelength absorption or emission, as the dark current of the device increases exponentially with temperature.

1.1.2 Homoepitaxy

The deposition of a material onto a substrate made from the same material is termed homoepitaxy. However, the band gaps accessible using homoepitaxy of III-V semiconductors are restricted to binary alloys and the available substrates.

1.2 III-V alloys, heteroepitaxy, and strain

The growth of different semiconductors in contact with each other is termed heteroepitaxy. If the different semiconductor materials have a different band gap then structures such as quantum wells and barriers can be created, with the band alignment dependent on the conduction and valence band offsets.

1.2.1 Ternary III-V alloys

While binary III-V semiconductors can be used to make a limited range of devices, far more flexibility is offered by alloying two binary materials to produce a ternary alloy. The lattice constant a of a ternary alloy can be described using Vegard's law, see equation 1.2 [7].

$$a(GaAs_{1-x}Bi_x) = (1-x)a(GaAs) + xa(GaBi) \tag{1.2}$$

The band gap of most ternary alloys can be modelled in a similar way, with the addition of a material-dependent bowing parameter. The lattice constants and band gaps of a variety of III-V semiconductors are plotted in figure 1.3.

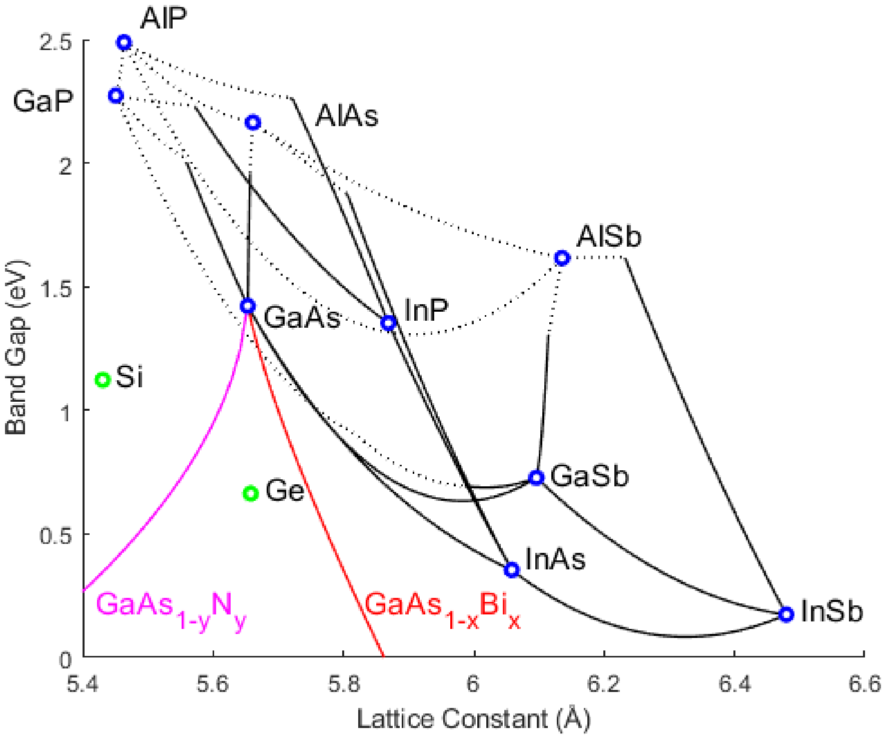

FIGURE 1.3: Lattice constant plotted against band gap for III-V semiconductors. Binary alloys are displayed as blue points, with ternary alloys as solid (direct bandgap) or dashed (indirect bandgap) lines. The alloys GaAsN and GaAsBi are plotted in magenta and red respectively. The group IV elements Si and Ge are included for completeness. Data from [2], except GaAsN [14] and GaAsBi [10]

1.2.2 Band gap of GaAsBi

However, highly-mismatched alloys such as GaAsBi have a more complicated band gap composition dependence [8, 9]. In GaAsBi, the localised bismuth atoms give rise to an energy level close to the GaAs valence band maximum. The interaction of the localised states with the valence band maximum induces a splitting of the valence band into two sub-bands, E_+ and E_-, with the higher energy sub-band becoming the new valence band edge. As described by Mohmad [10], the energy of the sub-bands relative to the GaAs valence band maximum is given in equation 1.3.

$$E_{\pm} = \frac{E_{Bi} \pm \sqrt{E_{Bi}^2 + 4xC_{Bi}^2}}{2} \tag{1.3}$$

Here E_{Bi} is the energy of the localised bismuth states, C_{Bi} is a parameter that models the strength of the interaction between the localised bismuth states and the valence band of GaAs, and x is the bismuth content.

The shift of the conduction band in GaAsBi is modelled as varying linearly between the values of GaAs and GaBi, see equation 1.4 [10].

$$E_{CB-VCA} = E_g - \Delta E_{CBM} x \tag{1.4}$$

Here E_g is the conduction band minima of GaAs relative to the valence band maxima, and ΔE_{CBM} is the conduction band offset between GaAs and GaBi [8, 9]. The band gap of GaAsBi is then found using equation 1.5 [10].

$$E_g(GaAsBi) = E_{CB-VCA} - E_{+} \tag{1.5}$$

The parameters C_{Bi}, E_{Bi}, and ΔE_{CBM} were treated as fitting parameters and are calculated by Mohmad as 1.65, -0.4, and 2.3 eV, respectively [10]. The variation of the band offsets and the band gap of GaAsBi upon incorporation into GaAs are shown in figure 1.4.

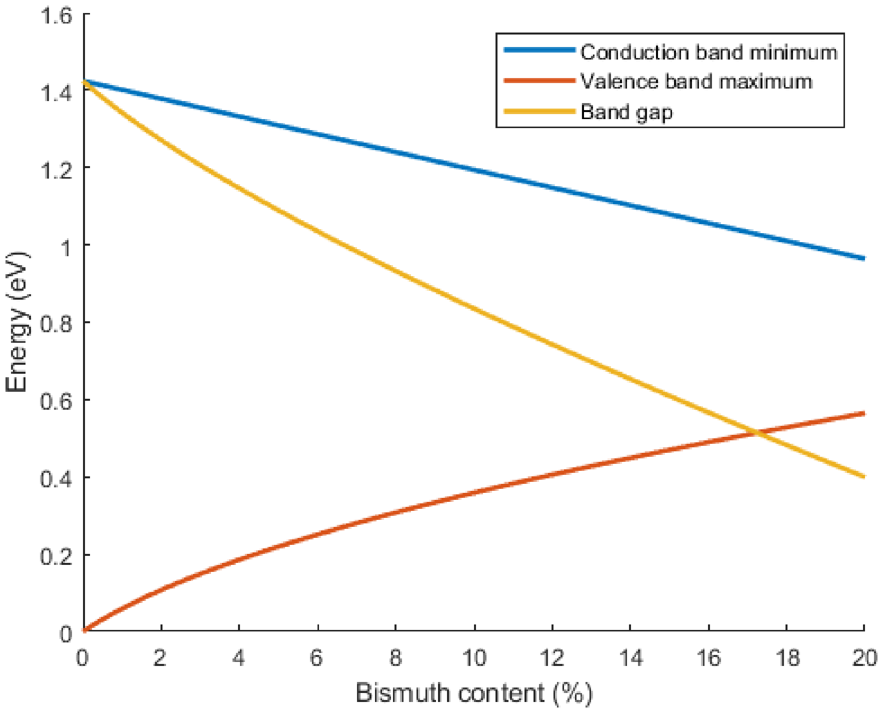

FIGURE 1.4: Band offsets and band gap of GaAsBi relative to the valence band maximum of GaAs as a function of bismuth content

From figure 1.4, the band gap of GaAsBi decreases rapidly as the bismuth content is increased. At 1 % bismuth, approximately 72 % of the band gap reduction is caused by the valence band shift. By 5 % bismuth, this has reduced to 66 %. The model predicts that GaAsBi should reach a negative band gap at 30 % bismuth and that GaBi should have a band gap of -2.34 eV. This extrapolation of the band gap of GaBi is in poor agreement with theoretical modelling, which suggests a value of -1.45 eV [19]. However, the model is in good agreement with experimental data for bismuth contents less than 12 %.

1.2.3 Localised states in GaAsBi

The dilute concentration and large size of the bismuth atoms, relative to the arsenic atoms that they replace, leads to non-uniform perturbations in the periodic potential in the crystal. This manifests as a distribution of radiative localised states extending into the band gap. From power and temperature dependent PL measurements, Wilson et al. identified the presence of two Gaussian distributions below the mobility edge contributing to the localised density of states [**?**]. The two Gaussian distributions were attributed to short range alloy disorder and excess hole traps caused by Bi-induced point defects during growth. Richards et al. calculated that the localised states extend up to 75 meV below the mobility edge [28]. The effect of the localised states is to broaden the emission and absorption spectra of GaAsBi layers.

1.2.4 Lattice mismatch and strain relaxation

From figure 1.3, a large range of ternary III-V alloys have been studied, with direct band gaps between 0 and 2.3 eV. However, in reality the compatibility of an alloy with a given substrate is restricted by the mismatch strain between the alloy layer and the substrate. A large lattice mismatch will lead to the build up of strain as the layer thickness increases, eventually leading to the formation of misfit dislocations at the interface. The lattice mismatch strain f is defined in equation 1.6 [12].

$$f = \frac{a_s - a_l}{a_l} \tag{1.6}$$

The epilayer is said to be in tensile or compressive strain for $f > 0$ and $f < 0$ respectively. As the growth proceeds, the residual strain energy stored in the pseudomorphic epilayer is a function of the lattice mismatch and the layer thickness. Eventually the layer becomes so thick, and the strain becomes so large, that it is energetically favourable for threading dislocations that are already present in the epilayer to move to the substrate/epilayer interface and become misfit dislocations. The point at which this happens is known as the Matthews-Blakeslee critical thickness h_c [13], and is shown in equation 1.7 [12].

$$h_c = \frac{b(1 - \nu cos^2(\alpha))(ln(h_c/b) + 1)}{8\pi|f|(1 + \nu)cos(\lambda)} \tag{1.7}$$

Here $\nu = 0.312$ is the Poisson ratio for GaAs, b is the length of the Burgers vector for the dislocation, α is the angle between the Burgers vector and the line vector for the dislocations, and λ is the angle between the Burgers vector and the vector in the direction of the dislocation with respect to the substrate. Misfit dislocations are highly deleterious to the optoelectronic performance of the epilayer. Therefore, it is critical to avoid strain relaxation where possible.

For 60° dislocations on $a/2$<110>$\{111\}$ slip systems, $cos(\alpha) = cos(\lambda) = 0.5$, and $b = 0.4$ nm. The critical thickness of an epilayer as a function of its lattice mismatch strain is shown in figure 1.5.

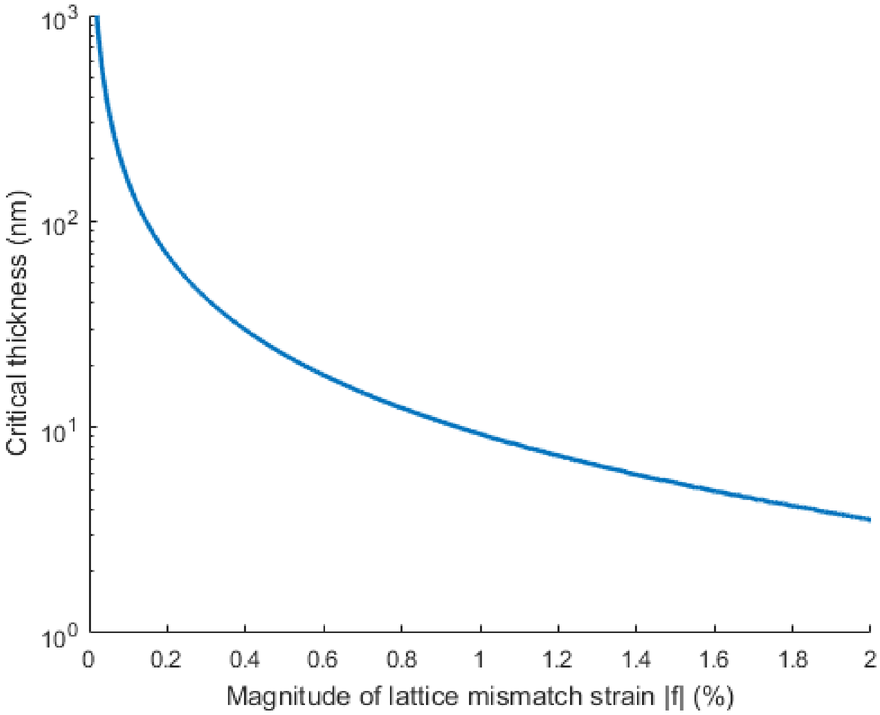

FIGURE 1.5: Matthews-Blakeslee critical thickness as a function of the lattice mismatch strain

From figure 1.5, the Matthews-Blakeslee critical thicknesses for 1% and 2% mismatch strain are roughly 9.5 and 3.5 nm respectively on GaAs. However, different authors give different numbers for the Matthews-Blakeslee critical thickness [12, 13, 18], which highlights how difficult it is to measure in practice.

When there are no more threading dislocations left in the strained layer further strain relaxation cannot occur until the strain energy is large enough for the generation of further dislocations. Therefore, there is a second critical thickness, above which the relaxation of strain by dislocation generation severely degrades the epilayer properties [17] [18].

1.2.5 Band gap of GaAs based ternary III-V alloys as a function of mismatch strain

Semiconductor devices emitting or absorbing in the near-infrared (750-2500 nm) are used in a huge variety of applications. One of the main factors in the affordability of the devices is the cost of the substrate, with InAs and InP substrates being many time more expensive than GaAs. For devices based on GaAs, the accessible spectral range is limited by the mismatch strain of the deposited epilayers. The band gap dependence on the mismatch strain of several GaAs based alloys (InGaAs [2], GaAsSb [2], GaAsBi [10], GaAsN [14]) is shown in figure 1.6.

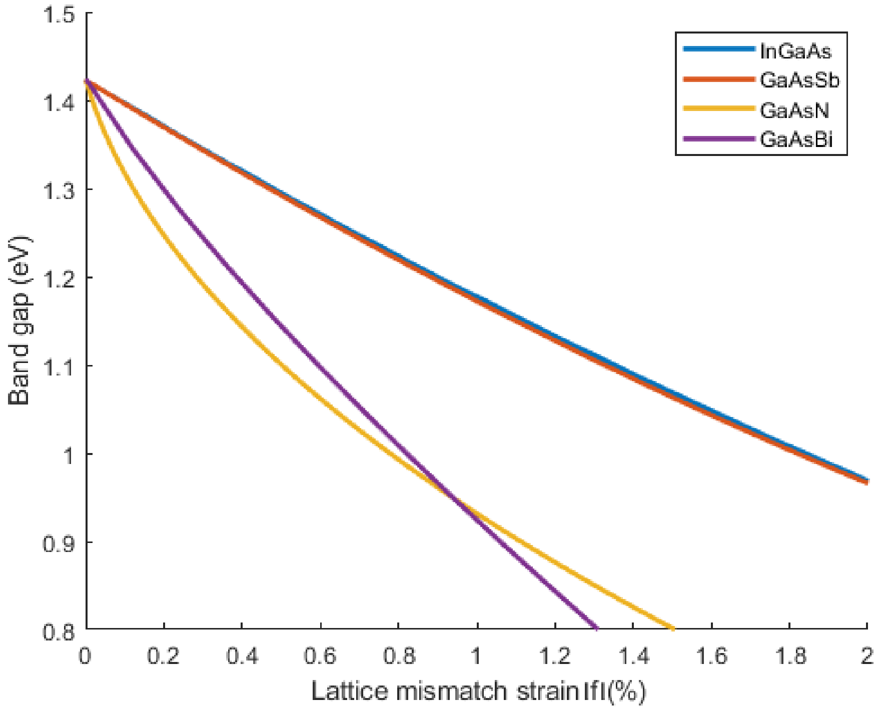

FIGURE 1.6: Magnitude of lattice mismatch strain relative to a GaAs substrate, plotted against band gap for GaAs based III-V semiconductors. Note that GaAsN is tensile-strained on GaAs while the other alloys are all compressively strained on GaAs.

From figure 1.6, devices made from InGaAs and GaAsSb can reach a band gap of 1 eV, however, the layer thickness would have to be less than 3.5 nm (from figure 1.5) to avoid strain relaxation, at which point quantum confinement would severely blue shift the ground state transition energy. GaAsN and GaAsBi have a larger change in band gap for a given amount of mismatch strain and can reach a 1 eV band gap with only 0.8% mismatch strain on GaAs. This corresponds to a critical thickness of around 12 nm. Therefore, these two alloys have greater flexibility for growing near-infrared optoelectronic devices on a GaAs substrate, and can reach smaller band gaps without strain relaxation.

Due to the severe degradation in optoelectronic properties with strain relaxation, the trade-off between layer thickness and effective band gap restricts the use of bulk layers in optoelectronics applications to lattice-matched or near-lattice-matched materials such as $In_{0.53}Ga_{0.47}As/InP$ [20].

1.3 Doping of semiconductors and related devices

By substituting the atoms in a semiconductor crystal lattice with small concentrations of impurity atoms, the electrical properties of the crystal can be dramatically altered. The impurity atoms are required to have a different number of valence electrons compared to the atoms being replaced in the host material. If the impurity has one more (fewer) valence electron than the atom it replaces the impurity is known as a donor (acceptor), as the impurity atom can contribute a free electron (hole) to the semiconductor, and the resulting doped semiconductor is known as n-type (p-type).

The situation described above is easiest to understand for elemental semiconductors such as silicon, however for III-V semiconductors, the doping behaviour depends on where the dopant atoms are substituted into the lattice. Group II elements can be used to replace the group III atoms to produce a p-type semiconductor, and group VI elements can be used to replace the group V elements to produce an n-type semiconductor. Common p-type dopants for use with III-V semiconductors include beryllium and zinc.

Group IV elements such as silicon can be used as either an n-type or p-type dopant (amphoteric dopant), depending on whether a group III or group V atom is substituted. Silicon doping typically produces n-type GaAs during MBE growth, although there have been investigations into forming p-type GaAs using silicon doping [11].

In this work beryllium and silicon are used as p-type and n-type dopants respectively. The effect of adding dopants is to add extra energy levels in between the valence band and the conduction band for electrons to occupy. These energy levels are close to the conduction band (valence band) in an n-type (p-type) semiconductor, meaning that the electrons can be easily excited into the conduction band (acceptor states).

1.3.1 PN junction

One of the most useful semiconductor devices is the pn junction, consisting of an interface between a p-type and an n-type semiconductor. Pn junctions are widely used in diodes, LEDs, and transistors.

At equilibrium the n-type region has an excess of electrons which can diffuse across the junction to the p-type region, leaving behind a positively charged ion in the n-type region. The minority electrons can then penetrate a certain distance into the p-type region before recombining with a hole. Similarly, the excess holes in the p-type region can diffuse to the n-type region, leaving behind negatively charged ions. These two processes form the diffusion current. The result is that the junction becomes depleted of mobile carriers, forming a depletion region which extends a small distance into the n and p-type layers. The build-up of ions creates an electric field across the junction, causing the carriers to drift in the opposite direction to the diffusion current: this is the drift current. The magnitude of the voltage at the point when the diffusion current and drift current are equal and opposite is known as the built-in potential V_{bi}. A diagram of a pn junction at zero bias is shown in figure 1.7.

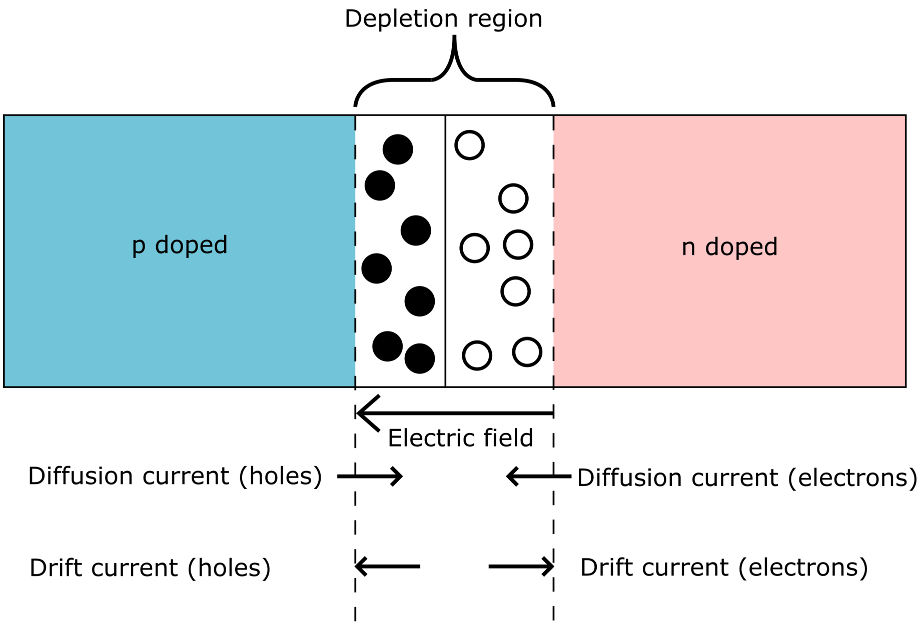
Depletion region
p doped
n doped
Electric field
Diffusion current (holes)
Diffusion current (electrons)
Drift current (holes)
Drift current (electrons)

FIGURE 1.7: Pn junction at zero bias. The filled circles represent electrons, and the open circles represent holes.

The conduction properties of a pn junction vary considerably if a bias voltage V is applied. In the case of forward bias (positive terminal connected to the p-type side) the voltage across the junction becomes $V_{bi} - V$, indicating that an increase in forward bias voltage will decrease the potential barrier across the junction. This results in an increase in the current flowing across the junction.

The width of the depletion region decreases as the carriers are pulled towards the junction. In the case of negative bias the voltage across the junction becomes $V_{bi} + V$, indicating that an increase in reverse bias voltage will increase the potential barrier across the junction. The result is that only a small current can flow across the junction. The width of the depletion region increases as the carriers are forced away from the junction.

1.3.2 PIN junction

A pin diode is similar to a pn diode, but with the addition of a thick intrinsic layer (i-region) between the n and p-type layers. Ideally, the i-region is fully depleted of charge carriers at zero bias, however, in practice the width of the depletion region depends on the concentration of impurities in the i-region. In addition, dopants from the n and p-type layers can diffuse into the i-region during growth, acting as impurities. A reverse bias can be applied across the device to fully deplete the i-region. When an incoming photon is absorbed in the i-region of a pin diode it creates an electron-hole pair, which is then separated by the electric field across the depletion region, due to the bias voltage across the device. Only the carriers near to the depletion region contribute to the current so that a wider depletion region can lead to a device with increased photo-responsivity. Therefore, the pin structure is often used in photo-detectors and solar cells.

1.4 Light emitting diodes

Light emitting diodes (LEDs) are common optoelectronic devices that have a wide range of applications due to their low cost, highly efficient conversion of electricity into light, and peak emission wavelengths in the ultra-violet, visible, and near-infrared regions of the spectrum. Semiconductor LEDs are based on pn or pin diodes, with the current flowing across the depletion region leading to radiative recombination between electrons and holes. The current, and hence the light output of the diode, is greatly increased by operating the device in forward bias.

The emission wavelength of the LED is determined by the band gap of the material in the depletion region, meaning that the active region does not need to be made from the same material as the substrate or the cladding layers. While a bulk active region is viable in an LED the probability of the electrons and holes coming into contact and recombining is not optimal. The radiative recombination rate can be increased by incorporating quantum wells into the depletion region. Electrons and holes that fall into the quantum well are trapped which localises the carriers into a smaller density. This increases the spatial overlap of the electron and hole wavefunctions and leads to a higher radiative recombination rate. Careful consideration of the well and barrier materials and their composition is necessary to successfully confine the carriers and achieve emission at the desired wavelength.

Aside from an active region embedded inside the depletion region of a pn or pin diode an LED structure contains several additional features which improve the light output. While the growth undertaken in this work does not contain any LED specific optimisations it is useful to know what improvements could be expected if using an optimised structure. LEDs are typically fabricated using a contact pattern which covers as little of the top surface as possible to ensure that the opaque contact material does not block the emitted light. Alternatively, the LED may be fabricated with a transparent contact material such as indium tin oxide or aluminium doped zinc oxide [33].

When an electron and a hole recombine in the active region a photon is emitted in a random direction. However, the light is only usable if it is emitted from the surface of the LED. The growth of a distributed Bragg reflector (DBR) can help to reflect light that is emitted downwards back towards the surface, thereby improving the usable light output. A DBR typically consists of an AlGaAs/GaAs superlattice, with the thickness and number of periods optimised for the desired peak wavelength of the LED [32].

III-V semiconductor materials often have a relatively high refractive index leading to light being totally internally reflected unless it is within a narrow cone of escape with respect to the surface. For a GaAs/air interface the escape cone occupies a solid angle of approximately 0.25 sr for 1050 nm light, i.e. only 2% of the light escapes the top surface of the LED. This is before considering that around one third of the light emitted into the escape cone will be reflected at the interface. Therefore, LEDs often make use of a surface mount epoxy lens which has a refractive index in between that of GaAs and air. The small change in refractive index increases the size of the escape cone at the GaAs: epoxy interface, and the top surface of the lens can be curved to prevent total internal reflection at the epoxy: air interface and to focus the light [31].

LEDs also typically have a thick transmissive layer to spread the current evenly over the chip and prevent current crowding and subsequent heating. For a near-infrared LED, the current spreading layer is typically a several micron thick layer of AlGaAs with an aluminium content above 45% to ensure an indirect band gap and efficient transmission of the light emitted from the active region to the surface [32].

1.5 Near-infrared broadband light sources & optical coherence tomography

One potential application which may suit dilute bismide semiconductors is as a near-infrared broadband light source. Such light sources are commonly used in optical coherence tomography (OCT) which is a non-invasive medical imaging technique that uses low coherence interferometry to generate 2D and 3D images of subsurface features in biological tissue, giving doctors valuable information about the patients health.

A key metric of the OCT imaging system is the axial imaging resolution Δz which is proportional to the square of the central wavelength of the light source λ_0 and inversely proportional to its spectral width $\Delta\lambda_0$, see equation 1.8.

$$\Delta z = \frac{2ln2}{\pi}\frac{\lambda_0^2}{\Delta\lambda_0} \tag{1.8}$$

Equation 1.8 is only valid for a Gaussian shaped emission spectrum whereas the axial resolution is degraded if the emission spectrum of the light source is non-Gaussian. For example, in [24] the calculated axial resolution of an OCT system using a broadband 1200 nm light source was degraded from 2.5 µm to 2.9 µm due of the emission spectrum being non-Gaussian.

There are several near-infrared wavelength bands suitable for OCT imaging based on the absorption coefficient of the target tissue. The light must be weakly absorbed by the tissue in order to image features that are deeper below the surface: this restricts the central wavelength of the light source. The wavelength range 1000-1060 nm is used for ophthalmology applications as this wavelength has the greatest penetration depth in eye tissue [21, 22]. Since the central wavelength is fixed by the application the axial resolution of the OCT system is most easily improved by increasing the spectral width of the light source: there is a need for broadband light sources with emission centred around 1000-1060 nm.

Several different technologies are used as light sources for OCT, including swept lasers, luminescent doped fibers, and super-luminescent diodes. Super-luminescent diodes based on InGaAs quantum wells are the most widespread technology for broadband light sources above 1000 nm due to their relatively low cost and small size, with a typical spectral width of 50-70 nm. Swept lasers and luminescent doped fibers can offer slightly higher performance at greatly increased cost.

1.5.1 State of the art broadband light sources

There is a great deal of flexibility for designing LEDs based on quantum wells to give an broader emission spectrum: by incorporating quantum wells with different thickness or composition, or by incorporating wells which have transitions between excited states, e.g. e2 $\rightarrow$ hh2, which is orders of magnitude more likely than the e1 $\rightarrow$ hh2 transition. Modelling the emission spectrum when including excited states is complicated since the prominence of higher order transitions changes with the injection current, which could result in a non-Gaussian emission spectrum and thus a lower axial resolution of the OCT system.

In [23], the authors demonstrated a layer of InGaAs grown close to its critical thickness on a GaAs substrate emitting at 1000 nm with a FWHM of 80 nm. Indium migration and desorption was enhanced due to a high growth temperature resulting in InGaAs 3D nanostructures with a large size and composition distribution.

The authors of [25] reported a broadband light source based on InAs quantum dots, with central wavelengths of between 1120 and 1190 nm and a FWHM of around 160 nm. The authors relied on a wide distribution in the size of the self-assembled quantum dots and included four layers of dots with different capping layer thicknesses to sequentially shift the emission wavelength, thereby forming a broad spectrum.

1.5.2 Output power requirements for an OCT light source

In [26], the authors calculated the maximum safe exposure limit for the human retina as 2 mW for a 10 second exposure using 1060 nm light. This represents the upper limit on how intense the GaAsBi devices must be to compete with InGaAs based LEDs for retinal imaging. However, the actual power during use of the OCT system is likely to be much lower: in [27] the power incident on the pupil was 226 μW, using 564 nm light. This was despite the maximum permissible exposure limit being 3.6 mW at 564 nm for a 2 hour exposure.

1.5.3 Applicability of GaAsBi to broadband light sources

Quantum well LEDs with GaAsBi active regions may have potential as broadband light sources for OCT applications. As discussed in section 1.2.3, localised states lead to a significant broadening of the luminescence from GaAsBi. By combining the luminescence from several different quantum wells, or from excited state transitions in a single quantum well or series of identical quantum wells, the overall emission spectrum can be broadened, as shown in figure 1.8.

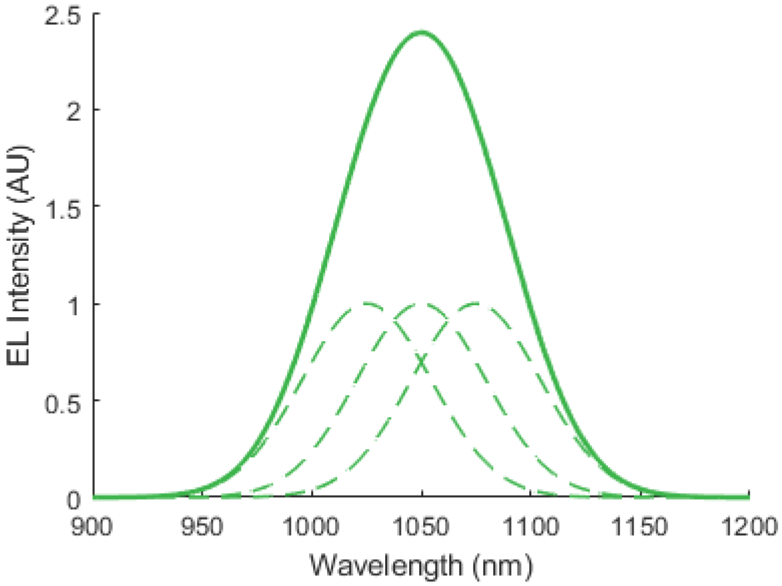

FIGURE 1.8: Simulated output spectrum (solid line) from GaAsBi quantum well based LED emitting at 1050 nm based on the sum of three component spectra (dashed lines), which could be from three different quantum wells or from a single quantum well with three radiative transitions.

The overall output spectrum of a GaAsBi LED, with its large distribution of radiative localised states, may therefore be made broader than an InGaAs LED for the same level of device complexity (e.g. the same number of wells).

According to figure 1.4, the target central wavelength of 1000 to 1060 nm (corresponding to band gaps of 1.238 to 1.167 eV) can be reached by bulk GaAsBi with a bismuth content of 2.51 to 3.65%, respectively [10]. For a quantum well LED the bismuth content should be higher (approximately 4 to 5%) with the necessary value dependent on the well width and the degree of blue shift resulting from the quantum confinement. This should enable fully-strained quantum wells on a GaAs substrate emitting near the target central wavelength.

Several authors have reported that the luminescence intensity of GaAsBi/GaAs heterostructures peaks at around 3.5 to 4.5% bismuth due to enhanced band offsets and the surfactant effect of the bismuth atoms on the growth [29, 30]. The decrease in luminescence intensity observed after 4.5% bismuth was attributed to bismuth-related growth defects and strain relaxation. This range of bismuth contents corresponds to a band gap which is close to the desired value for an OCT light source.

If the output power can reach the necessary level, GaAsBi LEDs may be a promising as a broadband light source for OCT imaging. This will require incorporating a high quality GaAsBi QW active region into an optimised LED structure.

1.6 Summary

The basic structural and optical properties of GaAs and GaAsBi have been introduced. In addition, the operation of relevant semiconductor diodes has been discussed. GaAsBi may be a promising material for a broadband light source for OCT imaging due to its significant band gap reduction with only a small bismuth incorporation and broad emission due to radiative transitions from localised states.

Bibliography

[1] H. C. Casey and M. B. Panish, *Heterostructure Lasers*, Academic Press, New York, Part A, 1978

[2] I. Vurgaftman et al., *Band parameters for III-V compound semiconductors and their alloys*, Journal of Applied Physics **89**, 5815 (2001)

[3] S. Adachi, *GaAs, AlAs, and* $Al_xGa_{1\text{-}x}As$*: Material parameters for use in research and device applications*, Journal of Applied Physics **58**, R1 (1985)

[4] V. P. Labella et al., *Atomic structure of the GaAs(001)-(2x4) surface resolved using scanning tunneling microscopy and first-principles theory*, Physical Review Letters **83**, 15 (1999)

[5] Y. P. Varshni, *Temperature dependence of the energy gap in semiconductors*, Physica **34**(1), 149-154 (1967)

[6] S. J. Sweeney and S. R. Jin, *Bismide-nitride alloys, promising for efficient light emitting devices in the near and mid infrared*, Journal of Applied Physics **113**, 043110 (2013)

[7] L. Vegard, *Die konstitution der mischkristalle und die raumfullung der atome*, Zeitschrift für Physik **5**(1), 17-26 (1921)

[8] K. Alberi et al., *Valence band anticrossing in mismatched III-V semiconductor alloys*, Physical Review B **75**, 045203 (2007)

[9] K. Alberi and O. D. Dubon, *Valence band anticrossing in* $GaBi_xAs_{1\text{-}x}$, Applied Physics Letters **91**, 051909 (2007)

[10] A. R. Mohmad et al., *Localization effects and band gap of GaAsBi alloys*, Physica Status Solidi B **251**(6), 1276-1281 (2014)

[11] A. A. Quivy, *P-type doping of GaAs (001) layers grown by MBE using silicon as a dopant*, Journal of Crystal Growth **206**(3), 171-176 (1999)

[12] J. E. Ayers, *Heteroepitaxy of Semiconductors*, CRC Press, Boca Raton, Florida, 2007

[13] J. W. Matthews and A. E. Blakeslee, *Defects in epitaxial multilayers: I. Misfit dislocations*, Journal of Crystal Growth **27**, 118-125 (1974)

[14] W. Shan et al., *Band anticrossing in III-N-V alloys*, Physica Status Solidi B **223**, 75-85 (2001)

[15] K. Krambock et al, *Arsenic antisite-related defects in low temperature MBE grown GaAs*, Semiconductor Science and Technology **7**, p. 1037-1041 (1992)

[16] A. A. Bernussi et al., *Optical and structural properties of low temperature GaAs layers grown by molecular beam epitaxy*, Brazilian Journal of Physics **24**, 1 (1994)

[17] A. V. Drigo, *On the mechanisms of strain release in molecular-beam-epitaxy-grown* $In_xGa_{1-x}As$*/GaAs single heterostructures*, Journal of Applied Physics **66**, 1975 (1989)

[18] P. R. Griffin et al., *Effect of strain relaxation on forward bias dark currents in GaAs/InGaAs multiquantum well p–i–n diodes*, Journal of Applied Physics **80**, 10 (1996)

[19] A. Janotti et al., *Theoretical study of the effects of isovalent coalloying of Bi and N in GaAs* Physical Review B **65**, 115203 (2002)

[20] T. W. Nee and A. K. Green *Optical properties of InGaAs lattice-matched to InP* Journal of Applied Physics **68**, 5314 (1990)

[21] H. M. Subhash and R. K. Wang, *Advanced Biophotonics: Tissue Optical Sectioning*, 179, CRC Press, Boca Raton, Florida (2014)

[22] A. Zhang et al., *Multifunctional 1050 nm Spectral Domain OCT System at 147 kHz for Posterior Eye Imaging* Sovremennye Tehnologii v Medicine **7**, 1 (2015)

[23] N. Ozaki et al., *Growth of quantum three-dimensional structure of InGaAs emitting at 1 µm applicable for a broadband near-infrared light source*, Journal of Crystal Growth **477**, 230-234 (2017)

[24] S. Chen et al., *GaAs-based superluminescent light-emitting diodes with 290-nm emission bandwidth by using hybrid quantum well/quantum dot structures*, Nanoscale Research Letters **10**, 340 (2015)

[25] N Ozaki et al., *Superluminescent diode with a broadband gain based on self-assembled InAs quantum dots and segmented contacts for an optical coherence tomography light source*, Journal of Applied Physics **119**, 083107 (2016)

[26] S. Hariri et al., *Limiting factors to the OCT axial resolution for in-vivo imaging of human and rodent retina in the 1060nm wavelength range*, Optics Express **17**(26), 24304-24316 (2009)

[27] J. Yi et al., *Human retinal imaging using visible-light optical coherence tomography guided by scanning laser ophthalmoscopy*, Biomedical Optics Express **6**(10), 3701-3713 (2015)

[28] R. D. Richards et al., *Telecommunication wavelength GaAsBi light emitting diodes*, IET Optoelectronics **10**, 2, 4, p. 34-38 (2016)

[29] A. R. Mohmad et al., *The effect of Bi composition to the optical quality of* $GaAs_{1\text{-}x}Bi_x$, Applied Physics Letters **99**, 042107 (2011)

[30] D. Dagnelund et al., *Identification of an isolated arsenic antisite defect in GaAsBi*, Applied Physics Letters **104**, 052110 (2014)

[31] N. Dushkina, *Handbook of Optical Metrology: Principles and Applications, Second Edition* Edited by Toru Yoshizawa, CRC Press, Boca Raton, Florida (2017)

[32] H. K. H. Choy, *Design and fabrication of distributed Bragg reflectors for vertical cavity surface emitting lasers* PhD thesis, Massachusetts Institute of Technology (1998)

[33] D. Chen et al., *High-Performance GaN-Based LEDs With AZO/ITO Thin Films as Transparent Contact Layers*, IEEE Transactions on Electron Devices **64**, 6 (2017)

Chapter 2

Molecular Beam Epitaxy

2.1 Introduction

Molecular beam epitaxy is a technique that can be used to deposit thin films of materials onto a heated substrate inside a vacuum chamber. A large variety of elements are compatible with MBE, such that a huge number of technologically useful alloys and structures may be studied and produced on an industrial scale. MBE draws from the fields of surface chemistry, vacuum science, cryogenics, and semiconductor physics, to enable the deposition of thin films with monolayer level precision and atomically flat interfaces.

The MBE system used in this work was manufactured by Omicron and was assembled in late 2008. Effusion cells for aluminium, gallium, indium, arsenic, bismuth, silicon, and beryllium are fitted to the system to allow growth of semiconductor alloys based on the group III-arsenides. The MBE system uses 11.4 x 11.8 mm rectangular substrates which are cleaved from larger wafers.

The machine also contains a scanning-tunnelling microscope in an adjacent vacuum chamber, connected to the MBE growth chamber via a transfer tube. After growth in the MBE chamber, the epilayers may be transferred in-vacuo into the STM for further analysis. This allows study of the surface reconstruction without oxidation of the surface or the adsorption of atmospheric gases that would be caused by ex-situ transfer. However, the STM was not used in this work, and will not be discussed further.

2.2 Operating principles

In an MBE system, beams of molecules are generated through thermal evaporation of an ultra-pure source material. One or more of these molecular beams are directed towards a heated crystalline substrate where the molecules can be adsorbed. Thereafter, the molecules can either migrate around the surface before finding a suitable site to incorporate into the growth front, or desorb from the surface.

The temperature of the substrate must be carefully controlled to enhance the mobility of the adatoms, while minimising their thermal desorption. The optimum temperature for growth is further complicated if more than one element is being deposited, meaning the element that has a higher vapour pressure has to be oversupplied to overcome the larger losses due to desorption.

The deposition process can be studied using RHEED and takes place in an ultra-high vacuum to minimise the incorporation of residual gas atoms into the thin films. A cryo-panel is typically used to remove waste heat from the vacuum chamber, and also acts as a vacuum pump to further reduce the pressure in the system.

These operating principles will be explored in greater detail in this chapter.

2.2.1 Effusion cell design and operation

To generate the molecular beams, effusion cells are widely used. Several variants of effusion cell are used in MBE, depending on the necessary level of control over the beam flux and the properties of the source element. However, the basic design of most effusion cells is similar, and consists of an ultra-pure source element held inside a conical ceramic crucible. This crucible is heated from the outside by a tantalum filament, which is supported by struts made of pyrolytic boron nitride. The filament is designed to heat the crucible evenly, and the shape of the crucible is intended to give a relatively constant beam flux despite depletion of the source material. An electrical current is passed through the filament, and a thermocouple on the outside of the crucible is used for temperature feedback. The beam flux can be controlled by changing the temperature of the source material and can be shut off entirely by moving a shutter blade into the beam path. A specialised algorithm operating on the host PC controls the current to ensure stable cell temperatures and minimal overshoots when changing the temperature of the cell. A steel water cooling assembly typically surrounds the outside of the heating coil, to reduce heating of the MBE chamber by the cell. The effusion cell is held in place by a ConFlat flange and can be removed for maintenance or replaced entirely with an effusion cell containing another element.

The growth chamber is designed such that the effusion cells are mounted below or horizontally relative to the substrate. Several of the source elements (Al, Ga, In, Bi) are liquid at the required operating temperatures, and would leak from the crucible if mounted upside down.

Source purity

The source materials used in an MBE machine can range in purity from 4N (99.99 %) to 8N (99.999999 %), depending on the element and its intended use. The market for such high purity metals is rather small, and thus the cost is roughly exponentially dependent on the purity. For the growth of devices made from mature alloys with extremely low dark currents, higher purity elements are necessary. For the growth of technologically immature alloys like GaAsBi, dark currents in devices are more likely to be dominated by material defects than by impurities, and it is difficult to justify the cost of using the highest purity source elements; see chapter 4 for an investigation into the dark currents of GaAsBi.

Crucible design

The crucibles used in effusion cells are typically made of pyrolytic boron nitride, which can be produced at high purity, has excellent resistance to thermal shock, is chemically inert with most other compounds, has low wettability with most liquid metals used in MBE, has good thermal conductivity, and high electrical resistance.

Other materials such as pyrolytic graphite, alumina, quartz, beryllium oxide, magnesium oxide, tungsten, and tantalum can be used depending on the application.

Effusion cell design considerations for specific elements

Modifications to the basic effusion cell design are necessary for most elements. It is useful to split the considerations for using a particular element into three categories: the engineering challenges involved in generating a usable and stable molecular beam, the maturity of the growth of compounds of the chosen element, and its toxicity or other dangerous properties.

The widely used group III elements (Al, Ga, and In), and Bi have relatively low toxicity, and can be used in an effusion cell that closely matches the description given in section 2.2.1. However, Al is typically used in a cold-lip effusion cell to prevent the Al from creeping up the side-wall of the crucible. Ga is typically used in a hot-lip effusion cell to prevent condensation and Ga droplet formation near the orifice. The cold-lip and hot-lip effusion cells are designed to have a temperature gradient along the crucible by utilising heater coils that are more closely spaced towards one end of the cell.

Ga and Bi are denser in their liquid state than in their solid state. Upon freezing, the solid metal starts forming at the surface, and the liquid bulk of the metal becomes trapped in a finite volume. As the liquid cools further and the solid volume at the surface grows larger, the pressure in the liquid increases and the crucible can crack, spilling the remaining liquid metal onto the delicate heater coil assembly. To prevent this, these elements are held at a temperature significantly higher than their melting point when not in use. In order to conduct maintenance on the growth chamber, all of the effusion cells must be below 100 °C to prevent boiling of residual water in the water-cooling assembly, meaning that the source elements must be solidified. To avoid damage to the crucible during solidification of the metals for maintenance (especially with Bi), the temperature of the effusion cell is ramped slowly through the freezing point, typically 0.1 °C/minute, compared to 30 °C/minute during normal operation. The risk of crucible damage is lessened somewhat with Ga since it can be kept at 70 °C during maintenance due to its low melting point of 30 °C. To prevent loss of temperature control during power outages, uninterruptible power supplies (UPS) systems are used.

The widely used group V elements (P, As, and Sb) are typically used in a valved cracker effusion cell, which consists of two heating stages separated by a valve. The two heating stages have minimal thermal crosstalk due to a water cooling shroud and can be set at different temperatures. The temperature of the first stage (crucible temperature) controls the rate at which the source evaporates, with the vast majority of the evaporating group V molecules being tetramers (As_4 in this work). Depending on the growth process being studied, the temperature of the second heating stage can be set to break the tetramers into dimers (As_2 in this work). The second stage, also known as a cracker, is a thin tube containing tantalum filaments which can further heat the evaporant before it reaches the growth chamber. In this work, the crucible temperature is typically set to 370 °C, and the cracker temperature is set to 650 °C (for As_4) or 1000 °C (for As_2). The difference in temperature required for the two processes (evaporation and cracking) shows the large difference in the intermolecular (Van der Waals bonding) and intramolecular (covalent) bond energies.

Arsenic is significantly more toxic than the group III elements used in this work [18], and as such it is beneficial to have a larger volume of As in the effusion cell to reduce the refilling frequency and minimise the handling of As by the users. For reference, the As crucible used in this work has a volume of 500 cm^3, while the other sources are 10-100 cm^3. Valved cracker effusion cells are therefore typically larger than the cells used for the group III elements, and more expensive due to their extra components.

Since the valve can be set to open, closed, or any value in between, the use of a valve allows the beam flux to be rapidly changed to different values whereas a shutter mechanism only allows the beam to be on or off. This is important for the growth of multiple-quantum well and superlattice structures where the optimum group V overpressure for growth may be different for each layer in the structure. If a shuttered cell were used for the group V element, the source temperature would have to be varied for every layer. Due to the large thermal mass of the source element in the effusion cell, changing the temperature takes at least 15 minutes to obtain a stable beam flux. Clearly, the use of a valve should greatly decrease the growth time for such a structure.

The dopants used in this work are Si and Be, for n and p type, respectively. Both of these elements are solid at their typical operation temperatures and can be used in standard effusion cells. However, due to the low concentration of dopant atoms in a typical epilayer relative to the concentration of the III-V atoms, the rate at which the dopant source material is depleted during a typical growth campaign is several orders of magnitude lower than for the group III and V elements. Therefore, a smaller volume of the dopant elements can be used, and the two dopant sources are commonly used in a dual-dopant effusion cell, which consists of two independently heated crucibles with an integrated water cooling shroud between them to reduce thermal crosstalk. This allows two source materials to be installed on a single port of the MBE system.

Other III-V elements not described here (B, Tl, N, P, Sb) have additional engineering and safety requirements for producing a usable atomic or molecular beam. However, a description of the challenges involved in using these elements in MBE is beyond the scope of this work.

Shutter transients

When the source material is at thermal equilibrium inside the (closed) effusion cell, the tantalum shutter blade reflects a portion of the thermally emitted radiation from the source and reduces the heater power necessary to keep the source at the desired temperature. When the shutter is opened the reflected radiation is no longer present, and the surface of the source material cools slightly. This can result in a decrease in the beam flux after the source is opened, as the control algorithm has to respond and increase the power supplied to the cell, as shown in figure 2.1. These so-called shutter transients are more prevalent for small capacity effusion cells where the source material has a smaller thermal mass.

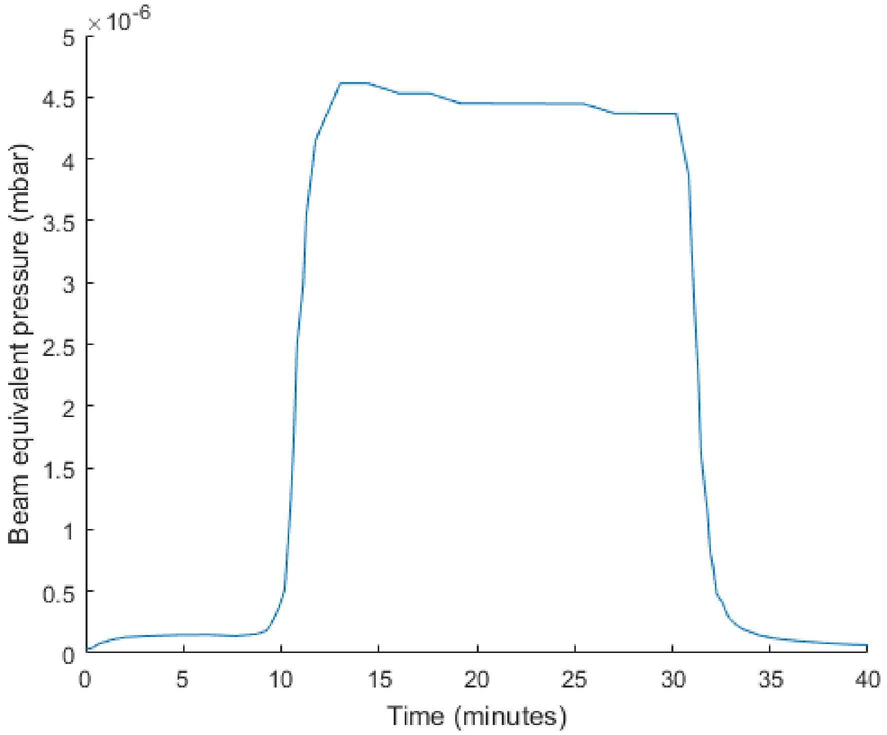

FIGURE 2.1: Beam flux measurement of Ga cell operating at 970 °C, showing a shutter transient. The cell was opened at 9 minutes and closed at 31 minutes. Data measured using the MBE-STM machine.

From figure 2.1, the initial flux of 4.6x10^{-6} mbar decreases to 4.4x10^{-6} mbar over the course of around 20 minutes, which should result in a reduction of the deposition rate by approximately 5%. Shutter transients are especially important when growing quantum wells, as the growth conditions can change over the first few minutes of growth.

Beam fluxes

The rate F at which molecules are emitted from the effusion cells as a function of the source temperature T can be modelled as an Arrhenius process, see equation 2.1.

$$F = Aexp(-E/k_B T) \tag{2.1}$$

Here E is the heat of vapourisation per molecule, and A is a fitting parameter which takes into account the shape of the crucible, the size of the cell orifice, the distance between the cell and the substrate, and the amount of source material remaining in the cell. Alternatively, the beam flux may be modelled using the semi-empirical Antoine equation, as in [17]. The Arrhenius model was used in this work, as it has only one fitting parameter, whereas the Antoine equation has three. In most effusion cells the beam flux can be changed by varying the source temperature. However, effusion cells fitted with a valve can also vary the parameter A by changing the size of the cell orifice.

The vapour pressures of the elements used in this work are plotted in figure 2.2. Note that the beam equivalent pressure at the wafer surface is much lower than the values shown in figure 2.2, due to the divergent nature of the molecular beam and the small solid angle occupied by the wafer as viewed from the effusion cells.

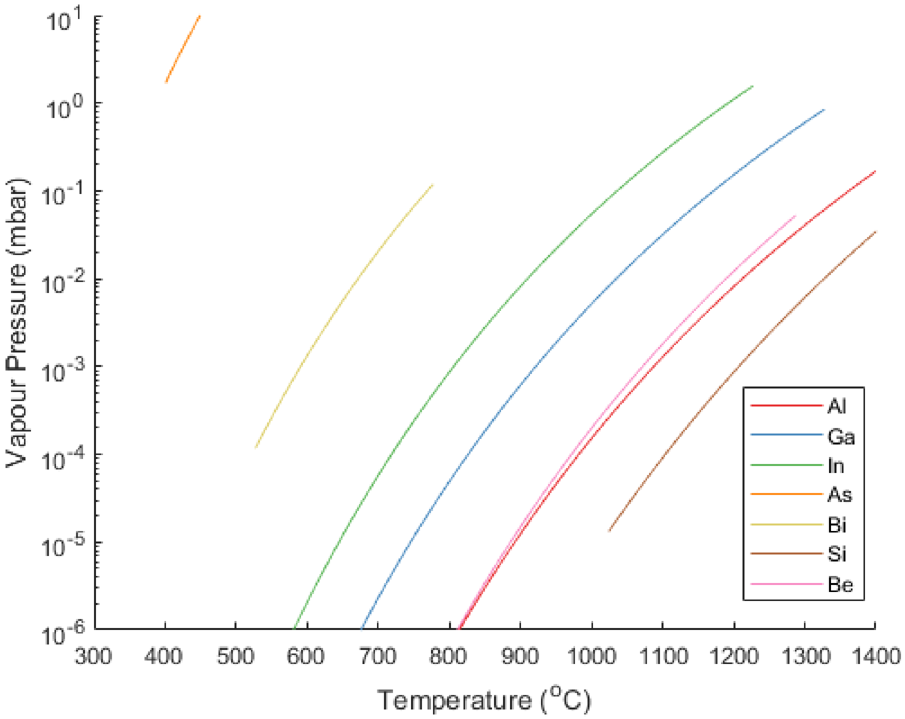

FIGURE 2.2: Vapour pressures of the elements used in this work, as a function of temperature. Sources: Al, Ga, In, Be [22]. As [23]. Bi [24]. Si [25]

2.2.2 Wafer heating and temperature calibration

The wafer surface temperature is a critical parameter in the growth of thin films using MBE as it affects the adatom mobility and desorption rate. Too cold and the adatoms lack enough thermal energy to migrate to a step edge, and instead incorporate where they land on the substrate. This leads to a large density of anti-site defects [11]. Conversely if the wafer temperature is too hot, the thermal energy of the adatoms can exceed the surface binding energy, leading to desorption. For this work, the temperature range of interest is broadly 250 to 700 °C.

Wafer heating

In the MBE system used in this work, the wafers are heated radiatively from behind by a heater block, which comprises a pyrolytic graphite filament running through a pyrolytic boron nitride diffuser plate. A current is passed through the filament, heating the diffuser plate, which in turn heats the wafer. The wafer is held parallel to the diffuser plate at a distance of approximately 5 mm, to heat it evenly. Most MBE machines feature rotating substrate stages to ensure a more uniform beam flux at all points on the wafer surface. However, the MBE system used in this work does not feature substrate rotation since the substrates are relatively small.

There are several techniques for measuring the wafer temperature in MBE; thermocouples, infrared thermometry, band-edge thermometry, and by observing surface reconstruction changes via RHEED. Here we note that band-edge thermometry measures the mean bulk temperature of the wafer whereas infrared thermometers and RHEED transitions measure the wafer surface temperature. Clearly, the wafer surface temperature is desired as the growth process is happening at the surface of the wafer. A thermal gradient between the front and back of the wafer may be present, especially if the emissivity of the two surfaces is different (as in the case of a single-side polished wafer). However, this gradient is likely small due to the relatively high thermal conductivity of GaAs at 600 °C [12], and the small thickness of the wafer (typically 0.3-0.6 mm). Coupled with the difficulty of obtaining wafer temperatures in MBE, this temperature gradient can be neglected.

Thermocouples

Thermocouples are a contact method of temperature measurement and consist of two different metals connected at a junction. The junction is placed into close thermal contact with the target, and a temperature dependent voltage is generated, which can be calibrated and used to measure the temperature. Thermocouples are effective over a wide range of temperatures and are extremely cheap compared to the other techniques covered here. However, to get an accurate measurement of the substrate surface temperature a thermocouple would have to be located on the surface of the wafer, which would interfere with the growth. Thermocouples placed near to the substrate can be used to give an approximate measure of the substrate temperature, however the error can be >100°C [13].

Infrared thermometry

Infrared thermometry (also known as pyrometry) is a non-contact temperature measurement technique and includes single pixel pyrometers and thermal imaging cameras. Pyrometers measure the intensity of infrared radiation given off by hot objects and are calibrated using black body furnaces at a known temperature, which have an emissivity close to 1. The spectral radiance of a real object is multiplied by its emissivity, which defines how well the surface can absorb and re-emit radiation at a given wavelength. Applied to GaAs epitaxy, the emissivity of the wafers varies as a function of wavelength and temperature [14].

Three quantities will contribute to the signal detected by the pyrometer: the thermal radiation emitted from the wafer, the reflection of background radiation off the front of the target, and the transmission of light from the substrate heater through the substrate. Background reflections may have a large effect on the measurement due to other hot objects inside the vacuum chamber. For example, the arsenic cracker is typically operated at 650 to 1000 °C and has a line of sight to the wafer. Specular reflections off the front of the wafer are negligible since the viewport and cracker are unlikely to be at the same angle with respect to the substrate. Instead, diffuse reflections from the rough rear surface of the wafer are more likely to contribute to the signal measured by the pyrometer.

As the heater is significantly hotter than the substrate, light from the heater with energy smaller than the band gap will be mostly transmitted through the substrate. For the temperature range 250-700 °C, the consequence is that the operational wavelength of the pyrometer is restricted to < 940 nm. However, the spectral radiance of a black body object in this temperature range will peak at >2000 nm, meaning that the pyrometer is restricted to a region of the spectrum where the wafer is not emitting much light, which limits the applicability of pyrometers to GaAs epitaxy. Pyrometers are also expensive and require the use of one of the MBE machine view ports.

Band-edge thermometry

Band-edge thermometers are a significant upgrade on pyrometers for GaAs epitaxy, and rely on the temperature dependence of the band gap of semiconductors to measure their temperature. The band gap of a semiconductor varies according to the Varshni equation [15]. The light from a tungsten lamp is focused onto the substrate, and photons with energy greater than the bandgap are absorbed. Photons with energy smaller than the bandgap are transmitted and are reflected off the back surface of the substrate. The reflection spectrum can be analysed to identify the absorption edge of the substrate. The specular reflection from the front of the substrate contains some light with energy greater than the substrate band gap as this light has not passed through the semiconductor. Therefore, a diffuse reflection is analysed instead of the specular reflection. Alternatively, the substrate heater can be used as the light source with the light transmitted through the substrate modified by the band gap. However, this is not effective when the heater is at low temperature, and not emitting much light. The temperature of the substrate can then be calculated using the band gap and the Varshni equation. Band edge thermometry is less effective if a thin heteroepitaxial layer with a different band gap to the substrate is deposited. Band edge thermometers can be accurate to 1 °C, however they are expensive and rely on using at least one viewport of the MBE system [16].

RHEED as a tool for wafer temperature calibration

Observing surface reconstruction changes using RHEED is a less accurate but a more cost effective method of measuring the wafer surface temperature, relative to pyrometry and band-edge thermometry. Since a RHEED system is likely to be installed on an MBE machine for growth rate measurements (see section 2.4), it is cost effective to also use it for wafer temperature calibration.

The RHEED surface reconstruction transitions used for temperature calibration in this work are: the removal of an As cap (295 °C), c(4x4) to (2x4) transition (400-425 °C), and the removal of the native surface oxide (580-600 °C). These tests are typically repeated every couple of weeks, to account for the heating conditions drifting over time.

For the first transition: a thick layer of As can be deposited for around 1 hour with the valve fully open, and the substrate held at room temperature. By comparison with the growth conditions used in this work (growth rate 0.6 ML/s, with the As valve 59% open to achieve 1:1 As:Ga atomic flux ratio), the As layer will be approximately 500 monolayers thick. Due to the low temperature, the As atoms stick where they land and form an amorphous layer. Since the surface is no longer crystalline, the electrons from the RHEED beam are scattered diffusely and the RHEED screen shows a relatively uniform "hazy" pattern. The wafer heating current is increased in small increments every 15 minutes, until the As atoms desorb at approximately 295 °C [31] and the underlying surface reconstruction becomes visible on the RHEED screen.

The c(4x4) to (2x4) transition is due to the surface atoms rearranging into a different reconstruction to minimise the surface free energy. In the absence of an As flux, the transition occurs at 400 °C [31], and the surface becomes less As-rich, whereas if an As flux is incident on the surface the transition occurs at a higher temperature. The c(4x4) and (2x4) diffraction patterns are shown in figures 2.3 and 2.4.

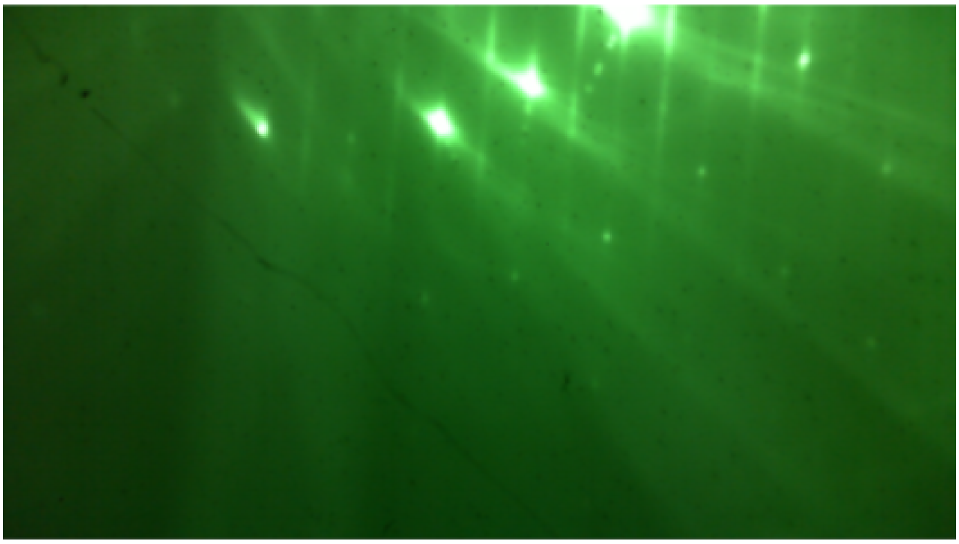

FIGURE 2.3: RHEED pattern of GaAs c(4x4) reconstruction. Kikuchi lines are also visible in this figure

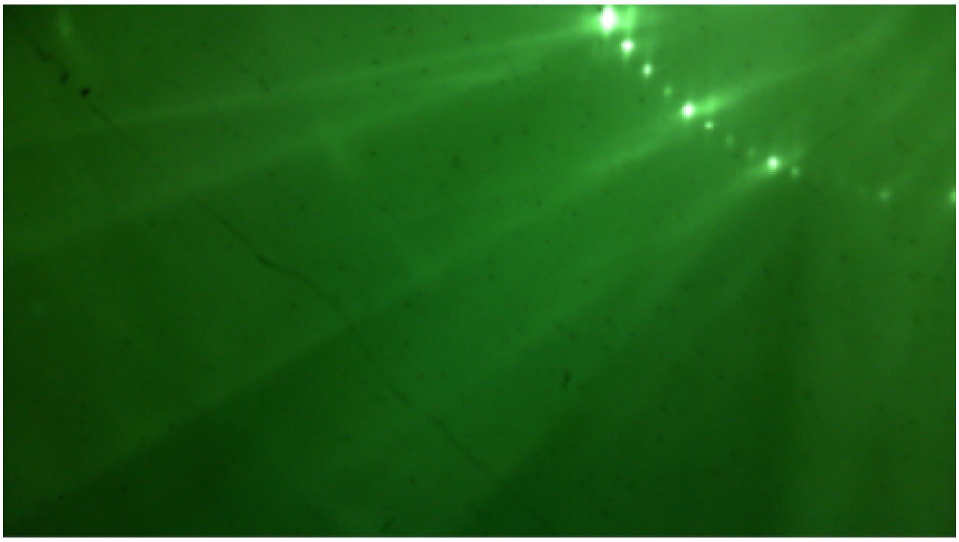

FIGURE 2.4: RHEED pattern of GaAs (2x4) reconstruction, showing the 4x pattern

The amorphous surface oxide must be removed before growth can commence, which is typically done by heating the wafer under an As flux for around half an hour. The removal of the oxide corresponds to an increase in the intensity of the diffraction pattern. For the purposes of temperature calibration, the wafer temperature is incrementally increased every 30 minutes until the oxide has desorbed, which begins at around 580 °C [33]. See figures 2.5 and 2.6 for images of the RHEED pattern before and after the surface oxide has been removed: these two images were taken with the wafer at the same orientation to clearly show the change in brightness of the pattern.

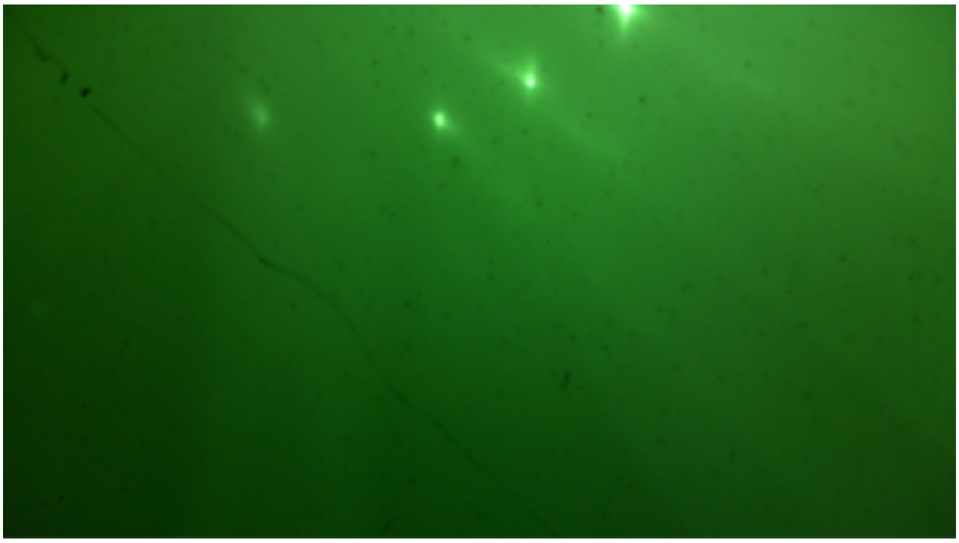

FIGURE 2.5: RHEED pattern of GaAs (001) surface before removal of surface oxide

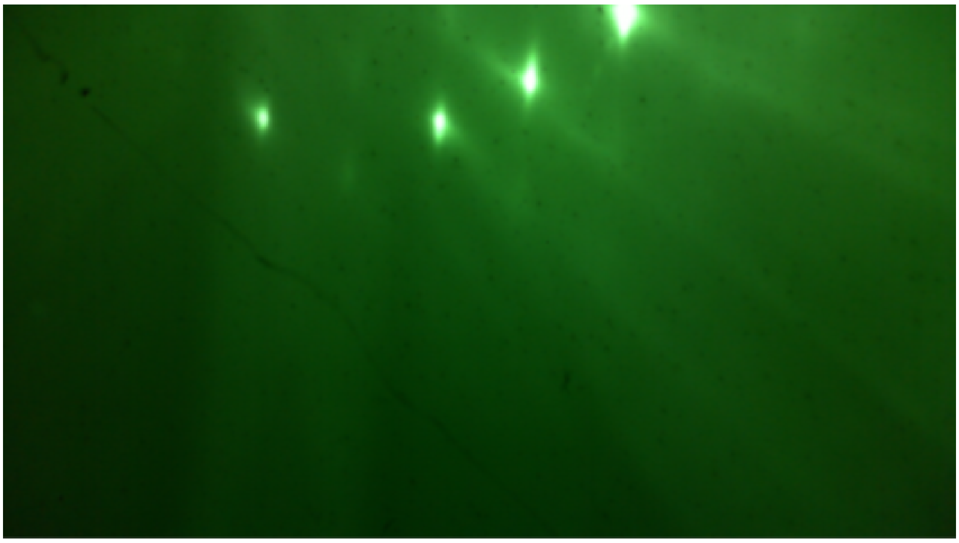

FIGURE 2.6: RHEED pattern of GaAs (001) surface after removal of surface oxide

By finding the heater current necessary to heat the wafer to one of the three transition temperatures, a calibration curve can be generated, see figure 2.7. A quadratic polynomial is used to fit the data, allowing the heater current for intermediate temperatures to be determined.

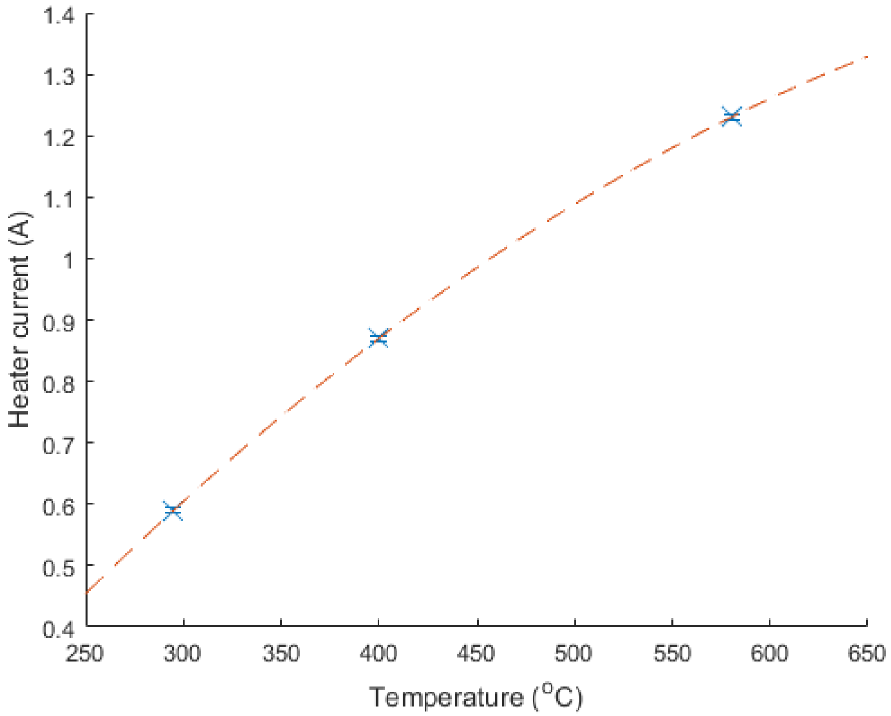

FIGURE 2.7: Relationship between heater current and wafer surface temperature for GaAs n+ (001). The dashed line is a quadratic fit to the data, and the error bars are the uncertainty in the current from the limited resolution of the power supply (±0.005 A)

The power supply used to heat the wafer has a current resolution of 0.01 A, meaning that the uncertainty in the current measurement is ±0.005 A. From figure 2.7, this should lead to a precision of roughly ±3 °C in the temperature measurement. In other words, the reproducibility of the wafer temperatures should be ±3 °C, neglecting that the wafer temperature may be non-uniform or may drift over time.

Estimating the accuracy of the temperature calibration is more difficult, as the rate of the transitions is dependent on the temperature. For example, the As atoms in the cap will evaporate from the surface at a lower temperature than 295 °C given a long enough time. Consequently, there is a large uncertainty in assigning a single temperature to these transitions.

Other transitions such as (2x4) to (4x2) in the absence of an As flux, which occurs at between 570 and 600 °C, could also be used as an additional reference point [32].

From the international temperature scale of 1990 [34], temperatures are defined by the freezing point of pure metals. A metal is heated until liquid and allowed to cool, while being observed with a pyrometer. As the metal passes through its freezing point, the temperature plateaus, which is visible with the pyrometer. In theory, such an experiment looking for the phase change could be performed in an MBE machine, by depositing aluminium (melting point 660 °C) or bismuth (271 °C) onto a substrate held at room temperature and observing changes in the RHEED pattern or intensity upon melting of the metal. Assuming the deposited metal had a rough surface due to the low deposition temperature, upon melting it should become smoother if it wets the substrate. This should result in an increase in the reflected electron beam intensity. Alternatively, if the metal forms into isolated droplets on the surface, the underlying substrate diffraction pattern may start to become visible. This method of wafer temperature calibration is advantageous because it is based on a well-defined physical transition instead of a rate-driven process such as evaporation or a reconstruction transition. However, coating the wafer surface with a metal would alter its heating profile, since the spectral emissivity of the metal and wafer are unlikely to be similar. Therefore, this technique is unfortunately probably not applicable to MBE.

2.2.3 Growth of GaAs with MBE

Interaction of atoms on substrate

After leaving the crucible, the individual atoms and molecules in the molecular beam can either hit or miss the substrate, with the probability of hitting the substrate dependent on several factors: the angle of the effusion cells with respect to the substrate, the design of the effusion cells, and the distance between the source and the substrate. There is also a trade-off between the number of effusion cells on an MBE machine and the amount of source material that hits the substrate. In an extreme case, mounting the substrate at the orifice of a cell would give a high effusion cell efficiency but would only enable deposition using that cell. At the other extreme, a large number of cells could be accommodated if they were sufficiently far from the substrate. However, it would be difficult to align the molecular beams with the substrate, and difficult to attain a high source flux at the substrate without running the cells at elevated temperature (leading to regular cell replenishment and maintenance). Therefore, the design of the MBE system is optimised to accommodate the necessary number of cells for a particular growth type (e.g. III-As) while still being able to attain a high and uniform flux from the cells. A calculation by Bastiman suggests that only 0.1% of the gallium and arsenic in the effusion cells is incorporated into the substrate as epilayers in the MBE-STM system [37], with the remainder being deposited on the vacuum chamber walls. This calculation compared an estimate of the volume of GaAs deposited between refilling the effusion cells with the volume of Ga and As put into the cells.

The behaviour of the molecular beam upon hitting the substrate depends on the species of molecule, the substrate temperature, and the substrate material. Under ideal conditions, the incoming atoms and molecules stick to the substrate but have enough thermal energy to migrate around the surface until they find a suitable lattice site to incorporate into the bulk of the substrate, typically at one of the terrace edges. If the substrate temperature is too high then the atoms will have enough energy to desorb from the substrate and escape into the vacuum, with a negligible probability of coming into contact with the substrate again. If the substrate temperature is too low, then the atoms will not have enough energy to migrate around the surface and will instead incorporate where they land. This leads to a high defect density and a corresponding degradation of the optical and electronic properties of the epilayers. The optimum temperature for growth of a III-V alloy is further complicated as at least two species of adatoms are present, which may have different vapour pressures (e.g. Ga and As).

On the MBE-STM machine a cracker on the arsenic cell is used to choose between As_2 and As_4. The adsorption behaviour of As_2 and As_4 is different and has important consequences for the growth of dilute bismide alloys [38].

During the growth of GaAs, the incorporation coefficient of arsenic atoms from As_2 molecules adsorbed on the surface depends on the gallium flux. When As_2 dimers are adsorbed on the surface they form a reservoir from which As atoms can incorporate into the bulk crystal. For the case where the Ga atomic flux is less than the As atomic flux, an equal number of gallium and arsenic atoms are incorporated into the crystal and excess As is desorbed from the reservoir [39].

For the case where the gallium atomic flux is greater than or equal to the arsenic atomic flux, the incorporation coefficient of the arsenic atoms (in the form of As_2 adsorbed on the surface) is unity. The point at which the gallium and incorporable arsenic atomic fluxes are equal is known as a stoichiometric flux ratio.

The incorporation coefficient of As atoms from As_4 molecules adsorbed on the surface during the growth of GaAs also depends on the gallium flux, however the process is more complicated than for As_2. Two As_4 tetramers that are adsorbed on the surface can interact, contributing two As_2 dimers to the surface reservoir of incorporable As, with an As_4 tetramer desorbed from the surface in the process. Therefore, the incorporation coefficient of the As atomic flux saturates at 0.5 with an increasing Ga flux, with the rest of the As atoms desorbing as tetramers [40].

The sticking coefficient of Ga is unity under 470 °C, while at 600 °C the surface lifetime is approximately 10 seconds [41]. For MBE growth of GaAs, the desired number of As and Ga atoms incorporated is equal. Due to the high sticking coefficient of Ga and the Ga flux dependent incorporation coefficient of As, the deposition rate is proportional to the Ga flux. In this case, the optimum growth temperature of around 580 °C provides a high mobility for Ga (and As) adatoms, leading to smooth surfaces. The As atoms lost to desorption are replaced by oversupplying As, with a typical As_2:Ga flux ratio of 3-8 [42]. If an excess gallium flux is present then the surface becomes gallium rich and gallium droplets form, from which a crystalline GaAs surface suitable for MBE growth cannot be recovered.

Therefore, in MBE growth the substrate temperature must be accurately calibrated and controlled, with different substrate materials requiring separate calibration. RHEED transitions were used to determine the substrate temperature in this work, as detailed in section 2.2.2.

Growth modes

The growth of thin films via MBE can proceed via several modes: layer-by-layer (Frank-Van der Merwe [46]), step flow, island growth (Volmer-Weber [45]), and layer-plus-island growth (Stranski-Krastanov [44]).

Layer-by-layer growth occurs when the adatoms have an extremely high mobility, such that the growth of a new monolayer only starts after the previous monolayer has completed.

However, achieving such a high adatom mobility is difficult in practice, especially when growing a compound semiconductor with constituents that have different surface binding energies. The result is that a second monolayer begins to form before the first monolayer is complete. Therefore, step flow growth is commonly used to produce high quality epitaxial layers by giving the adatoms a larger number of sites to incorporate. This is achieved by introducing a large number of terraces on to the wafer surface by cutting the substrate with a small angular offset (typically 0.1 °) from the desired crystal plane ((001) in this work). For growth at a suitably high temperature, the migration length of the adatoms is larger than the spacing between the terraces, and the adatoms migrate to the terrace edges where they incorporate. As growth progresses, the terrace edges move across the wafer.

If the growth temperature is too low then the mobility of the adatoms is reduced and they instead form into islands with nearby adatoms. These islands can form into 3D structures over time, leading to a roughening of the surface.

Layer-plus-island growth can occur in heteroepitaxy if there is a lattice mismatch between the substrate and the deposited layer. The growth of epilayers with a lattice mismatch to the substrate can initially proceed pseudomorphically until a critical thickness is reached. As the epilayer becomes thicker the growth process can change to island growth as the degree of strain relaxation becomes greater.

Defects in GaAs

Arsenic atoms sitting on the gallium lattice sites (As antisite defects) are prominent in GaAs growth at low temperature [15]. Interstitial atoms and vacancies were also observed in low temperature grown GaAs [16]. These defects act as non-radiative recombination centres which will increase the dark current and reduce the luminescence efficiency for this material.

2.2.4 Vacuum system

Ultra-high vacuum is a requirement for MBE growth for two reasons: the pressure must be low enough for the molecular beams to reach the substrate without colliding with air molecules, and the incorporation rate of impurities into the thin film must be much lower than the film growth rate.

Requirements of the vacuum system

For the first consideration: the molecular beams will typically be much hotter than the gas between the effusion cell and the substrate. At atmospheric pressure, the beam molecules will rapidly lose most of their thermal energy through repeated collisions with the air molecules, will be scattered and eventually deposited on the chamber walls. This is undesirable as the effusion cell would have to be run at a greatly elevated temperature to produce a usable flux of molecules at the substrate surface, and the source material would have to be replenished more often. On the other hand, if there were a perfect vacuum in the chamber, the beam molecules would travel ballistically in the direction of the substrate. In a real vacuum system, the pressure cannot be zero, but the pressure must be low enough that the vast majority of the molecules do not collide with the residual gas molecules. From modelling the beam scattering process as a collision between two hard spheres, the mean free path λ of an atom of diameter d emitted from an effusion cell at temperature T into a vacuum system at pressure P can be determined, see equation 2.2 [1].

$$\lambda = \frac{k_B T}{\sqrt{2}\pi d^2 P} \tag{2.2}$$

Here k_B is the Boltzmann constant. In the MBE system used in this work, the distance from the effusion cells to the substrate is approximately 0.5 m. If this distance is used as the mean free path, and typical values are used for the other parameters (gallium atoms: diameter 0.27 nm, emitted from an effusion cell at 1000 °C) the necessary vacuum system pressure is 10^{-3} mbar.

For the second consideration: it is undesirable for air molecules to incorporate into the thin film, or to have a large surface coverage, and thereby interfere with the adsorption processes of the growth molecules. In semiconductor epitaxy, the air molecules can act as dopants, can cause structural defects, and can act as non-radiative recombination centres. The rate that residual gas molecules impinge on an epilayer surface $F_{impurities}$ is dependent on their mass m, temperature, and the residual gas pressure in the vacuum system, and can be calculated using the Hertz-Knudsen formula [9], see equation 2.3.

$$F_{impurities} = \frac{P}{\sqrt{2\pi m k_B T}} \tag{2.3}$$

In the low-pressure regime, there is a negligible rate of collisions between residual gas molecules. However, estimating the temperature of the residual gas is difficult as there are several surfaces (e.g. cryopanel, effusion cells, chamber walls) at different temperatures inside the chamber.

Under the assumptions that the impurities do not perturb the zinc-blende crystal structure of the semiconductor, that the impurity flux is much smaller than the gallium flux, and that the impurity adatoms are immediately buried by the deposition of further gallium and arsenic atoms, the impurity concentration in the thin film may be roughly estimated from the ratio between the impurity incorporation rate $S.F_{impurities}$ and the gallium flux F_{Ga}, where S is the sticking coefficient of the impurity, see equation 2.4.

$$\frac{S.F_{impurities}}{F_{Ga}} = \frac{Growth\ rate\ (impurities)}{Growth\ rate\ (Ga\ atoms)} = \frac{Concentration\ (impurities)}{Concentration\ (Ga\ atoms)} \tag{2.4}$$

As an example, assuming that the residual gas is comprised wholly of one species of molecule for simplicity (in this case oxygen molecules), the impurity concentration can be calculated. The sticking coefficient of oxygen onto a GaAs surface depends strongly on temperature and the degree of saturation of Ga dangling bonds on the surface - values of between 10^{-8} and 10^{-4} are given in the literature [10]. The impurity concentration incorporated into a GaAs layer is estimated for a range of residual gas pressures and sticking coefficients in figure 2.8.

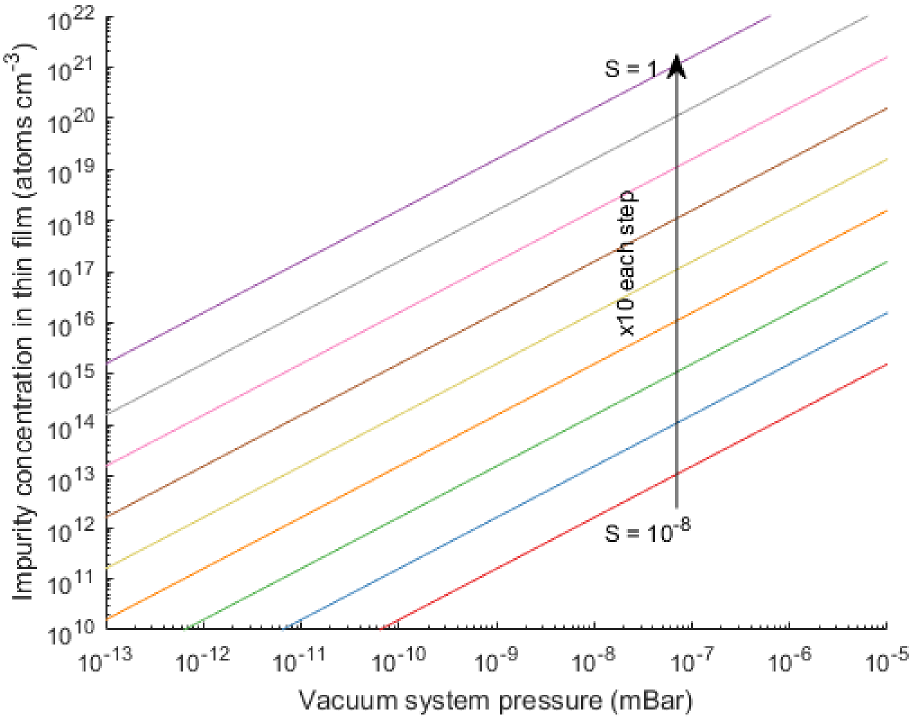

FIGURE 2.8: Calculated impurity concentration in GaAs thin films, as a function of the vacuum system background pressure. The sticking coefficient S is varied from 10^-8 to 1, and the Ga flux corresponds to a typical growth rate of 0.6 ML/s.

The MBE system used in this work has an ultimate pressure of approximately 5x10^{-10} mbar. This is the pressure in the growth chamber immediately after a bake-out, when all the effusion cells are at room temperature. At this point, the rate of molecules leaking into the chamber is equal to the rate that the molecules can be pumped out of the chamber. When the effusion cells are heated to their standby temperatures, the pressure increases to 2x10^{-9} mbar due to further outgassing of the components.

From figure 2.8, if a sticking coefficient of 10^{-4} is assumed for residual gas atoms (the worse case scenario), a vacuum system background pressure of 2x10^{-9} mbar should lead to an impurity concentration of around 10^{15} cm^{-3}. This is around 1000 times lower than the concentration of the dopant atoms in the p-type and n-type GaAs layers grown in this work. Despite the many assumptions involved, this second requirement (low impurity incorporation) on the vacuum pressure is several orders of magnitude more demanding than the first requirement on the vacuum system (mean free path of molecular beams).

Mass spectrometry

The composition of the residual gas in the chamber can be analysed using a mass spectrometer, see figure 2.9.

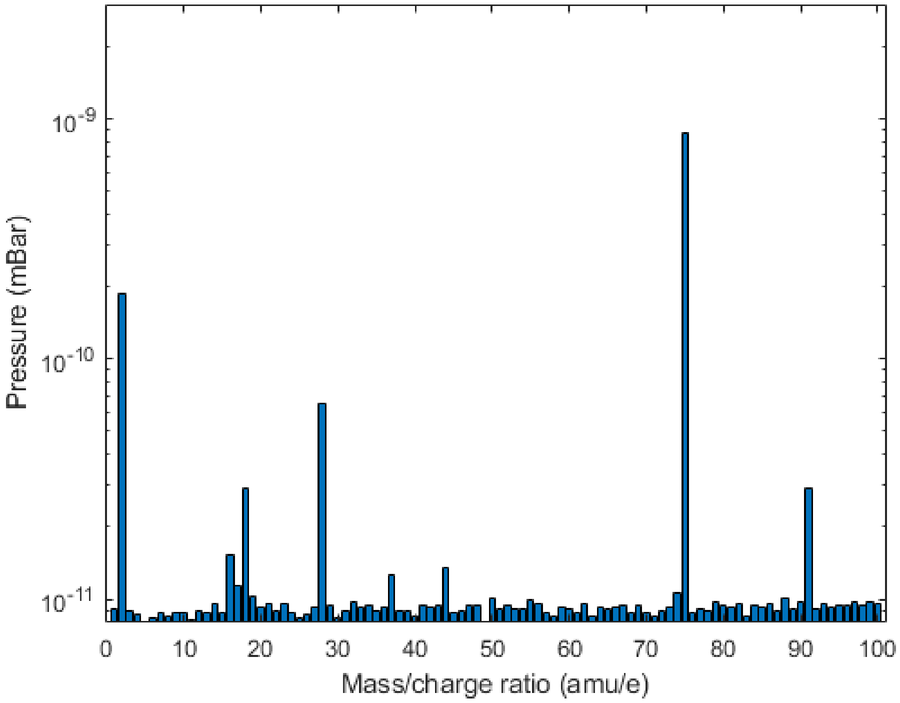

FIGURE 2.9: Output of mass spectrometer attached to the growth chamber of the MBE system. These data were taken before a growth run, such that the growth chamber had not been opened to the entry chamber for over 12 hours.

From figure 2.9, there are a number of peaks corresponding to different constituents of the residual gas. The peak at 2 amu/e (atomic mass units divided by the elementary charge) is due to molecular hydrogen, which is gradually outgassed from the stainless-steel chamber walls. Hydrogen is difficult to remove from the system using a turbo-molecular pump as it is an extremely light molecule.

If there were a significant leak of air into the chamber, one would expect to see peaks from atmospheric gases at 18 (H_2O), 28 (CO, N_2), 32 (O_2), and 44 amu/e (CO_2). The rate at which a particular air molecule will leak into the chamber through any microscopic gaps in the ConFlat flanges from outside should be proportional to the size of the molecule and its atmospheric abundance. CO_2 and O_2 molecules are a similar size, however oxygen is approximately 500 times more abundant in the atmosphere, so one would expect the partial pressure of O_2 to be much higher than that of CO_2 (neglecting that the pumping efficiency of both molecules could be different). However, there is no peak at 32 amu/e, meaning either: there is no leakage of O_2 into the chamber above the detection limit of the mass spectrometer (approximately 10^{-11} mbar), or the oxygen molecules rapidly react with the arsenic in the chamber to produce AsO (peak at 91 amu/e). In the first case, if no oxygen is leaking into the chamber, then it is logical to conclude that other similarly sized air molecules are not leaking into the chamber. Therefore, the origin of the peaks at 18 and 44 amu/e must be due to continuous outgassing from the components inside the vacuum chamber. The peak at 28 amu/e could be composed of CO outgassing, or the dry N_2 gas that is used to vent the entry lock chamber prior to loading a wafer.

The peaks at 16 and 17 amu/e are probably due to methane and ammonia respectively. These constituents could be due to the reaction of hydrogen with CO_2, CO, or N_2 inside the chamber.

The largest peak (75 amu/e) is due to atomic arsenic, and potentially doubly ionised As_2. Doubly ionised atomic arsenic should cause a peak at 37.5 amu/e, however this peak shows up at 37 amu/e as the mass spectrometer software rounds the data to the nearest integer.

The peak at 91 amu/e is due to AsO, which will be desorbed from the wafers during the oxide removal stage prior to growth. AsO could also in theory be produced from the reaction of arsenic with oxygen molecules that leak into the vacuum chamber.

During growth, the pressure increases up to 10^{-5} mbar. However, this is mainly due to the use of the arsenic source during growth. In this case, the incorporation of residual gas atoms should be minimal, and the growth of opto-electronic devices is enabled.

Design of vacuum system

The loading of new wafers into the growth chamber, and the outgassing and removal of the surface oxide introduce new contaminant molecules into the growth chamber. The design of the vacuum system is therefore important to minimise the residual gas pressure, see figure 2.10.

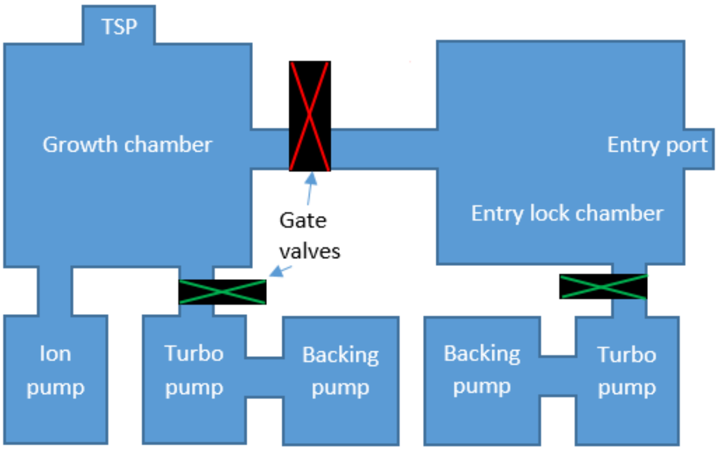

FIGURE 2.10: Diagram of the MBE-STM used in this work. Each of the two main chambers should also have a vacuum monitoring gauge (more than one gauge is preferable, for redundancy) - these are not shown for simplicity. The effusion cells, RHEED system, cryo-panel, substrate stage, and wafer transfer mechanism are also not shown here. The black boxes represent vacuum gate-valves, with green indicating the valve is open, and red indicating the valve is closed. Note that the MBE machine in this work does not have a wafer preparation chamber, and that the entry lock chamber connects directly to the growth chamber via a gate valve

From figure 2.10, the design of the system achieves a low pressure in the growth chamber, while minimising air ingress during wafer loading. The purpose of the preparation chamber is to outgas the wafers, and to remove as much air as possible from the system before introducing the wafers to the growth chamber. Unfortunately, the MBE system used in this work does not have a preparation chamber, and the wafers are introduced directly from the entry lock chamber into the growth chamber. If the wafers were loaded directly into the growth chamber or preparation chamber from the lab, the ultimate pressure would be poor. In addition, these chambers have a relatively large volume, meaning that a more powerful and expensive vacuum pump would be needed to pump the system from atmospheric pressure to ultra-high vacuum in a reasonable time (e.g. 12 hours overnight in preparation for the next day's growth).

Instead, the wafers are loaded into an entry lock chamber, which is pumped using a turbo-molecular pump backed with a scroll pump. The entry lock chamber has a small volume relative to the other two, and this allows it to be quickly pumped down to its ultimate pressure (approximately $8\text{x}10^{-7}$ mbar) in a few hours. The small volume of the entry lock chamber and the use of a small orifice connecting it to the growth chamber help to minimise the number of air molecules that get into the growth chamber.

The various effusion cells, chambers, vacuum gauges, pumps, viewing ports, and transfer mechanisms are held together using steel bolts. The ConFlat flange design is widely used for ultra-high vacuum applications and consists of a sharp circular steel knife blade on the mating surface of each of the two vacuum components that are to be joined. Upon tightening, these two knife edges bite into a soft metal gasket, which deforms to fill any small defects in the knife edges. The gasket is usually made of oxygen-free, high thermal conductivity copper but may also be silver plated if corrosion resistance is required. Alternatively, the gasket can be made of viton if re-usability is important, as in the case of an entry lock chamber (albeit with slightly reduced performance). If utilised correctly, ConFlat flanges can operate to 10^{-13} mbar. However, ConFlat flanges require practice to install correctly, and are slow to install (compared to the Klein flange design). In addition, the copper gaskets are not reusable as they are physically deformed when the steel knife-edge bites into them, adding to operating costs.

The materials used to construct the vacuum system must be carefully chosen. Internal metal components must retain their strength and shape at temperatures up to 1000 °C so are usually constructed of high purity molybdenum, tungsten, and tantalum. Insulating elements are often made of pyrolytic boron nitride. All materials used inside an MBE system must have a low vapour pressure and must be able to withstand the bake out procedure. In addition, most of the external components (water cooling pipes, shutter motors, cameras) must be removed prior to the bake out, as they contain plastic components which would otherwise melt.

The growth chamber must be opened to atmosphere periodically for refilling effusion cells and replacing burnt-out ion-gauge filaments. To bring the system up to atmospheric pressure, the chamber is vented with pure nitrogen gas obtained from the boil-off from a tank of liquid nitrogen. The flow of nitrogen gas is kept on after the chamber is opened to reduce backflow of air into the chamber. After the maintenance is complete, the entire MBE machine is baked at 125 °C for several days with the vacuum pumps operating to remove water vapour that may have condensed inside the chambers. Turbomolecular pumps (and their backing pumps) contain large electric motors which require operating temperatures of <50 °C, so must therefore be located outside the baking enclosure. This typically involves installing the turbomolecular pumps on the end of a long tube or hose, which reduces their efficacy somewhat as the residual gas molecules must ballistically travel into the pump to be removed from the vacuum chamber.

Vacuum pumps

Ultra-high vacuum is obtained in MBE by using several types of vacuum pump, which are effective over different ranges of pressure and have different efficiencies for pumping the various residual gas species. Vacuum pumps can be broadly divided into two categories: gas binding and gas transfer.

Gas binding vacuum pumps consist of a large surface area to which residual gas molecules can stick via a process which depends on the type of pump. However, this surface has a finite capacity for residual molecules and must be regenerated periodically. Types of gas binding vacuum pumps include titanium sublimation pumps, ion pumps, and cryo-panels. These pumps are useful for attaining and maintaining ultra-high vacuum, but do not have the capacity to pump down a chamber from atmosphere.

A titanium sublimation pump (TSP) works by chemically gettering residual gas molecules with titanium and consists of a filament inside the vacuum chamber through which a large current is passed periodically. The filament subsequently heats up, causing the titanium to evaporate and coat the surfaces of the vacuum chamber which have line-of-sight access to the TSP. Titanium is an extremely reactive element, so any residual gas atoms that come into contact with the titanium coated chamber walls will bind to it and be removed from the vacuum. As the titanium coating of the chamber walls is depleted the pumping capacity is reduced, and the coating must be regenerated. TSPs are simple to operate and maintain and are effective at pumping a wide range of gases including water vapour, carbon monoxide, carbon dioxide, nitrogen, and oxygen. However, TSPs are ineffective at pumping hydrogen [2]. The TSP has to be positioned in the MBE chamber in such a way as to avoid coating other sensitive instruments with titanium.

Ion pumps operate by ionising residual gas atoms and using an electric field to accelerate them into a solid cathode, where they react with the cathode material and become trapped. The ion pump consists of a set of hollow electrically isolated anode tubes with a cathode made of titanium at each end. Large permanent magnets are placed around the electrodes outside the vacuum chamber. A voltage of roughly 3-7 kV is applied across the electrodes, which attracts free electrons to the anode tubes. The electrons are then trapped by the magnetic field, resulting in a cloud of high energy electrons oscillating around the axes of the anode tubes. If a neutrally charged residual gas atom moves into an anode tube, there is a high probability that it will collide with an electron, becoming ionised. The high electric field then accelerates the positively charged ion into the negatively charged cathode where reacts with the titanium cathode and becomes embedded. There is also a chance that the ion colliding with the cathode will cause additional titanium to be sputtered over nearby surfaces, which will further reduce the pressure in the chamber in the same manner as a TSP. Ion pumps can reach ultimate pressures of 10^{-11} mbar and are effective at pumping many different types of residual gas molecule, such as noble gases, hydrogen, and nitrogen. However, the vacuum chamber must be roughly pumped before the ion pump is used since the ion pump does not have the capacity to work at atmosphere [3, 4].

Cryo-panels are commonly used in MBE to maintain an ultra-high vacuum, and to absorb any excess heat in the chamber. Cryo-panels consist of a large copper panel that is exposed to the vacuum chamber on one side and cooled on the other side by a liquid nitrogen reservoir. When a gas atom collides with the cryo-panel it can stick to the surface and become trapped, depending on the species of gas and the temperature of the cryo-panel. In this work, the temperature of the cryo-panel is controlled by opening a valve that allows nitrogen to escape from the liquid nitrogen reservoir. The valve is controlled by a PID controller that uses a thermocouple located at the reservoir exhaust for feedback. Liquid nitrogen usage contributes significantly to the running costs of an MBE machine, with a typical machine using 100-250 litres per day. The temperature of the cryo-panel is set to -90 °C in the MBE-STM, which gives effective pumping of water vapour and hydrocarbons while conserving liquid nitrogen [5].

Gas transfer pumps can be used continually, and exhaust atoms and molecules from the vacuum chamber to atmosphere or to a backing pump. Types of gas transfer pumps include turbo-molecular pumps, scroll pumps, and rotary vane pumps. The main disadvantage of gas transfer pumps is that they contain many moving parts which are noisy and require regular servicing, increasing downtime. It is important that pump oil cannot flow back into the vacuum chamber, therefore oil-free pumps are widely used.

Turbo-molecular pumps are widely used in MBE systems due to their large pressure range of operation (10^{-3} to 10^{-10} mbar) and high pumping speeds. Turbo-molecular pumps consist of a series of rotor and stator fan blade pairs, with the geometry of the rotors and stators such that the gas molecules preferentially hit the underside of the blades and are accelerated towards the exhaust of the pump. When the molecules are deflected by the rotor blades, the molecule is accelerated, and the blade speed is added to the thermal velocity of the molecule. The mean free path of the gas atoms must be larger than the spacing between the rotors and stators so that the atoms do not lose energy through collisions with other atoms before being accelerated by the next rotor blade. This means that a turbo-molecular pump cannot exhaust to atmosphere and must be used in conjunction with a backing pump capable of 10^{-2} mbar, usually a scroll or rotary vane pump. Turbo-molecular pumps are more effective at pumping heavy molecules, since the mean thermal velocity of light molecules such as hydrogen is much higher than the blade speed [6, 7].

Scroll pumps are widely used as backing pumps for turbo-molecular pumps due to their low maintenance operation and ability to exhaust to atmosphere. Scroll pumps consist of two interleaving spiral tracks that are in contact, one of which is fixed while the other oscillates so as to orbit the first track. During operation, a pocket of gas becomes trapped and compressed by the movement of the tracks until it reaches the centre of the spiral, where it is compressed to a smaller volume (and correspondingly higher pressure) and is exhausted to atmosphere. Scroll pumps can attain an ultimate pressure of around 10^{-2} mbar [8] and use PTFE tip-seals as lubricant for the tracks instead of oil.

Rotary vane pumps are commonly used as backing pumps for turbo-molecular pumps and consist of a cylindrical chamber containing an eccentrically mounted rotor. The rotor houses several vanes, which can extend and retract to stay in contact with the chamber walls as the rotor spins. The vanes form sealed compartments within the chamber. The gas enters the pump and is trapped when one of the vanes sweeps across the inlet. As the rotor turns the gas is forced into a smaller volume, increasing the pressure. When the pressure in the compartment exceeds atmospheric pressure, the gas is expelled from the pump. Rotary vane pumps are capable of reaching an ultimate pressure of 10^{-3} mbar and are typically used to back turbo-molecular pumps. Rotary vane pumps use oil vapour as a lubricant and coolant, so the pump must be designed such that the pump oil cannot flow back into the vacuum chamber [8].

Vacuum gauges

It is important to monitor the background pressure in the growth chamber to ensure that the vacuum system is functioning properly. The presence of a source of contaminants is relatively easy to verify and locate if the contaminated object (e.g. an effusion cell) causes an increase in the pressure when heated. It is also important to monitor the pressure in the entry lock chamber as contaminants that are present in the entry lock can make their way into the growth chamber when the separating gate valve is opened. The pressure range of interest in the growth chamber is approximately 10^{-4} to 10^{-11} mbar. In the MBE-STM growth chamber, two ion gauges are used for pressure measurement. Ion gauges emit electrons from a hot filament which are accelerated towards a positively charged grid. The electrons pass through the grid and can then collide with and ionise residual gas atoms. The residual gas ions are then collected by a thin grounded wire. The ions generate a current in the wire that is dependent on the pressure in the vacuum system. Ion gauges are accurate to $\pm 30\%$ and have different detection efficiencies for different molecules [35, 36]. In the MBE-STEM, an ion gauge can be moved in front of the wafer substrate to measure the beam equivalent pressure at the wafer. However, the large uncertainty makes ion gauges a poor method for measuring effusion cell fluxes.

2.3 Comparison of MBE with competitor growth techniques

MBE allows a high degree of control over the thickness and composition of deposited materials and is compatible with a wide range of evaporant materials, including group II-VI, III-V, IV semiconductors and their respective dopant elements. The ability to grow semiconductor heterostructures with sub-monolayer precision and abrupt interfaces allow complicated devices to be grown using MBE, such as lasers, LEDs, solar cells, and photodetectors. These characteristics also allow research into low dimensional quantum systems and novel semiconductor alloys such as dilute nitrides and dilute bismides.

However, MBE is not the only technique for growing semiconductor devices, and has several advantages and disadvantages compared to other techniques. The main competitor to MBE for the growth of III-V semiconductors is metal-organic vapour phase epitaxy (MOVPE), also known as metal-organic chemical vapour deposition

(MOCVD). MOVPE growth proceeds via the decomposition of metal-organic precursor molecules (e.g. triethylgallium, trimethylbismuth) at the wafer surface [26].

MOVPE is a thermodynamically limited growth technique such that the decomposition of the precursors happens near thermal equilibrium [29]. MBE, on the other hand, is a kinetically limited growth technique, meaning that the epilayer composition is mainly determined by the source fluxes. In the case of GaAsBi, the optimum temperature for growth is generally below 400 °C, and even lower for high bismuth content (>5 % Bi) alloys. At such low temperatures, the precursor molecules used in MOVPE have trouble dissociating. Nevertheless, MOVPE has been used extensively for the growth of GaAsBi [26–28].

MBE can create more abrupt heterojunction interfaces than MOVPE, as the source fluxes are controlled using motorised shutters. The shutters used in this work can close in 0.2 seconds, which is faster than the typical time to deposit a monolayer in MBE (1.67 seconds at a growth rate of 0.6 ML/s). In MOVPE, the deposition occurs under an overpressure of the precursor gases, which remain in the chamber for some time after the precursor flow is shut off, resulting in slightly less abrupt interfaces than in MBE.

Both MBE and MOVPE use a range of toxic materials for deposition. However, MOVPE uses precursors in the gas phase, which requires additional safety measures. In MBE, the toxic materials are in the solid or liquid phase and sealed inside a vacuum system for the vast majority of their time on-site. Therefore, there is a greater risk of a dangerous chemical leak with MOVPE.

For industrial production of semiconductor wafers, MOVPE is more commonly used due to its ability to grow many wafers at the same time, using a much higher growth rate. This results in a higher throughput of wafers using MOVPE compared to MBE. In addition, MBE systems consume large amounts of liquid nitrogen, typically 100-250 litres per day, further adding to the running costs.

MBE and MOVPE share several disadvantages; they are both extremely expensive, meaning that research activity and industrial production is restricted to large universities and companies. Typical installations cost several hundred thousand pounds, with running costs of thousands more per year. Both techniques also use large amounts of electricity and create a moderate amount of toxic waste in the form of contaminated components and waste semiconductor wafers. The end-of-life disposal of contaminated reactors must also consider the ecological impact.

2.3.1 Advantages and disadvantages of the MBE-STM used in this work

Relative to typical MBE installations, the MBE machine used in this work has some notable differences. Many MBE machines use 2-inch diameter or larger wafers for growth. However, the MBE-STM is relatively small and the wafer transfer tube is too narrow to allow for the use of 2-inch wafers. Therefore, the as-packaged wafers are cleaved into 11.4 x 11.8 mm squares before being loaded into the reactor. This has several benefits: 10 wafer squares can be obtained from each 2-inch wafer, resulting in lower expenditure on wafers per growth. In addition, due to the small size of the squares, highly uniform epilayers can be grown without rotating the substrate. This simplifies the system since a separate motor and power supply to rotate the wafer are not necessary. In addition, the RHEED analysis does not need to take account of the rotation. Other authors have deliberately grown on 2-inch wafers without rotation in order to measure the flux gradients and the resulting influence on epilayer composition and quality, allowing the mapping of a wide range of the growth parameter space with only a single growth run [47]: this is unfortunately not possible on the MBE-STM due to the relatively small wafers and high uniformity.

As an additional drawback, the area of material available for characterisation is limited, meaning that only a limited amount of device fabrication or destructive measurements (such as transmission electron microscopy) can be carried out.

The MBE-STM also does not have a preparation chamber, meaning that wafer outgassing must take place in the growth chamber. This has a deleterious effect on the dark currents of epilayers grown in this machine due to the higher partial pressure of atmospheric gases in the deposition chamber prior to growth. However, the small volume of the entry chamber allows it to reach an acceptable vacuum ($< 10^{-7}$ mBar) in only a few hours. This allows wafers to be loaded into the growth chamber relatively quickly and compensates for the lack of a wafer storage area inside a preparation chamber (as is often the case on other MBE machines), enabling multiple growth runs per day.

2.4 Reflection high energy electron diffraction

In-situ monitoring of the deposition process is vital to growing layers of the desired thickness and composition. RHEED can be used to observe phase changes on the substrate surface during growth, and can be used to determine the source fluxes, substrate temperature, and to get a qualitative measure of the surface roughness. RHEED offers real time feedback, and as such is a valuable tool for an MBE grower. Alternatively, the growth rate could also in theory be determined by using XRD to calculate the layer thicknesses of an AlGaAs/GaAs or InGaAs/GaAs superlattice. However, this is slow, and the source fluxes are prone to drift over time as the cells become depleted so that a superlattice structure would have to be grown regularly to have an accurate calibration of the deposition rates.

2.4.1 Operating principles

In a RHEED system, high energy electrons (8-20 keV) are generated via thermionic emission from an electron gun. The electrons are focused into a small diameter and low divergence beam using electric and magnetic fields. Further electron optics allow the beam to be steered such that it impinges on the substrate surface. The electron gun is positioned such that the electron beam is incident on the substrate surface at an angle of typically 1-3 °, see figure 2.11. The small angle ensures that the component of the electrons' momentum perpendicular to the surface is much smaller than the component parallel to the surface, meaning that the electrons do not penetrate more than a few monolayers into the surface before being reflected off one of the crystal planes. RHEED is therefore extremely sensitive to the condition of the surface, and to the arrangement of the atoms at the surface. After reflection, the electrons can undergo constructive and destructive interference leading to a diffraction pattern. The electrons then strike a phosphorescent screen, which emits visible light upon absorbing the energy from the electrons. The shape of the diffraction pattern is then visible on the screen and can be analysed by the operator using a camera system and specialist software. When high energy electrons strike a target, X-rays can be produced. Therefore, the phosphorescent screen is typically attached to a leaded glass view port to prevent X-rays from leaking into the lab.

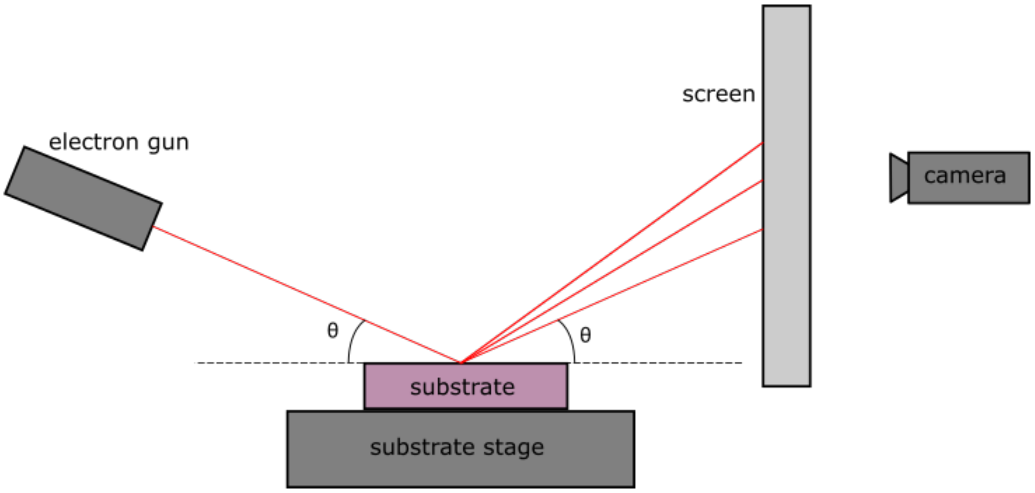

FIGURE 2.11: Diagram of the RHEED system. The angle θ is exaggerated in this image for clarity

2.4.2 Surface reconstructions

As discussed in section 1.1, the atoms on the wafer surface form into a reconstruction. The arrangement of the surface reconstruction is dependent on: the crystal plane of the wafer surface, the wafer surface temperature, the composition of the surface, and the incoming source fluxes. The surface reconstruction can be identified from its RHEED pattern, and correlated with other measurements (pyrometer temperatures, beam equivalent pressures) to create a reconstruction map for a particular material. Such maps are a valuable tool for crystal growers and enable the use of RHEED to measure the wafer surface temperature.

2.4.3 Theory

The electron beam undergoes constructive interference producing a diffraction pattern only at specific angles. At the maxima of the diffraction pattern: the diffraction condition is met, and the momentum of the electrons is conserved.

For the first case, the diffraction condition is given by Bragg's law [30], see equation 2.5, where n is an integer denoting the order of the diffraction, λ is the de Broglie wavelength of the electrons, d is the spacing between the atomic planes near the substrate surface, and θ are the angles at which the diffraction condition is met.

$$n\lambda = 2d.sin(\theta) \tag{2.5}$$

Since the electrons are diffracted by only the top few monolayers, there is no diffraction condition perpendicular to the wafer surface. The usual reciprocal lattice of the bulk structure is then modified to consist of reciprocal lattice rods, which are infinitely long and perpendicular to the wafer surface. The spacing of the reciprocal lattice rods a^* is related to the lattice constant a by equation 2.6.

$$a^* = \frac{2\pi}{a} \tag{2.6}$$

For the second case, the electrons are considered to scatter elastically so that the magnitude of the electron wavevector before and after the scattering event are the same. Inelastically scattered electrons can penetrate deeper into the semiconductor and give rise to Kikuchi lines on the phosphorescent screen [19, 20]. However, inelastically scattered electrons do not contribute significantly to the RHEED oscillations [21]. All the possible end points of the wavevector of an elastically scattered electron form a sphere centred on the scattering site in reciprocal space, known as the Ewald sphere.

To satisfy both of the conditions, and for constructive interference to occur, the scattered electron wavevector must terminate on one of the reciprocal lattice rods and on the surface of the Ewald sphere: in other words, at the intersection of the Ewald sphere and the reciprocal lattice rods.

2.4.4 Practical use of RHEED in MBE

In theory, the smaller the angle between the electron beam and the substrate, the more surface sensitive the diffraction pattern becomes, and the easier it is to see the characteristic reconstruction pattern. However, in reality the electron beam starts to clip on the substrate mounting mechanism as the angle is reduced to the point where the RHEED pattern becomes indistinguishable. In addition, the MBE system used in this work can only view the RHEED pattern along one direction of the wafer, due to the design of the substrate mounting mechanism.

The most important use of RHEED in an MBE system is for the determination of the source fluxes and deposition rate. The sticking coefficients for the group III elements (Al, Ga, and In) are often approximated as 1, whereas the sticking coefficients for As and Bi vary strongly with the wafer surface temperature. Due to this large difference in sticking coefficients, the procedure for finding the source fluxes is different for the group III and group V elements.

2.4.5 Group III flux measurement using RHEED

During growth, the intensity of the spots in the diffraction pattern oscillates, with the frequency of oscillation corresponding to the time taken to grow a complete monolayer. This process can be understood in terms of layer-by-layer growth. For an initially atomically flat substrate, the RHEED signal should be at a maximum as diffuse scattering of the electron beam off the surface is unlikely. Upon initiating growth, the incoming molecular beams strike the substrate and can become adsorbed. These adatoms can then migrate around the surface (assuming the growth is taking place at an optimised temperature), and bond to other adatoms to minimise the surface free energy, forming into islands which are a single monolayer thick. At this point, the RHEED intensity is somewhat reduced due to diffuse scattering of some of the electrons at the surface. As further adatoms bond to the edge of the islands the surface coverage of the islands increases until 50% of the surface is covered by islands, at which point the RHEED signal should be at a minimum. As the monolayer deposition proceeds further, the gaps between islands are gradually filled in, and the

RHEED signal begins to increase. When the gaps are fully filled, an atomically flat surface is recovered, and the RHEED signal should again be at a maximum. This process is illustrated in figure 2.12.

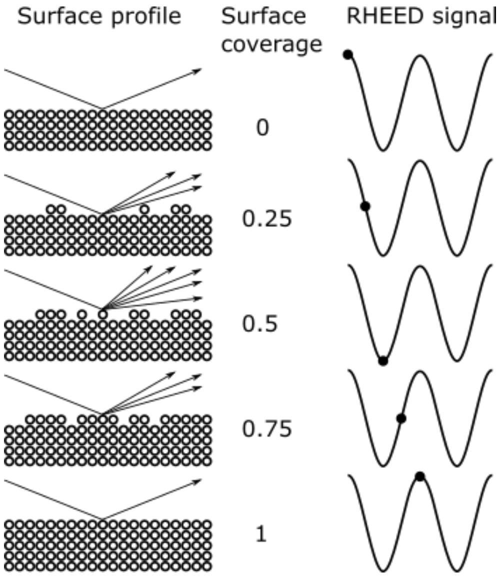

FIGURE 2.12: Illustration of the diffuse scattering of the electron beam, and its influence on the RHEED signal intensity, during the growth of a single monolayer

In reality, a second monolayer begins to form on top of the islands in the first monolayer before the first monolayer is complete. This is due to the limited mobility of the adatoms, and acts to reduce the intensity of the diffraction pattern through diffuse scattering of the electrons. A third monolayer can begin to form on top of the second monolayer, and so on, before the first monolayer is complete. This further increases the surface roughness, and results in the oscillations being damped, see figure 2.13 for an example of real RHEED oscillations.

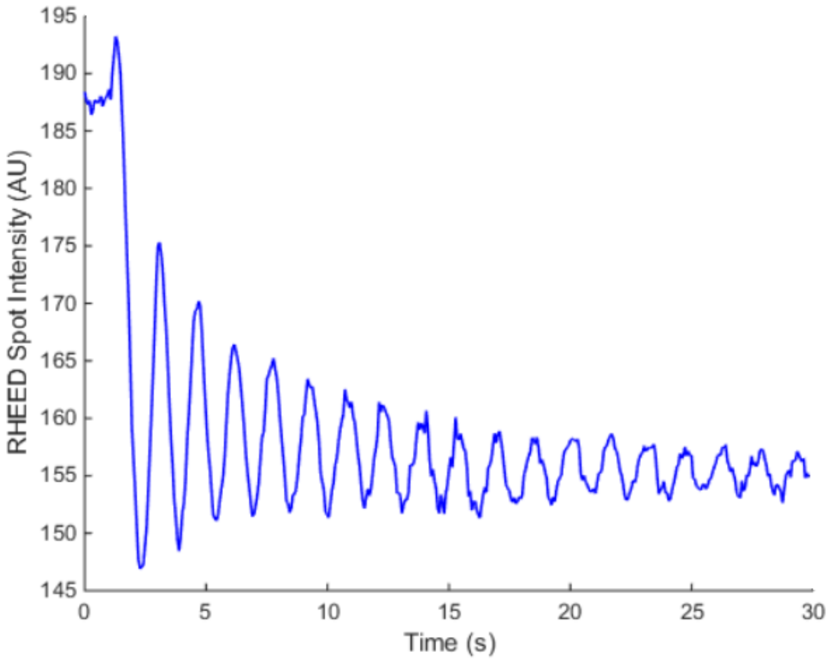

FIGURE 2.13: Typical RHEED intensity oscillations during MBE growth of GaAs, gathered using custom software package with USB webcam

As discussed in section 2.2.3, for GaAs epitaxy under an As overpressure, the growth rate is dependent only on the Ga flux. Therefore, the oscillation frequency of the RHEED pattern can be used to derive the Ga flux. From the zinc-blende crystal structure of GaAs (see figure 1.1), the unit cell consists of two monolayers of material. Clearly, each monolayer consists of two Ga and two As atoms in an area a^2, where a is the lattice constant. A deposition rate of 1 ML/s then corresponds to a flux of 2 Ga atoms in area a^2 per second. This relationship is summarised in equation 2.7.

$$F_{Ga} = \frac{2 * Growth\ rate}{a^2} \tag{2.7}$$

This equation is also valid for the determination of Al and In flux rates when growing the binary compounds AlAs and InAs, respectively, assuming that the sticking coefficients of the group III elements are unity. For deposition of ternary alloys containing more than one group III element, such as AlGaAs, InGaAs, and InAlAs, the total growth rate is the sum of the two group III constituent growth rates. This method cannot be used to directly calculate the group V flux. Instead, the group V flux is determined relative to the group III flux.

2.4.6 Group V flux measurement using RHEED

Once the Ga flux has been determined, the point at which the As and Ga fluxes are equal can also be found, to give the As flux relative to the Ga flux.

Under optimal growth conditions for GaAs, the As is over-supplied to compensate for thermal desorption from the wafer, with the degree of As oversupply related to the growth temperature. In this case, the surface has an As-rich (2x1) reconstruction during growth. If the As is under-supplied, the surface becomes Ga-rich, forming a (4x2) reconstruction during growth. Attempting to grow a thick layer under Ga-rich conditions leads to the formation of Ga droplets and a rough surface, which ruins the wafer beyond recovery. Changing from As-rich to Ga-rich growth, the diffraction pattern shows a clear transition, and the As valve position at which this transition occurs can be identified. This test can also be repeated using different wafer temperatures to determine the temperature dependence of the As desorption. The As flux can then be calculated relative to the Ga flux.

A similar flux calibration procedure is not possible for Bi since this would involve observing the transition between a Ga-rich and Bi-rich reconstructions in the growth of GaBi on a GaBi substrate (or a substrate with a similar lattice constant to GaBi). Since GaBi is not thermodynamically stable as a solid compound [43], an alternative method for calculating the Bi flux is necessary, as discussed in section 4.3.2.

2.4.7 Camera system and image processing

As previously discussed, the diffracted electrons strike a phosphorescent screen, which emits visible light, allowing the diffraction pattern to be viewed by a camera. Typically, a monochrome silicon camera is used to observe the RHEED pattern, however these can be expensive (>£1000). In this work, a colour USB webcam was used. In a colour camera, the colour information is generated using a mosaic of red, green, and blue filters (known as a Bayer filter), which is placed above or deposited onto the pixels of the sensor. Interpolation algorithms are then used to reconstruct a colour image from the Bayer filter-modified output of the sensor, and are designed to produce an image similar to what a typical human eye would observe. Due to this interpolation, a colour camera using a Bayer filter is slightly worse at resolving detail in a scene, relative to a monochrome sensor based on the same silicon sensor chip.

The phosphorescent screen used in this work emits mainly green light, meaning that the half of the pixels that are covered with blue and red elements of the Bayer filter will not detect the light (neglecting any transmission of the green light through the blue and red elements). Therefore, the sensitivity of colour cameras is lower than that of monochrome cameras.

However, colour USB cameras are extremely cheap due to the economy of scale associated with the enormous demand for mobile phone cameras and webcams. In this work, a custom designed software package was written in Matlab to view the webcam video feed and calculate growth rates in the MBE system. For an example of the capability of this system, see figure 2.13

2.5 Summary

Molecular beam epitaxy is a widely used method for creating high quality semiconductor materials. Developments in vacuum technology and element purity, along with accurate temperature control of effusion cells and substrate heaters have led to semiconductor devices with low defect densities and impurity concentrations. In addition, this means that the growth of novel dilute bismide semiconductors that have a narrow growth window is possible. The deposition rate can be determined in-situ using RHEED along with a camera and specialised imaging software.

Bibliography

[1] Q. Liu and Z. Cai, *Study on the characteristics of gas molecular mean free path in nanopores by molecular dynamics simulations*, International Journal of Molecular Science **15**, 12714-12730 (2014)

[2] D.J. Harra and W. H. Hayward, *Sorption of nitrogen by titanium films*, International Symposium on Residual Gases in Electron Tubes, 1967

[3] Gamma Vacuum, *Ion pump operation brochure*, p. 1, `http://www.gammavacuum.com/files/7213/8737/7402/Gamma_Operation_v2.pdf` [Accessed 21 August 2018]

[4] Agilent Technologies, *Ion pumps catalogue*, p. 25, `https://www.agilent.com/cs/library/catalogs/public/06_Ion_Pumps.pdf` [Accessed 21 August 2018]

[5] R. B. Lewis et al., *Closed cycle chiller as a low cost alternative to liquid nitrogen in molecular beam epitaxy*, Journal of Vacuum Science and Technology B **31**, 03C116 (2013)

[6] M. Iqbal et al., *Design modification in rotor blade of turbo molecular pump*, Nuclear Instruments and Methods in Physics Research Section A, **678**, 88-90 (2012)

[7] Pfeiffer Vacuum *The Vacuum Technology Book*, Volume II, c. 4, p.83 `https://www.pfeiffer-vacuum.com/en/info-center/vacuum-technology-book/` [Accessed 18 August 2018]

[8] Kurt J. Lesker Company, *Pump Classifications Technical Notes*, sections 4-3, 4-4 `https://www.lesker.com/newweb/vacuum_pumps/vacuumpumps_technicalnotes_1.cfm` [Accessed 20 August 2018]

[9] R. M. Nix, *Why is UHV required for surface studies?*, Queen Mary University of London, `http://www.chem.qmul.ac.uk/surfaces/scc/scat4_2.htm` [Accessed 20 August 2018]

[10] W. Ranke and K. Jacobi, *Composition, structure, surface states, and O_2 sticking coefficient for differently prepared GaAs($\bar{1}\,\bar{1}\,\bar{1}$)As surfaces*, Surface Science **63**, 33-44 (1977)

[11] L. Gelczuk et al., *Deep-level defects in n-type GaAsBi alloys grown by molecular beam epitaxy at low temperature and their influence on optical properties*, Scientific Reports **7**, 12824 (2017)

[12] R. H. Bogaard and C. Y. Ho, *Thermal Conductivity of Gallium Arsenide at High Temperature*, in: P. H. Hasselman and J. R. Thomas, Thermal Conductivity 20, Springer, Boston, MA, 1989

[13] J. Taylor, *Infrared Training Notes*, Land Infrared, 2008

[14] P. J. Timans, *The experimental determination of the temperature dependence of the total emissivity of GaAs using a new temperature measurement technique*, Journal of Applied Physics **72**, 660 (1992)

[15] Y. P. Varshni, *Temperature dependence of the energy gap in semiconductors*, Physica **34**(1), 149-154 (1967)

[16] S. R. Johnson, *Optical bandgap thermometry in molecular beam epitaxy*, PhD thesis, University of British Columbia, p.11, 1995

[17] R. Prasad et al., *Vapour pressure of bismuth calculated from Mg + Bi and Pb + Bi alloys using a transpiration technique*, Journal of Chemical Thermodynamics **9**, 593-601 (1977)

[18] R. N. Ratnaike, *Acute and chronic arsenic toxicity*, Postgraduate Medical Journal **79**(933), 391-396 (2003)

[19] S. Kikuchi, *Diffraction of cathode rays by mica*, Japanese Journal of Physics **5**, 83-96 (1928)

[20] P. Hirsch et al., *Electron Microscopy of Thin Crystals*, Butterworths/Krieger, London/ Malabar FL, 1977

[21] W. Braun et al., *Surface morphology dependence of plasmon inelastic scattering in RHEED*, Surface Science **399**, 234-238 (1998)

[22] C. B. Alcock et al., *Vapour pressure equations for the metallic elements: 298-2500K*, Canadian Metallurgical Quarterly **23**(3), 309-313 (1984)

[23] R. Celmer et al., *Vapour pressure of arsenic*, Canadian Metallurgical Quarterly **23**(2), 169-172 (1984)

[24] A. T. Aldred and J. N. Pratt, *Vapor pressure of liquid bismuth*, Journal of Chemical Physics **38**, 1085 (1963)

[25] L. Brewer, *The thermodynamic and physical properties of the elements*, Report for the Manhattan Project, 1946

[26] L. Nattermann et al., *MOVPE growth of Ga(AsBi)/GaAs using different metalorganic precursors*, Journal of Crystal Growth, **426**, 54-60 (2015)

[27] H. Fitouri et al., *Study of GaAsBi MOVPE growth on (100) GaAs substrate under high Bi flow rate by high resolution X-ray diffraction*, Microelectronic Engineering **88**(4), 476-479 (2011)

[28] H. Kim et al., *Characteristics of OMVPE grown GaAsBi QW lasers and impact of post-growth thermal annealing*, Journal of Applied Physics **123**, 113102 (2018)

[29] R. Pelzel, *A comparison of MOVPE and MBE growth technologies for III-V epitaxial structures*, CS MANTECH Conference, pp.105-108, New Orleans, LA, 13-16 May 2013

[30] W. H. Bragg and W. L. Bragg, *The reflexion of X-rays by crystals*, Proceedings of the Royal Society London A, **88**(605), 428-438 (1913)

[31] F. Bastiman, *In situ surface studies of III-V semiconductor compounds*, PhD thesis, University of Sheffield, p.105, 2010

[32] A. Nemcsics and J Takacs, *Investigation of the hysteretic phenomena in RHEED intensity change in the study of surface reconstruction*, Acta Polytechnica Hungarica **7**(5), 109-128 (2010)

[33] Y. Asaoka et al., *In situ control of the desorption process of GaAs surface native oxide by direct Ga beam irradiation*, International Conference on Molecular Beam Epitaxy, San Francisco, CA, 15-20 September 2002

[34] H. Preston Thomas, *The international temperature scale of 1990*, Metrologia **27**(1), 3-10 (1990)

[35] Granville-Phillips Advanced Vacuum Measurement Solutions, *Introduction to Bayard-Alpert ionization gauges*, `http://mmrc.caltech.edu/Vacuum/Teledyne%20Hastings/Ion%20Gauges.pdf` [Accessed 21 August 2018]

[36] Epimax Ltd, *PVCX Ion Gauge Specification*, `http://www.epimax.com/pvci/pvcinfo.html` [Accessed 21 August 2018]

[37] F. Bastiman, *MBE Dreams: Efficiency of Effusion Cells*, blog article: `https://faebianbastiman.wordpress.com/2014/08/29/mbe-dreams-efficiency-of-effusion-cell/` [Accessed 18 August 2018]

[38] R. D. Richards et al., *Molecular beam epitaxy growth of GaAsBi using* As_2 *and* As_4, Journal of Crystal Growth **390**, 120-124 (2014)

[39] C. T. Foxon and B. A. Joyce, *Interaction kinetics of* As_2 *and Ga on 100 GaAs surface*, Surface Science **64**(1), 293-304 (1977)

[40] F. Bastiman, *In Situ Surface Studies of III-V Semiconductor Compounds*, PhD thesis, University of Sheffield, p.20, 2010

[41] C. T. Foxon and B. A. Joyce, *Interaction kinetics of* As_4 *and Ga on 100 GaAs surfaces using a modulated molecular beam technique*, Surface Science **50**(2), 434-450 (1975)

[42] G. R. Bell et al., *Nanoscale effects of arsenic kinetics on GaAs(001)-(2×4) homoepitaxy*, Surface Science **423**(2-3), L-280-L284 (1999)

[43] N. Elayech et al., *Thermodynamic study of the ternary system gallium-arsenic-bismuth*, Physica Status Solidi C **12**(1-2), 138-141 (2015)

[44] I. N. Stranski and L. Krastanow, *Zur Theorie der orientierten Ausscheidung von Ionenkristallen aufeinander*, Abhandlungen der Mathematisch-Naturwissenschaftlichen Klasse IIb. Akademie der Wissenschaften Wien **146**, 797-810 (1938)

[45] M. Volmer and A. Weber, *Keimbildung in übersättigten Gebilden*, Zeitschrift für Physikalische Chemie 119, 277 (1926)

[46] F. C. Frank and J. H. van der Merwe, *One-dimensional dislocations I-III*, Proceedings of the Royal Society of London A **198**, 205 (1949), **198**, 216 (1949), **200**, 125 (1949)

[47] J. Puustinen et al., *Analysis of GaAsBi growth regimes in high resolution with respect to As/Ga ratio using stationary MBE growth*, Journal of Crystal Growth **511**, 33-41 (2019)

Chapter 3

Characterisation techniques

There are a large number of characterisation methods that are applicable to MBE grown semiconductor epilayers. These methods can be broadly split into three categories: structural, optical, and electrical measurements. A summary of the techniques used in this work is given in this section.

3.1 X-ray diffraction

X-ray diffraction (XRD) is a non-destructive technique which allows the measurement of several key structural properties of an epilayer, such as the composition, layer thicknesses, and the degree of relaxation. These parameters are typically calculated by comparing the measured data to an iterative simulation of the structure. In addition, the agreement between the simulation and data can give a qualitative estimate of the abruptness of heteroepitaxial interfaces and the existence of any compositional variation. XRD is a fast measurement and does not require additional fabrication steps, meaning that it can be used to quickly obtain feedback for the growth optimisation of future epilayers.

3.1.1 Operating principles

In an XRD measurement, a monochromatic beam of collimated x-ray photons is directed at the semiconductor epilayer. The wavelength of the X-rays is similar to the spacing between adjacent atomic planes in the epilayer leading to diffraction of the X-rays. The diffraction pattern is measured using a detector mounted near the epilayer. The epilayer position, beam position, and detector position are controlled using stepper motors to obtain a high signal and a high angular resolution in the measurement.

3.1.2 Theory – bulk homoepitaxial and heteroepitaxial layers

Each incoming x-ray can undergo one of several processes: specular reflection off one of the planes of atoms, diffuse reflection off surface features or structural defects, or absorption by the crystal.

In the context of this work, we note that bismuth should be effective at absorbing x-rays due to its high density and atomic number, which are similar to lead. However, the GaAsBi epilayers studied in this work are extremely thin (<1500 nm) and have a relatively low concentration of bismuth (<6% of the As atoms replaced with Bi).

The diffuse reflection of X-rays is enhanced if the surface is rough or covered in droplets resulting in a lower count rate in the XRD measurement. In this work the presence of droplets and other surface defects is studied by Nomarski microscopy, see section 3.2.

X-rays that are specularly reflected from the atomic planes will make up the overwhelming majority of the X-rays that form the diffraction pattern. Each atomic plane can be considered a weakly reflecting surface, with the overall penetration depth of the X-rays dependent on the reflectivity of each plane. At certain angles of the incident beam the reflected x-rays undergo constructive interference, which can lead to nearly 100% reflection. The diffraction of X-rays of wavelength λ by a perfect crystal lattice with plane spacing d can be described using Bragg's law [11], as shown in equation 3.1. Here, ω is the diffraction angle, at which maxima in the intensity of the diffracted X-rays will be observed, and n is an integer denoting the diffraction order.

$$n\lambda = 2d.sin(\omega) \tag{3.1}$$

The diffraction process is shown diagrammatically in figure 3.1.

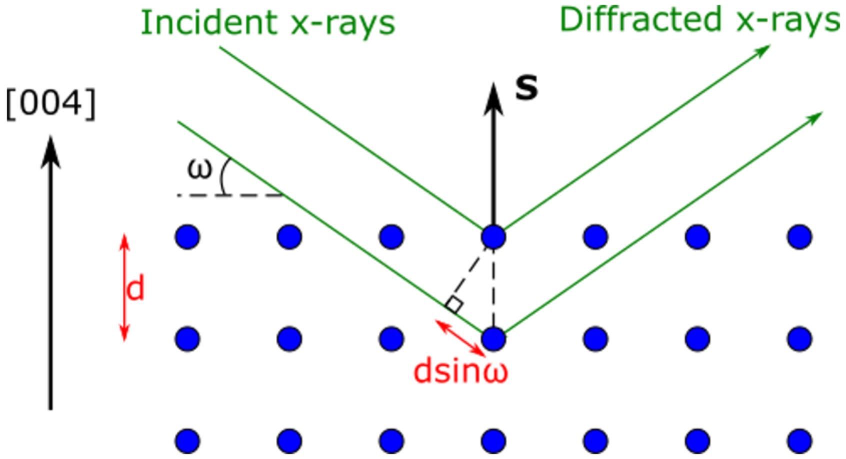

FIGURE 3.1: Diagram of the diffraction of X-rays from the (004) plane of a perfect crystal

In figure 3.1, the planes of atoms being studied are parallel to the substrate surface: this is known as a symmetric scan. In this case, the plane normal direction $[hkl]$ is parallel to the diffraction vector **S**, which is the vector that bisects the incident and diffracted beams. The Bragg condition can be met by many different crystal planes: for asymmetric scans (e.g. 224, 113) where the atomic plane is not parallel to the surface, the wafer is rotated to ensure that the diffraction vector is parallel to the plane normal direction, and reciprocal space mapping can be used to find the parameters of interest. The plane spacing d is related to the Miller indices of the crystal plane (hkl) via equation 3.2.

$$d = \frac{a}{\sqrt{h^2 + k^2 + l^2}} \tag{3.2}$$

Here a is the lattice constant of the epilayer. The above example considers a homoepitaxial layer whereas heteroepitaxial layers are the focus of this work. For a heteroepitaxial layer with the same crystal structure as the substrate, the relaxed lattice constant is not necessarily the same. For cases where the lattice mismatch is small, growth can proceed pseudomorphically, with the in-plane lattice constant of the epilayer (a_l) being deformed to match that of the substrate (a_s), see figure 3.2. To accommodate the strain energy, the out-of-plane lattice constant (c) is tetragonally distorted.

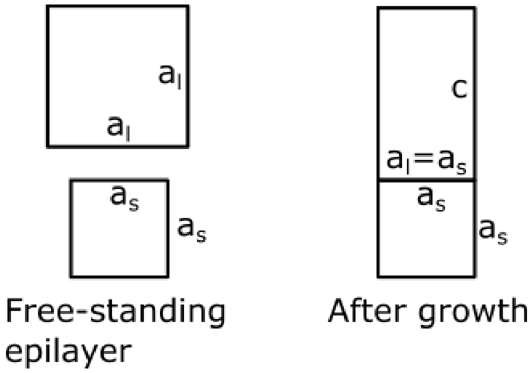

FIGURE 3.2: Lattice constants of the substrate (a_s) and epilayer (a_l) when the alloys are free-standing and after deposition. Note that the out-of-plane lattice constant (c) is distorted to accommodate the strain. The zinc-blende unit cell structure of the semiconductors studied in this work is approximated by a square for simplicity

The atomic plane spacing of a strained heteroepitaxial layer is therefore different from the plane spacing in the substrate, which results in a secondary diffraction peak at a different angle to the substrate peak. The intensity of the secondary peak is roughly proportional to the thickness of the epilayer, up to a point. This peak is also typically less intense than the substrate peak in which case the penetration depth of the x-rays is much greater than the epilayer thickness. The FWHM of the epilayer peak is inversely proportional to its thickness. In addition, if the epilayer is non-uniform in the growth direction or in the plane of the substrate, on a length scale comparable to the x-ray spot size, the layer can contribute several diffraction peaks to the XRD spectrum.

X-rays reflected from the top and bottom interfaces of the epilayer can constructively interfere to produce fringes which are superimposed on top of the substrate and epilayer diffraction peaks. Since the epilayer is typically several hundreds or thousands of times thicker than the atomic plane spacing, the angular separation between the higher order diffraction peaks is much smaller. The prominence of these fringes is a qualitative indication of the abruptness of the top and bottom epilayer interfaces. An example of a simulated XRD spectrum is shown in figure 3.3.

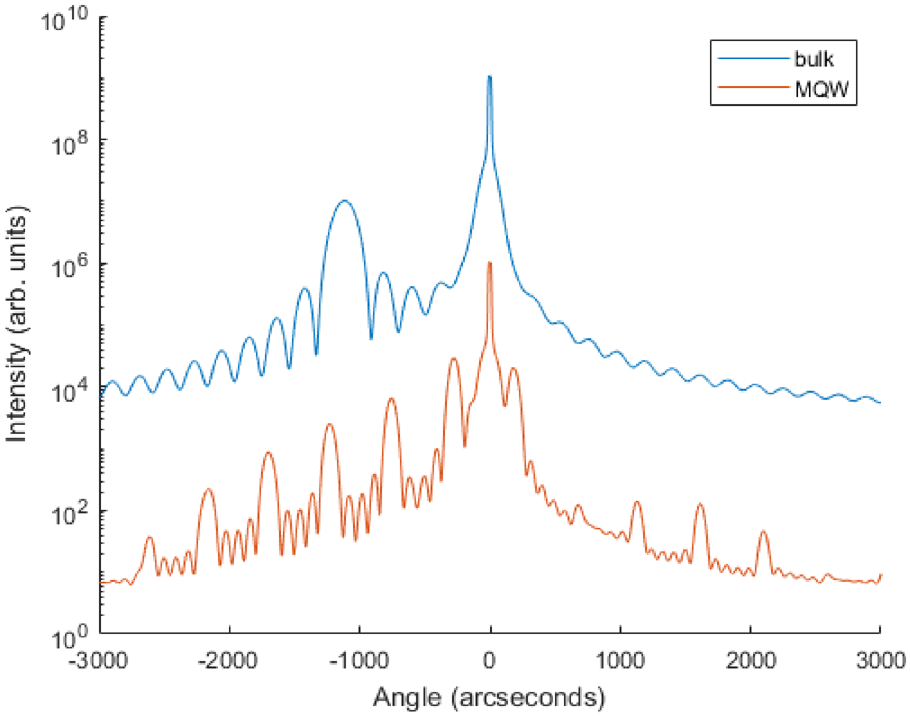

FIGURE 3.3: Example of XRD simulated data: a bulk GaAsBi layer (blue), and a 5 period GaAsBi/GaAs MQW (orange). The two scans are vertically offset for clarity.

3.1.3 Theory – superlattices and multiple-quantum wells

The XRD spectra of superlattices and MQWs contain a series of satellite peaks, which are caused by constructive interference between x-rays reflected from the periodic interfaces between the superlattice layers. The closest superlattice peak to the substrate peak is termed the zero order superlattice peak, with the splitting to the substrate peak dependent on the average lattice constant of a single period of the superlattice. The angular spacing between the other superlattice peaks is determined by the thickness of each superlattice period. Additional fringes corresponding to the total thickness of the MQW stack are superimposed on top of the satellite peaks. See figure 3.3 for a simulated MQW XRD spectrum.

3.1.4 Production of X-rays and design of diffractometer

An XRD measurement is usually performed in an all-in-one system, which features interlocked doors made of leaded glass that heavily attenuate the X-rays and protect the lab users. In this work, a Bruker D8 Discover X-ray diffractometer was used.

The X-ray beam is produced via the collision of electrons with an anode. A high voltage power supply (30 KV in this work) is connected across a cathode and the anode to accelerate electrons that are thermionically emitted from the cathode. The emission and acceleration of the electrons takes place in a vacuum to ensure that they do not lose energy through collisions with air molecules. The electrons strike the anode and can produce X-rays. The intense electron beam causes the anode temperature to increase since the heat transfer away from the anode is limited to black body radiation and conduction through the mounting mechanism due to the vacuum. To ensure that the anode does not melt it is typically disk-shaped and can be rotated. An X-ray-transparent window is used to couple the X-rays out of the tube and into the beam optics.

The anode in the XRD system used in this work is made from copper, which has an extremely high thermal conductivity. This helps to dissipate heat in the anode, despite the relatively low melting temperature of copper. Depending on the application, other anode materials may also be used, such as tungsten, cobalt, or molybdenum.

The X-ray spectrum emitted from the anode is the sum of X-rays produced via bremsstrahlung and characteristic x-rays that are material specific. Bremsstrahlung (translation: braking radiation) is the emission of a photon when a high energy charged particle (in this case an electron) is deflected by another charged particle (in this case an atomic nucleus). Since the distance of closest approach of the electron can vary, the degree to which the electron is deflected varies, and therefore bremsstrahlung generates a continuous spectrum of X-rays. A highly intense beam of monochromatic x-rays is desired for XRD measurements. While the bremsstrahlung process will contribute a small number of X-rays to the beam at the desired wavelength, the power is spread across the entire spectrum. Hence bremsstrahlung is not suitable to produce the X-ray beam by itself.

Characteristic X-rays are produced when a high energy electron transfers its energy to another electron which is in one of the inner orbitals of an atom. The second electron is promoted to a higher energy level or ejected from the atom, creating a vacancy. When an electron from one of the outer shells of the atom falls into the vacancy, a characteristic X-ray is emitted. The transition energies between different electron orbitals are material dependent, such that the anode material determines the wavelength of the characteristic X-rays that are emitted. In this work, the characteristic X-rays are emitted from the copper anode via the transition of an electron in the 2p orbital to the 1s orbital (known as the Kα transition). The resultant X-ray spectrum from this transition is in fact a doublet due to a small splitting between the energy levels in the 2p orbital, with the two peaks termed Kα1 (at 0.154056 nm) and Kα2 (at 0.154439 nm) [4]. Characteristic X-rays typically have a high intensity and a narrow linewidth making them ideal for use in XRD measurements.

However, the X-ray beam is not monochromatic at this point, and one of the two Kα lines, the continuous bremsstrahlung spectrum, and any higher energy characteristic X-rays (e.g. Kβ) must be filtered out of the beam. The higher energy characteristic X-rays are heavily attenuated through the use of a nickel foil filter, the weaker of the two Kα lines (Kα2) is removed using a monochromator, and the beam is collimated using parabolic mirrors.

The collimated beam is then directed towards the sample stage, passing through a slit on its way. The wider the slit, the greater the intensity of the X-ray beam upon hitting the sample. However, this comes at the cost of reduced angular resolution.

In this work, the wafer was mounted on a porous ceramic vacuum chuck, which prevents it from moving when the stage is rotated to be vertical. The stage can be rotated (azimuth, altitude) or translated (x, y, z) in five different directions to allow for accurate positioning of the wafer with respect to the X-ray beam. The position of each of the goniometers and translation stages are controlled by stepper motors.

Upon diffraction by the sample, the X-rays strike a germanium detector. In a triple-axis XRD system, the angular acceptance range of the detector is limited, which increases the angular resolution of the measurement at the expense of signal intensity. A simplified diagram of the equipment design is shown in figure 3.4. Here θ is the angle between the wafer and the detector.

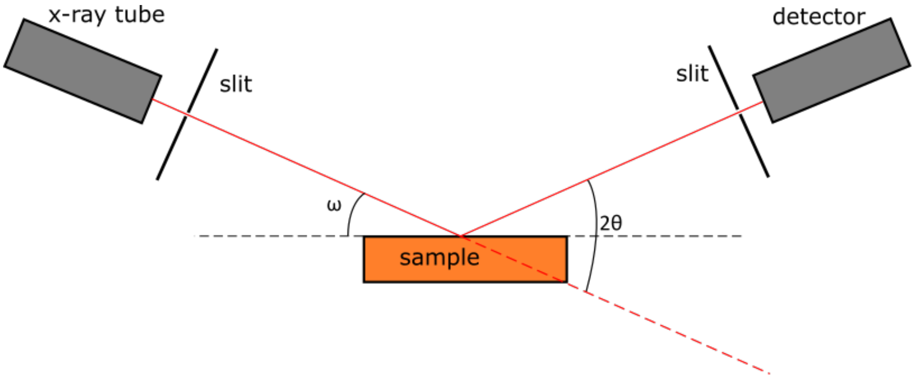

FIGURE 3.4: Diagram of XRD measurement. The collimating mirror and monochromator are not shown for clarity

3.1.5 Measurement procedure

After placing the wafer on the stage, each of the rotation and translation drives is optimised to obtain the highest possible X-ray intensity for the substrate diffraction peak at the detector. In the XRD system used in this work (Bruker D8 Discover), the X-ray source was kept static, and the stage and detector rotated. There are several different types of scans: rocking curves (varying ω, while detector is static), detector scans (2θ is varied, while sample stage is static), and coupled scans (where both 2θ and ω are varied, such that $\omega = 1/2 * 2\theta + offset$. Rocking curves and detector scans are typically used for alignment of the beam on the sample, however the XRD peak width in a rocking curve is related to the crystallite size in the target.

For high quality XRD measurements, both a high angular resolution and a high signal to noise ratio are desirable. A long acquisition time can be used to achieve a high signal to noise ratio. Typically, the crystallographer will take a low-resolution scan first to verify the presence of an epilayer diffraction peak and thickness fringes, before running a high-resolution scan with a longer integration time.

The measurement can then be compared to a fit calculated using specialist software. The user inputs an initial “guess” of the layer thicknesses and compositions, and the software attempts to fit a model to the data. Typically, the user is required to give a relatively accurate initial “guess” of the material parameters to prevent the software from finding a local minimum in the fitting.

3.1.6 Effect of strain relaxation on XRD pattern

When the Matthews-Blakeslee critical thickness of an epilayer is exceeded the lattice constant of the epilayer reverts towards its free-standing value, and its diffraction peak shifts relative to the substrate peak. This results in dislocations that are already present in the material moving to the interface and becoming misfit dislocations, which is deleterious to the device performance. If the epilayer is strain relaxed then any subsequent layers can be pseudomorphically strained to the epilayer. For example, if a deposited GaAsBi layer is heavily relaxed, then any subsequent layers of GaAs grown above the GaAsBi can be fully strained to the GaAsBi. This results in a tensile GaAs peak which does not occur at the same angle as the substrate GaAs peak. The presence of strain-relaxation can also be verified using Nomarski microscopy (see section 3.2).

3.1.7 Lattice constant of GaBi

The lattice constant of GaBi is crucial to determining the bismuth incorporation in XRD measurements. Several authors have extrapolated the lattice constant of GaBi, with the value varying depending on the host material and the assumptions made for the elastic constants of GaBi. Puustinen gives a value of 0.633 nm, assuming that GaBi has the same elastic constants as GaAs [15], while Song and Rajpalke give values of 0.623 and 0.627 nm, respectively, based on treating GaBi as having the same elastic constants as GaSb [13, 14]. The value of the GaBi lattice constant was taken to be 0.633 nm in this work. However, the values calculated by Song and Rajpalke are likely to be more accurate since there is less of a size difference between antimony and bismuth than between arsenic and bismuth.

3.1.8 Summary

XRD is widely used for rapid feedback during growth optimisation of semiconductors using MBE due to its ability to accurately obtain layer thicknesses, compositions, and estimates of the degree of relaxation. These attributes make XRD a valuable tool for a crystal grower.

3.2 Nomarski microscopy

Also known as differential interference contrast microscopy, Nomarski microscopy is an optical imaging technique that is used to view the surfaces of MBE grown wafers, and can yield information about the surface roughness, droplet density, and the presence of strain relaxation. A typical research-grade optical microscope can be modified into a Nomarski microscopy using additional optical components.

3.2.1 Theory and equipment design

A diagram showing the arrangement of the optical elements in a Nomarski microscope is shown in figure 3.5. A hot-filament bulb is used as a light source for Nomarski microscopy and emits a broad spectrum of randomly polarised light. This light passes through a polariser and is then split into 0°and 90° polarised light by a Wollaston prism. The two orthogonally polarised beams are also spatially separated by a small distance known as the shear (typically around 0.2 µm) by the Wollaston prism, and are unable to interfere with each other. The two beams then pass through the wafer, at slightly different locations. If the two locations on the wafer have a different refractive index or semiconductor thickness, the optical path length is modified. The light passes through a second Wollaston prism that recombines the two beams, which then undergo constructive or destructive interference depending on their optical path length difference. The interference causes the light intensity to be modified for a given point in the image, which results in increased contrast in the image formed on the camera sensor.

Nomarski microscopy can provide useful information about the sub-surface and surface condition of an epilayer, which is difficult if not impossible to infer from optical microscopy [2]. Additionally, the presence of strain relaxation in an epilayer can be qualitatively verified if a "cross-hatch" pattern is present in the Nomarski images [3]. For examples of Nomarski images, see sections 4.6 and 5.5.

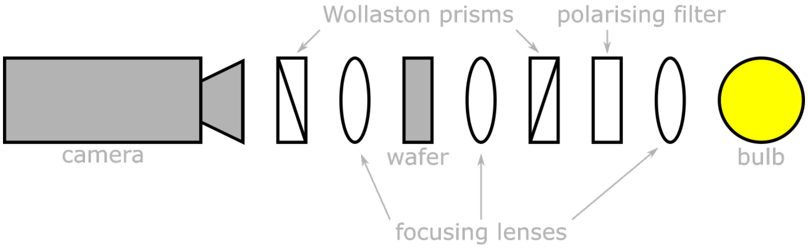

FIGURE 3.5: Arrangement of optical elements in a Nomarski microscope

3.3 Photoluminescence spectroscopy

Photoluminescence spectroscopy is a fast and non-destructive optical measurement which can be used to determine the distribution of optically active states in a semiconductor. This allows the band gap to be found. Investigations into the energy levels of defects and localised states are possible by varying the measurement conditions (e.g. incident laser power, device temperature, laser wavelength) and observing the effect on the emitted photoluminescence. The composition of a ternary semiconductor can be extracted by comparing the band gap to previous empirical and theoretical models, and PL can also be used to give a qualitative estimate of the optical quality of the material.

3.3.1 Operating principles

A laser is directed at the semiconductor, where it can be absorbed and excite carriers. In order to excite electrons from the valence band to the conduction band, the laser photons must have an energy greater than the band gap. The electrons in the conduction band can then recombine with holes in the valence band resulting in the emission of a photon with energy equal to the band gap. The spectrum of the emitted photons is measured using a monochromator coupled to a photodetector.

3.3.2 Theory

For a semiconductor at zero kelvin, the valence band is completely full, and the conduction band is completely empty. However, the energy separation between the valence band maximum and the conduction band minimum is small enough that at room temperature, electrons can gain enough energy to be excited into the conduction band, which allows the semiconductor to conduct electricity.

While this process can happen spontaneously at equilibrium if an electron gains enough energy to be excited into the conduction band, the use of laser photons as an excitation source vastly increases the rate of excitation, and hence the rate of photon emission. This enhanced rate of photon emission allows its spectrum to be easily measured.

However, there are many pathways for the carriers to recombine, many of which are non-radiative and do not result in the emission of a photon. These non-radiative pathways can be due to structural defects, impurities, and transitions with other bands. Therefore, the intensity of the band gap emission provides a qualitative estimate of the number of defects and impurities in the semiconductor.

A simplified diagram showing the relevant excitation recombination processes in a direct band gap semiconductor is shown in figure 3.6. For an indirect band gap semiconductor, a more complicated diagram, showing the location of the conduction band minimum and valence band maximum in *k*-space is required, however this is beyond the scope of this work since GaAsBi is a direct gap semiconductor [1].

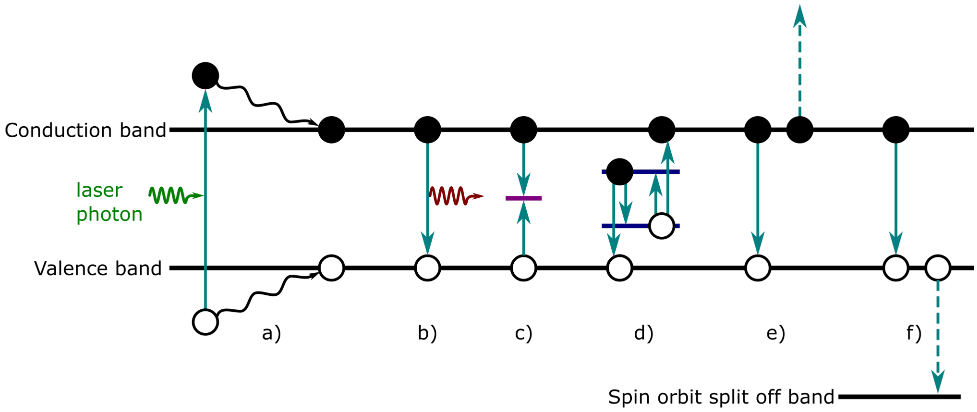

FIGURE 3.6: Diagram of relevant excitation and recombination processes in a direct band gap semiconductor: a) radiative excitation and relaxation to band edge, b) radiative recombination, c) recombination via defect level, d) recombination via dopant states (these transitions can result in the emission of a photon, and the dopant energy levels are much closer to the conduction and valence bands, but this is not shown for clarity), e) CHCC Auger recombination, f) CHSH Auger recombination. The teal arrows denote transitions, and the black lines denote the conduction and valence bands.

Figure 3.6a) shows radiative excitation of an electron to the conduction band via the absorption of a laser photon. Since the laser photon has a much greater energy than the band gap, the electron is excited from a state deep in the valence band to a metastable state in the conduction band. Alternatively, the electron could be excited from the valence band maximum, however this would require the absorption or emission of a phonon to conserve momentum, which is far less likely. The electron and hole rapidly thermalise to the band edges such that luminescence with energy greater than the band gap is unlikely. This generation rate of carriers via this process is proportional to the laser power.

Figure 3.6b) shows the radiative recombination of an electron and a hole, with the emission of a photon with energy equal to the band gap. Measuring the light emitted by this process is the operating principle of PL. In a real PL measurement this emission is broadened due to the energy distribution of the carriers and compositional variation of the epilayer across the laser spot. This process occurs when a hole and electron come into close proximity. Therefore the recombination rate R_{rad} is proportional to the density of both carrier types n and p, see equation 3.3. Here B_{rad} is the radiative recombination coefficient.

$$R_{rad} = B_{rad} n p \tag{3.3}$$

Figure 3.6c) shows recombination of carriers via a defect level which is inside the forbidden energy gap. This group of recombination processes is also known as Shockley-Read-Hall recombination [5, 6] and do not result in the emission of a photon: the energy of the carriers is dissipated via the emission of phonons (which results in heating of the crystal). Such an energy level can be caused by impurity atoms or structural defects in the semiconductor, which give rise to a localised variation in the band structure. SRH recombination processes include: electron capture (an electron relaxes from the conduction band to the defect level), hole capture (recombination of an electron in the defect level with a hole in the valence band, electron emission (thermal excitation of an electron in the defect level to the conduction band, and hole emission (thermal excitation of a hole in the defect level to the valence band). The SRH recombination process occurs when a single carrier encounters a defect level, therefore the recombination rate is proportional to carrier density n and the density of defects, see equation 3.4. Here B_{SRH} is the Shockley-Read-Hall recombination coefficient, which takes into account the defect density.

$$R_{SRH} = B_{SRH} n \tag{3.4}$$

Figure 3.6d) shows recombination via shallow dopant energy levels inside the band gap. This recombination can result in the emission of a photon, which can lead to additional peaks in the PL spectrum at longer wavelength.

Figure 3.6e) and 3.6f) show CHCC (**C**onduction band to **H**eavy hole band, and **C**onduction band to higher energy state in the **C**onduction band) and CHSH (**C**onduction band to **H**eavy hole band, and **S**pin orbit split off band to **H**eavy hole band)Auger recombination respectively. These processes are similar in that they involve the recombination of an electron and hole, but instead of emitting a photon (as in radiative recombination) the energy goes into exciting another carrier. In CHCC Auger recombination the energy goes to another electron in the conduction band, which is excited to a higher energy state in the conduction band, after which it promptly thermalises back to the band edge. In CHSH Auger recombination the energy goes to another hole in the valence band, which can be excited into the spin orbit split off band. Since Auger recombination is a three-particle interaction, the recombination rate is proportional to the cube of the carrier density, see equation 3.5. Here B_{Auger} is the Auger recombination coefficient, and the process shown is CHCC Auger recombination (for CHSH recombination n^2p should be replaced with np^2).

$$R_{Auger} = B_{Auger} n^2 p \tag{3.5}$$

Auger processes are major loss mechanisms in devices which operate with high carrier densities (e.g. InGaAsP/InP 1.55 μm lasers). In a III-V semiconductor the energy gap between the valence band maximum and the spin orbit split off band is chiefly dependent on the atomic number of the group V element [16]. As bismuth is incorporated into GaAs the band gap decreases and the spin orbit splitting increases. The two are theorised to be equal for approximately 10% bismuth. If the band gap is reduced further then the CHSH Auger process is suppressed which could lead to more efficient lasers operating in the 1.55 μm telecomms band.

For an intrinsic semiconductor under steady state conditions, the carrier density is stable over time and the carrier generation rate G is equal to the total recombination rate, which is the sum of the recombination rates of the various processes discussed above, see equation 3.6.

$$\frac{dn}{dt} = 0 = G - R_{SRH} - Rrad - R_{Auger} \tag{3.6}$$

By substituting the equations for the individual recombination processes into equation 3.6, equation 3.7 is obtained. Here Auger recombination is neglected since it dominates the device performance only at extremely high carrier densities.

$$G = B_{SRH}n + B_{rad}np \tag{3.7}$$

From equation 3.7, the dominant recombination mechanism depends on the carrier concentration, which, in the case of PL, is dependent on the laser power. Alternatively, in electroluminescence the carrier concentration is dependent on the injection current.

If radiative recombination is dominant in the device, $B_{SRH}n << B_{rad}np$ and equation 3.8 is obtained.

$$G \approx B_{rad}np \tag{3.8}$$

In which case the emitted light through radiative transitions is linearly proportional to the carrier generation rate.

When non-radiative recombination is dominant, $B_{SRH}n >> B_{rad}np$ and equation 3.9 is obtained.

$$G \approx B_{SRH}n \tag{3.9}$$

However, to obtain the dependence of the PL signal, $B_{rad}np$ on the carrier generation rate G, equation 3.9 must be rearranged to find n. Assuming that $n \approx p$, this results in equation 3.10.

$$B_{rad}n^2 = B_{rad}\frac{G^2}{B_{SRH}^2} \tag{3.10}$$

In which case the PL signal is proportional to the square of the carrier generation rate.

For an epilayer with a low rate of non-radiative recombination the carrier lifetime will be large. This means that the rate of radiative recombination should be higher and the observed PL (or EL) signal should be higher. Radiative recombination is a loss mechanism in a solar cell. However, minimising the loss of carriers through non-radiative recombination is more important than minimising the radiative recombination. Therefore, a the brighter the PL from a device the better suited it is for solar cell applications.

3.3.3 Equipment design

A diagram showing the PL equipment design is shown in figure 3.7.

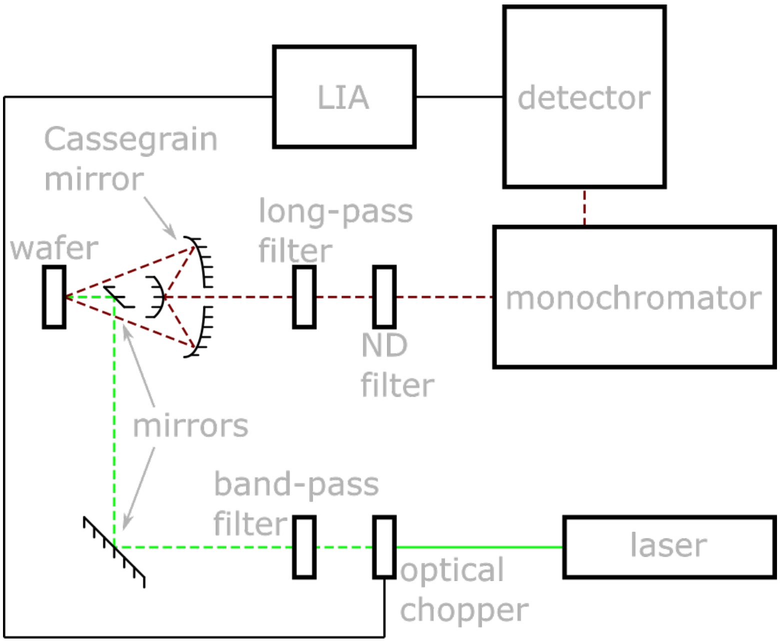

FIGURE 3.7: Diagram of the photoluminescence equipment

The laser used in this work for PL measurements was a continuous-wave frequency doubled Nd:YAG (neodymium doped yttrium aluminium garnet) laser operating at 532 nm, with a maximum power output of 2 W. This wavelength is easily visible to the naked eye, meaning that (up to a certain laser power) the blink reflex is able to protect the eye from damage by the laser. The laser beam path is also enclosed using safety curtains (except during beam alignment work), and the user can wear goggles that have a high optical density at 532 nm for increased eye protection.

The laser also emits light at 1064 nm (up to 10 mW) as a by-product of the frequency doubling process: this light must be filtered out of the beam using a band pass or short pass filter, or else it will show up in the measured spectrum. However, this light is useful as a reference to calibrate the monochromator.

The laser is directed towards the wafer using mirrors and focused into a spot using a lens. The wafer is mounted vertically on a metal plate using vacuum grease, which is attached to a translation stage. The emitted light is captured by a Cassegrain mirror, which consists of a large primary mirror and a smaller secondary mirror to direct the photons towards a monochromator or spectrometer. The use of a mirror-based optical assembly to collect the light does not introduce chromatic aberrations, as a lens would.

A GaAs wafer has a reflectivity of 0.37 at 532 nm at room temperature [7]. Therefore, a significant fraction of the laser light is reflected from the front surface. This light must be filtered out of the spectrum after the Cassegrain mirror using a long-pass filter. In addition, the long-pass filter must stop 2nd order diffracted light from interfering with the measurement. For example, if the user wishes to measure a spectrum in the range 800 to 1500 nm, the 2nd order diffraction of 750 nm light will be passed through the monochromator at the same point as the 1st order diffracted 1500 nm light, therefore a 780 nm long-pass filter can be used to remove this light.

A neutral density (ND) filter can also be inserted in the beam path to attenuate the light and modify the range of the measurement.

The main component of the monochromator is a diffraction grating, which separates the incoming photons according to their wavelength. The spectral components of the beam are diffracted at different angles, meaning that the larger the distance the light has to spread out, the higher the resolution of the monochromator. A large wavelength range can be analysed by rotating the grating such that each wavelength falls on an output slit in turn. The grating is rotated using a stepper motor, and the width of the entrance and exit slits can be increased to give a higher signal, at the expense of a greater bandpass of light. In this work, a 55 cm monochromator is used in conjunction with a 600 grooves/mm blazed grating, which is designed to reduce the amount of 0 order diffracted light (analogous to specularly reflected light from a flat surface) and increase the amount of 1st order diffracted light.

Alternatively, a spectrometer with integrated detector could be used instead of a monochromator and separate detector. However, spectrometers have reduced resolution and offer no flexibility with the detector choice, for the study of different wavelength ranges, despite being cheaper.

The detector used in this work is a LN_2 cooled germanium detector, which has an excellent specific detectivity in the spectral range 800 to 1700 nm. The Ge sensor is held inside a vacuum to prevent condensation, with a transparent window to pass light from the monochromator. The sensor is in thermal contact with an LN_2 reservoir, to reduce its dark current.

In order to reduce the effects of stray light on the measurement, the laser light is optically chopped, such that the PL is emitted in pulses. The chopper contains an optical sensor which measures its rotation frequency and passes it to a lock-in amplifier. The detector output is also coupled to the LIA, which then removes signals that are not the same frequency as the chopper rotation. One possible source of background light is fluorescent room lights, which oscillate with a frequency of 50 Hz (the mains frequency). To remove such light from the measured signal, the chopper rotation frequency must not be set to 50 Hz (or any integer multiple of 50 Hz).

Dedicated computer software operates the monochromator, reads the data from the LIA, and controls the laser.

3.3.4 Measurement procedure and practical considerations

For a room temperature PL measurement, the wafer is mounted on the stage using vacuum grease. The stage is translated to obtain the highest PL intensity. Low temperature measurements are also possible using a helium compressor and a cryostat, however this was not utilised in this work.

The depth at which carriers are created depends on the laser wavelength and the absorption coefficient of the epilayers at that wavelength. For 532 nm light, the penetration depth in GaAs is around 250 nm [8]. The relative intensity of the GaAs PL peak compared to the GaAsBi peak is approximately determined by where the carriers are created. However, this neglects the possibility that minority carriers can migrate in the device before recombining due to either diffusion or drift in the presence of an electric field. The thermal energy ($k_B T$) at room temperature is 26 meV, and processes that have an activation energy (energy barrier) much larger than the thermal energy are unlikely to occur. The band offsets between GaAs and GaAsBi are approximately 23 meV/%Bi in the conduction band, and up to 65 meV/%Bi in the valence band [9], electrons (holes) are unlikely to pass from the GaAsBi into the GaAs at room temperature if the GaAsBi layer contains more than approximately 3% Bi (1% Bi). However, the carriers can easily migrate into the GaAsBi from the GaAs before recombining. This results in the GaAsBi PL peak being brighter than one would expect based purely on where the carriers are excited.

3.3.5 Summary

Room temperature PL is commonly used during growth optimisation, to measure the composition of ternary alloys and to get a qualitative measure of the material quality. Additional studies into the dominant recombination mechanism and distribution of states can be carried out using power dependent and low temperature PL measurements respectively.

3.4 Fabrication of contacts using photolithography

For detailed electrical characterisation of the grown devices, metal contacts must be fabricated on the wafer. The fabrication procedure is relatively straightforward in theory. However, due to equipment downtime, limited availability, and the expense involved: not every wafer grown on the MBE machine was fabricated and hence electrical measurements were not routinely used as feedback for the growth optimisation.

The diodes studied in this work all make use of a common back contact, while the front of the wafer is split into many different contact areas. For the deposition of the back contact, the wafer was thoroughly cleaned using solvents and placed upside down in a bell-jar evaporator. The metals (InGeAu for n-type contact) were subsequently evaporated onto the wafer under a vacuum. The wafer was annealed at 420 °C to ensure that the ohmic contacts are obtained.

For the front contacts, the contact area pattern was generated on the wafer using ultra-violet photolithography. A chemical (photoresist) which degrades upon exposure to UV light was deposited evenly on the front surface via spin-coating. A mask pattern formed by opaque and transparent sections on a glass slide was placed close to the surface of the wafer and aligned using a microscope. The minimum feature size used in this work was approximately 10 µm, which is much larger than the wavelength of the UV light. Consequently, the mask pattern did not need to consider diffraction of the light. A UV bulb was directed at the wafer, and the sections of photoresist not covered by the mask pattern were exposed and degraded. The exposure time and photoresist thickness are critical for effectively transferring the mask pattern onto the wafer. The degraded photoresist was then removed using a developer, and the wafer was cleaned with de-ionised water. The front contact (AuZnAu for p-type GaAs) was then deposited using the bell jar evaporator. The remaining photoresist which was not exposed to the UV light was then removed using acetone, which also removed the gold that was deposited on top of the resist. Further annealing at 360 °C was performed to ensure that the contacts are ohmic.

To isolate the devices from each other, the wafer was coated with more photoresist and put back into the mask aligner. The photoresist was exposed to the UV lamp using a mask that is the inverse of the previously used one, such that the gold coated contact areas are covered. After the exposed photoresist was removed using the developer, the semiconductor around the devices was removed using an etchant, to form mesa structures. The etchant used in this work was a 1:1:1 mixture of HBr, acetic acid, and potassium dichromate, which gives smooth etched surfaces for GaAs (001) [10]. It was assumed that this etchant is also effective for GaAsBi, since no systematic studies of GaAsBi etchants have been published to the author's knowledge. After etching, the photoresist covering the contact areas was removed and the devices were ready for electrical characterisation. An image of several mesa structures is shown in figure 3.8.

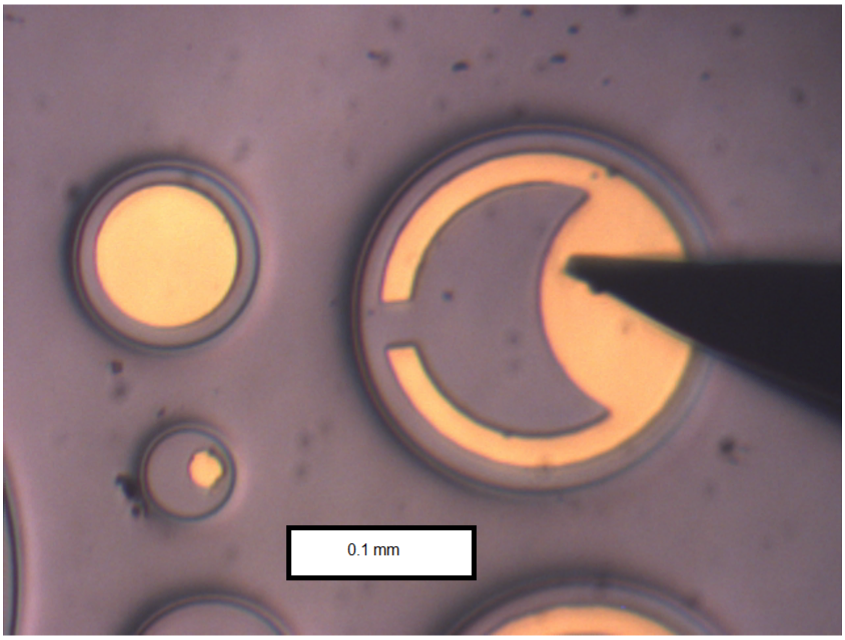

FIGURE 3.8: Microscope image of front contact mesa structures on surface of wafer

The mask used in this work was designed for characterisation of photodetectors, with the "half-moon" cut-out shape functioning as a window for light to reach the semiconductor. However, this mask has some drawbacks for EL and photovoltaic characterisation, as discussed in chapter 5.

All of the device fabrication in this work was performed by Faezah Harun.

3.5 Current-voltage

Current-voltage (IV) measurements can be performed on the fabricated devices. A microscope is used to view the mesa devices and probe the front contact. The wafer is placed on a gold-coated glass slide to probe the common back contact. The probes are connected to a picoammeter which can be controlled using specialist PC software. The picoammeter scans through a range of voltages and records the current. For measuring the dark current of the devices, the microscope light is switched off and the experiment is covered with a black cloth.

3.5.1 IV characteristics of diodes

The current I flowing through of a diode as a function of the bias voltage V can be described using the Shockley diode equation [12] see equation 3.11.

$$I = I_s \exp\left(\frac{qV}{nk_BT}\right) - I_s \tag{3.11}$$

Here q is the elementary charge, k_B is the Boltzmann constant, and T is the temperature. The reverse saturation current I_s describes the current at reverse bias and the intercept of the forward bias with the ordinate axis. The ideality factor n accounts for the imperfections present in real diodes, and typically ranges between 1 and 2. A value of 1 corresponding to an ideal diode. An ideality factor of 2 indicates that the recombination of carriers in the i-region is dominated by trap-assisted recombination. If the ideality factor is greater than 2 a more complicated model of the device must be considered.

3.6 Electroluminescence

Electroluminescence (EL) is a similar technique to photoluminescence, but the carriers are injected electrically via probing of the device, rather than by the absorption of laser photons. As such, the equipment used in EL is similar to that shown in figure 3.7. The recombinations mechanisms seen using EL are the same as in figure 3.6. However, in an LED the vast majority of the recombination occurs in the depletion region. Therefore, the emission spectrum depends on the material in the i-region, which may be a different material than the n and p-type in the case of a heterojunction pin diode.

For EL measurements, the fabricated contacts were probed directly (as opposed to mounting the device on a header), and the emitted light was focussed into a monochromator coupled to a LN_2 cooled Ge detector.

Since not all of the grown devices were fabricated with electrical contacts, EL was not used as feedback for subsequent growth runs. EL is an measurement of the optoelectronic quality of the epilayer, with high material quality and ohmic contacts necessary for operation. In addition, EL measurements are closer to the real-world applications of semiconductor devices, making the demonstration of EL an important milestone in the development of a novel alloy.

3.7 Summary

There are a large number of methods for characterising semiconductor devices. XRD and PL can be used to provide rapid feedback during growth campaigns, and can also be used for detailed investigations into the structural and optical properties of the epilayers. The fabrication of electrical contacts on the wafers enables measurement of the dark current which can be used to infer the dominant recombination mechanism in the i-region. EL measurements are an important milestone in the development of novel semiconductor alloys such as GaAsBi.

Bibliography

[1] Z. Zhou et al., *Absorption properties of GaAsBi based p-i-n heterojunction diodes*, Semiconductor Science and Technology **30**, 094004 (2015)

[2] John Innes Centre *Nomarski (DIC) Microscopy*, `https://www.jic.ac.uk/microscopy/more/T5_5.htm` [Accessed 10 August 2018]

[3] J. R. Bickford, *Sparse gallium arsenic to silicon metal waferbonding for heterogeneous monolithic microwave integrated circuits*, PhD Thesis, University of California, San Diego, pp.58-59 (2008)

[4] H. Berger, *Study of the Kα emission spectrum of copper*, X-ray Spectroscopy **15**(4), 241-243 (1986)

[5] W. Shockley and W. T. Read Jr., *Statistics of the recombinations of holes and electrons*, Physical Review **87**(5), 835-842 (1952)

[6] R. N. Hall, *Electron-hole recombination of germanium*, Physical Review **87**(2), 387 (1952)

[7] A. D. Rakic and M. L. Majewski, *Modeling the optical dielectric function of GaAs and AlAs: Extension of Adachi's model*, Journal of Applied Physics **80**, 5909 (1996)

[8] J. O. Akinlami and A. O. Ashamu, *Optical properties of GaAs*, Journal of Semiconductors **34**(3), 032002 (2013)

[9] A. R. Mohmad et al., *Localization effects and band gap of GaAsBi alloys*, Physica Status Solidi **251**(6), 1276-1281 (2014)

[10] S. Adachi and K. Oe, *Chemical etching characteristics of (001) GaAs*, Journal of the Electrochemical Society **130**(12), 2427-2435 (1983)

[11] W. H. Bragg and W. L. Bragg, *The reflexion of X-rays by crystals*, Proceedings of the Royal Society London A, **88**(605), 428-438 (1913)

[12] W. Shockley, *The theory of p-n junctions in semiconductors and p-n junction transistors*, The Bell System Technical Journal **28**, 3, p. 435-489 (1949)

[13] M. K. Rajpalke et al., *High Bi content GaSbBi alloys*, Journal of Applied Physics **116**, 043511 (2014)

[14] Y. Song et al., *Growth of $GaSb_{1-x}Bi_x$ by molecular beam epitaxy*, Journal of Vacuum Science and Technology B **30**, 02B114 (2012)

[15] J. Puustinen et al., *Variation of lattice constant and cluster formation in GaAsBi*, Journal of Applied Physics **114**, 243504 (2013)

[16] S. J. Sweeney and S. R. Jin, *Bismide-nitride alloys: Promising for efficient light emitting devices in the near- and mid-infrared*, Journal of Applied Physics **113**, 043110 (2013)

Chapter 4

Growth of GaAsBi pin diodes with different conditions

4.1 Introduction

The development of GaAsBi optoelectronic devices has been limited by growth difficulties. The bismuth incorporation into GaAs is heavily dependent on the growth temperature and the source fluxes of the three constituent species. In addition, the bismuth atoms tend to segregate out of the bulk due to a large difference in atomic radius between the bismuth and the arsenic atoms that it is replacing. The surface lifetime of the bismuth adatoms at the low growth temperatures involved is large enough that the bismuth atoms form into droplets on the surface.

Despite recent advances in the growth of GaAsBi [9, 12], the influence of the growth conditions on the dark currents of GaAsBi optoelectronic devices is not known. In this work, a systematic series of GaAsBi pin diodes was grown using MBE. This series of devices allows the influence of the bismuth content and growth temperature on the PL, XRD, and IV can be independently studied.

4.2 Review of GaAsBi growth investigations

In this section a review of growth investigations into GaAsBi will be given to help frame this work in the broader context of the field.

4.2.1 Early reports of GaAsBi growth

GaAsBi was first grown by MOVPE in 1998 by Oe and Okamoto, who noted a relatively small change in the band gap with temperature and a large band gap reduction caused by the incorporation of bismuth. They concluded that dilute bismides were promising materials for use in semiconductor lasers due to this apparently temperature insensitive band gap and the possibility for lattice matching to InP substrates in the form of InGaAsBi [1].

One of the first demonstrations of GaAsBi grown using MBE was reported by Tixier et al. [2]. The authors found that for growth temperatures above 450 ° C the incorporation of bismuth into GaAs is negligible. The authors also found that a stoichiometric arsenic to gallium flux ratio enhances the incorporation of bismuth, likely due to bismuth and arsenic competing for lattice sites.

4.2.2 Growth of GaAsBi at low temperatures using a stoichiometric arsenic flux

Young et al noted that bismuth has a strong tendency to surface segregate during MBE growth, necessitating the use of low growth temperatures to incorporate bismuth into GaAs. The authors grew GaAsBi layers using MBE using growth temperatures of 320 to 380 °C and used in-situ diffuse light scattering to detect the formation of gallium and bismuth droplets on the sample surfaces during growth [3]

Richards et al. grew GaAsBi layers using MBE using both As_2 and As_4, under different As_2:Ga and As_4:Ga flux ratios [14]. The authors concluded that arsenic assisted bismuth desorption is negligible during MBE growth, and that the incorporation of bismuth into GaAs does not depend on the arsenic species used for the epilayer. The authors suggested that As_4 is more suitable than As_2 for the growth of GaAsBi, as they found that the range of As_4:Ga flux ratios with which bismuth can be incorporated is much wider than for As_2.

4.2.3 Growth rate dependence of bismuth incorporation

Ptak et al. introduced the concept of a kinetically limited growth regime for GaAsBi [4]. This concept explains an apparent limit to the amount of bismuth that could be incorporated under certain growth conditions, as observed by Lu et al. [5] and Moussa et al. [31]. The authors grew GaAsBi devices using MBE with different growth rates and bismuth fluxes and measured the RMS surface roughness using atomic force microscopy. The authors identified a growth window which gave smooth surfaces. For layers with low growth rates and high bismuth fluxes the bismuth atoms formed into droplets on the surface of the sample instead of being incorporated into the bulk, leading to a high RMS roughness. However, layers grown with the same bismuth flux at a higher growth rate had a smoother surface. A high RMS roughness was also observed for samples with high growth rates and low bismuth fluxes, indicating that bismuth can act as a surfactant to improve the quality of GaAs grown at such a low temperature (315 °C was used in this work). The authors showed that the incorporation of bismuth into GaAs is possible at a range of different growth rates, and that in the growth window that led to smooth surfaces the bismuth atoms had a unity sticking coefficient, indicating that the bismuth content was limited by the bismuth flux. This means that a high degree of control over the bismuth content is possible in this kinetically limited regime.

4.2.4 Growth temperature dependent limit to bismuth incorporation

Richards et al. grew GaAsBi devices using MBE at different growth temperatures and measured the bismuth content. The authors found that in the kinetically limited growth regime, the bismuth content was independent of the growth temperature. Above a certain growth temperature the bismuth content decreased linearly as the temperature increased, with zero incorporation above 440 °C. The authors concluded that there is an upper limit on the amount of bismuth that can be incorporated at a given growth temperature, which does not depend on the growth rate, arsenic species, arsenic overpressure, or bismuth flux [14].

4.2.5 Theoretical growth models of GaAsBi

Lu et al. proposed a model for the growth of GaAsBi using MBE. In this model the bismuth atoms accumulate into a metallic surface layer that is weakly bonded to the surface [5]. The bismuth atoms then incorporate into the crystal lattice from the surface layer. The authors attempted to predict the bismuth incorporation achieved with different growth conditions, by modelling the rate at which bismuth atoms are incorporated into the crystal and desorbed from the crystal surface by incoming arsenic atoms.

Lewis et al. also proposed a model for the growth of GaAsBi using MBE [8]. The authors grew samples with a range of arsenic fluxes, and found the bismuth content to be independent of the As_2:Ga flux ratio with gallium rich conditions. This is contrary to the Lu et al. model. The authors concluded that the amount of bismuth that is incorporated is highly sensitive to the surface coverage of gallium and arsenic during growth. The authors also concluded that a low growth temperature is required as a bismuth-gallium bond can be thermally broken, leading to the ejection of the bismuth atom from the crystal. The authors also demonstrated the growth of GaAsBi containing 22% bismuth, including XRD results. However the authors did not disclose any photoluminescence data.

Zhou proposed a third growth model [6]. The author stated that one of the assumptions made by Lewis, that the Ga atoms landing on Bi terminated sites have the same behaviour as when they land on other Ga atoms, is false. Consequently, Zhou's model shows a different transition between the flux-limited and temperature-limited bismuth incorporation regimes.

4.2.6 Growth of GaAsBi with high bismuth content

Bennarndt et al reported growth of GaAsBi/GaAs and InGaAsBi/InP with up to 20% bismuth. The authors also attempted to grow $GaAs_{0.68}Bi_{0.32}$ lattice matched to InP, however, XRD measurements showed evidence of spinodal decomposition [13].

4.2.7 PL intensity improvement with bismuth incorporation

Several authors have found that the PL intensity decreases with an increasing Bi content for GaAsBi [12, 26]. However, other studies have found that the PL intensity increased up to 4.5% Bi [18, 19]. This was attributed to enhanced carrier confinement and an increased surfactant effect of the Bi atoms using higher Bi fluxes. After 4.5% Bi the decreasing PL intensity was attributed to an increasing density of non-radiative recombination centres.

4.2.8 GaAsBi growth studies

The effect of the growth rate on the PL and surface roughness of GaAsBi alloys was investigated by Mohmad et al. [25]. For the growth of GaAsBi with 6.5% Bi, a higher growth rate was found to result in more intense PL.

Bahrami-Yekta et al. studied the dependence of PL on the growth temperature, bismuth flux, and arsenic overpressure [12] using As_2. The authors found that growth at low temperatures leads to enhanced bismuth incorporation with less intense PL.

An increased As_2 overpressure led to a reduced Bi content with more intense PL. Two epilayers with a similar Bi content grown at different temperatures were compared using LTPL with the layer grown at higher temperature showing a lower density of shallow localised states in the band gap.

The growth of GaAsBi with ultra-violet illumination during growth was reported by Beaton et al. [9]. This resulted in narrow PL spectral widths, albeit at low bismuth contents (<1%). The authors also discussed how the fraction of the surface covered by bismuth adatoms correlates with the density of bismuth droplets.

Vardar et al. investigated the mechanisms of droplets formation and bismuth incorporation in GaAsBi [7]. Bi was found to act as a surfactant for the As-rich growth of GaAsBi. However, Bi acted as an anti-surfactant for Ga-rich growth, inducing the formation of Ga-Bi composite droplets.

4.2.9 Deep-level transient spectroscopy studies into GaAsBi defects

Mooney et al. studied deep level defects in n-type GaAsBi and GaAs grown at low temperatures[28]. The authors found that the dominant traps in GaAsBi were defect complexes involving arsenic anti-site defects. The ultra-violet laser illuminated layers grown by Beaton et al. [9] were also tested by Mooney et al. [29]. The GaAsBi layers grown with ultra-violet illumination had a similar concentration of mid-gap electron and hole traps.

Deep level defects in n-type GaAsBi were also investigated by Gelczuk et al. [27]. The authors found that Bi incorporation reduced the total trap concentration by over two orders of magnitude compared to GaAs grown under the same conditions. At least two types of Bi-related traps were identified and studied using deep-level transient spectroscopy.

4.2.10 Previous studies into GaAsBi diodes

Hunter et al. calculated the absorption coefficient of $GaAs_{1-x}Bi_x$ pin diodes using photocurrent measurements. The devices had a photoresponse up to almost 1300 nm [30].

Zhou et al. investigated the absorption of light by GaAsBi pin diodes with a range of bismuth contents. The devices all displayed a direct band gap. In addition, the Urbach tailing of the absorption coefficient below the band gap was extended over a large wavelength range. This was attributed to bismuth-induced localised states inside the band gap [16].

A literature review of quantum well diodes based on GaAsBi will be given in section 5.2.

4.3 Growth of GaAsBi using MBE

4.3.1 Preparation for growth

Numerous preparatory steps are necessary before the GaAsBi growth can be initiated. The wafers were delivered as 2-inch diameter discs, and must first be cleaved into 11.4 x 11.8 mm rectangles to fit into the mounting mechanism. The cleaving was performed using a Loomis scribe and break system, which uses a diamond-tipped scribing tool to score the surface, and a roller to cleave the wafer.

Occasionally the cleaving resulted in minor cracking of the wafer, instead of a perfectly straight cleave along a crystal plane. This can lead to semiconductor dust lying on the wafer surface, which must be removed. Typically the dust was removed using a compressed nitrogen gun, or washed away using isopropanol.

After being loaded into the growth chamber, the wafers were outgassed at approximately 400 °C and the vacuum pressure was monitored using an ion gauge. After around 30 minutes the arsenic valve was fully opened and the wafer temperature was increased to 600 °C to remove the native surface oxide. The RHEED pattern was studied during this step, to verify the removal of the oxide. The substrate surface is roughened by the oxide removal process, so a GaAs buffer was deposited to recover a smooth surface for the GaAsBi growth.

4.3.2 Bismuth flux calibration

The gallium and arsenic fluxes were calibrated using RHEED, as described in section 2.4. Calibrating the Bi flux in the same way is not possible as the binary compound GaBi is not stable. Instead, Bi was deposited for 1 hour onto a GaAs substrate held at room temperature. The substrate was then heated to just above the Bi melting point so that the Bi gathered into large droplets on the surface. The droplets were then measured using a microscope, see figure 4.1.

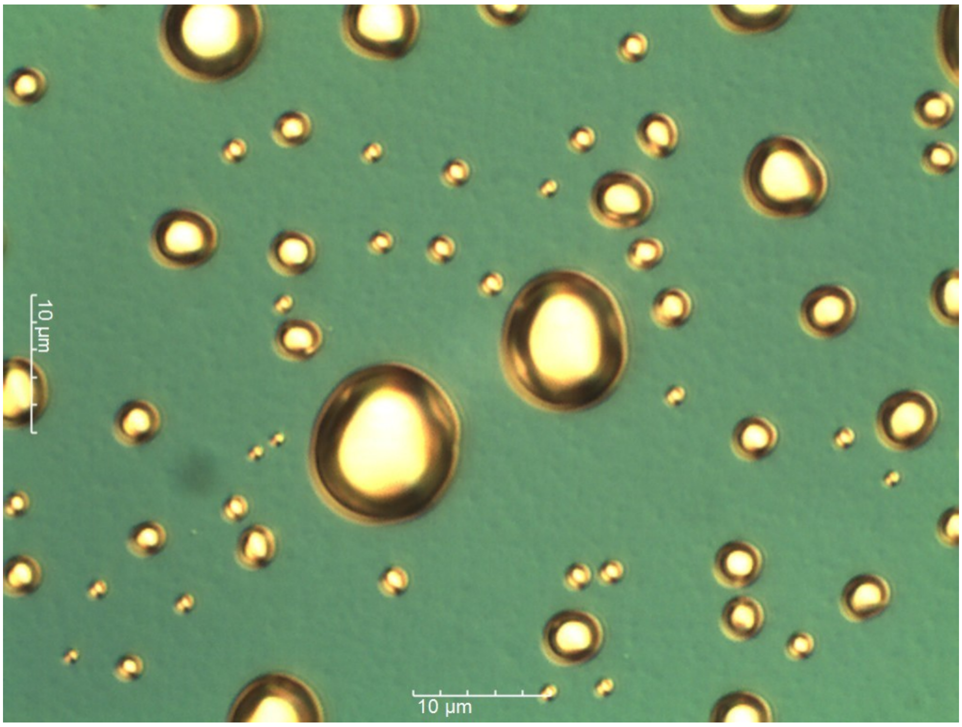

FIGURE 4.1: Microscope image of bismuth droplets on a GaAs substrate, for the purpose of determining the bismuth flux

From figure 4.1, under the somewhat poor assumption that the droplets are hemispherical, the volume of the deposited Bi and hence then Bi flux per unit area per unit time can be calculated.

4.3.3 Silicon and beryllium flux calibration

In this work, the Si and Be fluxes were calibrated by growing 1000 nm thick layers of n or p-type GaAs on an undoped GaAs substrate. The dopant concentration was then calculated using Hall-effect measurements. A small piece of indium was pressed into each corner of the wafer, to serve as contacts.

4.4 List of devices

Ten devices were grown in this work, see table 4.1. Five of the devices form a series grown at 375 °C using different bismuth fluxes, and six devices form a series grown with the same bismuth flux using different growth temperatures. Note that one of the devices (STG-34, bold in table) is shared between both series, being grown with a bismuth beam equivalent pressure (BEP) of 1.06x10^{-7} mbar at 375 °C. The devices were grown in a random order to remove any potential drift of the source fluxes or substrate temperature across the growth campaign.

Device name	Growth temperature (°C)	Bismuth BEP (x10^{-7} mbar)
STG-3D	375	0.50
STG-3A	375	0.76
STG-34	**375**	**1.06**
STG-3B	375	1.50
STG-39	375	2.12
STG-3C	355	1.06
STG-37	365	1.06
STG-36	385	1.06
STG-35	395	1.06
STG-38	405	1.06

TABLE 4.1: List of devices grown for this work

The growth conditions are visualised graphically in figure 4.2.

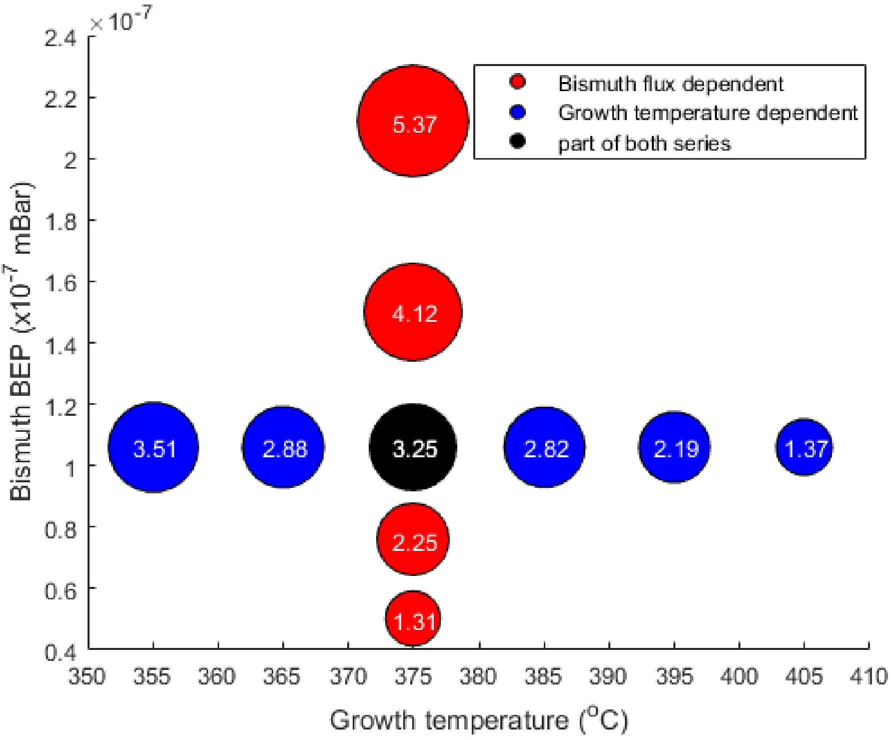

FIGURE 4.2: Graphical representation of the growth conditions for the GaAsBi bulk devices grown in this work. The size of the circles corresponds to the bismuth content (in %) of the devices as measured by XRD, which is also shown inside each circle in text.

From figure 4.2, two devices contain roughly 2.2% bismuth (STG-3A and STG-35), and another two contain roughly 1.3% (STG-3D and STG-38), despite being grown under different conditions. This allows the influence of the growth temperature and bismuth flux on the device properties to be independently studied.

The first pair (STG-3A and STG-35) was a fortunate coincidence. However, for the other pair the growth conditions of the second device (STG-3D) were adjusted to grow a device with close to the same bismuth content of the first device (STG-38, 1.37%) for comparison. The result (1.31% bismuth) shows the level of control over the bismuth incorporation that may be achieved under ideal conditions.

4.5 Growth

The devices were grown in February 2016 on 0.1° offcut GaAs (001) n+ substrates, using the MBE-STM in Sheffield. The undoped bulk GaAsBi layer was grown as the i-region in a pin diode structure to enable electrical measurements, with GaAs forming the n and p-type layers. The only difference between the devices was the growth temperature and bismuth flux used to grow the i-region.

The devices were designed to have a relatively thin 100 nm GaAsBi layer to avoid strain relaxation, which would obfuscate any comparative characterisation. A thicker layer would provide greater insight into light absorption in the diode, but there is no guarantee the devices would be fully strained. A diagram of the device structure is shown in figure 4.3.

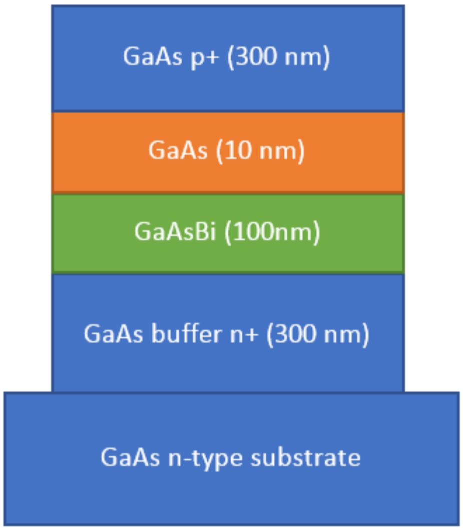

FIGURE 4.3: Diagram of the device structure for the bulk GaAsBi pin diodes. The p++ layer at the top of the stack is not shown here

4.5.1 Growth of GaAs n-type and p-type layers

The n and p-type GaAs layers were grown at 577 °C using As_2 [11], with dopant concentrations of $2\text{x}10^{18}$ cm^{-3} and $4\text{x}10^{18}$ $cm^{-}3$ respectively. The As:Ga atomic flux ratio was approximately 1.6:1 to prevent desorption of arsenic from roughening the surface. The growth rate was measured after deposition of the n-type layer using RHEED oscillations, and the temperature of the gallium cell was adjusted if necessary to give a growth rate of 0.60 ± 0.01 ML/s. Due to the Ga cell being moderately depleted, the cell temperature required to achieve 0.60 ML/s increased from 1007 to 1011 °C during the growth run. This procedure was required to ensure that the bismuth incorporation was not influenced by variations in the growth rate across the series.

A thin (<15 nm) layer of p++ doped GaAs was grown at the top surface to provide a highly doped region to which electrical contacts could be formed. This was accomplished by reducing the temperature of the gallium cell by roughly 45 °C, leading to an increase in the doping concentration.

4.5.2 Growth of GaAsBi i-region

Prior to the growth of the GaAsBi layer, the bismuth shutter was opened to generate a wetting layer of bismuth on the surface [8], and the RHEED pattern underwent a transition from an arsenic terminated c(4 x 4) to a bismuth terminated (n x 3) reconstruction. The time taken for this transition to occur was recorded and is plotted in figures 4.4 and 4.5 for the two series (growth temperature dependent and Bi flux dependent, respectively). The transition times were recorded using a stopwatch and have a relatively large uncertainty of ± 2 seconds, since the operator subjectively determined the point at which the transition occurred. For similar measurements in the future the RHEED camera software should be used to monitor the intensity of the spots in the reconstruction, with a suitable metric for determining the completion of the reconstruction transition.

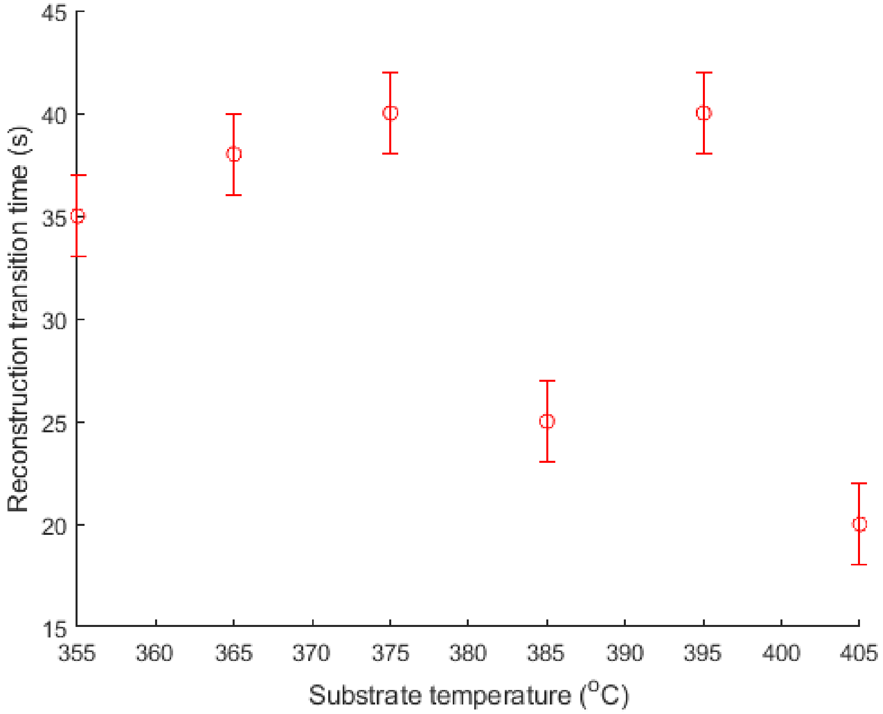

FIGURE 4.4: Time taken for the RHEED pattern to change to a bismuth terminated reconstruction after opening the bismuth shutter, depending on the substrate temperature

From figure 4.4, two of the devices (at 385 and 405 °C) show an anomalously short time to undergo the c(4 x 4) to (n x 3) transition. One would expect the transition time to increase exponentially with temperature since desorption of the bismuth atoms is more likely, and the other four devices show this behaviour. It is unlikely that the bismuth flux was larger than predicted for the devices grown at 385 and 405 °C due to the bismuth incorporation devices: see section 4.8.3. Instead, the time could have been incorrectly recorded.

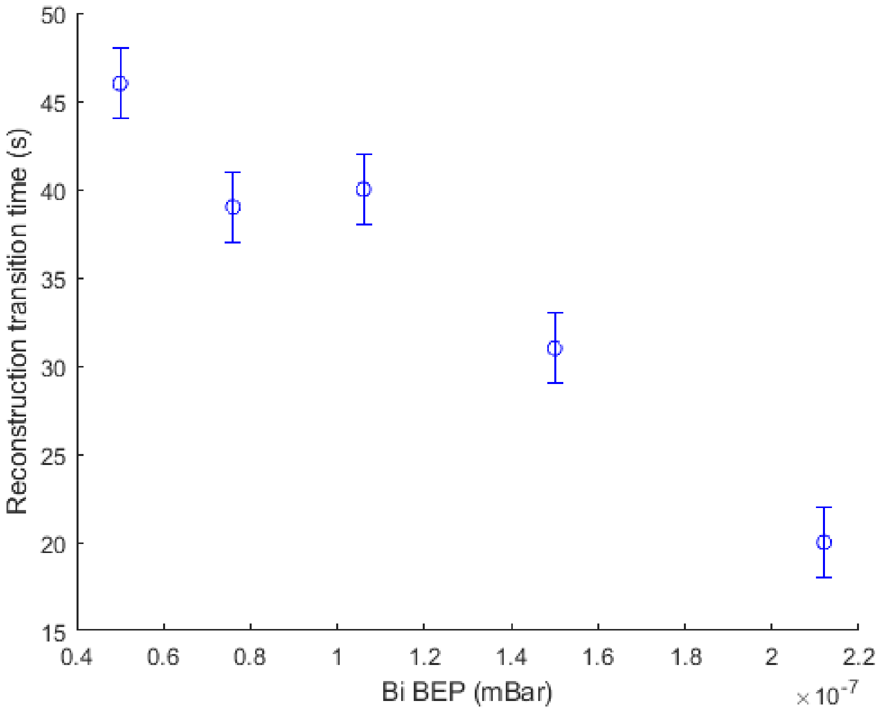

FIGURE 4.5: Time taken for the RHEED pattern to change to a bismuth terminated reconstruction after opening the bismuth shutter, depending on the bismuth BEP

From figure 4.5, the transition time shows strong negative correlation with the Bi BEP, as expected.

After the formation of the bismuth terminated-reconstruction, the Ga cell was immediately opened and the GaAsBi growth commenced. If the bismuth wetting coverage is too large then it is possible that this could result in surface droplets [9], or an increase in the bismuth incorporation near the start of the epilayer, as seen in [10]. As_4 was used for the growth of the GaAsBi layers [13, 14] using an As:Ga atomic flux ratio of roughly 2:1. Since the maximum incorporation coefficient of As atoms into the bulk from an As_4 flux is 0.5, the incorporable As flux was approximately equal to the Ga flux. A 10 nm GaAs capping layer was grown on top of the GaAsBi layer after a short pause to prevent the bismuth atoms from diffusing to the surface during growth of the p-type layer. The GaAsBi layer was annealed for approximately 45 minutes at 577 °C while the As cracker temperature was changed to give As_4 and during growth of the p-type GaAs layer.

4.6 Nomarski microscopy

After growth the devices were studied using Nomarski microscopy to observe defects and to check whether any of the layers had undergone strain relaxation. Representative Nomarski images of several of the devices are shown in figures 4.6 to 4.9.

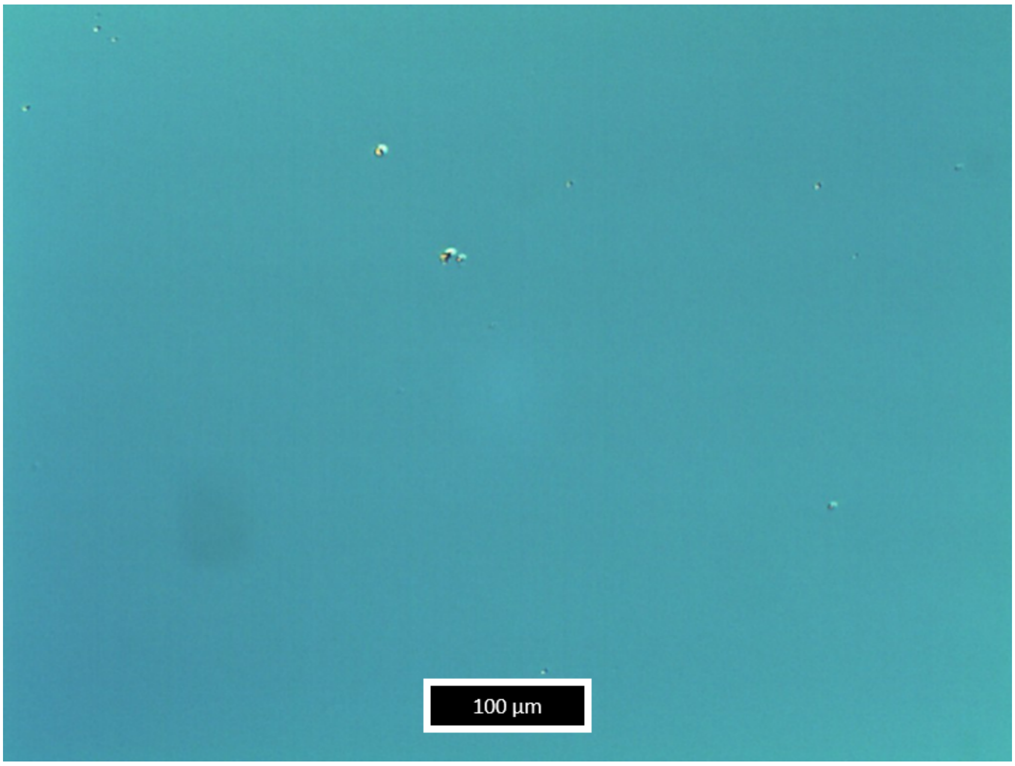

FIGURE 4.6: Nomarski image of STG-38 (1.37% Bi) at 10x magnification

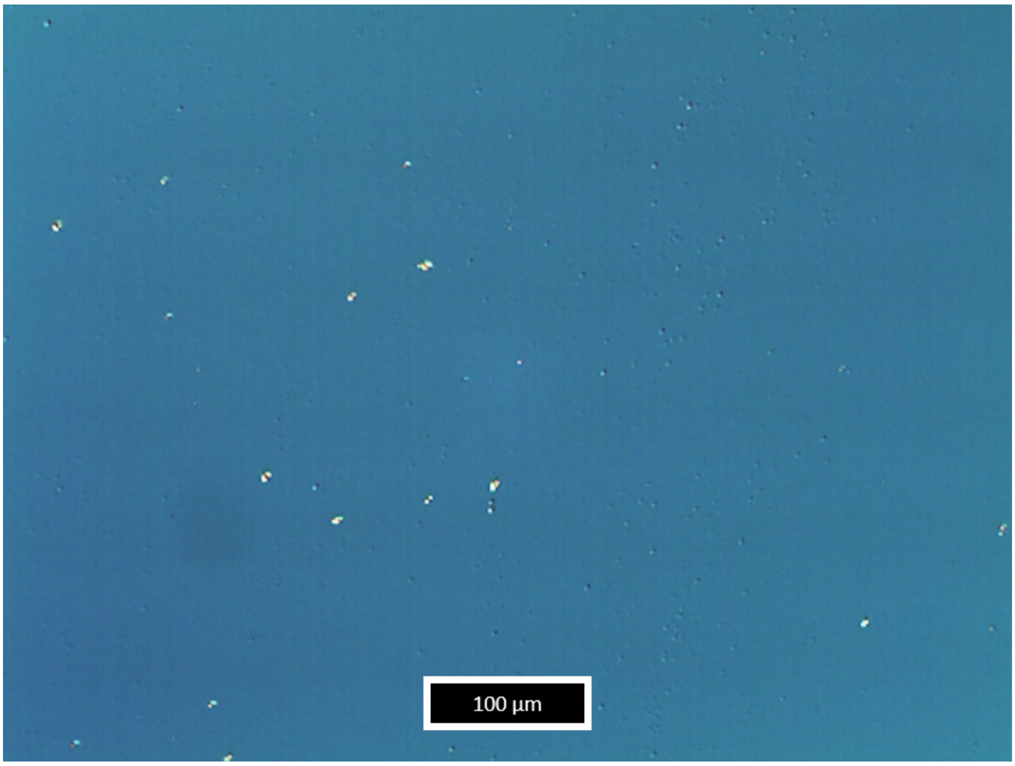

FIGURE 4.7: Nomarski image of STG-3D (1.31% Bi) at 10x magnification

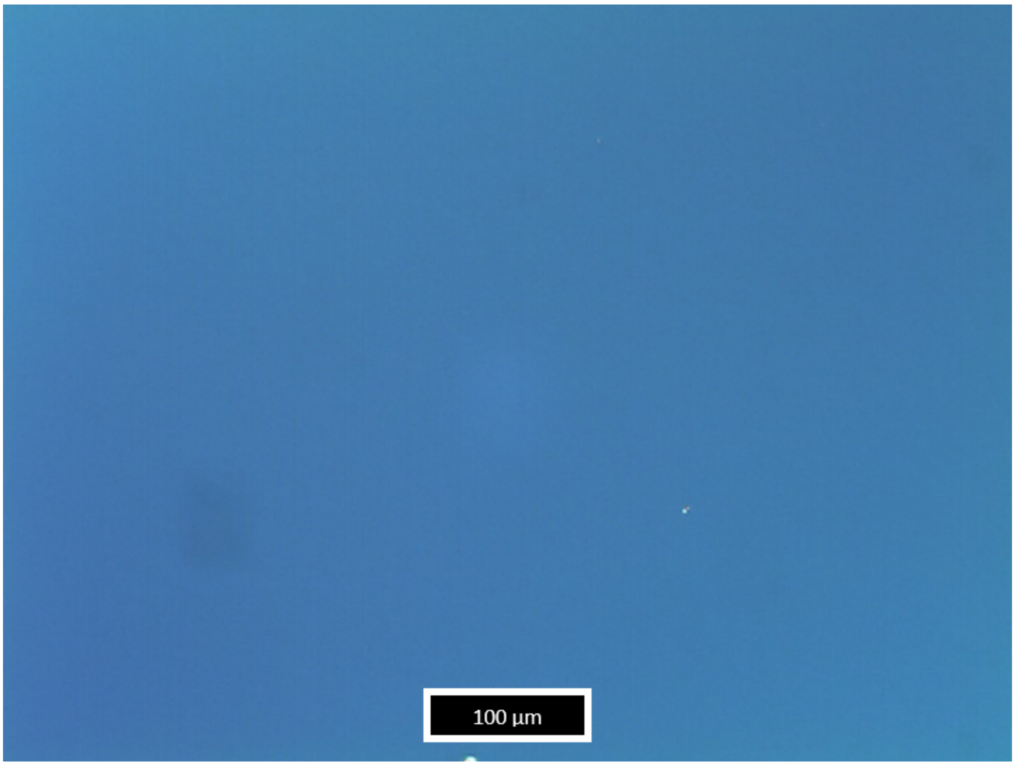

FIGURE 4.8: Nomarski image of STG-34 (3.25% Bi) at 10x magnification

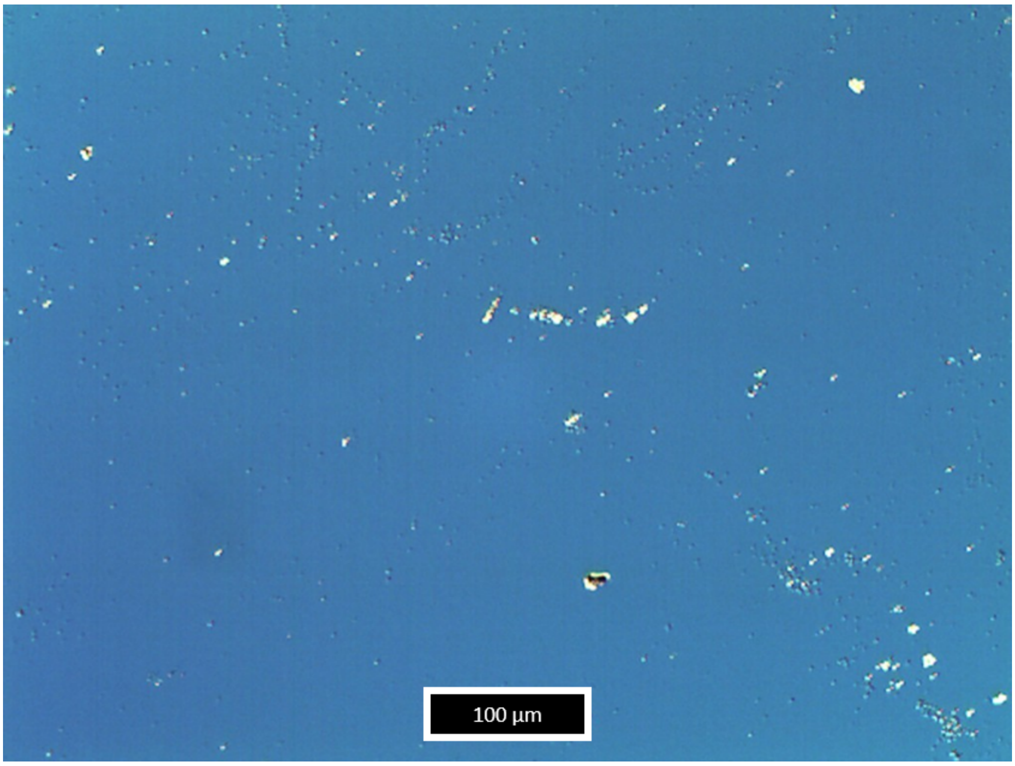

FIGURE 4.9: Nomarski image of STG-3B (4.12% Bi) at 10x magnification

From figures 4.6 to 4.9, the devices show a varying density of droplet-like defects.

To address the origin of the droplet-like defects, image thresholding was used to segment the images and allow automatic counting of the droplets. This procedure is described in more detail in section 5.5. The density of droplet-like defects in each device was counted, and is plotted in figure 4.10.

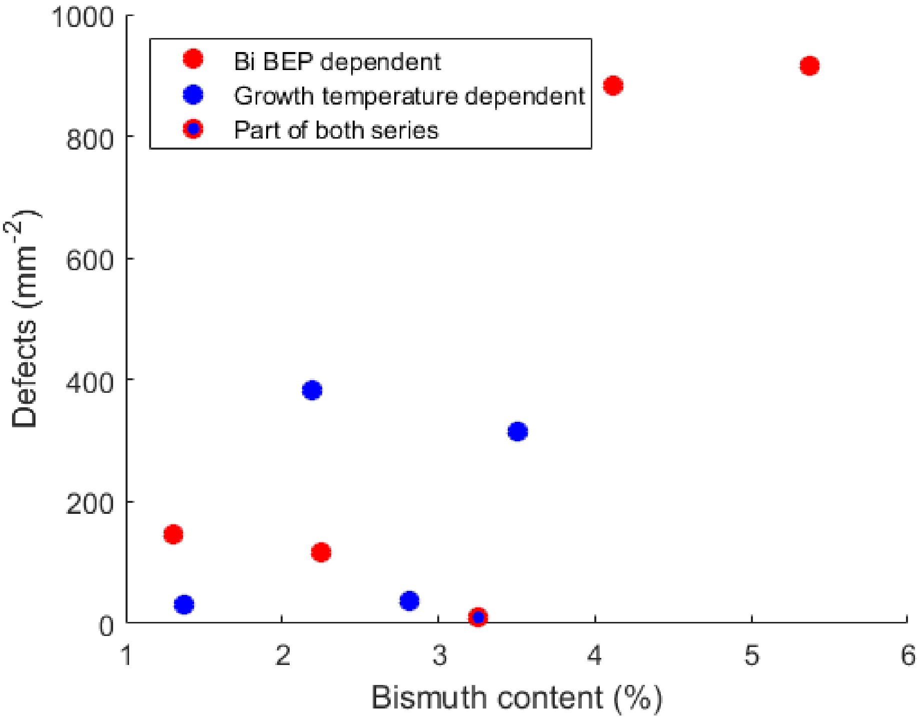

FIGURE 4.10: Density of droplet-like defects in Nomarski images of GaAsBi pin diodes, as a function of bismuth content

From figure 4.10, there is no correlation between the droplet density and the Bi content for the devices with less than 4% Bi. The defects in these devices are therefore likely gallium droplets resulting from the cell spitting, or background impurities incorporated from the growth chamber.

The devices with 4.12 and 5.37% Bi show an increased density of defects, which are likely bismuth droplets. These two devices were probably grown close to the Bi content saturation limit at their growth temperature, with the excess Bi atoms not incorporating in the bulk and instead forming into droplets on the surface.

4.7 X-ray diffraction

A Bruker D8 Discover X-ray diffractometer was used to measure (004) $\omega - 2\theta$ scans of the GaAsBi pin diodes, and RADS Mercury simulation software was used to fit the data assuming that the GaAsBi comprised a single uniform layer, see figures 4.11 and 4.12.

4.7.1 XRD dependence on bismuth BEP

The XRD spectra and modelled spectra of the set of devices grown at 375 °C using different bismuth BEPs is shown in figure 4.11.

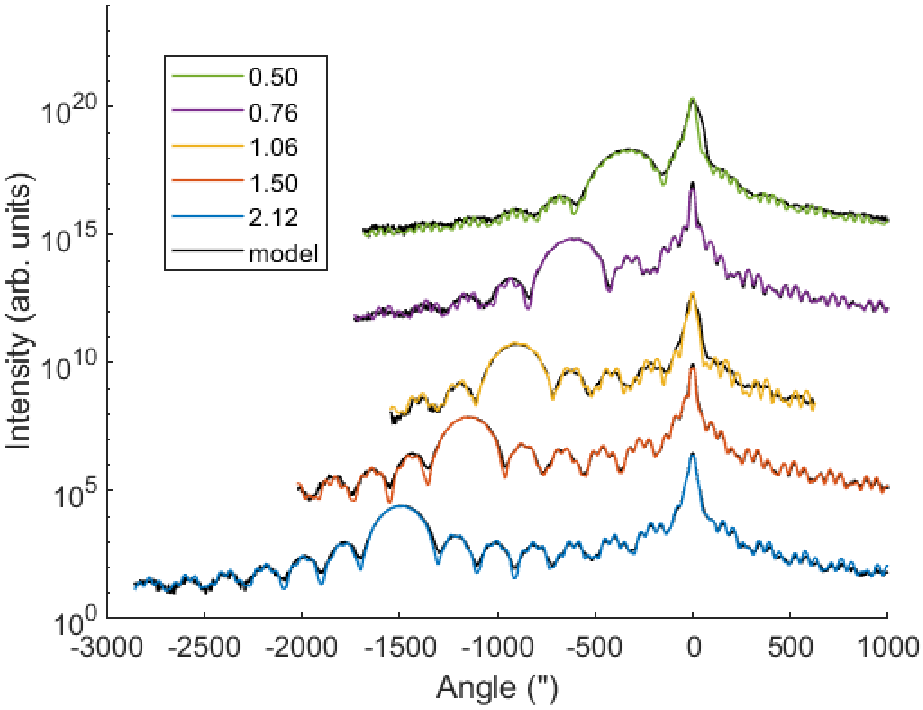

FIGURE 4.11: XRD spectra of GaAsBi bulk devices grown with different bismuth BEPs. The legend describes the bismuth BEP in units of 10^{-7} mbar, and the scans are offset relative to the substrate peak for clarity

From figure 4.11, the GaAsBi layers show up as broad peaks on the low angle side of the substrate peak, with the splitting dependent on the bismuth content. The intensity of the GaAsBi diffraction peaks relative to the substrate peak is similar across the series, evidence that the GaAsBi layers are all a similar thickness. The bismuth content increases with an increasing bismuth BEP, indicating that the growth is taking place in the bismuth-flux-limited growth regime.

Two distinct sets of thickness fringes with a different period are visible in most of the scans: the fringes with a smaller period are due to interference between x-rays reflected off the front surface of the wafer and the interface between the GaAsBi and p-type GaAs. The fringes with a larger period are from interference between x-rays reflected off the top and bottom interfaces of the GaAsBi layer. Therefore, it is possible to infer the quality of the interfaces in each device. In general, all the devices show an excellent agreement with the simulation with the exception of the device grown with a Bi BEP of 0.50x10^{-7} mbar (STG-3D). The smaller period thickness fringes are not visible for this device meaning that the GaAsBi layer has a rough upper interface (since the surface is relatively free from defects, see figure 4.7). This device has a low bismuth flux and a relatively low growth temperature meaning that the surfactant effect may be insufficient to produce an atomically flat upper interface during the time that the GaAsBi layer was annealed.

4.7.2 XRD dependence on growth temperature

The XRD spectra of the set of devices grown with a bismuth BEP of 1.06x10^{-7} mbar at different temperatures is shown in figure 4.12.

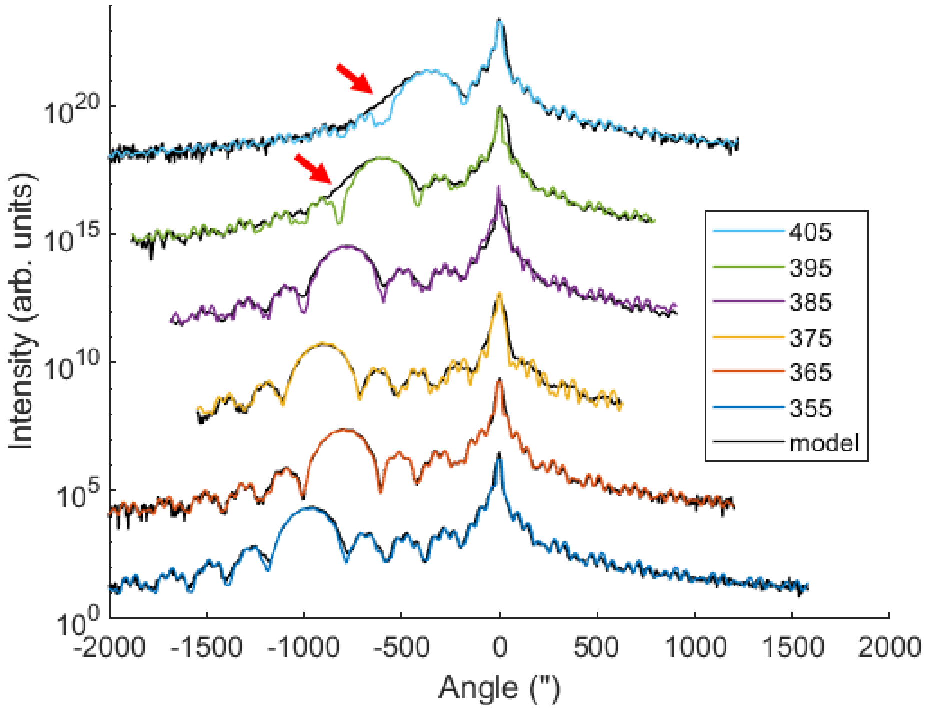

FIGURE 4.12: XRD spectra of GaAsBi bulk devices grown at different temperatures. The legend describes the growth temperature of each device in °C, and the scans are offset relative to the substrate peak for clarity. The red arrows highlight regions where the model agrees poorly with the data, caused by a varying bismuth content across the layer

From figure 4.12, the substrate diffraction peaks are generally less sharp than predicted by the model, with a shoulder on the high angle side. The bismuth content of the GaAsBi layers generally decreases with an increasing growth temperature due to enhanced bismuth evaporation and a reduction in the wetting layer surface coverage, which agrees with other studies from the literature [9, 12].

For the devices grown at 395 and 405 °C the GaAsBi diffraction peak is broadened, particularly on the low angle side - these features are marked with red arrows. The XRD fit for these devices is worse than the device grown at 355 °C, despite containing a lower bismuth content.

4.7.3 Bismuth content inhomogeneity

To investigate the origin of the poor agreement between the single layer simulation and the data, the simulation was modified to consist of a bilayer with the thickness and bismuth content of each layer allowed to vary. The bilayer XRD fit of device STG-38 (bismuth content 1.37%, grown at 405 °C) is shown in figure 4.13, alongside the XRD spectrum of the other device which has a similar bismuth content (STG-3D, 1.31% Bi, grown at 375 °C) for comparison.

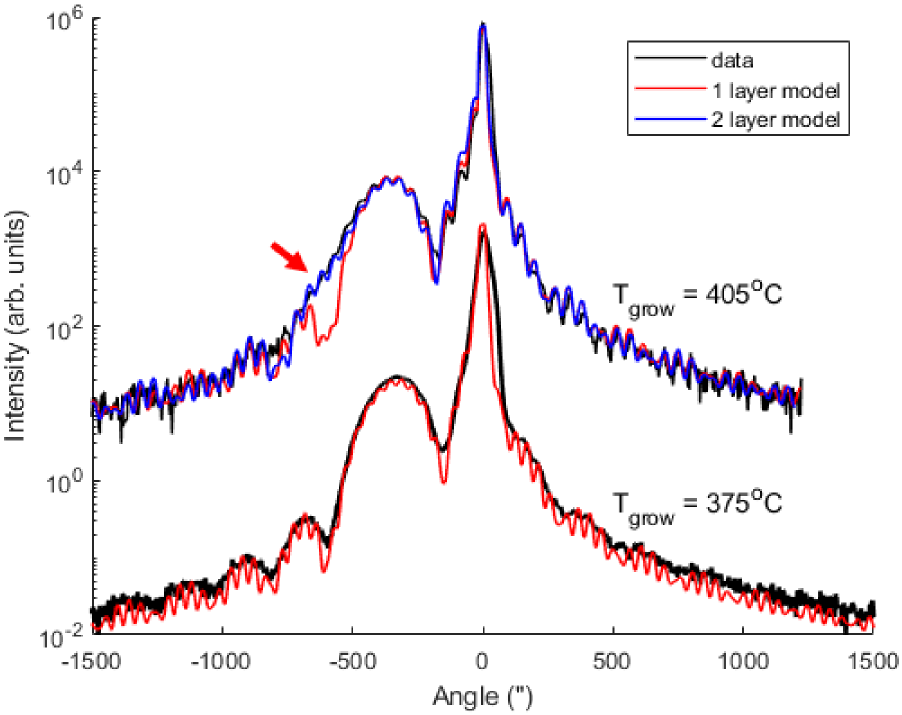

FIGURE 4.13: XRD spectra of pair of devices with 1.3% bismuth, (top) STG-38 (grown at 405 °C) and (bottom) STG-3D (grown at 375 °C). The red arrow shows the region of the spectrum where the single layer model fails to fit the data.

From figure 4.13, the two devices have a similar bismuth content despite being grown at different substrate temperatures. For the device grown at 405 °C, the simulation treating the GaAsBi as a single uniform layer (red line) is a poor fit to the data at around -600 arc seconds (shown by the red arrow). However, the two-layer fit has an excellent agreement with the spectrum.

The fitting parameters (layer thickness and bismuth content) calculated by the single layer and two-layer models of the device grown at 405 °C (STG-38) are shown graphically in 4.14.

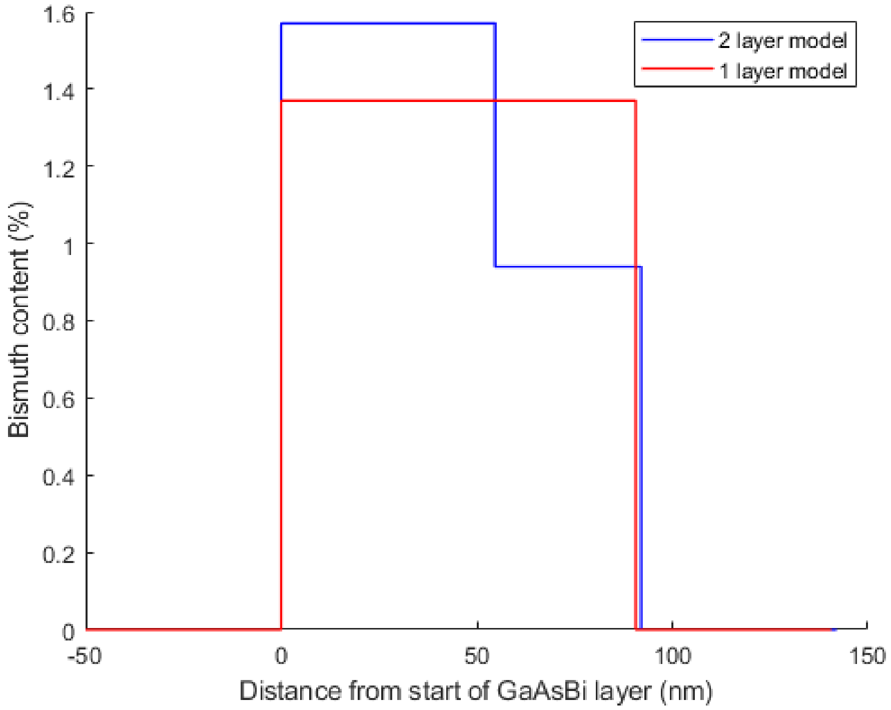

FIGURE 4.14: Bismuth incorporation profiles in the GaAsBi layer of the device grown at 405 °C (STG-38), as calculated using single layer (red line) and bilayer (blue line) XRD simulations. The growth direction is to the right.

From figure 4.14, the two-layer simulation shows a relatively large difference in bismuth content and thickness for the bilayers (blue line), with a higher bismuth content closer to the substrate, similar to [10]. The real bismuth incorporation profile in the layer is almost certainly more complex than this two-layer model. However, choosing a more complicated simulation (i.e. with 3 or more GaAsBi layers) results in diminishing returns in the closeness of the fit and is offset by increased uncertainty in the fitting parameters.

In addition, it is possible that the bismuth content is varying in the plane of the surface since the XRD spot is relatively large (2 mm across). This inhomogeneity could be on the atomic scale due to the incorporation dynamics of the bismuth atoms creating regions of high and low bismuth content. However, in [15] the authors found that lateral composition modulation was more prevalent at lower growth temperatures due to differences in the surface mobility of the group V atoms. Alternatively, the bismuth content could be varying across the entire wafer due to flux gradients during growth. However, this is also unlikely as position-dependent PL measurements show no significant change in the peak emission wavelength across the wafer (not shown here).

The bismuth incorporation profile would be better measured using atom probe tomography [15] or cross-sectional TEM [10]. Analysis of the device grown at 395 °C (STG-35) shows a similar trend in that the XRD spectra is a better fit using a two-layer model (not shown here). Thus, it seems likely that the GaAsBi layers grown at higher temperatures have a non-uniform bismuth content in the growth direction.

4.7.4 XRD fitting parameters for devices

The layer thickness and bismuth content of the GaAsBi devices were calculated using the XRD simulation software, and are shown in table 4.2.

Device name	Growth temperature (°C)	Bismuth BEP (x10^{-7} mBar)	Bismuth content (%)	Layer thickness (nm)
STG-3D	375	0.50	1.31	85
STG-3A	375	0.76	2.25	90
STG-34	**375**	**1.06**	**3.25**	**96**
STG-3B	375	1.50	4.12	96
STG-39	375	2.12	5.37	96
STG-3C	355	1.06	3.51	95
STG-37	365	1.06	2.88	95
STG-36	385	1.06	2.82	91
STG-35	395	1.06	2.19	93
STG-38	405	1.06	1.37	91

TABLE 4.2: Bismuth content and thickness of the devices studied in this work, from XRD simulations assuming a single uniform layer of GaAsBi

From table 4.2, the layers are all thinner than the intended 100 nm, which is probably due to shutter transients in the gallium cell during growth. The uncertainty in the layer thickness is ±3 nm, and the uncertainty in the bismuth content is ±0.05% .

The bismuth content of the devices will be discussed further in section 4.8.3.

4.8 Photoluminescence spectroscopy

A 300 mW continuous wave laser operating at 532 nm was used to optically excite carriers in the devices, with the emitted luminescence measured using a monochromator coupled to an LN_2 cooled Ge detector. The laser power density is estimated at 120 W/cm^2.

4.8.1 PL dependence on bismuth BEP

The PL spectra of the set of devices grown at 375 °C using different bismuth BEPs are shown in figure 4.15.

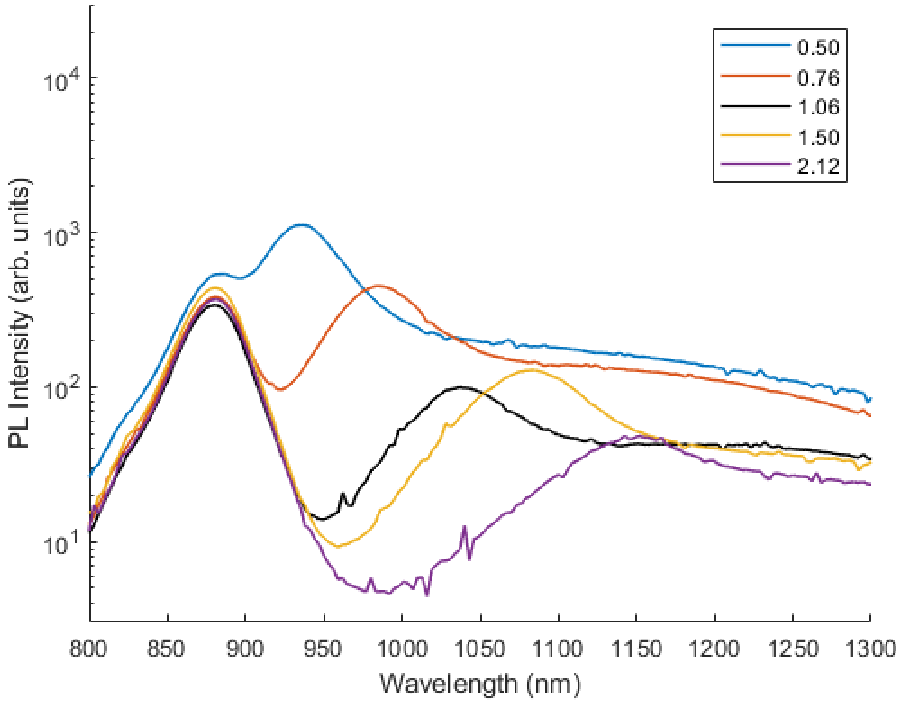

FIGURE 4.15: PL spectra of devices grown with different bismuth BEPs. The legend describes the bismuth BEP in units of 10^{-7} mbar

From figure 4.15, the devices grown with different bismuth BEPs all show PL emission due to the GaAsBi layer in the wavelength range 935 to 1155 nm. The intensity of the GaAsBi luminescence generally decreases with increasing bismuth content, in contrast to [18] and [19]. However, the device grown with a bismuth BEP of 1.06x10^{-7} mBar at 375 °C (black line) shows weaker PL than the two devices that show longer wavelength emission (yellow and purple lines).

In [18] and [19], the authors optimised the PL intensity for a given bismuth incorporation by varying the growth parameters, and observed an increasing PL intensity for up to 4.5% bismuth (emitting around 1100 nm). In this work, the growth parameters were varied systematically such that trends in the device properties can be observed independent of bismuth content. The devices in [18] and [19] were grown using optimised conditions whereas the devices grown in this work were not.

The peak at 880 nm is a similar intensity for all of the devices, with a FWHM of around 42 nm. The intensity of 880 nm light emitted by the n-type GaAs layer (as measured at the surface) should depend on the absorption coefficient of the GaAsBi layer. Therefore, the majority of the photons at 880 nm are probably emitted in the 300 nm thick p-type GaAs layer. The penetration depth of the laser in GaAs is around 250 nm based on the absorption coefficient at 532 nm [17]. However, many carriers created in the p-type GaAs will migrate and recombine non-radiatively at the wafer surface.

An extremely broad and weak peak is also present around 1150-1200 nm. This peak is probably due to recombination via dopant states in the GaAs layers as similar peaks were measured for unused doped GaAs substrates.

The FWHM of the GaAsBi PL emission will be studied in further detail in section 4.8.5.

4.8.2 PL dependence on growth temperature

The PL spectra of the set of devices grown with a bismuth BEP of 1.06x10^{-7} mbar at different temperatures are shown in figure 4.16. This graph has the same ordinate scale as figure 4.15, to allow a comparison between the two growth series.

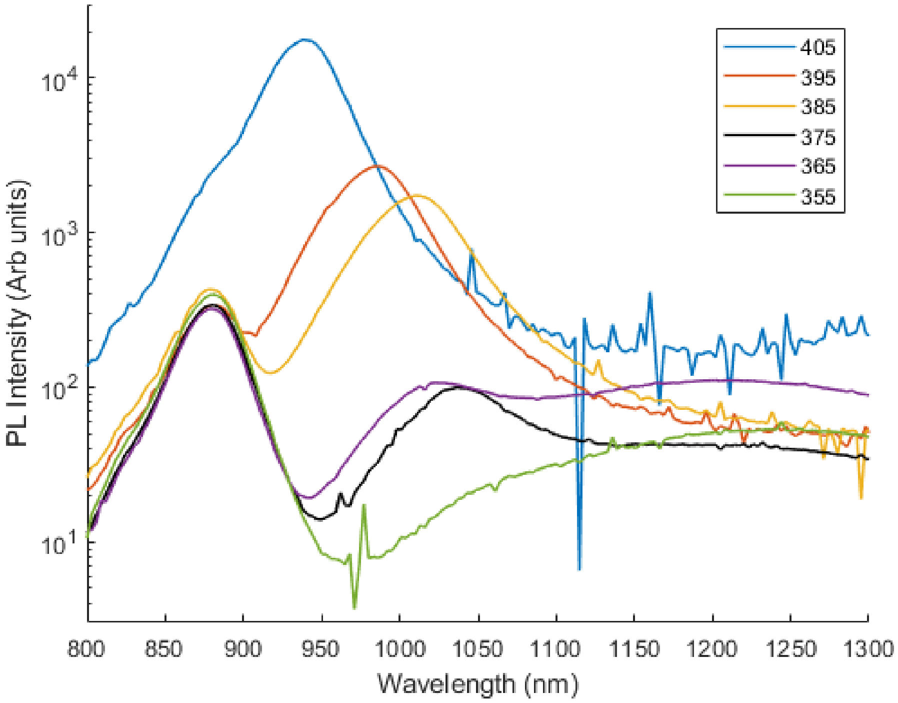

FIGURE 4.16: PL spectra of devices grown at different temperatures. The legend describes the growth temperature in °C. Note that the devices were measured using neutral density filters and scaled to take this into account. Therefore, the noise floor is different for several of the spectra.

From figure 4.16, a decrease in the growth temperature leads to a decrease in the GaAsBi PL intensity and a red-shift of the peak emission wavelength. The device grown at 405 °C (STG-38, blue line) has a GaAs PL peak that appears to be more intense than the other devices. However, the GaAsBi peak is more intense and broad enough to dominate the luminescence at this wavelength such that the GaAs peak appears as a small shoulder on the larger GaAsBi peak.

The PL peak of the device grown at the lowest temperature (355 °C, green line) is extremely weak, and shows up as a shoulder on the dopant luminescence peak. It is likely that the density of non-radiative recombination centres in this device is high due to the low growth temperature.

4.8.3 Bismuth content of layers as calculated using PL and XRD

The bismuth content of the devices is plotted in figures 4.17 and 4.18 as a function of the bismuth BEP and the growth temperature, respectively. The bismuth content was calculated using both XRD and PL, with a close agreement indicating that the layer is uniform. The bismuth content was calculated from the PL peak wavelength using the model published by Mohmad [20], assuming that the PL peak wavelength corresponds to the band gap of the layer. The bismuth content from XRD was calculated using the XRD simulation software, with the GaAsBi diffraction peak splitting with respect to the GaAs peak proportional to the bismuth content.

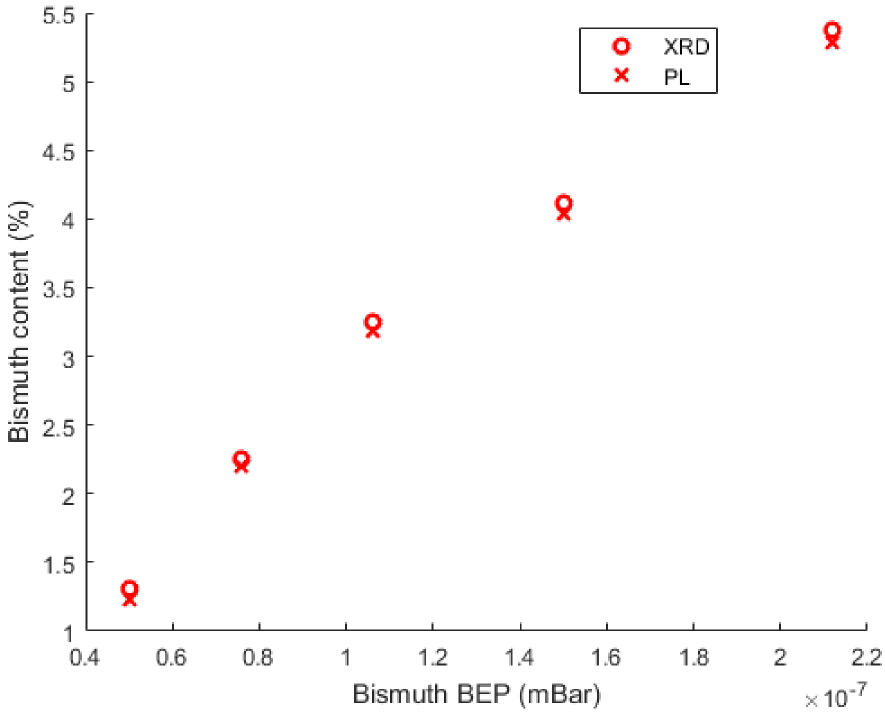

FIGURE 4.17: Bismuth content calculated using XRD and PL, as a function of the bismuth BEP

From figure 4.17, the bismuth incorporation increases approximately linearly up to 1.06x10^{-7} mbar. However, for further increases in the Bi BEP, the Bi incorporation increases sub-linearly, possibly approaching a saturation limit. The devices with 4.12 and 5.37% bismuth show a significantly higher density of droplets in the Nomarski images (see section 4.6). Therefore, it seems likely that the limit to the amount of bismuth that can be incorporated into GaAs under a stoichiometric As_4 flux for growth at 375 °C is approximately 6-7%, with the excess bismuth atoms forming into droplets.

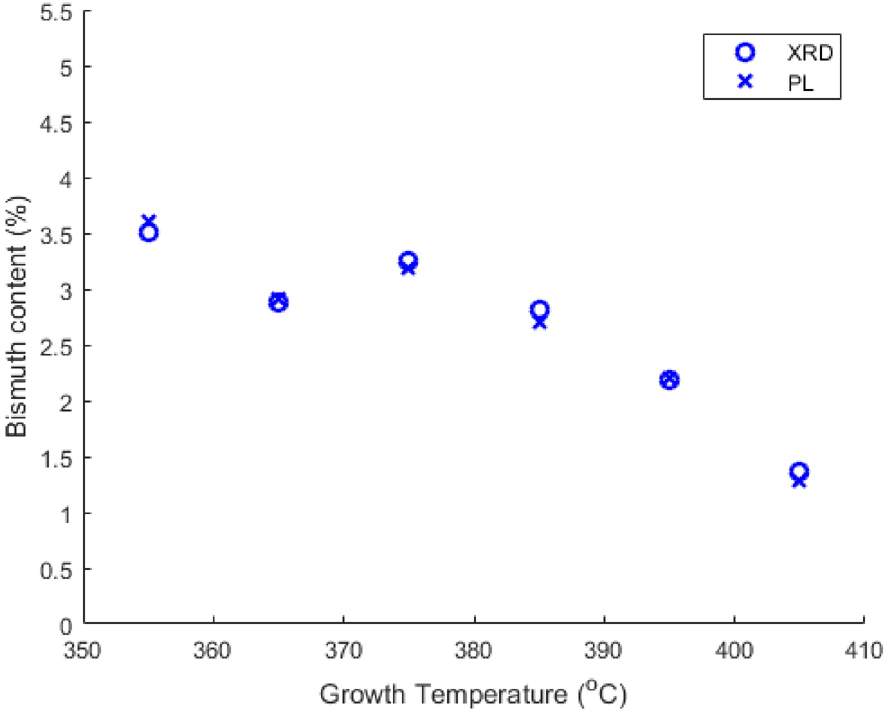

FIGURE 4.18: Bismuth content calculated using XRD and PL, as a function of the growth temperature

From figure 4.18, the bismuth content increases rapidly as the growth temperature is decreased from 405 to 375 °C, corresponding to a reduced desorption of the bismuth atoms and a greater surface coverage of the bismuth wetting layer. For growth below 375 °C, the bismuth content appears to be tending towards a limit of roughly 3.75 - 4%, which indicates that the desorption of bismuth atoms is negligible at this temperature, and that the bismuth incorporation coefficient is approaching unity.

The device grown at 365 °C shows an anomalously low bismuth content from both XRD and PL measurements. This device was grown 4th out of the total series of 10 devices, such that drift in the growth conditions over time is unlikely to be the cause of the low Bi incorporation. To obtain an unexpectedly low bismuth content, the growth temperature, growth rate, or arsenic flux could be higher than intended, or the bismuth flux could be lower than intended. From studying the saved growth recipe for this device, human error (e.g. entering the wrong temperature for a cell) was not to blame. Ultimately, this device does not fit the trend shown by the other devices, which highlights the narrow growth window and difficulty in reliably growing GaAsBi devices.

4.8.4 Integrated PL as a function of bismuth content

From figures 4.17 - 4.18, both the growth temperature and the bismuth flux affect the bismuth incorporation and the PL intensity. To better compare the effect of the growth conditions on the PL intensity, the integrated PL (IPL) is plotted against the bismuth content of the devices in figure 4.19. By comparing the devices in this way, the influence of the growth conditions can be independently investigated, such that the growth conditions which give the brightest PL for the desired emission wavelength can be found.

The integrated PL was calculated by fitting the spectra as the sum of three Gaussian peaks corresponding to GaAs, GaAsBi, and dopant luminescence. This allows the calculation of the PL emission (intensity and FWHM) from the GaAsBi layer even when the spectrum is dominated by GaAs or dopant luminescence.

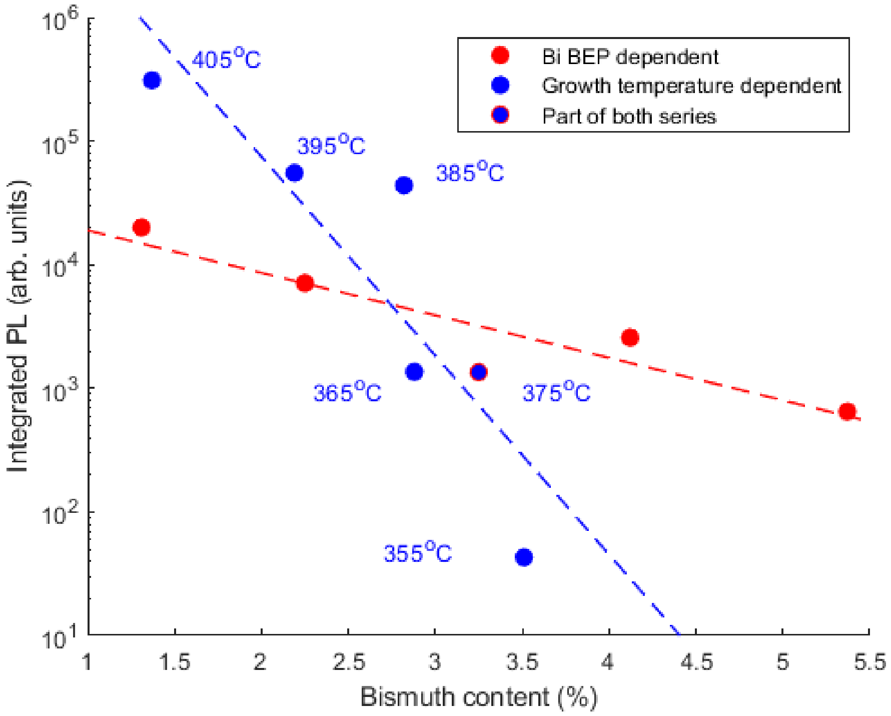

FIGURE 4.19: Integrated photoluminescence as a function of bismuth content for both series of GaAsBi pin diodes with the device that is part of both series marked in both colours. The devices plotted in red were all grown at 375 °C with varying Bi BEPs, while the devices plotted in blue were grown at different temperatures with the same Bi BEP. The dashed lines are fits to the data.

From figure 4.19, the integrated PL intensity decreases exponentially as the Bi content increases for both series of devices. However, the gradient of the decrease is much steeper for the devices grown at different temperatures (blue circles). Comparing the two devices containing 1.3% Bi (and also the two containing 2.2%), the device grown at higher temperature has significantly brighter PL emission. For a given Bi content, growth at higher temperature produces devices with a lower density of non-radiative recombination centres. These non-radiative centres are unlikely to be misfit dislocations as the devices are all fully strained, and are instead probably anti-site or interstitial defects. However, the precise identity of these defects is unclear. In [21] it was found that rapid thermal annealing at 600 °C completely quenches As_{Ga} anti-site defects in GaAsBi. The same authors noted that no Bi_{Ga} anti-site defects were present in their epilayers.

Note that the device grown at the lowest temperature (STG-3C, 3.51% Bi) has extremely weak PL (green line in figure 4.16) such that the uncertainty in its IPL is much larger than for the other devices.

4.8.5 Spectral width of PL as a function of bismuth content

The FWHM of the GaAsBi PL peaks were calculated from the width of the Gaussian peak fit outlined above, and plotted as a function of the bismuth content, see figure 4.20.

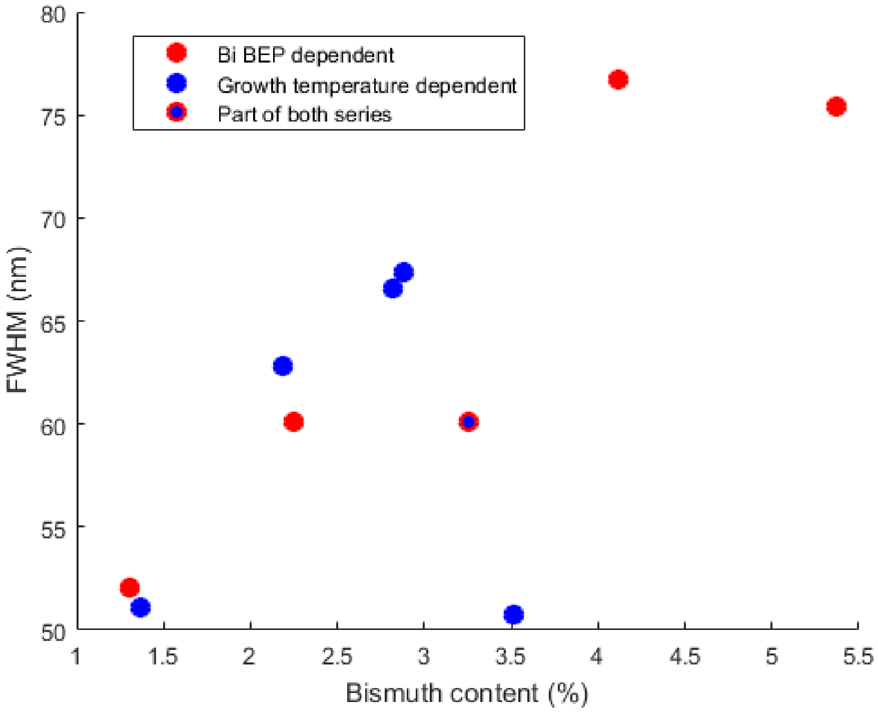

FIGURE 4.20: Dependence of PL FWHM on bismuth content, calculated using Gaussian fitting of the PL data

The uncertainty in the PL FWHM is relatively large and estimated at ±5 nm. This is due to the presence of two other peaks in the spectra, and in some cases the weak PL from the GaAsBi layer. The FWHM of the device with 3.51% Bi (lowest blue circle in figure 4.20) corresponds to the green line in figure 4.16 with the emission being a weak shoulder on the dopant luminescence peak. Consequently the FWHM of this device is likely highly inaccurate. A repetition of this graph using electroluminescence should remove the uncertainty in the FWHM caused by the presence of other peaks.

The PL spectral linewidth of the other GaAsBi devices appears to be increasing with the bismuth content irrespective of the growth conditions or PL intensity. The incorporation of the bismuth atoms is probably introducing a large number of localised states near the valence band edge leading to a broadening of the FWHM [22].

The two devices with 1.3% Bi show a large difference in PL intensities. However, the density of bismuth-induced localised states near the band edge does not appear to be affected by the growth conditions since the two devices have similar FWHM values. This is also true for the two devices with 2.2% Bi. A broad distribution of localised states extending into the band gap will result in a slow decrease in the absorption coefficient below the band gap [16, 23], and more advanced growth methods may be necessary to reduce the PL line width of GaAsBi alloys to improve performance for multi-junction photovoltaics applications [9]. However, this result highlights the increase in FWHM that can be achieved using GaAsBi devices and is promising for the development of broadband light sources.

4.9 Current–voltage

The as-grown devices were fabricated into annular mesa devices with a common back contact. The dark current of the devices was measured as a function of bias voltage to compare the devices based on their growth condition. At least 5 mesas were tested on each device, and the one with the lowest dark current density was chosen for analysis, see figure 4.21. This was based on the rationale that there are several stages during growth and fabrication which could lead to a degradation of the mesa performance, but nothing that could improve its performance relative to others on the same wafer.

In most cases the forward dark currents show a small variability between mesas on the same wafer, and scale with area. Therefore, the dark current is dominated by bulk recombination and there is negligible recombination occurring at the surfaces on the side walls of the mesa. This is expected since the mesa is less than 1 μm tall and between 50 and 400 μm in diameter. The large aspect ratio of the device reduces the efficacy of the current spreading, as outlined in section 5.10.3 for a similar set of devices. One would expect the current spreading to improve if a thicker p-type layer were utilised. However, if the current spreading were too severe carriers would spread to the mesa side walls and recombine without reaching the i-region, as illustrated in [32].

The exception was device STG-36 (grown at 385 °C with a bismuth content of 2.82%), which had a factor of two difference in dark current between the different sized devices in forward bias. The most likely reasons for this discrepancy are insufficient cleaning or too much/ too little annealing during the fabrication process. The discrepancy is unlikely to be related to the growth since this device has a reasonably low density of bismuth droplets (see figure 4.10).

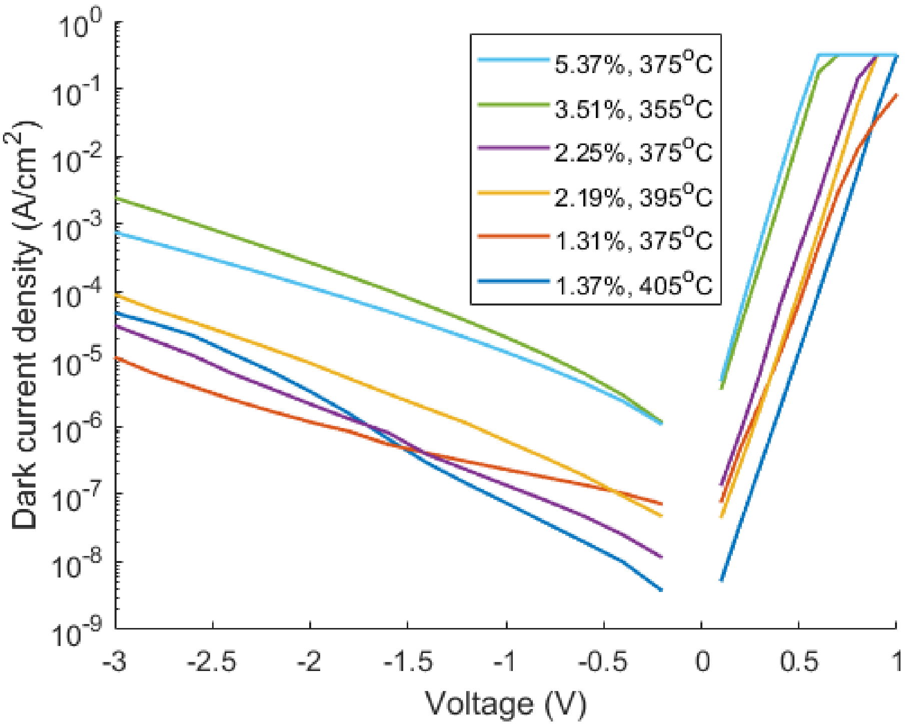

FIGURE 4.21: Dark current density as a function of bias voltage for GaAsBi pin diodes. Not all of the devices are plotted for clarity. The legend denotes the bismuth content and growth temperature of each device

From figure 4.21, in forward bias the devices all exhibit diode-like behaviour, with ideality factors close to 2. This indicates that non-radiative recombination or recombination in the depletion region dominates the JV curves of the devices. The dark currents in forward bias generally increase with the bismuth content. At high forward bias the dark current of some of the devices is limited by series resistance (characterised by the line curving over at high forward bias) and/or the compliance limit of the source-measure unit (characterised by the flat section in forward bias at around $3\text{x}10^{-1}$ A/cm^2).

In reverse bias, there is more variation between mesas on the same wafer, and not all the devices have dark currents that scale with area. In addition, several of the devices show a changing gradient in the dark current density, meaning that the dominant generation-recombination process is changing as a function of reverse bias. Low resistance paths, possibly at the edge of the mesa structures, probably have a large impact on the reverse dark currents.

To better investigate how the dark currents change as a function of the growth conditions, the reverse saturation current density (J_{sat}) of the diodes was used as a figure of merit for the device performance, see figure 4.22. Previous studies have shown that J_{sat} is related to the dislocation density in strained MQW devices [24]. The Shockley diode equation was used to calculate J_{sat}, based on the forward bias data.

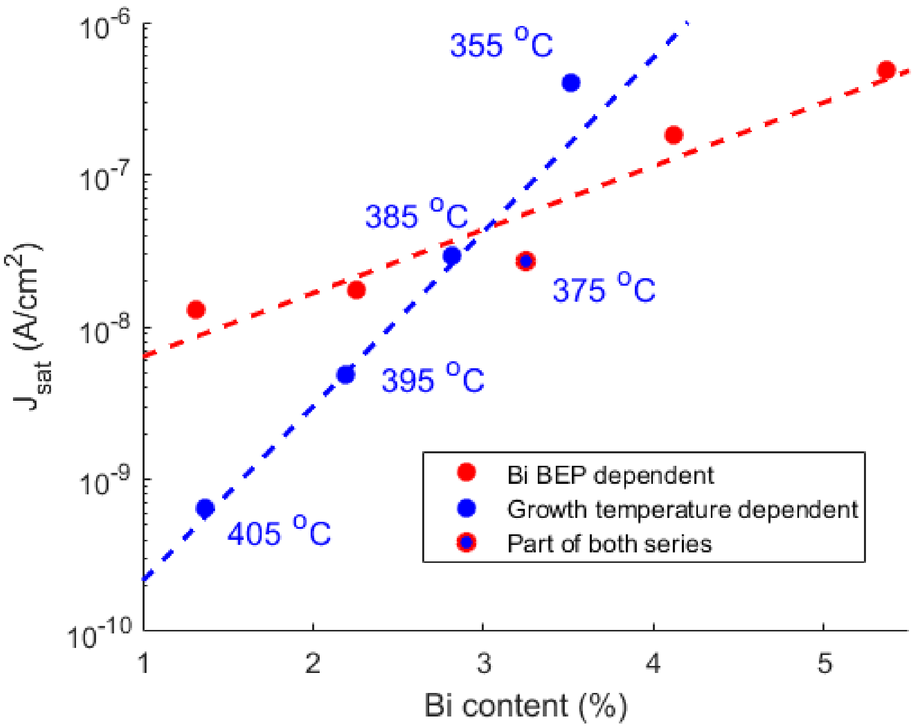

FIGURE 4.22: Reverse saturation current density of GaAsBi diodes calculated from the Shockley diode equation and the forward bias data, as a function of the Bi content. The annotations denote the growth temperatures of the diodes, with the devices plotted in red all grown at the same temperature (375 °C). The device grown at 365 °C is not plotted here as it has an anomalously low Bi content compared to the other devices

From figure 4.22, J_{sat} increases exponentially as the bismuth content increases. However, the gradient of the increase is much steeper for the devices grown at different temperatures (blue circles) than for the devices grown with different Bi BEPs (red circles). Comparing the two devices containing 1.3% Bi, the device grown at higher temperature has a significantly lower J_{sat}. This is also true for the two devices with 2.2% Bi. This implies that growth temperature related defects have a greater impact than Bi related defects on the dark current of the devices. It is likely that the minority carrier lifetime is reduced for the diodes grown at lower temperatures due to a higher rate of defect assisted recombination. Therefore GaAsBi opto-electronic devices should be grown at the highest possible temperature.

4.10 Conclusion

A systematic series of GaAsBi pin diodes was grown using MBE with varying growth conditions. This allowed the influence of the growth temperature and bismuth content on the optoelectronic performance of the devices to be independently studied. The series of 10 devices represents the largest (to the authors knowledge) systematic study of GaAsBi devices grown under different conditions.

XRD measurements showed that growth at lower temperatures produces more uniform epilayers. This has implications for the growth of GaAsBi quantum well based devices where highly uniform wells are desirable. There is evidence that the bismuth atoms are acting as a surfactant to smooth the GaAsBi surface immediately after growth, since the device grown with the lowest bismuth flux is inferred to have a rough upper surface due to the low prevalence of interference fringes in its XRD spectrum.

PL measurements showed that growth at higher temperatures produces GaAsBi devices with brighter luminescence, for the same bismuth content, most likely due to a lower density of GaAs temperature related defects. Higher bismuth content was also found to reduce the PL intensity, presumably due to an increased density of bismuth related defects increasing the non-radiative recombination rate. However, other authors have noted that the luminescence from GaAsBi layers typically increases with bismuth content up to around 4% due to enhanced carrier confinement and an increased surfactant effect of the bismuth atoms on the growth. The discrepancy suggests that the optimum temperature, to give the brightest luminescence, varies as a function of bismuth content, since the devices in this work were not grown under ideal conditions.

The FWHM of the PL was not affected by the growth temperature, implying that the density of bismuth-induced localised states cannot be reduced by growth at a higher temperature. This is an important result for the development of GaAsBi broadband light sources as it highlights that the inherently large FWHM is a material specific property due to the localised states, and not the result of badly optimised growth. However, this result may prove to be a downside for photovoltaic applications, where a sharp absorption edge onset is desirable.

JV measurements show a similar trend to the PL measurements, in that growth at a higher temperature results in devices with lower dark currents, for the same bismuth content. Likewise, the dark currents also increased as the bismuth content increased. Therefore, devices which exhibit intense PL generally have a low dark current.

Further measurements are needed to verify the nature of the defects that are present in the devices to reinforce these conclusions.

Bibliography

[1] K. Oe and H. Okamoto, *New semiconductor alloy* $GaAs_{1\text{-}x}Bi_x$ *grown by metal organic vapor phase epitaxy*, Japanese Journal of Applied Physics **37**, L1283-L1285 (1998)

[2] S. Tixier et al., *Molecular beam epitaxy growth of* $GaAs_{1-x}Bi_x$, Applied Physics Letters **82**, 2245 (2003)

[3] E. C. Young et al., *Bismuth incorporation in* $GaAs_{1-x}Bi_x$ *grown by molecular beam epitaxy with in-situ light scattering*, Physica Status Solidi C **4**, 5, p. 1707-1710 (2007)

[4] A. J. Ptak et al., *Kinetically limited growth of GaAsBi by molecular-beam epitaxy*, Journal of Crystal Growth **338**, p. 107-110 (2012)

[5] X. Lu et al., *Effect of molecular beam epitaxy growth conditions on the Bi content of* $GaAs_{1-x}Bi_x$, Applied Physics Letters **92**, 192110 (2008)

[6] Z. Zhou, *Optimisation of GaAsBi Based Semiconductors*, PhD Thesis, p. 50, University of Sheffield (2018)

[7] G. Vardar et al., *Mechanisms of droplet formation and Bi incorporation during molecular beam epitaxy of GaAsBi*, Applied Physics Letters **102**, 042106 (2013)

[8] R. B. Lewis et al., *Growth of high Bi concentration* $GaAs_{1\text{-}x}Bi_x$ *by molecular beam epitaxy*, Applied Physics Letters **101**, 082112 (2012)

[9] D. A. Beaton et al., *Insight into the epitaxial growth of high optical quality* $GaAs_{1–x}Bi_x$, Journal of Applied Physics **118**, 235701 (2015)

[10] D. F. Reyes et al., *Bismuth incorporation and the role of ordering in GaAsBi/GaAs structure*, Nanoscale Research Letters **9**, 23 (2014)

[11] J. H. Neave et al., *Effect of arsenic species* (As_2 *OR* As_4) *on the crystallographic and electronic structure of MBE-grown GaAs(001) reconstructed surfaces*, Surface Science **133**(1), 267-278 (1983)

[12] V. Bahrami-Yekta et al., *MBE growth optimization for* $GaAs_{1\text{-}x}Bi_x$ *and dependence of photoluminescence on growth temperature*, Semiconductor Science and Technology **30**(9), 094007 (2015)

[13] W. Bennarndt et al., *Domains of molecular beam epitaxial growth of Ga(In)AsBi on GaAs and InP substrates*, Journal of Crystal Growth **436**, 56-61 (2016)

[14] R. D. Richards et al., *Molecular beam epitaxy growth of GaAsBi using* As_2 *and* As_4, Journal of Crystal Growth **390**, 120-124 (2014)

[15] C. R. Tait et al., *Spontaneous nanostructure formation in GaAsBi alloys*, Journal of Crystal Growth **493**, 20-24 (2018)

[16] Z. Zhou et al., *Absorption properties of GaAsBi based p–i–n heterojunction diodes*, Semiconductor Science and Technology **30**, 094004 (2015)

[17] J. O. Akinlami and A. O. Ashamu, *Optical properties of GaAs*, Journal of Semiconductors **34**(3), 032002 (2013)

[18] A. R. Mohmad et al., *The effect of Bi composition to the optical quality of* $GaAs_{1\text{-}x}Bi_x$, Applied Physics Letters **99**, 042107 (2011)

[19] X. Lu et al., *Composition dependence of photoluminescence of* $GaAs_{1\text{-}x}Bi_x$ *alloys*, Applied Physics Letters **95**, 041903 (2009)

[20] A. R. Mohmad et al., *Localization effects and band gap of GaAsBi alloys*, Physica Status Solidi B **251**(6), 1276-1281 (2014)

[21] D. Dagnelund et al., *Identification of an isolated arsenic antisite defect in GaAsBi*, Applied Physics Letters **104**, 052110 (2014)

[22] T. Wilson et al., *Assessing the nature of the distribution of localised states in bulk GaAsBi*, Scientific Reports **8**, 6457 (2018)

[23] R. D. Richards et al., *Photovoltaic characterisation of GaAsBi/GaAs multiple quantum well devices*, Solar Energy Materials and Solar Cells **172**, 238-243 (2017)

[24] J. P. R. David et al., *Effect of misfit dislocations on leakage currents in strained multiquantum well structures*, Applied Physics Letters **67**, 906 (1995)

[25] A. R. Mohmad et al., *The Effect of Growth Conditions to the Optical Quality of GaAsBi*, IEEE Regional Symposium on Micro and Nanoelectronics (RSM) (2015)

[26] K. Oe *Characteristics of semiconductor alloy* $GaAs_{1-x}Bi_x$, Japanese Journal of Applied Physics, Part 1: Regular Papers and Short Notes and Review Papers **41**, 5A, p. 2801-2806 (2002)

[27] L. Gelczuk et al., *Deep-level defects in n-type GaAsBi alloys grown by molecular beam epitaxy at low temperature and their influence on optical properties*, Scientific Reports **7**, 12824 (2017)

[28] P. M. Mooney et al., *Deep level defects in n-type GaAsBi and GaAs grown at low temperatures*, Journal of Applied Physics **113**, 133708 (2013)

[29] P. M. Mooney et al., *Deep level defects in dilute GaAsBi alloys grown under intense UV illumination*, Semiconductor Science and Technology **31**, 8 (2016)

[30] C. J. Hunter et al., *Absorption Characteristics of* $GaAs_{1-x}Bi_x$*/GaAs Diodes in the Near-Infrared*, IEEE Photonics Technology Letters **24**, 23 (2012)

[31] I. Moussa et al., *Atmospheric-pressure metalorganic vapour phase epitaxy optimization of GaAsBi alloy* Thin Solid Films **516**, 23, p. 8372-8376 (2008)

[32] H. Sugawara et al., *Semiconductor light-emitting device*, US Patent 5, 153, 889 (1992)

Chapter 5

Growth and electroluminescence characterisation of GaAsBi/GaAs multiple quantum wells

5.1 Introduction

GaAsBi is a promising material for the growth of a 1 eV sub-cell for use in multi-junction photovoltaics. The incorporation of more than 50 wells is necessary to absorb enough light to achieve current-matching with the other sub-cells. Many previous studies into GaAsBi quantum wells have mostly focused on pseudomorphics structures with less than 11 wells. Previous work conducted in Sheffield by Richards et al. studied up to 63 strained quantum wells. However, the device performance was severely degraded by the presence of catastrophic strain relaxation and a loss of carrier confinement. To improve on the work by Richards et al., a systematic series of strained GaAsBi/GaAs MQWs with between 2 and 120 periods was grown using MBE. The devices have a much lower strain per period of the MQW, which should result in higher performance for the devices with large numbers of wells. A review of relevant GaAsBi quantum well devices will be given in section 5.2.

5.2 Review of previous GaAsBi MQWs

A review of studies into GaAsBi quantum well devices from the literature will be presented in this section. Reports of GaAsBi LEDs, including bulk structures, will also be given.

5.2.1 Growth studies

The growth of GaAsBi/GaAs double quantum wells were grown by Fan et al. [38]. The authors investigated how to grow uniform wells without growth interruptions by varying the bismuth flux.

Fuyuki et al. demonstrated the first growth of a GaAsBi MQW structure, using AlGaAs barriers [39]. Satellite peaks in XRD measurements confirmed the presence of a MQW structure, with between 3.5 and 5% bismuth incorporated in the wells.

Butkute et al. reported the growth of GaAsBi MQW structures with AlAs barriers grown at low temperature with MBE and migration-enhanced epitaxy [40]. The authors found that the AlAs barriers blocked Bi from diffusing out of the wells during annealing at 750 °C. The authors also reported the presence of Bi quantum dots in the GaAsBi wells [41].

The growth of GaAsBi/GaAs MQWs was also investigated by Patil et al. [24]. The authors used different temperatures to grow the wells (350 °C) and barriers (550 °C), with 11 periods. This was done to reduce Bi segregation and increase the abruptness of the interfaces. PL was demonstrated at 10 K with the devices emitting at up to 1230 nm.

5.2.2 Optoelectronic studies and devices

Kopaczek studied the optical properties of GaAsBi/GaAs quantum wells using photoreflectance and PL [45]. The authors observed transitions between excited states in the wells confirming that GaAsBi/GaAs have a type I band alignment. The PL was dominated by localised states below 150 K, with an S-shape dependence of the PL peak wavelength on temperature.

The growth of a strain-compensated GaAsBi/GaAsP MQW device with 50 periods using MOVPE was reported by Kim et al. [36]. The PL peak of the device was at 1050 nm with 3.5% Bi incorporated. The device was tested as a single-junction solar cell.

Patil et al. demonstrated EL from an 11 period GaAsBi/GaAs MQW device [1]. Operation at 1230 nm was reported with injection current densities of up to 983 Acm^{-2}. Temperature dependent EL measurements showed a S-shaped shift in the peak wavelength. This was attributed to localised states in the GaAsBi.

5.2.3 Review of series C GaAsBi/GaAs MQWs

The devices grown by Richards et al. (series C) are compared to the devices grown in this work. Therefore, the review of the literature concerning these devices is kept separate for clarity.

Growth and structural investigation

The growth of a systematic set of GaAsBi/GaAs MQW devices with MBE was reported by Richards et al. [20] [44]. The authors noted that the wells were much thinner than intended. This effect was attributed to the incorporation of Bi from a physisorbed surface layer that takes a finite time to accumulate. TEM analysis of the 54 well device showed dislocations at the upper and lower MQW interfaces corresponding to strain relaxation. This was supported using XRD analysis, which also showed that the 54 well device was tilted with respect to the substrate. Nomarski microscopy images also showed significant subsurface damage for the devices with strain relaxation. By comparison with InGaAs devices, it was determined that the onset of strain relaxation occurs at a similar strain-thickness product for GaAsBi.

Optoelectronic studies

The PL of the devices with 54 and 63 wells was nearly two orders of magnitude weaker than the rest of the devices and red-shifted by 56 meV. This was attributed to the strain relaxation and a loss of quantum confinement.

The dark currents and photovoltaic characterisation of the devices was reported in [32]. The dark currents were around 20 times higher than a comparable strain-balanced InGaAs/GaAsP device. The GaAsBi devices showed a much longer wavelength absorption edge than a strained InGaAs/GaAs device. However the absorption onset was more gradual than the InGaAs device. The GaAsBi devices also showed a significant increase in the photocurrent at reverse bias which indicated incomplete photo-excited carrier extraction.

The poor carrier extraction was explored in more detail in [13]. At 100 K, under illumination from a 679 nm laser the devices exhibited a stepped profile in IV measurements. It was theorised that the holes were trapped in the wells at zero bias due to the large valence band offset, relative to the conduction band offset. Therefore, electrons could easily escape while holes could not. This resulted in a charging of the i-region, screening of the built-in electric field, and a reduction of the depletion width. As the depletion region moved past each individual well the carriers were extracted, leading to the stepped IV curve. This conclusion was supported by quantum mechanical calculations of the electron and hole bound state energies and their thermal escape time from the wells. Consequently, the design of future GaAsBi MQW structures for photovoltaic applications will have to take into account the disparity in electron and hole escape times. The authors stated that the incorporation of indium or nitrogen into the wells could help to alleviate this issue.

GaAsBi based bulk LEDs

The operation of a GaAsBi LED emitting at 987 nm was shown by Lewis et al. [43]. The minimum injection current density reported by the authors was 50 Acm^{-2}. The device consisted of an intrinsic 50 nm GaAs$_{0.982}$Bi$_{0.018}$ layer with 25 nm GaAs cladding layers. This structure was embedded in a pin diode.

Richards et al. demonstrated bulk GaAsBi based LEDs grown using MBE with 6% Bi [42]. Emission was obtained at around 1200 nm using current densities as low as 8 Acm^{-2}. From temperature dependent EL measurements the authors concluded that there is a continuous distribution of Bi-induced localised states extending up to 75 meV into the bandgap.

5.3 List of devices

The GaAsBi quantum well devices grown in this work are named G2, G5, etc. The prefix “G” indicates the year of growth (2016), and the number represents the number of quantum wells.

Richards et al. grew a complementary set of GaAsBi/GaAs MQW in Sheffield [20], and this set of devices is used as a comparison. These devices are referred to as QW3, QW5 etc. in the literature, however in this work they are referred to as C3, C5 etc. to distinguish them more clearly from series G.

A summary of the devices studied in this chapter is given in table 5.1.

Device name	Number of wells	Nominal well thickness (nm)	Nominal barrier thickness (nm)	Grower
G2	2	10	30	T. Rockett
G5	5	10	30	T. Rockett
G15	15	10	30	T. Rockett
G30	30	10	30	T. Rockett
G40	40	10	30	T. Rockett
G80	80	10	30	T. Rockett
G120	120	10	30	T. Rockett
C3	3	8	150	R. Richards
C5	5	8	97	R. Richards
C10	10	8	50	R. Richards
C20	20	8	22	R. Richards
C40	40	8	7.3	R. Richards
C53	53	8	3.4	R. Richards
C64	64	8	1.8	R. Richards

TABLE 5.1: Summary of devices grown in this work (series G) and devices grown by R. Richards [20] (series C), which are used as a comparison. The number in the device names indicates the number of wells in the MQW stack

The nominal structures of the devices in series C and G are shown in figures 5.1 and 5.2, respectively.

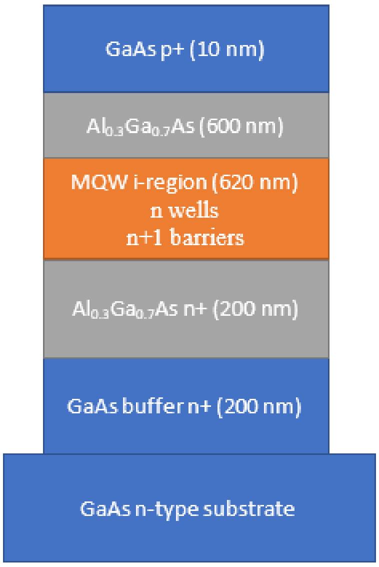
GaAs p+ (10 nm)
$Al_{0.3}Ga_{0.7}As$ (600 nm)
MQW i-region (620 nm)
n wells
n+1 barriers
$Al_{0.3}Ga_{0.7}As$ n+ (200 nm)
GaAs buffer n+ (200 nm)
GaAs n-type substrate

FIGURE 5.1: Nominal growth structure of series C GaAsBi/GaAs MQWs grown by Richards et al. For the structure of the i-region, see table 5.1

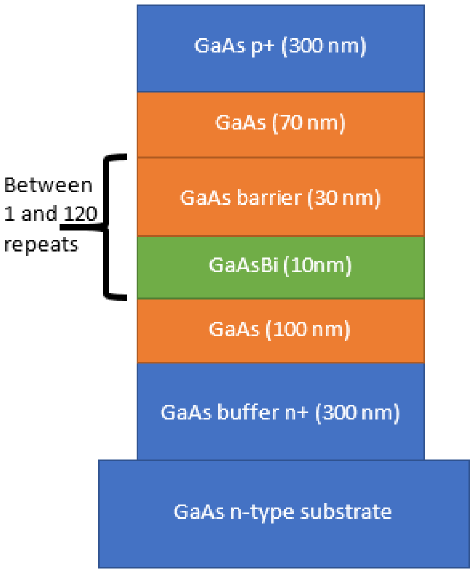

FIGURE 5.2: Nominal growth structure of series G GaAsBi/GaAs MQWs grown for this work. The top p++ layer is not shown in this diagram

From previously published work by Richards et al., devices C53 and C64 show a severe degradation of the PL intensity relative to the other devices [19]. These devices have thin barriers (3.4 and 1.8 nm, respectively), so the average strain per period of the MQW stack is large. In addition to the movement of dislocations to the lower interface of the MQW stack, these devices have also relaxed some of the strain through the generation of dislocations at the upper MQW interface [20]. It is also possible that there is a loss of carrier confinement in these devices which will further weaken the PL. The series C devices were reviewed in section 5.2.

The difference between the two series of devices can be visualised by plotting the average strain per period of the MQWs against the total thickness of the stack. The average lattice parameter per MQW period ($< a_{MQW} >$) can be calculated using equation 5.1.

$$< a_{MQW} >= \frac{t_b a_b + t_w a_w}{t_b + t_w} \tag{5.1}$$

Here t_b and t_w are the well and barrier thicknesses, respectively, and a_b and a_w are their free standing lattice constants. The average strain $< f_s >$ can then be calculated using equation 5.2.

$$< f_s >= \frac{< a_{MQW} > - a_s}{a_s} \tag{5.2}$$

Where a_s is the lattice parameter of the substrate. It is possible to independently adjust the band gap and strain in the MQW stack by varying the parameters in equation 5.1. The average strain are plotted against the total thickness of the MQW stack for both series of devices in figure 5.3.

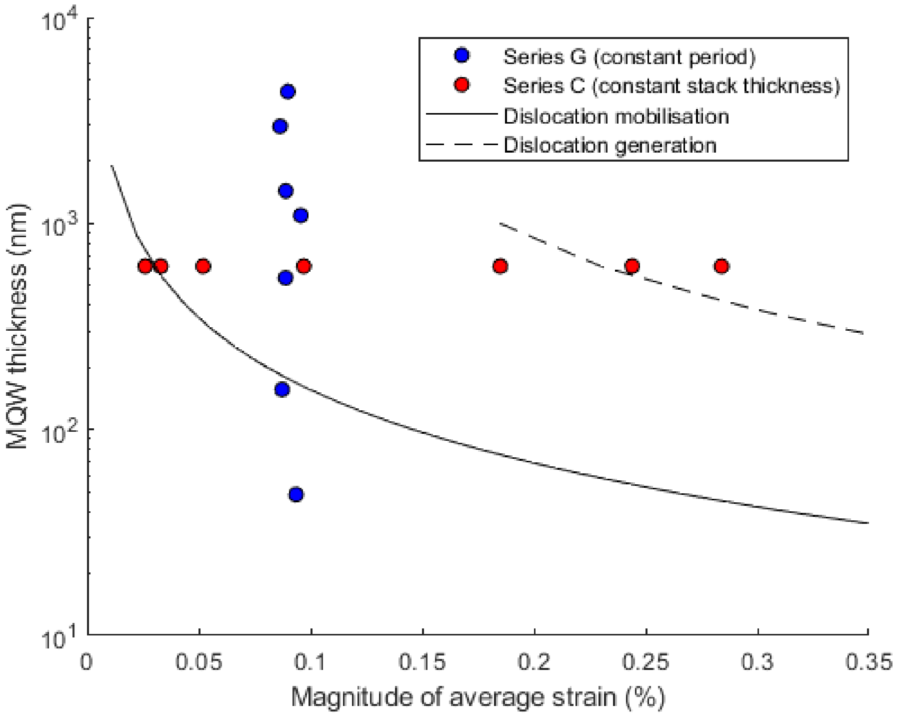

FIGURE 5.3: Magnitude of the average strain plotted against the total thickness of the MQW stack, for GaAsBi/GaAs MQWs. The solid black line is the Matthews-Blakeslee critical thickness which corresponds to the mobilisation of already present dislocations. The dashed black line corresponds to the point at which the strain energy is large enough to generate new dislocations [47].

The series C devices have the same stack thickness (nominally 620 nm) with different numbers of wells. The barriers in the devices are different thicknesses to accommodate the required number of (nominally 8 nm) wells. Devices C54 and C63 (the two red circles furthest to the right) are above the critical thickness for dislocation generation [47].

The series G devices have the same MQW period (nominally 40 nm) with different numbers of wells. Therefore, the average strain per period is the same throughout the series and the total thickness of the MQW stack is proportional to the number of wells. From figure 5.3, the series G devices have a lower average strain, due to the thicker barriers. This was expected to lead to a lower density of dislocations in the devices with more than 50 wells, a requirement for the development of MQW photovoltaics with a GaAsBi sub-cell.

5.4 Growth of MQW series G

The GaAsBi/GaAs MQW devices studied in this work were grown in January 2016 in an Omicron MBE-STM using n+ GaAs (001) substrates with a 0.1°offcut. The devices have a constant well and barrier thickness (nominally 10 nm and 30 nm, respectively), with between 2 and 120 quantum wells. The nominal structure of the devices is shown in figure 5.2.

Before growth of the MQW stack, the substrate was outgassed, had the surface oxide removed, and had an n-type GaAs buffer deposited. This procedure is discussed in more detail in section 4.3.1.

The MQW stack was grown inside the i-region of a pin diode structure to allow for electrical characterisation. The n-type, p-type, and undoped GaAs cladding layers were grown at 577 °C using As_2 [21] with an As:Ga atomic flux ratio of approximately 1.5:1 whereas the quantum wells and GaAs barriers were grown at 375 °C using As_4 [22, 23] with an atomic flux ratio of approximately 1.8:1. Note that due to the incorporation dynamics of As_4, only half the arsenic atoms can incorporate and this As:Ga flux ratio should result in a Ga-rich surface. However, this arsenic flux deficit was small enough, and the wells and barriers thin enough, that a Ga-rich RHEED reconstruction was not observed during the growth.

The p-type GaAs has a dopant concentration of $3x10^{18}$ cm^{-3}, and the n-type GaAs has a dopant concentration of $2x10^{18}$ cm^{-3}, calculated using separate doping control layers. The purpose of the 100 nm thick GaAs cladding layers was to prevent dopant atoms from diffusing from the n and p regions into the MQW stack.

The growth rate used in this work was 0.59 ML/s calculated using RHEED oscillations. The substrate temperature was kept at 375 °C during the growth of the barriers in contrast to [24] which used a higher temperature for the GaAs barriers.

The Bi BEP was $1.1x10^{-7}$ mbar as measured using an ion gauge that was moved in front of the substrate. The Bi shutter was opened for 30 seconds prior to the growth of the first quantum well to build up a wetting layer of Bi on the surface [25]. The RHEED pattern subsequently underwent a transition from an As terminated c(4 x 4) to a Bi terminated (n x 3) reconstruction [26]. At this point, the Ga shutter was opened, and the RHEED pattern changed to (n x 1). The growth was paused for 30 seconds after the growth of each quantum well, and for 60 seconds after each barrier to allow the surface to anneal. Similar growth interrupts have been shown to improve the interface quality in GaAs/AlAs superlattices [27]. The devices underwent further annealing at 577 °C during the growth of the upper GaAs layers for around 1 hour, which included the time for changing the arsenic cracker temperature to produce As_2.

After the growth of the top p-type GaAs, a thin (<15 nm) p++ layer of GaAs was grown during which the Ga cell temperature was decreased by roughly 45 °C. This led to a decrease in the growth rate from 0.6 to 0.35 ML/s, and a corresponding increase in the dopant concentration. The purpose of this layer is to provide a highly doped region to which electrical contacts can be formed.

5.5 Nomarski microscopy

The as-grown surfaces were first analysed using Nomarski microscopy to observe the type of defects and to establish the presence of strain relaxation in the layers. Representative Nomarski images of the devices are shown in figures 5.4 to 5.10.

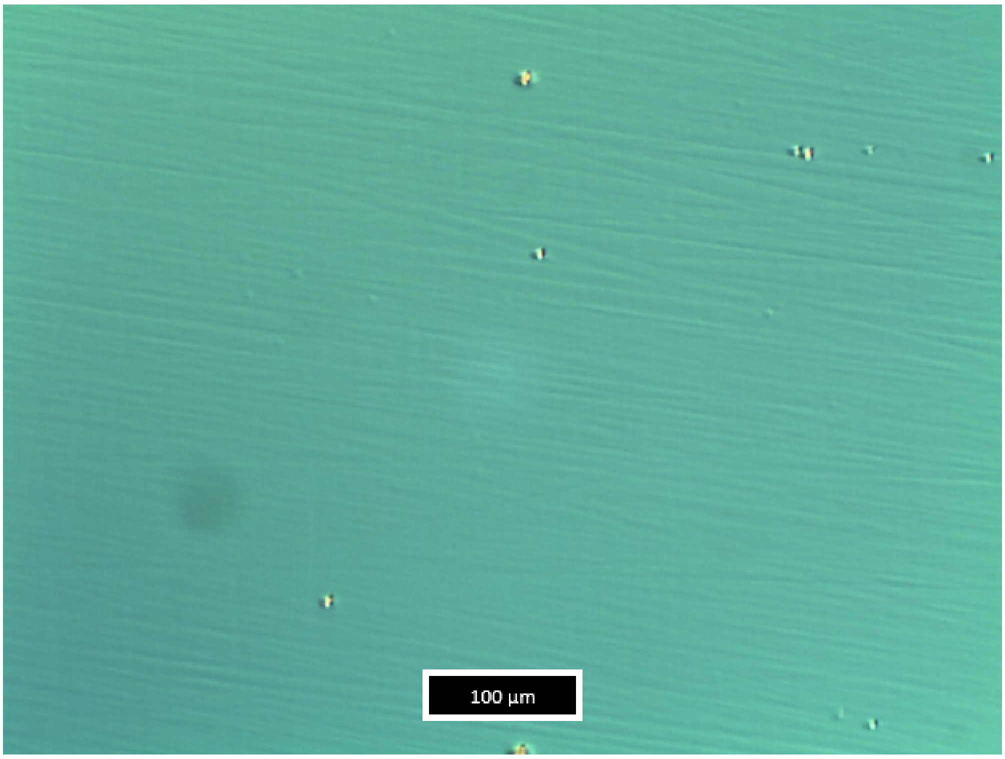

FIGURE 5.4: Nomarski image of G2, at 10x magnification

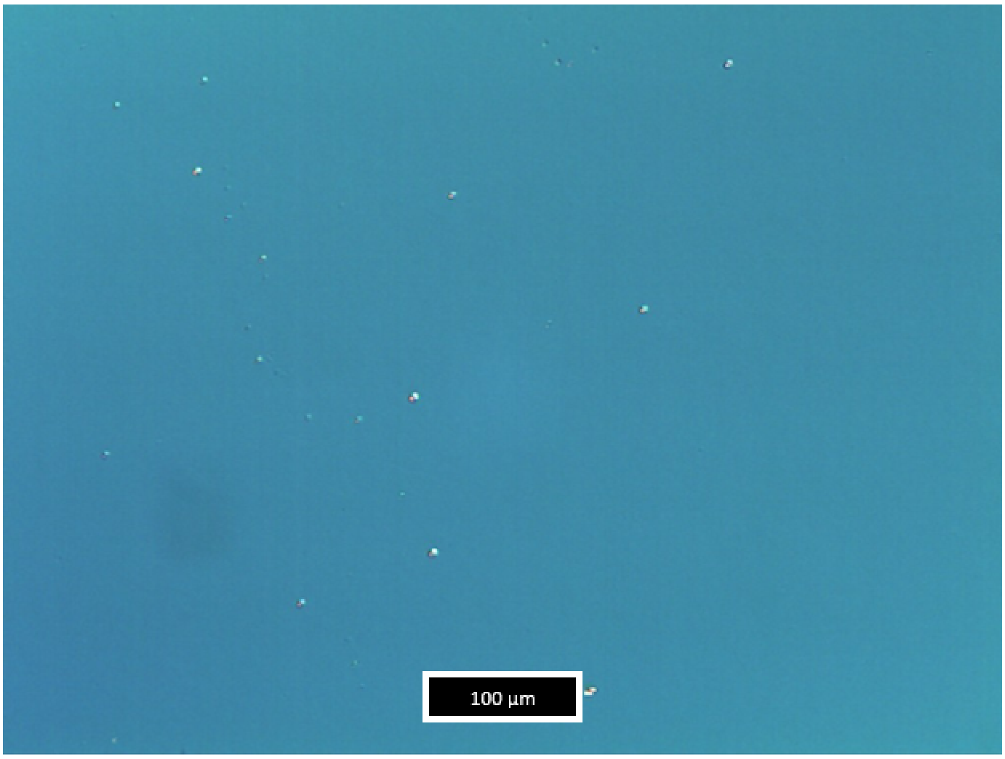

FIGURE 5.5: Nomarski image of G5, at 10x magnification

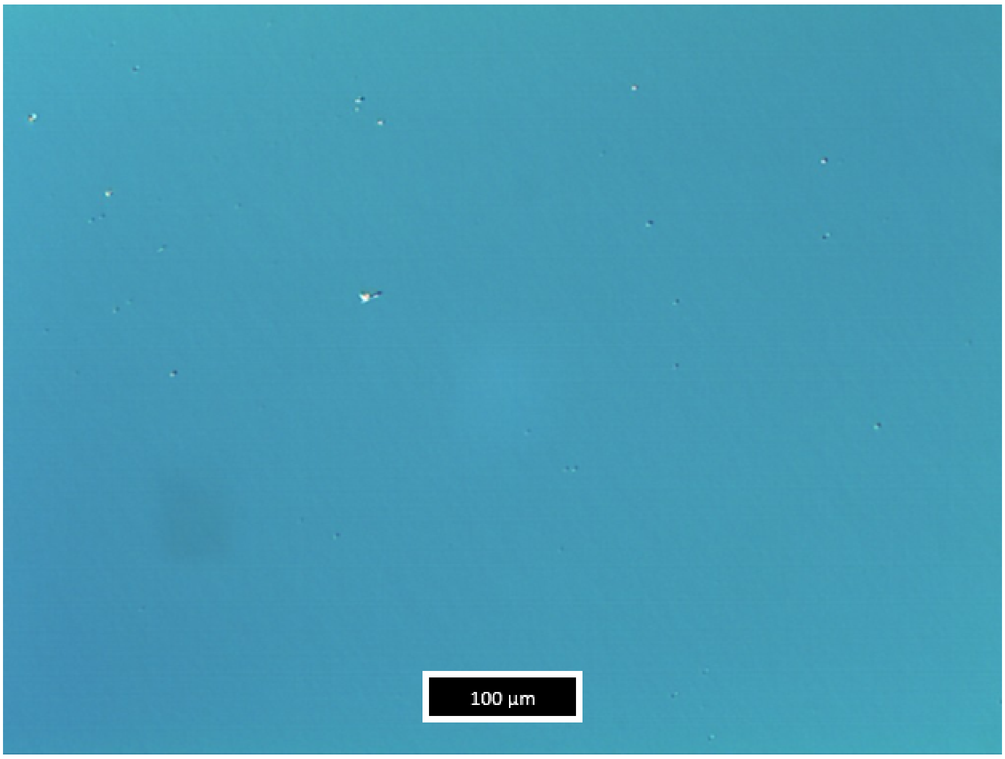

FIGURE 5.6: Nomarski image of G15, at 10x magnification

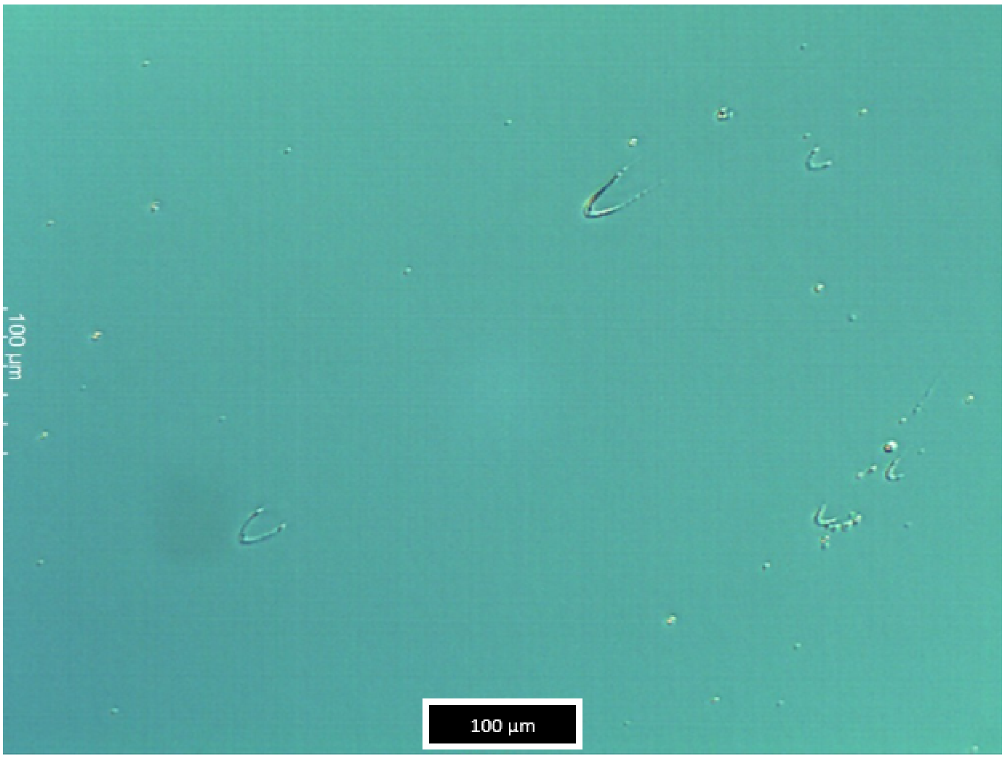
100 µm
100 µm

FIGURE 5.7: Nomarski image of G30, at 10x magnification

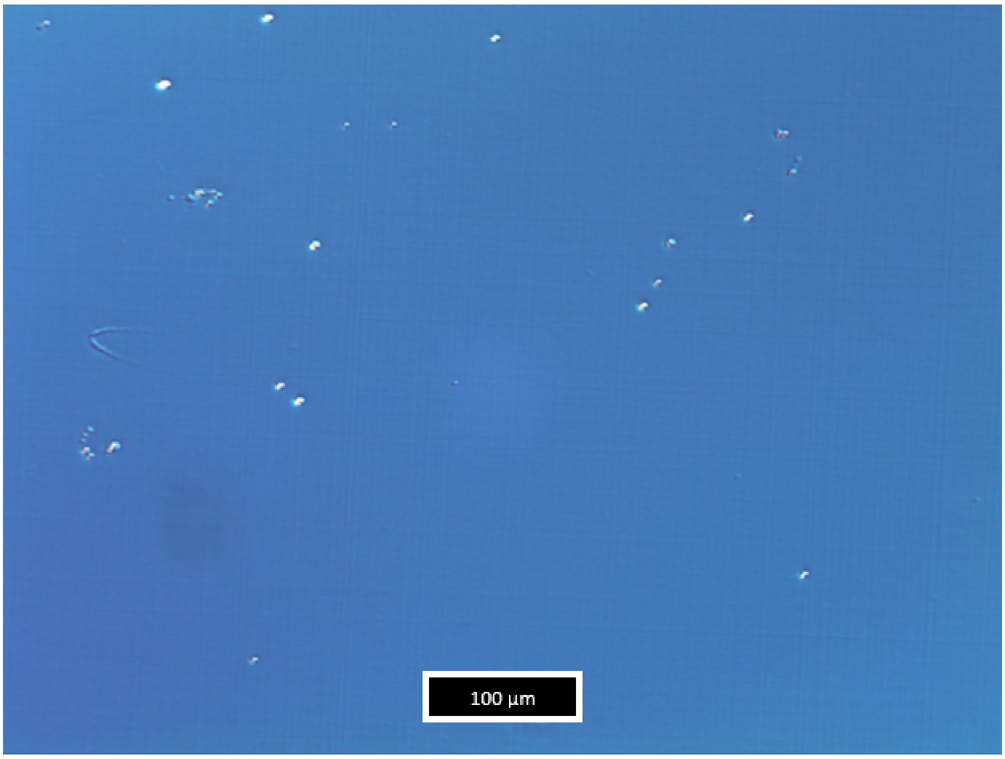

FIGURE 5.8: Nomarski image of G40, at 10x magnification

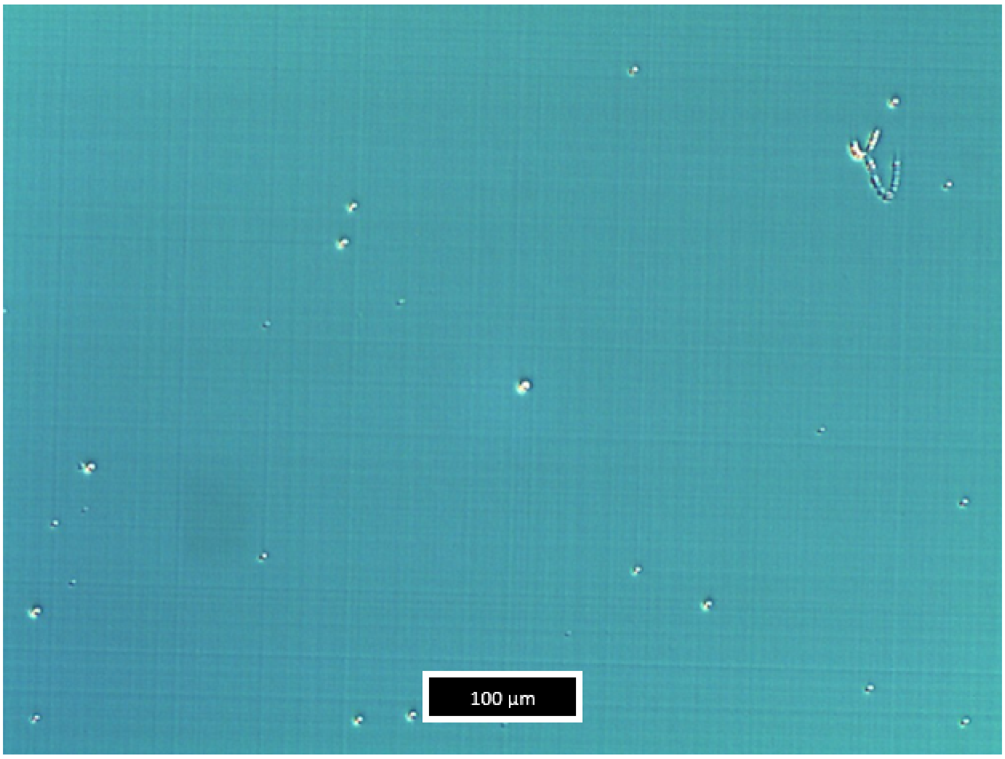

FIGURE 5.9: Nomarski image of G80, at 10x magnification

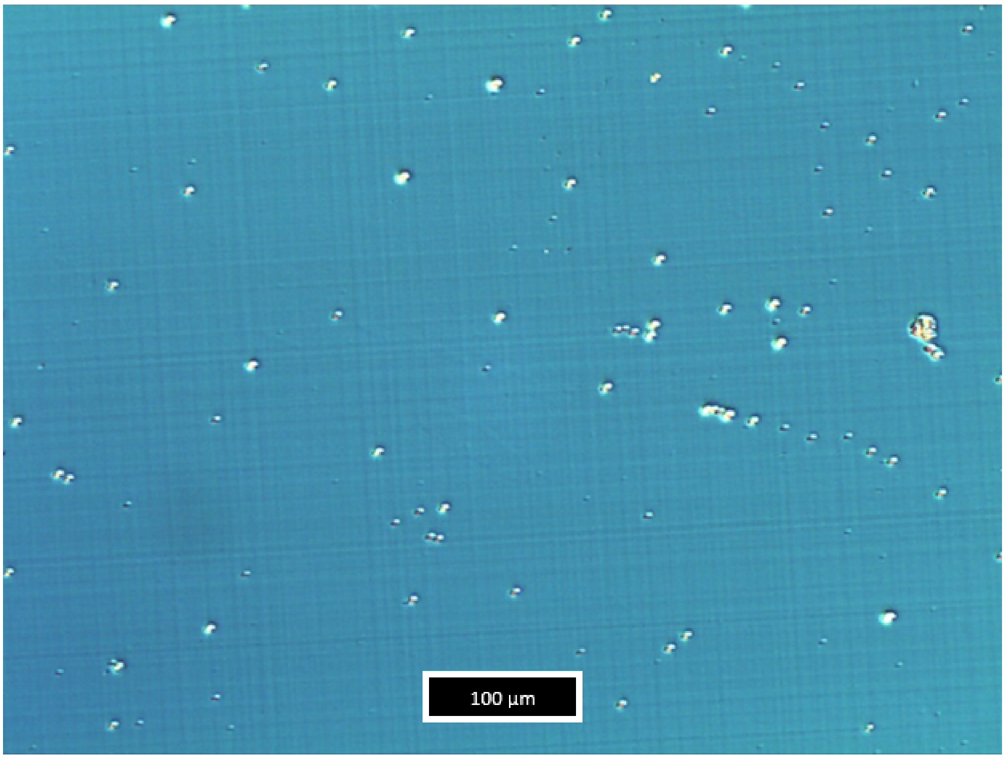

FIGURE 5.10: Nomarski image of G120, at 10x magnification

Device G2 (figure 5.4) shows a large number of scratch lines indicating that there is significant subsurface damage. However, it is unlikely that these lines are caused by strain relaxation as they are not orthogonal. In addition, these scratch lines are also present on the part of the wafer that was covered by the sample holding plate during growth (not shown in these images) indicating that the lines were formed before the substrate was placed in the MBE chamber. The most likely cause is over-aggressive cleaning of the substrate after the wafer was cleaved, specifically the use of a cotton bud to swab the surface. The cleaning procedure was changed to not use cotton buds after this effect was discovered.

The “horseshoe” shaped defects visible for devices G30, G40, and G80 (figures 5.7, 5.8, and 5.9) are also likely due to over-aggressive cleaning of the substrate. These defects appear to radiate out from a central point on the wafer (not shown in these images). After the previous cleaning procedure involving cotton buds was abandoned, the procedure was changed to spraying isopropanol onto the surface at high speed to try and remove the semiconductor dust that was left over from the cleaving process. It appears that this new cleaning procedure caused some damage to the substrate leading to the “horseshoe” shaped defects.

Devices G15 to G120 (figures 5.6 to 5.10) show an increasing prevalence of orthogonal lines indicating that strain relaxation is present in the devices. The density of these lines on the wafer does not appear to change with the number of wells, only their prominence.

From the Nomarski images, the devices show a varying density of droplet-like defects. To address the origin of the droplet-like defects, image thresholding was used to segment the images and allow automatic counting of the droplets, see figure 5.11.

Two approaches were used to segment the images: Otsu's method and morphological image erosion.

Otsu's method [28] assumes that the image contains two classes of pixels (droplets and the background in this case), and that the histogram of pixel intensities resembles a bi-modal distribution. However, this method is less effective for images where the contrast is low, and the background is not uniform, such as for G2.

The basis of image erosion is to use a "structure element" to roughly blur out features of a certain size (set by the user) to create a second image which is then subtracted from the original. The structure element was set as a disk of radius 7 pixels, roughly corresponding to the size of the droplets in the images. The result is an image showing the edges of the droplets in white on a black background. The downside to this technique is that the erosion does not completely remove the features from the images leading to a feature sometimes being counted twice by the computer.

A mixture of the two methods was used to analyse the density of the droplet-like defects in each image depending on the contrast and the uniformity of the background. A more thorough comparison of the two image thresholding techniques is beyond the scope of this work.

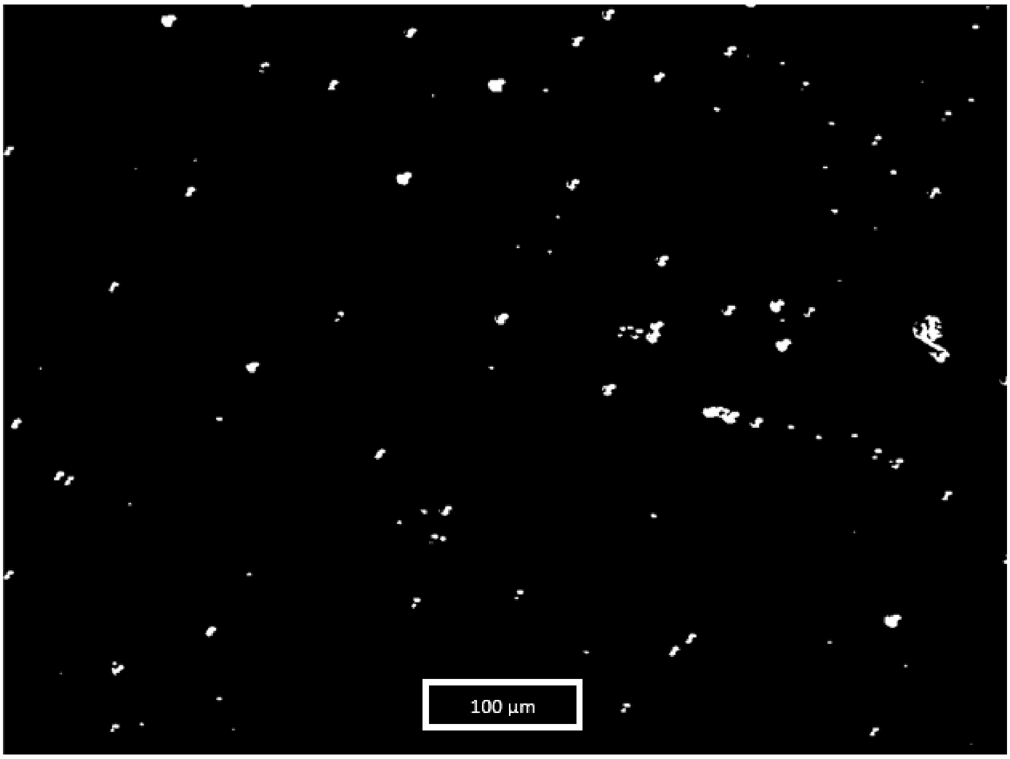

FIGURE 5.11: Nomarski image of G120 segmented using Otsu's method, showing the droplet-like defects as white features against a black background

The density of droplet-like defects in each device was counted using Matlab, and is plotted in figure 5.12.

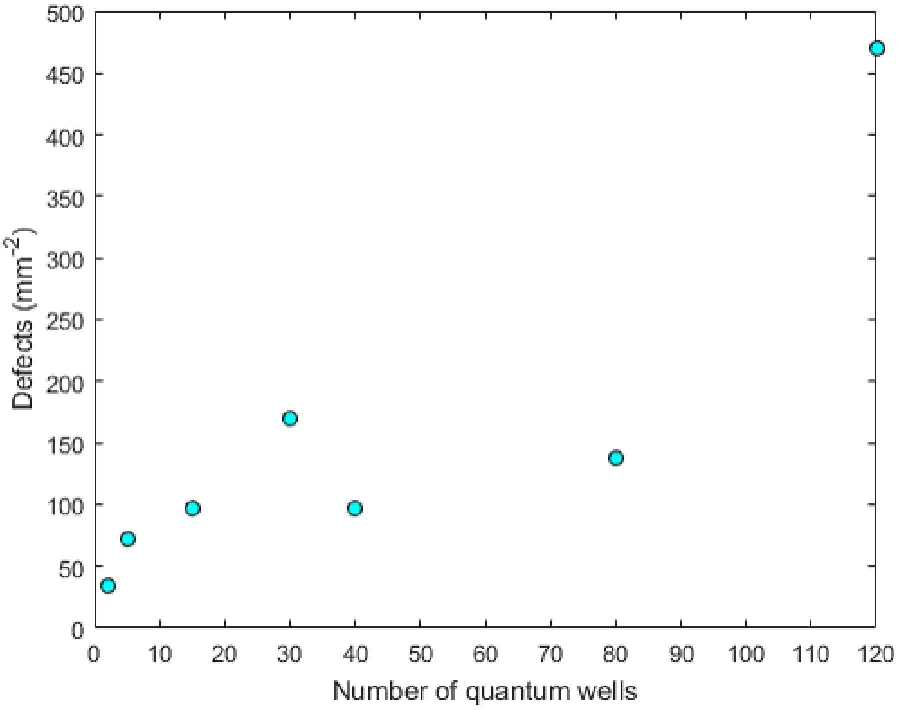

FIGURE 5.12: Density of droplet-like defects in the Nomarski images as a function of the number of quantum wells, calculated using image processing

The density of droplets shows weak positive correlation with the number of wells, from figure 5.12. If there were no correlation, the droplet-like defects could potentially be caused by the incorporation of residual gas atoms into the growing epilayer with the density instead correlating with the vacuum pressure on the day of growth. Therefore, it is possible that the droplets are caused by the gallium cell spitting or by bismuth droplets forming on the growing epilayer. One would expect gallium droplets to have a longer surface lifetime than bismuth droplets due to the higher vapour pressure of bismuth at the growth temperature (375 °C). Due to the long annealing steps between growth of the wells and barriers, it is likely that the droplets are caused by the gallium cell spitting.

5.6 X-ray diffraction

A Bruker D8 Discover X-ray diffractometer was used to measure (004) $\omega - 2\theta$ scans of the MQW structures, and RADS Mercury was used to fit the data, see figure 5.13.

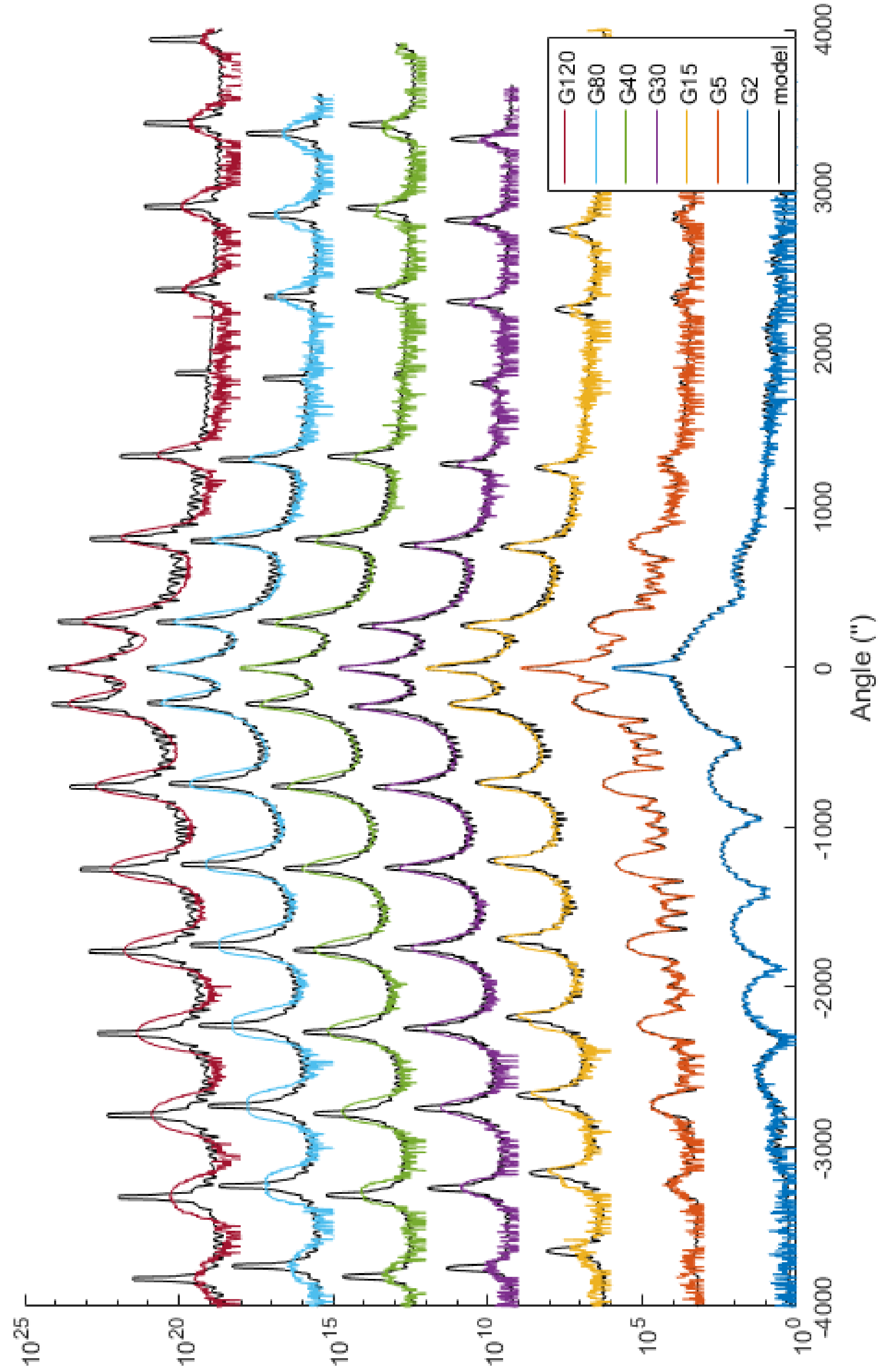

FIGURE 5.13: XRD scans and simulations of the GaAsBi/GaAs MQW devices

From figure 5.13, the devices all show prominent satellite peaks caused by the periodic wells and barriers in the MQW stack. The GaAs peak at 0 arcseconds is sharp for all of the devices, indicating that the GaAs regions are high quality. The period of the MQW is similar for all the devices as the satellite peaks occur at roughly the same angle in all the scans. In addition, the splitting of the 0-order satellite peak from the substrate peak indicates that the average Bi content per period is also similar for all the devices.

Thickness fringes are visible for G2 and G5, however they are much weaker for the devices with 15 or more wells. The point at which these fringes become weaker correlates strongly with the Matthews-Blakeslee critical thickness 5.3. and the appearance of orthogonal lines in the Nomarski images. From [47] the onset of strain relaxation above the Matthews-Blakeslee critical thickness involves dislocations becoming mobile and moving to the bottom interface of the MQW stack. If the bottom interface between the MQW stack and the GaAs underneath becomes roughened due to a high density of dislocations, this should result in the loss of the periodic interference that causes the thickness fringes.

The FWHM of the -1-satellite peak initially decreases as the number of periods in the MQW increases from G2 to G30. However, from G30 to G120 the FWHM increases and the closeness of the fit calculated by the XRD simulation software gets steadily worse as the number of quantum wells increases. There are many possible reasons for this, with several options outlined in figure 5.14.

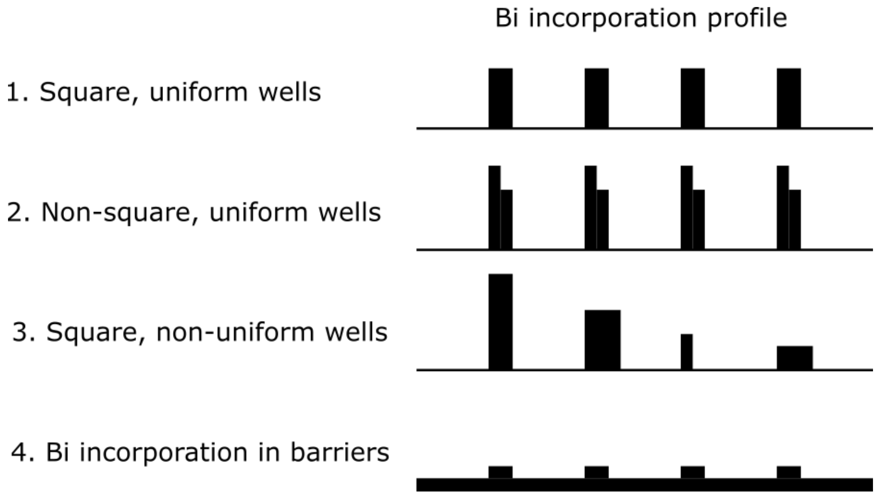
Bi incorporation profile
1. Square, uniform wells
2. Non-square, uniform wells
3. Square, non-uniform wells
4. Bi incorporation in barriers

FIGURE 5.14: Possible Bi incorporation profiles. In all four cases shown here the MQW period and the average bismuth content per period is the same, meaning that the 0-order satellite peak should occur at the same angle in XRD measurements

Firstly, the wells could be square and uniform with abrupt interfaces. As the number of wells increases, incomplete strain relaxation via dislocation mobilisation could be giving rise to a change in the lattice parameter in the growth direction. Strain relaxation is the most likely explanation for the broadening of the XRD satellite peaks as the MQW stacks are thicker than the Matthews-Blakeslee critical thickness 5.3. However, TEM measurements of GaAsBi/GaAs MQWs by Richards et al. show that misfit dislocations form at the lower interface of the stack rather than being spread throughout it [20].

Secondly, the wells could be identical, but with each well containing a non-uniform bismuth content similar to that observed in [29]. In this case, the luminescence should be coming from the region with the highest bismuth content.

Thirdly, it is possible that there is a variation in the composition and thickness of the quantum wells, either across the entire wafer due to flux gradients in the MBE machine, or on a microscopic scale due to clustering of Bi atoms. The effect of this phenomena would be to "blur-out" the superlattice peaks, since the XRD measures a spot that is roughly 2mm across. This would result in several peaks in the PL spectra of each device (assuming the wells are all optically active). However, the devices all show a single (albeit broad) PL peak.

Fourthly, bismuth could be incorporating into the barrier. This would rely on a significant number of bismuth adatoms present on the surface when growing the GaAs barriers. The surface lifetime of bismuth atoms on GaAs is dependent on the surface temperature and the incident arsenic flux and species, and was measured as 800 s at 415 °C under an As_4 flux in [23].

Ultimately, several of these effects could be present in the devices to a certain degree. Cross-sectional TEM measurements would provide further information on the relative bismuth incorporation and well width, as well as direct imaging of misfit dislocations as in [20].

5.6.1 XRD fitting parameters for devices

The results of the XRD simulations are shown in table 5.2, with the devices modelled assuming that the wells in each device are identical and square. More complicated simulations involving modelling the devices as non-identical wells or by introducing strain relaxation were found to give an acceptable fit for devices G30 to G120. Unfortunately, the introduction of more fitting parameters in an already complicated structure is not ideal as this increases the uncertainty in each fitting parameter.

Device	Bi content (%)	Well thickness (nm)	Barrier thickness (nm)	Period (nm)	Satellite peak FWHM (")
G2	4.29	7.95	32.46	40.41	208
G5	4.46	6.62	30.85	37.47	92
G15	5.23	5.89	32.54	38.43	39
G30	5.28	6.13	31.36	37.49	50
G40	5.20	5.67	31.07	36.74	57
G80	5.45	5.35	32.03	37.38	56
G120	5.49	5.41	31.22	36.63	74

TABLE 5.2: Summary of the XRD fitting parameters calculated using RADS Mercury

From table 5.2, the wells are much thinner than intended (10 nm), which could be caused by a gradual onset of Bi incorporation, as seen in [1]. In addition, the barriers are marginally thicker than the nominal thickness (30 nm). However, the period of the MQW is less than intended (40 nm) for all devices except G2, which is likely due to growth transients in the gallium cell resulting in a decrease in flux.

The bismuth content calculated by the software increases with the number of wells from 4.29 to 5.49%. It is unlikely that the bismuth content in the wells is increasing throughout each growth as more wells are deposited since this would result in multiple peaks in PL and EL (see section 5.10.1). Alternatively, if the devices with a greater number of wells have a significant degree of strain relaxation one would expect the zero-order diffraction peak to be shifted towards the substrate diffraction peak, and for the simulation software to calculate a higher bismuth content to shift the peak back to location observed in the measurement.

5.7 Photoluminescence spectroscopy

PL measurements were taken using a 532 nm CW laser operating at a power of 300 mW. This corresponds to a power density of approximately 120 W/cm^2 focused onto the device in a spot with a radius of roughly 250 µm. The PL spectra of a single quantum well test structure is shown in figure 5.15. This structure was grown without p-type doping in the upper GaAs layers, so could not be fabricated into a device for EL testing, and is not comparable to the devices with a greater number of wells.

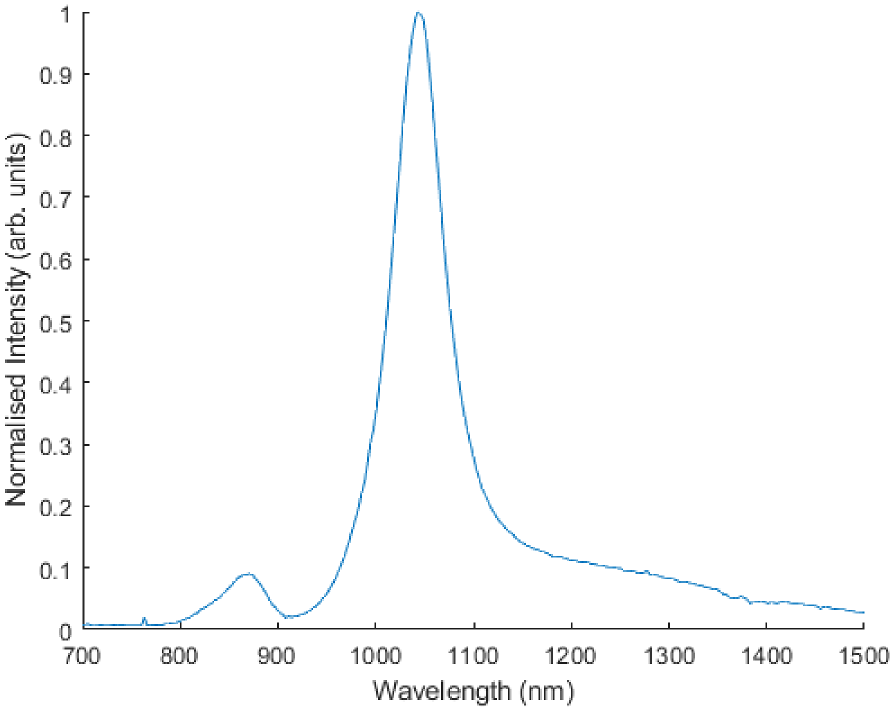

FIGURE 5.15: Normalised PL spectra of a single quantum well GaAsBi test structure using 120 W/cm2 excitation at 532 nm

From figure 5.15, the single quantum well test structure has a PL peak at 1043 nm with a FWHM of 68 nm. The peak at 870 nm is due to recombination in the GaAs layers.

The PL spectra of the MQWs with between 2 and 120 wells are shown in figure 5.16.

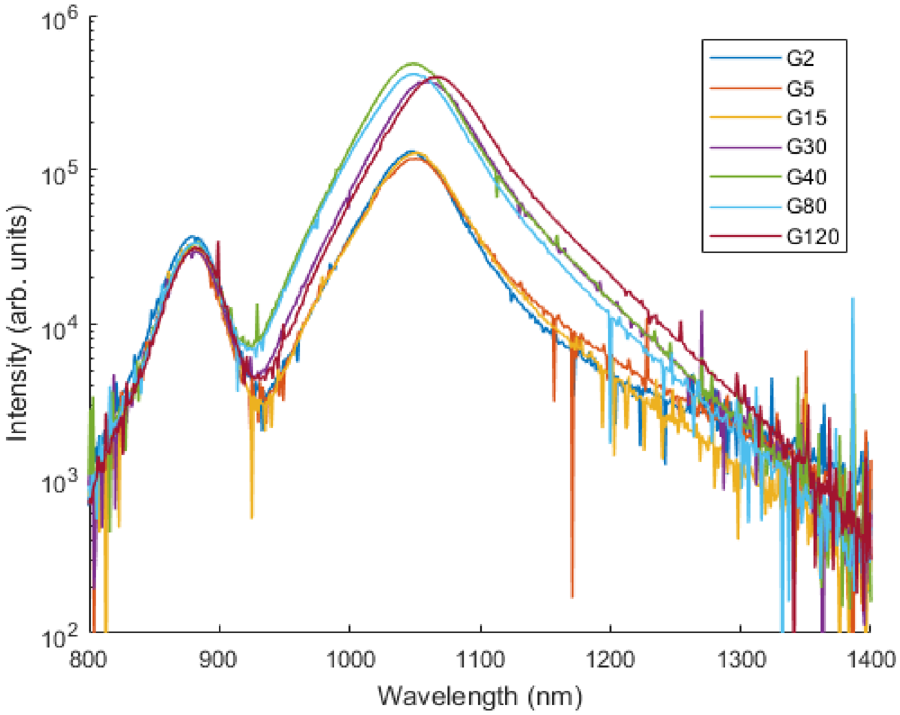

FIGURE 5.16: PL spectra of the GaAsBi devices using 120 W/cm2 excitation at 532 nm

From figure 5.16, the peak at 880 nm is a similar intensity for all the devices. This peak is likely dominated by to recombination in the p-type GaAs layer rather than recombination in the GaAs barriers in the MQW stack. The band gap of GaAs corresponds to a PL emission wavelength of 869 nm at room temperature, and the observed difference could be due to a miscalibration of the monochromator. Alternatively, the laser could be heating the device by approximately 40 °C, calculated using the Varshni model of band gap temperature dependence [30, 31].

There is a weak and broad peak at approximately 1200 nm in all the spectra corresponding to recombination via dopant states in the GaAs layers.

The GaAsBi wells all show a single relatively broad PL peak between 1047 and 1077 nm with spectral widths between 62 and 73 nm. There do not appear to be any radiative transitions between excited states in the wells as there are no smaller peaks superimposed on the short wavelength side of the main peak. In addition, the fact that the devices are emitting a single PL peak suggests that the wells are uniform throughout the MQW stack. However, this does not preclude the possibility that the wells are non-square as the carriers in a non-square well should migrate to the region with the lowest band gap (highest bismuth content) before recombining.

The data plotted for G120 was taken at the middle of the device. However, there was a relatively large variation in the PL intensity and wavelength across this device in one direction. The PL peak wavelength of this device varied from 1062 to 1077 nm across the device (not shown). It is possible that the bismuth content or well thickness vary across this device, or due to a varying degree of strain relaxation across the device.

A summary of the parameters that can be extracted from the PL data are shown in table 5.3. The PL peak intensities are normalised to the weakest peak (G5).

Device	Peak wavelength (nm)	Peak intensity (normalised)	FWHM (nm)
G2	1047	1.07	63
G5	1050	1	68
G15	1053	1.07	66
G30	1060	3.23	68
G40	1049	4.23	68
G80	1049	3.63	67
G120 (middle)	1067	3.37	70
G120 (top edge)	1062	5.17	73
G120 (bottom edge)	1077	1.13	73

TABLE 5.3: Summary of the PL data for the GaAsBi/GaAs MQWs

From table 5.3, the FWHM of the devices shows no correlation with the number of wells. The normalised peak intensity is plotted as a function of the number of wells in figure 5.17.

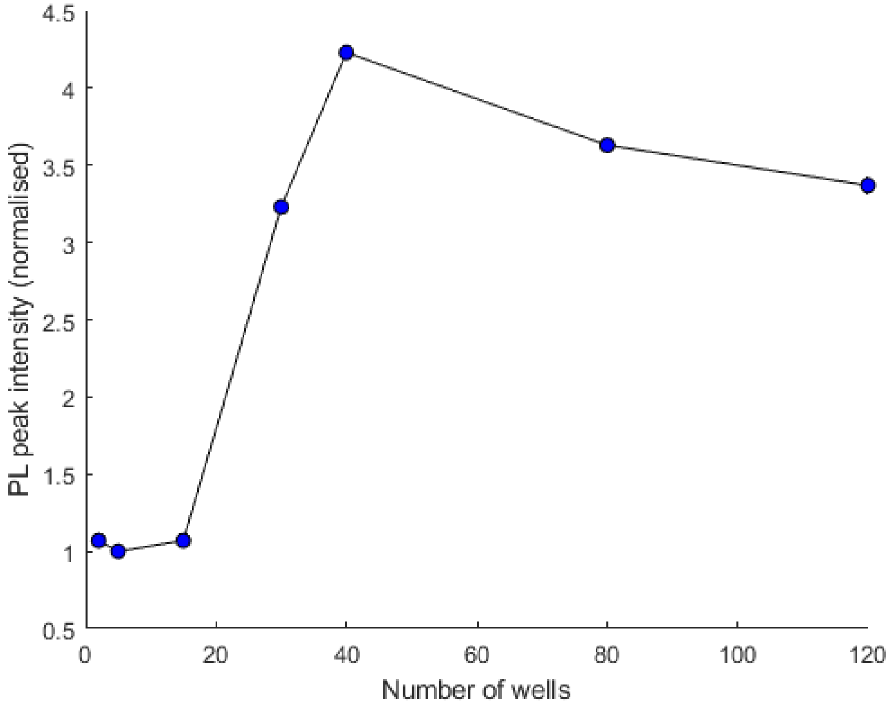

FIGURE 5.17: Relationship between number of quantum wells and the PL peak intensity for the GaAsBi MQW devices. The points are connected with the black line to guide the eye. The point shown for G120 is from the middle of the wafer

From figure 5.17, the first three devices (G2, G5, and G15) have a similar PL peak intensity, however the intensity per well decreases rapidly. Between 15 and 40 wells, the PL intensity increases linearly. It is unclear why the increase in PL intensity starts after 15 wells. The devices with 15 or more wells display signs of strain relaxation in Nomarski microscopy images (see section 5.5). One would expect the presence of misfit dislocations formed by strain relaxation to attenuate the PL intensity. However, if the dislocations are all forming at the lower interface of the MQW stack, as in [20], and since the carriers are all being optically injected via the laser, the condition of the lower MQW stack interface may have a negligible impact on the PL. The increase in PL intensity after 15 wells could therefore be explained if the strain-relaxed layers have a higher radiative efficiency than the strained layers. Alternatively, the apparently constant PL intensity for 2 to 15 wells could be due to noise in the data.

The decrease in PL peak intensity after 40 wells is due to strain relaxation. In addition, the laser light is less likely to penetrate to the lower wells in the stack, and the light emitted from the lower wells is less likely to reach the surface. For example, photons emitted from the bottom QW of the stack in G2, G40, and G120 have a 99, 89, and 73% chance of reaching the top of the stack, respectively, assuming that 100% of the photons are transmitted through the GaAs barriers and that the absorption coefficient is around 5000 cm^{-1} for 1060 nm light in $GaAs_{0.95}Bi_{0.05}$ [50].

5.8 Quantum well modelling and comparison with PL

The optical emission from the quantum wells can be modelled using the time-independent Schrödinger equation (TISE). Here it is assumed that the quantum well extends to infinity in the plane of the substrate such that the carriers are only confined in a single dimension. Therefore, the Schrödinger equation can be simplified into its 1-dimensional form, see equation 5.3. Applied to a quantum well, the wavefunctions form standing waves, and the energy eigenstates corresponding to the bound states may be calculated if the well width and band offsets are known.

$$\frac{-\hbar^2}{2m^*}\frac{d^2\psi(z)}{dz^2} + V(z)\psi(z) = E\psi(z) \tag{5.3}$$

Here $\hbar$ is Planck's reduced constant, m^* is the effective mass of the carrier, $\psi(z)$ is the wavefunction of the carrier, E is the energy eigenstates of the carrier, and $V(z)$ is the position dependent barrier and well potential energy for a carrier in a given band.

5.8.1 Band offsets

The barrier height $V(z)$ is defined relative to the GaAs conduction and valence band edges according to equation 5.4.

$$V(z) = \begin{cases} V_0 & \text{when } z < -L/2 \\ 0 & \text{when } -L/2 < z < L/2 \\ V_0 & \text{when } z > -L/2 \end{cases} \tag{5.4}$$

The three possible values for $V(z)$ correspond to the carrier in the GaAs barrier above the well, in the well, and in the GaAs barrier below the well, respectively. L is the width of the well and V_0 is the band offset between GaAs and GaAsBi in the conduction or valence band.

While the valence band maximum is widely thought to increase in energy relative to GaAs with bismuth incorporation, the behaviour of the conduction band minimum and the type of band alignment is still the subject of debate. Kudrawiec et al. observed transitions between the excited hole and electron states in a GaAsBi quantum well indicating a type I band alignment [2]. However, Patil et al. showed evidence for a type II alignment from low temperature PL measurements [1]. The nature and variation of the band alignment with bismuth incorporation heavily affects $V(z)$ and the calculated bound state energy levels.

In this work, it is assumed that the band alignment is type I, and the barrier heights are defined relative to the GaAs band edges as V_0^{CB} and V_0^{VB} for the conduction and valence bands, respectively, see equations 5.5 and 5.6, while the origin and calculation of these terms is described in more detail in section 1.2.2 [3–5].

$$V_0^{CB} = \Delta E_{CB} x \tag{5.5}$$

$$V_0^{VB} = \frac{E_{Bi} - \sqrt{E_{Bi}^2 + 4xC_{Bi}^2}}{2} \tag{5.6}$$

Here $\Delta E_{CB} = 2.3$ eV is the conduction band offset between GaBi and GaAs, $E_{Bi} = -0.4$ eV is the bismuth energy level, and $C_{Bi} = 1.65$ eV is the coupling energy between the bismuth level and the GaAs valence band maximum.

5.8.2 Effective mass approximation

For the boundary conditions, one would normally take the wavefunction ψ and its derivative $d\psi/dz$ to be continuous at the edges of the well. However, in this case the effective masses of the carriers are different in the well and barriers [6] so that particle flux is not conserved across the boundary. To resolve this issue, the second boundary condition can be replaced with taking $(1/m^*)d\psi/dz$ to be continuous, known as the BenDaniel-Duke boundary condition [10]. This has no fundamental justification but gives bound state energies that agree relatively well with experiment [7, 8]. The drawback of this approximation is the introduction of 'kinks' in the wavefunction at the edges of the well [9]. The effective masses used in this work (taking $\mathrm{GaAs_{0.95}Bi_{0.05}}$ as an example) are shown in table 5.4. The heavy hole and electron effective masses are similar for GaAsBi and GaAs and have a minor change with composition. However, the light hole effective mass in GaAsBi depends strongly on the bismuth content, and is much larger than in GaAs, reaching a value of 0.23 m_e (2.8 times the value for GaAs) for 4-7% Bi [6].

Material	m_e^*	m_{hh}^*	m_{lh}^*
GaAs	0.063	0.51	0.082
$\mathrm{GaAs_{0.95}Bi_{0.05}}$	0.063	0.45	0.23

TABLE 5.4: Effective masses used for calculating bound state energy levels in the GaAsBi/GaAs quantum wells, relative to the electron mass [6, 11]

5.8.3 Solution of Schrödinger equation using custom software

The full process showing the solution of the Schrödinger equation is not be given here as numerous derivations are available in the literature, see for example [12].

Matlab was used to write software to calculate the energy levels of the carriers in bound states taking the well width and bismuth content as inputs from the user, and interpolating the data of Maspero [6] to obtain the effective masses of the holes at the given bismuth content. The transcendental equations were solved graphically, and the software generated a plot of the band structure and bound state energies. By normalising the wavefunction, it is also possible to calculate the probability of the carriers being inside or outside the well. However, this is beyond the scope of this work: it was assumed that adjacent wells do not interact and the tunnelling of carriers between the wells is negligible due to the relatively thick barriers (30 nm).

5.8.4 Bound state energies in device G2

The Schrödinger equation was used to calculate the bound state energies for device G2 using the well width and bismuth content obtained from the XRD simulations ($L = 7.95$ nm, x= 4.29%), see figure 5.18.

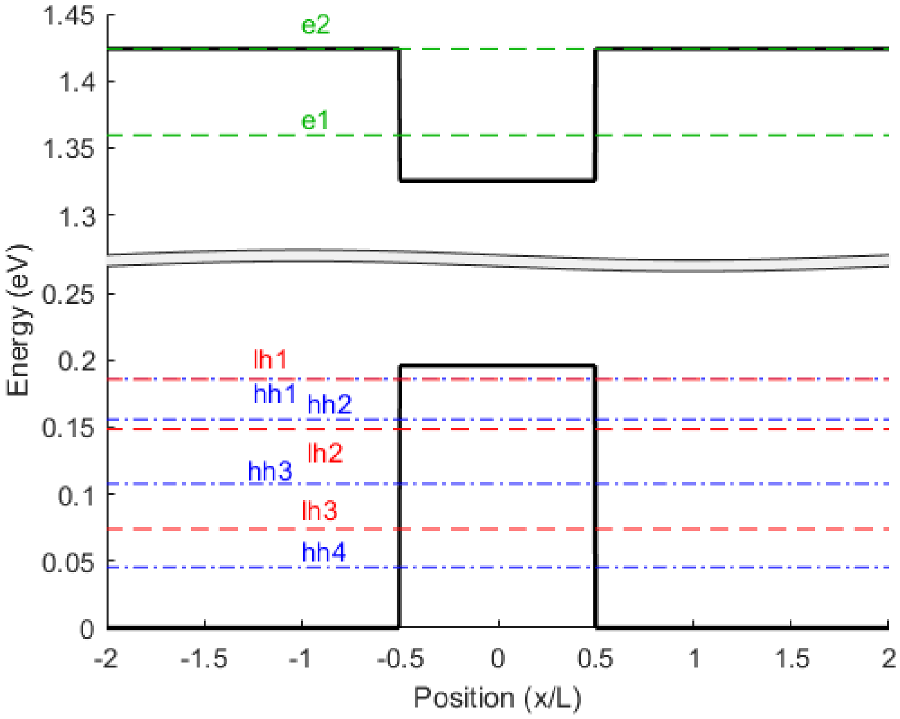

FIGURE 5.18: Diagram showing the band structure (black) for one of the GaAsBi quantum wells in device G2 using the structural parameters from XRD simulations ($L = 7.95$ nm, x= 4.29%). The bound state energies are shown for electrons (green), light holes (red), and heavy holes (blue).

From figure 5.18, there are four heavy hole states, three light hole states, and two electron states bound inside the quantum well.

The state e2 is weakly bound in the well since the conduction band offset is small in GaAsBi. This state has a binding energy of <1 meV, which is much smaller than the thermal energy at room temperature (k_BT = 26 meV). In fact, this binding energy is so small that the e2 state may not exist. For example, if the model is adjusted to make the Bi content less than 4.1% or the well thinner than 7.7 nm then only one electron bound state would exist in the well. The uncertainty in the XRD fitting parameters is estimated at ± 0.25% for Bi content, and ± 0.4 nm for the well width. Therefore, there is unlikely to be a significant electron population in state e2, even under high injection conditions, and transitions between e2 and other states can be neglected.

The binding energy of the e1 state is 65 meV, which is a factor of 2.5 times larger than the carrier thermal energy at room temperature. However, a small proportion of the electrons will still be likely to thermally escape the well since the range of energies in the thermal distribution is large. A loss of electron confinement would weaken the GaAsBi luminescence, and could result in recombination between electrons in the GaAs and confined holes in the GaAsBi at the edges of the wells.

The lh1 and hh1 states are nearly degenerate (<1 meV energy difference) such that the ground state transition is likely a mix between e1 $\rightarrow$ hh1 and e1 $\rightarrow$ lh1. Although seven hole states exist, the hole population in the excited states will typically be negligible under all but the highest injection conditions when the ground state population approaches the density of states. The lifetime of holes in the excited states is probably much shorter than the radiative lifetime so that the holes quickly relax to the ground state. Therefore, the probability of radiative recombination between e1 and the excited hole states is negligible compared to recombination between e1 and hh1/lh1. This is before considering that the e1 $\rightarrow$ hh2/lh2 transition is impossible in an infinite quantum well, since it violates one of the selection rules for transitions in an infinite quantum well, namely that the change in quantum number of the two states involved must be zero [8]. However, this selection rule is relaxed for the case of a finite quantum well, such that the transition is merely extremely unlikely rather than impossible.

The theorised dominance of the ground state transition in light emitting applications is supported by the presence of a single peak from the QWs in PL and EL measurements. However, transitions involving excited hole states are detectable using absorption and photocurrent measurements, as shown by Richards et al. in [13].

A contour plot of the ground state transition energy was generated by running the Matlab script in a loop across a range of well widths and bismuth contents, see figure 5.19. Due to the large increase in the light hole effective mass in GaAsBi, the lowest energy inter-band transition varies between e1 $\rightarrow$ hh1 and e1 $\rightarrow$ lh1 depending on the bismuth content. Therefore the smaller of the two is taken as the ground state transition at each point.

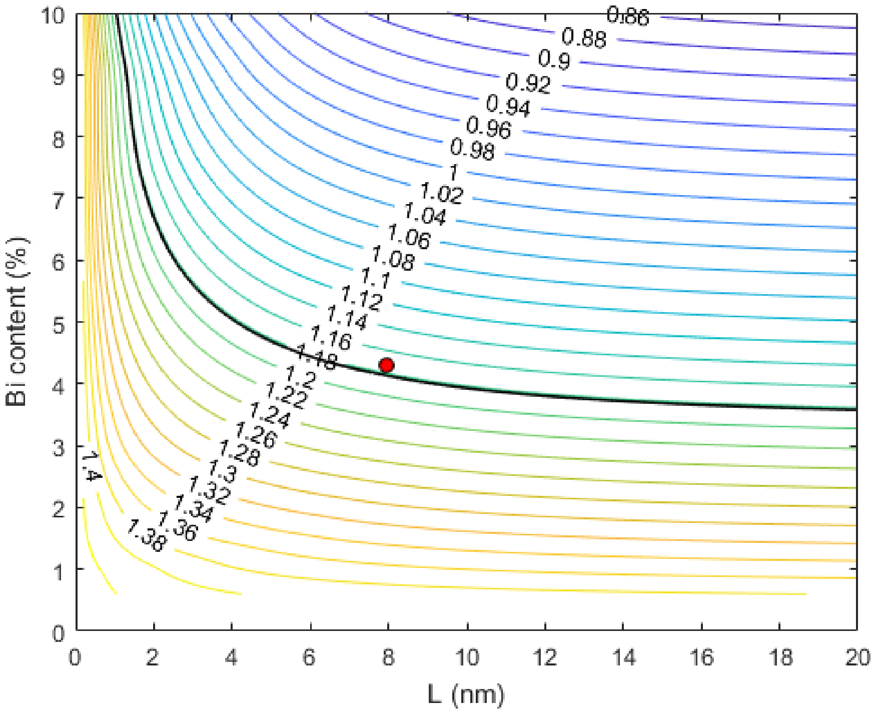

FIGURE 5.19: Contour plot of the dependence of the ground state transition energy in a GaAsBi/GaAs QW on the well width and bismuth content. The contour labels denote the transition energy. The red circle indicates the measured well width and bismuth content for G2 from the XRD simulation (L = 7.95 nm, x= 4.29%, see table 5.2). The black line is the contour corresponding to the measured ground state transition energy of G2 from PL (see 5.3), which has been highlighted for clarity.

From figure 5.19, the ground state transition energy varies as a function of the well width and bismuth content. In general, a higher bismuth content corresponds to a lower ground state transition energy. In the limit of thick wells (>20 nm), the confinement energy asymptotically tends towards zero and the transition energy approaches the bulk band gap of the GaAsBi. As the well thickness decreases, quantum confinement increases the ground state transition energy. There is a small kink in the contours at low well thicknesses and high bismuth contents (most noticeable for the black line at 9% Bi and 2 nm wells), which could be caused by the ground state transition switching from e1 $\rightarrow$ hh1 to e1 $\rightarrow$ lh1. Note that for thin wells with a low bismuth content, the band offsets will be insufficient to confine the carriers (particularly electrons in the conduction band) at room temperature.

In theory, the red circle corresponding to the measured structural parameters of the well should lie on the black line corresponding to the observed PL peak energy. In reality, there is a discrepancy between the ground state transition energy calculated using the 1D-TISE (1.174 eV) and the experimental PL data, (1.182 eV). The predicted ground transition energy was calculated using the 1D-TISE for all of the MQW structures based on the XRD fitting parameters, and is plotted in figure 5.20 against the measured PL peak energy.

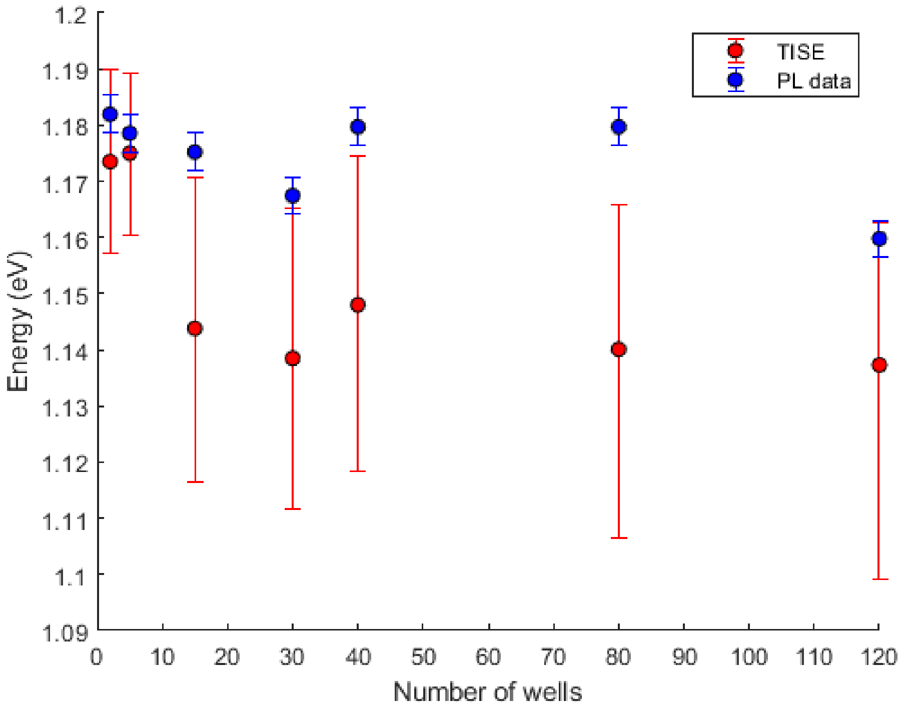

FIGURE 5.20: Comparison of PL peak energy and ground state transition energy for series of GaAsBi/GaAs MQWs. The error bars for the PL data assume an accuracy of ± 3 nm for determining the peak energy from the relatively broad PL emission

From figure 5.20, the devices all have a similar ground state transition energy from PL (approximately 1.18 eV) with the possible exception of G120 (1.16 eV). Since the devices were grown in a random order to eliminate the influence of source fluxes drifting over time, this is further evidence that the wells are relatively consistent between devices. Alternatively, the wells in separate devices could have completely different Bi content and thicknesses and, through coincidence, still have the same ground state transition energy (see figure 5.19). However, it is highly improbable that all the devices could have a similar ground state transition energy through coincidence.

For the case of G2 and G5, the TISE calculations have an excellent agreement with the PL data. However, for the devices with 15 or more wells there is worse agreement between theory and experiment which corresponds to the point at which the MQW stack exceeds the critical thickness , see figure 5.3.

If the strain in the layers is so large that dislocations are being generated [48] [47], the resulting strain relaxation could lead to a red shift of the ground state transition energy, as in [19]. However, the opposite is observed. The PL data are all blue shifted relative to the TISE calculations. G120 is possibly an exception to this as the theory has a reasonable agreement with the PL data indicating that the presence of strain relaxation might be starting to red-shift the PL although the magnitude of the red-shift is much smaller than that reported by Richards for devices C54 and C63.

Alternatively, it is possible that the XRD fitting parameters used for the TISE calculations are inaccurate due to the influence of strain relaxation via dislocation mobilisation. From figure 5.13, the XRD fitting gets less accurate for devices with 15 or more wells. This introduces a large uncertainty in the bismuth content and thickness of the wells. In figure 5.20, the error bars for the TISE calculations assume the uncertainty in the bismuth content is ± 0.25% for G2 and G5, and ± 0.5% for the devices with 15 or more wells. The uncertainty in the well thickness is the 95% confidence bound calculated by the fitting software, which increases with the number of wells (values ranging between 0.1 and 1.1 nm). When considering these error bars, the agreement between the theory and experiment is better. These error bars are likely an underestimate of the uncertainty in the transition energy as they do not consider any uncertainty in the band offsets or effective masses of the carriers.

Since the 1D-TISE calculations are consistently underestimating the ground state transition energy, it is likely that the XRD fitting is underestimating the well thickness and/or overestimating the bismuth content when strain relaxation is present in the MQW stack. Therefore, it is likely that the devices all contain between 4 and 5% bismuth.

5.9 Current – voltage

The as-grown devices were cleaved, with one quarter fabricated into mesa structures with annular top contacts and a common back contact. The dark currents of the devices were measured as a function of bias, see figure 5.21.

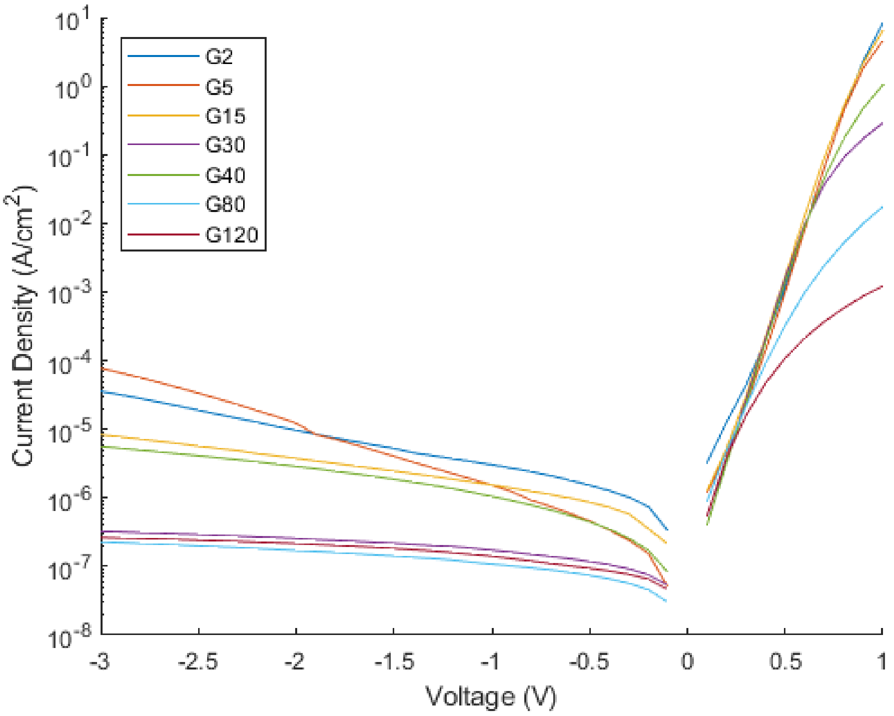

FIGURE 5.21: Dark currents as a function of bias for the GaAsBi/GaAs MQWs grown in this work

From figure 5.21, the devices all exhibit diode characteristics. However, the devices are severely affected by series resistance resulting in the forward dark currents "turning over". At least 7 mesa structures were measured on each device and the forward bias dark currents scale with area for all of the devices (within a factor of 2.2 at +0.4 V). Device G120 shows an increasing dark current and a less prevalent series resistance with smaller devices. The ideality factors of the devices are between 1.97 and 2.25 and show no correlation with the number of wells. The ideality factors of devices G80 and G120 are 2.4 and 2.3 respectively although this has a large uncertainty due to the series resistance.

The forward dark currents of the diodes do not appear to vary based on the number of wells. This is unusual, since from the ideality factor of the diodes one would expect defect-assisted recombination in the depletion region to be dominating the dark current. As the density of the defects is proportional to the volume of material available for recombination (i.e. the number of wells), there should be strong correlation between the saturation current density and the number of wells[37].

The reverse bias dark currents are generally higher for the thinner devices. Since the electric field strength scales with the thickness of the i-region the carriers can be extracted more easily in the thinner devices. However, the reverse bias dark currents do not scale closely with area, with around a factor of 5 variation in the dark currents of different sized devices at -3 V.

5.10 Electroluminescence

5.10.1 EL of all GaAsBi/GaAs MQWs using constant current

The EL spectra of the GaAsBi devices (series G) was measured using a custom-refitted SPEX 1871b monochromator, using Matlab software with an Arduino single-board computer to control the stepper motor inside the monochromator, see figure 5.22. The previous set of GaAsBi MQW devices grown by Richards in Sheffield (series C) was also tested to examine the effect of strain on the EL emission, see figure 5.23. The two sets of devices were measured on the same day with the same settings so that figures 5.22 and 5.23 are directly comparable. Three 200 µm radius devices were selected at random from each device for testing, and the emissions compared to quantify the variation in wavelength and intensity across the wafer. The typical variation between the three mesa structures tested on each wafer was ± 10% for the intensity (from the standard error of the mean), and ± 5 nm for the peak wavelength.

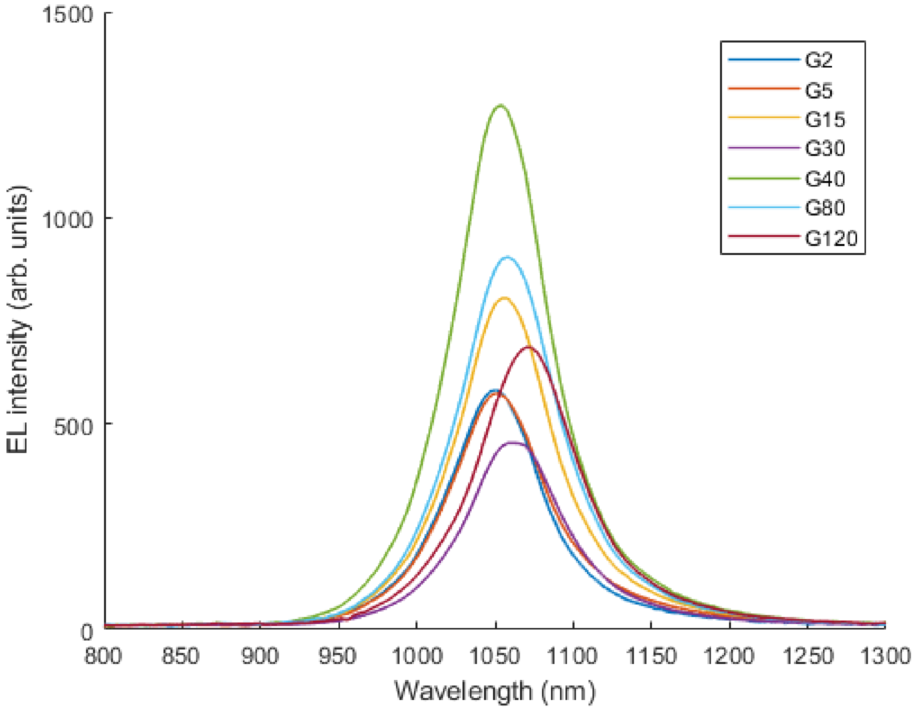

FIGURE 5.22: EL spectra of series G devices, GaAsBi/GaAs MQWs grown in this work, using 20 A/cm^2

From figure 5.22, the EL of the devices all show a broad peak in the wavelength range 1050-1070 nm. There is no visible peak at 870 nm when the data are viewed on a linear ordinate scale indicating that there is negligible recombination in the GaAs barriers. The intensity of the emission increases with the number of wells up to G40, except for G30 which has the weakest emission of the series. After G40, the EL intensity decreases with increasing well number. The spectral width of all the devices are between 70 and 76 nm.

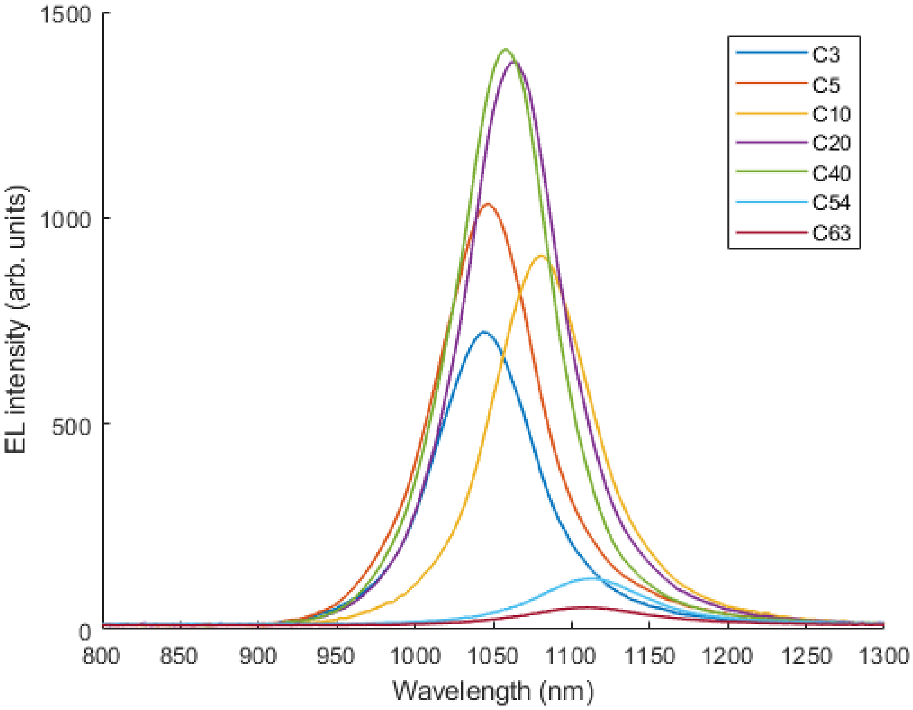

FIGURE 5.23: EL spectra of series C GaAsBi/GaAs MQWs grown by Richards et al. for comparison [20], using 20 A/cm^2

From figure 5.23, the series C MQWs are slightly brighter up to 40 wells than the series G devices grown in this work, with similar spectral widths between 72 and 76 nm. This is disappointing since series C were grown in 2012, four years prior to series G, although the two series were nominally grown at similar temperature (375 °C vs 380 °C). However, the wafer temperature is difficult to compare due to the 4 years between growth of the two series. The difference in emission intensity is likely due to higher material quality in the wells in series C. Given the results of chapter 4, that growth of GaAsBi at a higher temperature produces layers with brighter PL and lower dark currents, it is likely that series C was grown at a moderately higher temperature using a higher bismuth flux, closer to the temperature-limited growth regime. Although the p-type layer in the series C devices is twice as thick as for series G, both series suffer from poor current spreading.

The devices C54 and C63 have significantly weaker EL emission of around an order of magnitude lower than the other devices. The FWHM of these two devices is 90 and 114 nm respectively. The peak emission is also red shifted to around 1115 nm, which is consistent with PL measurements by Richards et al. [19].

5.10.2 Comparison of both series of GaAsBi MQW devices and the implications for GaAsBi MQW photovoltaics

To better compare the two series of MQWs, the integrated EL (IEL) signal can be plotted as a function of the number of wells. Due to unfortunate planning by the author, the devices were designed to have a different nominal well thickness (10 nm for series G, and 8 nm for series C), so the well number cannot be directly used to compare the series. However, the strain-thickness product considers differences in well thickness, barrier thickness, and bismuth content in the MQW stack making it a better metric to compare the two series, see figure 5.24. The strain thickness product is defined as the magnitude of the average strain in the MQW stack multiplied by the total thickness of the stack.

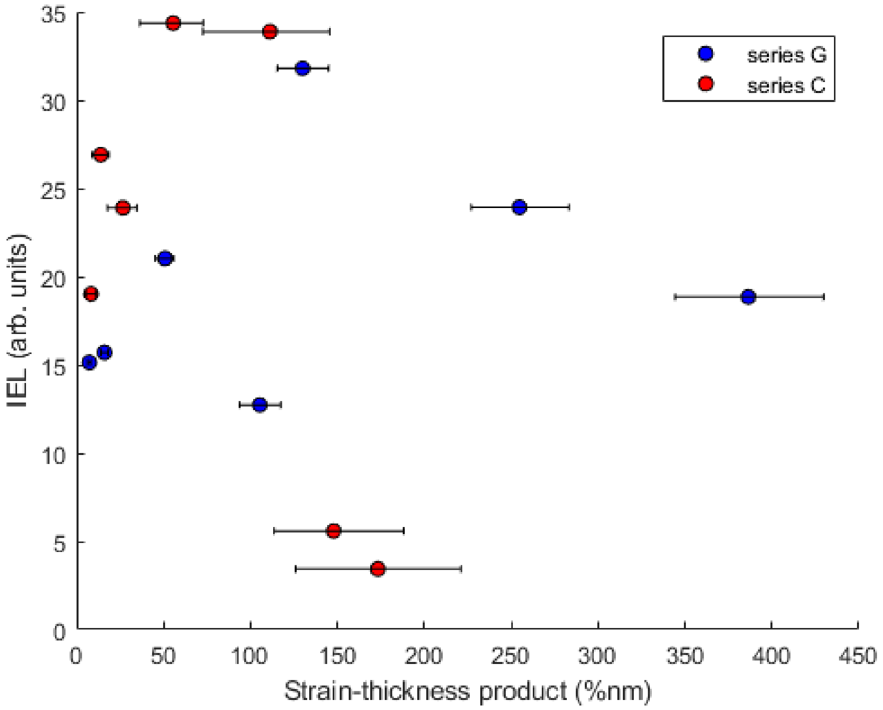

FIGURE 5.24: Integrated EL as a function of strain-thickness product for series G (blue circles) and series C (red circles), using 20 A/cm^2

From figure 5.24, the dependence of the IEL on the number of wells is clearer. For series G (blue circles), the IEL increases linearly up to G40 (128 %nm) before decreasing for G80 and G120. G30 (105 %nm) shows anomalously low performance (compared to its IPL, see figure 5.17).

Devices G80 and G120 show much brighter EL emission than C54 and C63, despite containing a greater number of (nominally) thicker wells. This is likely due to the lower average strain in G80 and G120 and is promising for PV applications, implying that more than 50 wells can be incorporated without a significant loss of performance.

However, from solar cell characterisation reported by Richards et al. in [33], device C63 has a high power conversion efficiency. This is due to the red-shift of the absorption edge caused by strain relaxation allowing more of the solar spectrum to be absorbed and the carriers extracted despite the large density of misfit dislocations.

To improve upon the PV performance of C63 for future GaAsBi based devices, the absorption edge of the quantum wells must be extended towards 1 eV without strain relaxation occurring. This is challenging for a pseudomorphic structure as the wells ideally need to be >10 nm to prevent the confinement energy from blue-shifting the absorption edge and must have a high bismuth incorporation >7%. Such a structure would have a relatively low critical thickness, and to incorporate >50 wells with a band gap of 1 eV, strain balancing may be necessary. The two most likely options are either incorporating nitrogen into the wells to form a GaAsBiN/GaAs MQW, or by incorporating phosphorus into the barriers to form GaAsBi/GaAsP [35, 36]. The electrons should be more strongly confined in both structures such that their thermal escape time should be closer to that of the holes in the valence band. This should prevent the incomplete carrier extraction and charging of the i-region observed in [13].

5.10.3 EL microscopy

During electrical testing of the devices, a camera was used to align the top probe tip onto the mesa structure. Direct imaging of the EL is possible if the camera is sensitive to the wavelength of the emission. The monochrome silicon camera used in this work (Quantalux CS2100M-USB) has a relatively low external quantum efficiency of approximately 2% at 1050 nm. A collage of EL microscopy images taken at an injection current density of 20 A/cm^2 is shown in figure 5.25.

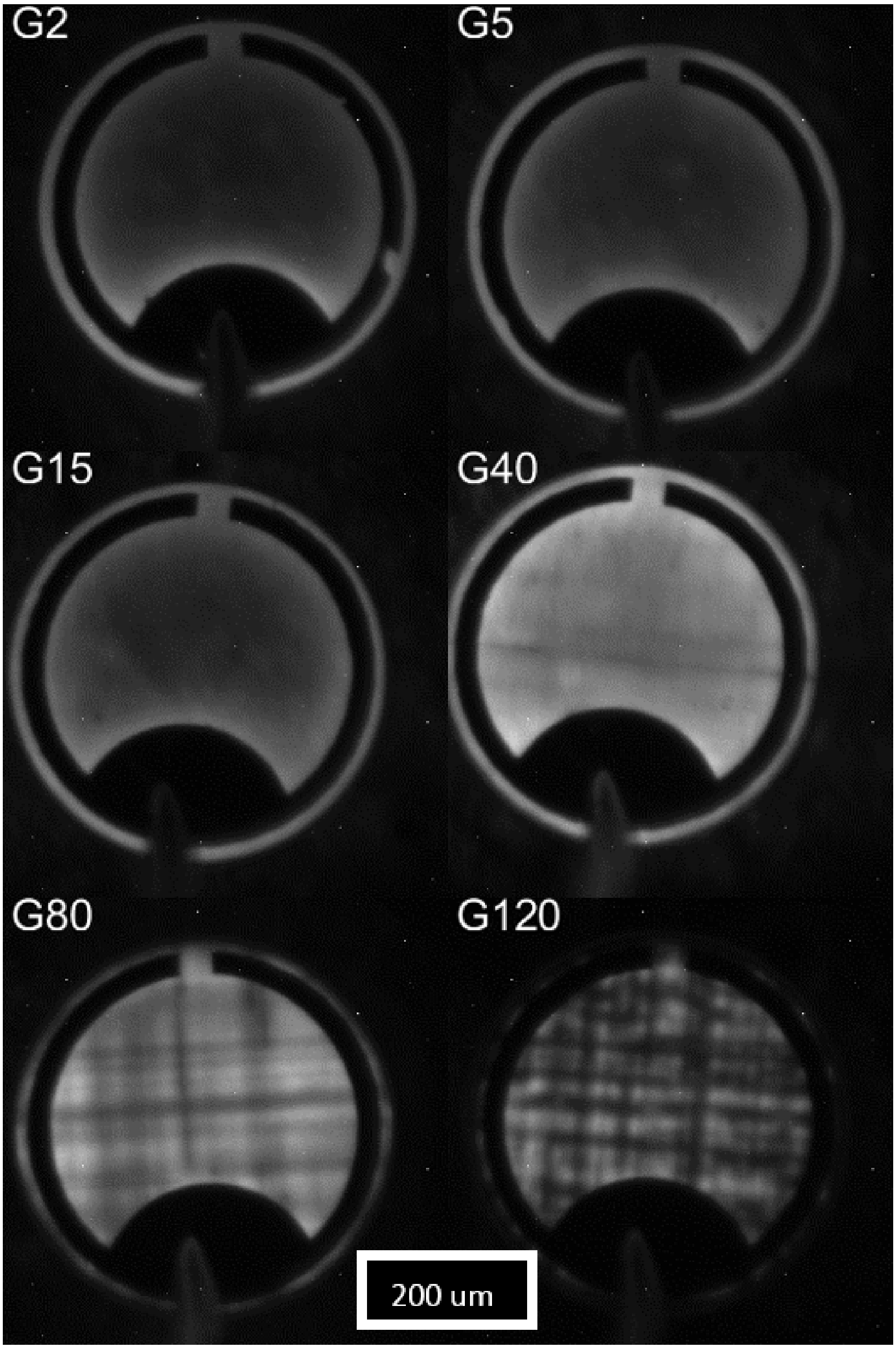

FIGURE 5.25: Collage of microscope images showing EL of GaAsBi/GaAs MQW devices using 20 A/cm^2. The shadow of the top contact probe tip is visible in the bottom middle of each device, and its effect on the EL intensity is neglected. The shadow of the gold contact shows up as the black "eyeball" inside the circular mesa. Device G30 is not considered for this analysis due to its anomalously low EL intensity relative to the other devices

From figure 5.25, the emitted EL is easily visible using a monochrome silicon camera despite the low EQE of the camera at the emission wavelength. The emission from devices G2, G5 and G15 is mostly coming from close to the gold contact pad showing poor current spreading. This is due to the relatively thin p-type GaAs region. If the current is spreading randomly through the structure, carriers are not likely to get close to the centre of the mesa since it has an extremely large aspect ratio (the p-type region is 0.3 µm thick, while the device has a 200 µm radius). Devices G40 and G80 appear to have better current spreading indicating that it continues in the i-region. Normally, an LED would be designed to have a thick (approximately 5 µm AlGaAs) window layer to enhance the current spreading, or an n-type GaAs current blocking layer above the i-region to stop current from passing through the mesa underneath the contact pad. In addition, a grid contact pattern could be used instead of the annular mesa pattern to shorten the distance that the current must spread out.

The consequence of the poor current spreading is that the current density varies across the device. The region where the current density is highest (under the contact pad) will produce the majority of the EL output. However, this light cannot escape the device due to the opacity of the gold contact and is reflected into the device where it can either be re-absorbed in the i-region or scattered off the rough bottom surface of the substrate. The current density in the part of the device that is visible (the annular window) is much lower than the quoted value.

The EL images also show a varying degree of dark lines in the mesa structures, which correlate strongly with the Nomarski microscopy images (see section 5.5) showing strain relaxation. From the high density of dark lines in the image of G120, dislocations are clearly having a major deleterious effect on the EL emission.

5.10.4 Current dependent EL of device G40

Current dependent EL measurements were taken using the brightest device (G40), with the results plotted in figure 5.26.

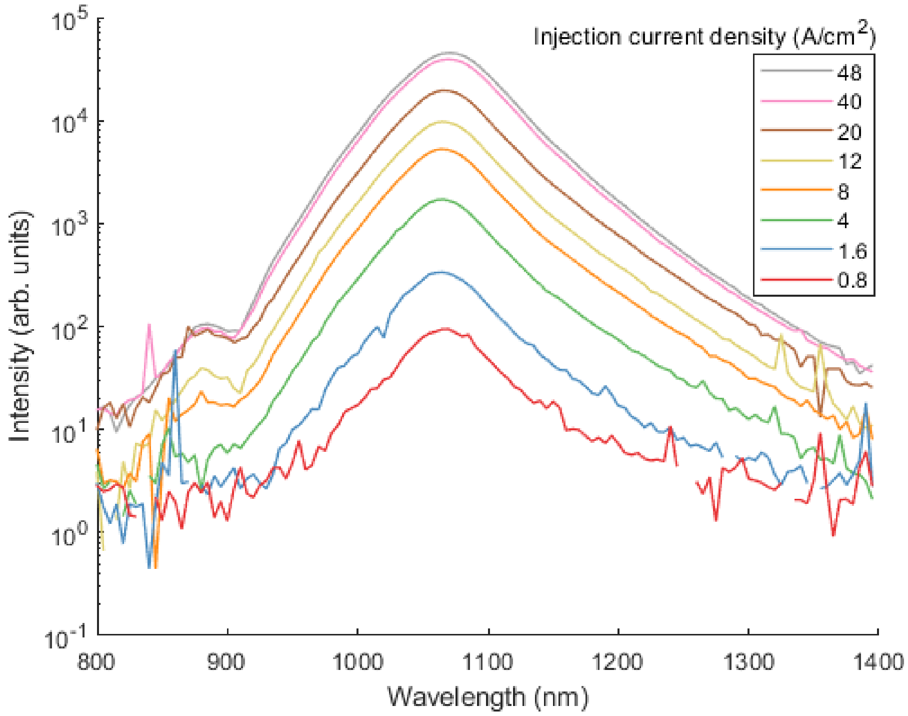

FIGURE 5.26: Current dependent EL measurements of G40

From figure 5.26, the EL intensity increases rapidly with the injection current. However, by 48 A/cm^2 the brightness is not increasing as quickly, and the peak is starting to red-shift. This suggests that the device is starting to heat up. Additionally, the FWHM of the emission increases from 68 nm at 0.8 A/cm^2 to 75 nm at 48 A/cm^2. A shoulder peak at 880 nm corresponds to recombination in the GaAs barriers, and is 280 and 430 times weaker than the central peak at 8 A/cm^2 and 48 A/cm^2, respectively.

To better investigate the integrated emission as a function of the injection current, a silicon power meter was used to measure the power output of the device. The power meter has a function that allows the user to set the wavelength of the measured light to account for the varying sensitivity of the photodiode. This introduces a large uncertainty into the power measurement since the EL spectrum is broad, and the photo-response of the silicon photodiode is changing rapidly over the range of wavelengths emitted by the device.

The power meter head was placed close to the device under test, and the solid angle occupied by the photodiode as viewed from the device was calculated to quantify the emission intensity in units of Watts per steradian, see figure 5.27. The power meter reading was also recorded with the current turned off to give a background reading which was subtracted. Note that the current densities given in the plot are too high due to the poor current spreading.

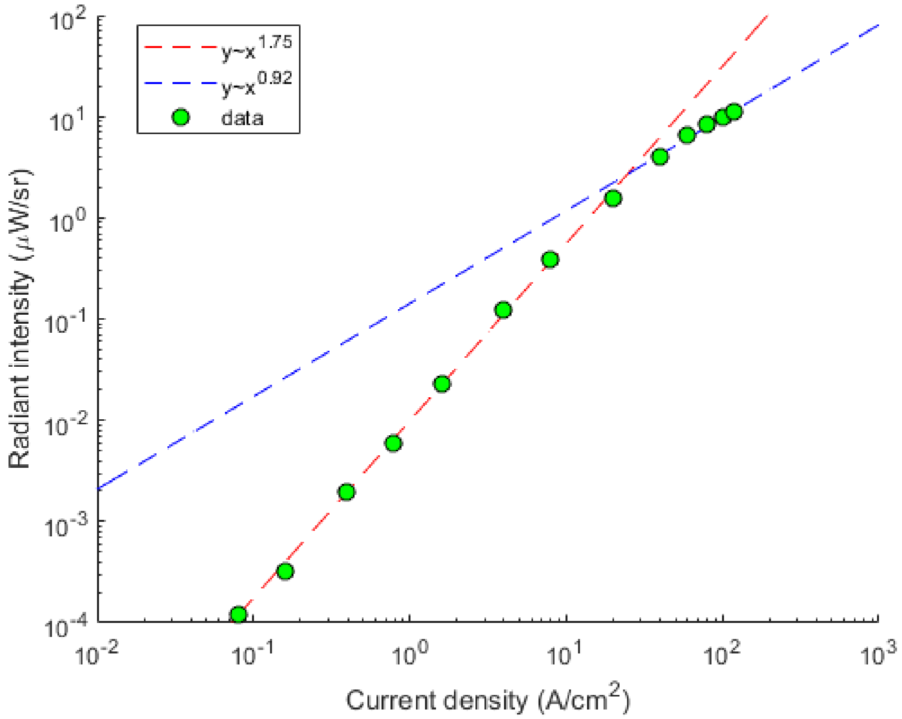

FIGURE 5.27: Current dependent radiant intensity of G40 EL emission

From figure 5.27, the EL intensity increases super-linearly from 0.1 to 10 A/cm^2, indicating that a mix of radiative and non-radiative recombination processes are present in the device. Above roughly 20 A/cm^2, the gradient changes to nearly 1. One might assume that this could be due to the non-radiative recombination centres in the device becoming saturated, with radiative recombination dominating thereafter. However, from figure 5.26, the EL peak starts to red-shift at the highest current densities. This, coupled with the fact that the test ended after 120 A/cm^2 when the device failed, likely means that the change in gradient is due to device heating, and not radiative recombination becoming dominant. This conclusion could be verified using a pulsed current source with a low duty cycle, which would allow the device to cool between pulses.

5.10.5 Comparison of GaAsBi EL with InGaAs MQW

To assess the suitability of GaAsBi for use in near infrared LEDs, the brightest MQW device grown in this work (G40) is compared to a state-of-the-art strain balanced InGaAs/GaAsP 65 well device grown for photovoltaic applications. A description of this device is given in [49]. In addition, the EL of the brightest (in terms of PL intensity) bulk (95 nm thick) GaAsBi device from chapter 4 (STG-38) is also included in the comparison. This device (STG-38) contains 1.3% bismuth and is one of the brightest GaAsBi epilayers grown in Sheffield. All three devices were fabricated with contacts that have the same annular mesa structure.

Note that none of these devices were specifically grown as LEDs meaning that the EL signal could be improved using a variety of growth and fabrication steps, e.g. by the inclusion of a distributed Bragg reflector, current blocking layer, or grid contact pattern.

Despite being grown for solar cell testing, the InGaAs device does have two design advantages for EL testing over the GaAsBi devices. Firstly, the use GaAsP barriers for strain balancing is expected to increase the EL signal by a factor of two [18]. Secondly, the use of a p-type layer that is 600 nm thick compared to the 300 nm in the GaAsBi devices will improve the current spreading. The boost to performance given by the enhanced current spreading is difficult to quantify, but an enhancement of up to 2x could be expected from the ratio between the p-type layer thickness in the two devices.

The EL spectra of the three LEDs are plotted in figure 5.28.

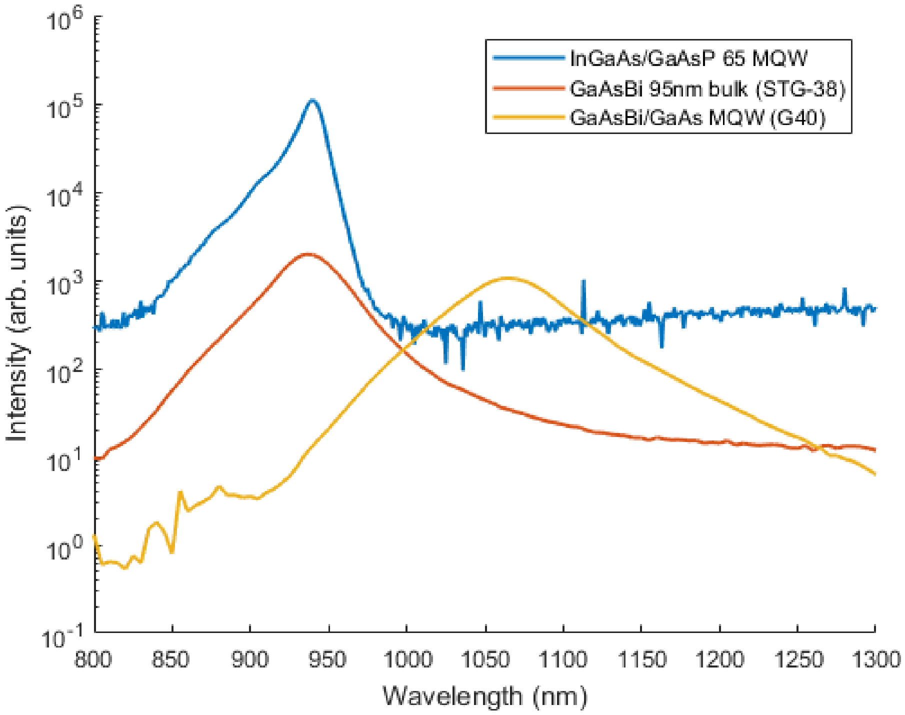

FIGURE 5.28: Spectra of three near-infrared LEDs operating at 8 A/cm^2: a strain balanced InGaAs/GaAsP 65 MQW device, a 95 nm bulk GaAsBi device grown in chapter 4, and the brightest of the GaAsBi/GaAs MQWs grown in this chapter (G40). Note that the noise floor of the InGaAs device appears more intense than it is in reality, since a neutral density filter was used to attenuate its emission

From figure 5.28, the InGaAs device has a central wavelength of 940 nm. On the short wavelength side of the peak, two shoulder peaks can be observed at 880 and 905 nm. These peaks are likely caused by transitions between excited states in the quantum wells. The bright emission and narrow FWHM of 21 nm are the result of highly optimised growth conditions.

Coincidentally, the GaAsBi bulk device has a similar central wavelength of 940 nm, with a FWHM of 45 nm. The peak emission from this device is around 50 times weaker than the InGaAs device. Due to the larger spectral width the IEL of this device is around 22 times weaker.

Device G40 has a longer wavelength peak at 1065 nm due to its higher bismuth content, and a FWHM of 68 nm. The peak emission of this device is roughly 100 times weaker than the InGaAs device and 2 times weaker than the GaAsBi bulk device despite emitting at a longer wavelength. The IEL of this device is a factor of 29 and 1.3 times weaker than the InGaAs and GaAsBi bulk devices, respectively. The GaAsBi devices have significantly broader emission than the InGaAs due to a large number of bismuth induced states near the valence band edge [46].

However, after considering the design advantages of the InGaAs device (strain balancing and thicker p-type layer for current spreading), its IEL is likely between 7.5 and 15 times that of device G40. The InGaAs device has a similar ideality factor (1.95) [33] to G40 (1.97), so that repeating the measurement using a different current density should not favour either device.

Overall, the GaAsBi devices show broad luminescence that is slightly less intense than a comparable InGaAs device. However, with future optimisation of the material quality and the use of an LED specific growth structure and contact pattern the performance could be increased significantly.

The brightest GaAsBi MQW device grown in this work (G40) has a peak radiant intensity of 11 μW/sr measured at the front of the wafer. Most of the light cannot be usefully coupled out of the device at present due to photons emitted in the wrong direction (towards the substrate), or due to total internal reflection from the top surface. The growth of a distributed Bragg reflector under the i-region could increase the radiant flux by up to a factor of 4 [34]. A surface mounted epoxy lens would help to reduce total internal reflection and to focus the light. The use of strain-balancing with GaAsP barriers or nitrogen incorporation in the wells could lead to a further increase of up to a factor of two in the radiant flux [18].

The LED optimisations discussed above could lead to a GaAsBi device with a surface-emitted radiant flux around 0.1 mW/sr. Further improvements in the radiant flux should be possible with improvements in the quality of the GaAsBi, for example by growth at a higher temperature.

We note that using the 200 μm radius devices for EL power measurements is not a fair comparison due to the poor current spreading in both devices. Using the smallest devices (25 μm radius) is a better comparison, and results in the InGaAs/GaAsP device having an output power around 3-4 times larger than the GaAsBi device [51].

5.10.6 Suitability of dilute bismides as an OCT light source

Since GaAsBi LEDs have significantly broader emission than comparable InGaAs structures (see figure 5.28), the incorporation of bismuth into a super-luminescent LED for a broadband light source could be useful for OCT imaging, either by incorporation into an existing design such as [17] to produce InAsBi quantum dots, or by designing a device with different GaAsBi quantum wells using figure 5.19. In addition, the use of InGaAsBi or GaAsBiN for the wells would increase the conduction band offset and the electron confinement energy enabling interband transitions between excited states for a further increased FWHM.

We note that the PL FWHM of the single quantum well GaAsBi test structure is 68 nm (77 meV) (see figure 5.15). For comparison, single quantum dot layers reported in [15] have a FWHM of between 39 and 49 nm (30 and 44 meV, respectively). The GaAsBi single quantum well device has FWHM that is between 38 and 74 % larger than that of a comparable InAs QD layers.

The devices in this work with more than 1 well have FWHM values of 70-76 nm since they were grown to be as uniform as possible. The relatively small increase in FWHM throughout the series of devices show the degree of uniformity that can be achieved using GaAsBi wells, and bodes well for controlling the growth of future devices with different well thicknesses and bismuth contents for broadband emission.

By using dilute bismide semiconductors the emission from each well or transition could be broadened, potentially allowing for a broader overall emission spectrum that is closer to Gaussian in line shape, leading to low cost light sources for higher axial resolution in OCT imaging.

5.11 Conclusions

A systematic series of strained GaAsBi MQW structures with different numbers of wells were grown using MBE. The devices had a lower average strain per period that previous devices grown in Sheffield by Richards et al. [20].

Nomarski microscopy images showed a low density of droplet defects and an increasing prevalence of cross hatch lines indicative of strain relaxation. XRD measurements showed satellite peaks corresponding to the periodic MQW structure. The satellite peaks were broader for the devices with more wells which was probably caused by a combination of strain relaxation and non-square wells.

The PL spectra of the devices showed broad peaks at around 1050 nm with FWHM values of around 70 nm. Quantum mechanical calculations using the Schrödinger equation showed an excellent agreement with the observed ground state transition energy from PL.

JV results showed that the dark current of the devices scaled with the size of the mesa structure in forward bias. However, the agreement in reverse bias was slightly worse. The forward dark currents of the devices did not scale with the number of wells. The reason for this is not understood.

EL spectra of the devices showed a similar peak wavelength and FWHM to the PL measurements. The devices were compared to the series grown by Richards et al. [20] as a function of their strain-thickness product. The 120 well device grown in this work showed more intense EL than the 63 well device grown by Richards. This is promising for the development of GaAsBi for photovoltaic applications as more than 50 wells can be incorporated without degradation of the performance associated with strain relaxation. The EL emission of the brightest device increased superlinearly with the injection current density indicating that non-radiative recombination via defects was dominant in the device. This device was compared to a highly-optimised strain-balanced InGaAs/GaAsP device to gauge the maturity of GaAsBi for optoelectronic devices. The GaAsBi device had an output power that was around 29 times weaker. However, the GaAsBi device had significant current spreading issues which, if resolved, would result in a more favourable comparison.

The applicability of GaAsBi LEDs as a broadband light source for OCT was discussed. A single quantum well GaAsBi test structure had a PL spectrum that was significantly broader than the FWHM of InAs quantum dot based LEDs with a single layer of dots from the literature. Since the emission from GaAsBi quantum wells is broader than InGaAs wells and InAs quantum dots, the construction of a light source with a significantly broader overall emission spectrum should be possible. Such a device could include several GaAsBi wells with different thicknesses, bismuth contents, or utilise transitions between excited states in the wells to achieve a broader emission spectrum.

Bibliography

[1] P. K. Patil et al., *GaAsBi/GaAs multi-quantum well LED grown by molecular beam epitaxy using a two-substrate temperature technique*, Nanotechnology **28**, 105702 (2017)

[2] R. Kudrawiec et al., *Experimental and theoretical studies of band gap alignment in* $GaAs_{1-x}Bi_x$*/GaAs quantum wells*, Journal of Applied Physics **116**(23), 233508 (2014)

[3] A. R. Mohmad et al., *Localization effects and band gap of GaAsBi alloys*, Physica Status Solidi B **251**(6), 1276-1281 (2014)

[4] K. Alberi et al., *Valence band anticrossing in mismatched III-V semiconductor alloys*, Physical Review B **75**, 045203 (2007)

[5] K. Alberi and O. D. Dubon, *Valence band anticrossing in* $GaBi_xAs_{1-x}$, Applied Physics Letters **91**, 051909 (2007)

[6] R. Maspero et al., *Unfolding the band structure of GaAsBi*, Journal of Physics: Condensed Matter **29**(7), 075001 (2017)

[7] R. Gomez Alcala et al., *Effective-mass approaches for one-dimensional quantum well structures: Comparison with multi-band results*, Superlattices and Microstructures **20**(1), 35-44 (1996)

[8] D. A. B. Miller, *Optical Physics of Quantum Wells*, in: Quantum Dynamics of Simple Systems – Proceedings of the 44th Scottish Universities Summer School in Physics, Stirling, August 1994, edited by G. L. Oppo et al., pp.239-266, SUSSP/Institute of Physics, 1996

[9] M. G. Burt, *The justification for applying the effective-mass approximation to microstructures*, Journal of Physics: Condensed Matter **4**(32), 6651 (1992)

[10] D. J. BenDaniel and C.B. Duke, *Space-charge effects on electron tunneling*, Physical Review **152**(2), 683-692 (1966)

[11] Ioffe Institute, *GaAs basic parameters at 300 K*, `http://www.ioffe.ru/SVA/NSM/Semicond/GaAs/basic.html` [Accessed 15 August 2018]

[12] K. Razi Naqvi and S. Waldenstrøm, *The finite square well: Whatever is worth teaching at all is worth teaching well*, arXiv:1505.03376 [physics.ed-ph]

[13] R. D. Richards et al., *Light-biased IV characteristics of a GaAsBi/GaAs multiple quantum well pin diode at low temperature*, Semiconductor Science and Technology **33**, 094008 (2018)

[14] D. A. Beaton et al., *Insight into the epitaxial growth of high optical quality* $GaAs_{1-x}Bi_x$, Journal of Applied Physics **118**, 235701 (2015)

[15] N. Ozaki et al., *Integration of Emission-wavelength controlled InAs Quantum Dots for Ultra-broadband Near-infrared Light Source* , Nanomaterials and Nanotechnology **4**, 26 (2014)

[16] A. Zhang et al., *Multifunctional 1050 nm spectral domain OCT system at 147 kHz for posterior eye imaging*, Sovremennye Tehnologii v Medicine **7**(1), 7-12 (2015)

[17] N Ozaki et al., *Superluminescent diode with a broadband gain based on self-assembled InAs quantum dots and segmented contacts for an optical coherence tomography light source*, Journal of Applied Physics **119**, 083107 (2016)

[18] H. Lee et al., *Enhanced output power of InGaAs/GaAs infrared light-emitting diode with* $Ga_xIn_{1\text{-}x}P$ *tensile strain barrier*, Current Applied Physics **17**(12), 1582-1588 (2017)

[19] R. D. Richards et al., *MBE grown GaAsBi/GaAs multiple quantum well structures: Structural and optical characterization*, Journal of Crystal Growth **425**, 237-240 (2015)

[20] R. D. Richards et al., *Growth and structural characterization of GaAsBi/GaAs multiple quantum wells*, Semiconductor Science and Technology **30**, 094013 (2015)

[21] J. H. Neave et al., *Effect of arsenic species* (As_2 *OR* As_4) *on the crystallographic and electronic structure of mbe-grown GaAs(001) reconstructed surfaces*, Surface Science **133**(1), 267-278 (1983)

[22] W. Bennarndt et al., *Domains of molecular beam epitaxial growth of Ga(In)AsBi on GaAs and InP substrates*, Journal of Crystal Growth **436**, 56-61 (2016)

[23] R. D. Richards et al., *Molecular beam epitaxy growth of GaAsBi using* As_2 *and* As_4, Journal of Crystal Growth **390**, 120-124 (2014)

[24] P. K. Patil et al., *GaAsBi/GaAs MQWs grown by MBE using a two-substrate-temperature technique*, Journal of Alloys and Compounds **725**, 694-699 (2017)

[25] R. B. Lewis et al., *Growth of high Bi concentration* $GaAs_{1\text{-}x}Bi_x$ *by molecular beam epitaxy*, Applied Physics Letters **101**, 082112 (2012)

[26] F. Bastiman et al., *Bi incorporation in GaAs(100) –* 2×1 *and* 4×3 *reconstructions investigated by RHEED and STM*, Journal of Crystal Growth **341**(1), 19-23 (2012)

[27] E. O. Göbel and K. Ploog, *Fabrication and optical properties of semiconductor quantum wells and superlattices*, Progress in Quantum Electronics **14**(4), 316 (1990)

[28] N. Otsu, *A threshold selection method from gray-level histograms*, IEEE Transactions on Systems, Man, and Cybernetics **9**(1), 62-66 (1979)

[29] D. F. Reyes et al., *Bismuth incorporation and the role of ordering in GaAsBi/GaAs structures*, Nanoscale Research Letters **9**, 23 (2014)

[30] I. Vurgaftman et al., *Band Parameters for III-V compound semiconductors and their alloys*, Journal of Applied Physics **89**, 5815 (2001)

[31] Y. P. Varshni, *Temperature dependence of the energy gap in semiconductors*, Physica **34**(1), 149-154 (1967)

[32] R. D. Richards et al., *Photovoltaic characterisation of GaAsBi/GaAs multiple quantum well devices*, Solar Energy Materials and Solar Cells **172**, 238-243 (2017)

[33] R. D. Richards et al., *High temperature characerization of GaAsBi/GaAs MQWs*, 9th International Conference on Bismuth Containing Semiconductors, Kyoto, Japan, July 2018

[34] T. Kato et al., *GaAs/GaAlAs surface emitting IR LED with Bragg reflector grown by MOCVD*, Journal of Crystal Growth **107**(1-4), 832-835 (1991)

[35] S. J. Sweeney and S. R. Jin, *Bismide-nitride alloys, promising for efficient light emitting devices in the near and mid infrared*, Journal of Applied Physics **113**, 043110 (2013)

[36] H. Kim et al., *Single junction solar cell employing strain compensated* $GaAs_{0.965}Bi_{0.035}$ /$GaAs_{0.75}P_{0.25}$ *multiple quantum wells grown by metal organic vapor phase epitaxy*, Applied Physics Letters **112**(25), 251105 (2018)

[37] D. B. Bushnell et al., *Effect of barrier composition and well number on the dark current of quantum well solar cells*, 3rd World Conference on Photovoltaic Energy Conversion, Osaka, Japan, 11-18 May, 2003

[38] D. Fan et al., *MBE grown GaAsBi/GaAs double quantum well separate confinement heterostructures*, Journal of Vacuum Science & Technology B **31**, 03C105 (2013);

[39] T. Fuyuki et al., *Growth of* $GaAs_{1-x}Bi_x/Al_yGa_{1-y}As$ *Multi-Quantum-Well Structures*, Japanese Journal of Applied Physics **49**, 7R (2010)

[40] R. Butkute et al., *AlAs As a Bi blocking barrier in GaAsBi multi-quantum wells: structural analysis*, Lithuanian Journal of Physics **57**, 1, p. 29-36 (2017)

[41] R. Butkute et al., *Bismuth Quantum Dots in Annealed GaAsBi/AlAs Quantum Wells*, Nanoscale Research Letters **12**, 436 (2017)

[42] R. D. Richards et al., *Telecommunication wavelength GaAsBi light emitting diodes*, IET Optoelectronics **10**, 2, 4, p. 34-38 (2016)

[43] R. B. Lewis et al., $GaAs_{1-x}Bi_x$ *light emitting diodes*, Journal of Crystal Growth **311**, p. 1872-1875 (2009)

[44] R. D. Richards et al., *MBE grown GaAsBi/GaAs multiple quantum well structures: structural and optical characterization*, Journal of Crystal Growth **425**, p. 237-240 (2015)

[45] J. Kopaczek et al., *Optical properties of GaAsBi/GaAs quantum wells: photoreflectance, photoluminescence and time-resolved photoluminescence study*, Semiconductor Science and Technology **30**, 9 (2015)

[46] T. Wilson et al., *Assessing the nature of the distribution of localised states in bulk GaAsBi*, Scientific Reports **8**, 6457 (2018)

[47] P. R. Griffin et al., *Effect of strain relaxation on forward bias dark currents in GaAs/InGaAs multiquantum well p–i–n diodes*, Journal of Applied Physics **80**, 10 (1996)

[48] A. V. Drigo, *On the mechanisms of strain release in molecular-beam-epitaxy-grown* $In_xGa_{1-x}As/GaAs$ *single heterostructures*, Journal of Applied Physics **66**, 1975 (1989)

[49] M. C. Lynch et al, *Spectral response and I-V characteristics of large well number multi quantum well solar cells*, Journal of Materials Science **40**, p. 1445-1449 (2005)

[50] Z. Zhou et al., *Absorption properties of GaAsBi based p-i-n heterojunction diodes*, Semiconductor Science and Technology **30**, 094004 (2015)

[51] T. B. O. Rockett et al., *Electroluminescence study of GaAsBi multiple quantum wells with varying well number*, submitted to Journal of Applied Physics (2019)

Chapter 6

Summary, conclusions, and future work

6.1 Summary

A systematic series of 100 nm bulk GaAsBi pin diodes were grown using MBE. The as-grown devices were characterised using Nomarski microscopy, XRD, and PL. The devices were fabricated into mesa structures with metal contacts and the dark currents were measured. The growth conditions were correlated with the structural and optoelectronic properties of the devices.

Strained GaAsBi/GaAs MQW pin diodes with a varying number of wells were grown using MBE. The as-grown devices were characterised using the same techniques as the bulk diodes. The devices were also characterised using EL and compared to a previous set grown in Sheffield.

6.2 Conclusions

Growth of bulk GaAsBi layers at higher temperatures was found to result in brighter PL and lower dark currents for a given bismuth content. However, XRD measurements showed the presence of epilayer inhomogeneity in the devices grown at high temperatures. Despite the inhomogeneity the growth of future GaAsBi epilayers should be performed at the highest possible growth temperature. This temperature will be different depending on the desired bismuth incorporation, since the growth of high bismuth content alloys is difficult at higher temperatures as the bismuth atoms segregate out of the bulk more readily and form into surface droplets.

The devices grown in this work with more than 40 wells showed improved performance compared to the previous set of diodes grown in Sheffield. This was attributed to a lower strain per period in the MQW stack and is promising for photovoltaic applications. From EL microscopy images and XRD the thicker devices are still heavily affected by strain relaxation. The PL and EL peaks of the devices are around 1050 nm, with FWHM values of around 70 nm. The emission wavelength of the strained GaAsBi MQWs show the great potential for band gap engineering that is possible with bismide alloys, when compared to a state-of-the-art strain-balanced InGaAs/GaAsP device that emits at 940 nm.

A light source operating around 1000-1050 nm with a large spectral width is desirable for OCT imaging. The band gap engineering capability and broad emission caused by bismuth induced localised states make GaAsBi a promising material for an OCT light source. The FWHM of the LEDs grown in this work is much greater than that of comparable InGaAs quantum well and InAs quantum dot based designs, for the same device complexity. The output power of the GaAsBi layers grown in this work may be sufficiently intense for use in an OCT system when grown as part of an optimised LED structure.

6.3 Future work

For the development of GaAsBi as a light source for OCT, the EL power output and the FWHM of the overall emission spectrum need to be increased.

For improving the EL intensity, based on the conclusions of chapter 4, one would ideally like to increase the growth temperature of the active region to reduce the density of temperature related growth defects. However, this may lead to the incorporation of a lower bismuth content due to the surface segregation of bismuth atoms during growth at higher temperatures. This will blue-shift the emission wavelength and reduce the density of localised states, and hence reduce the FWHM of the luminescence. To achieve the target emission wavelength the well would have to be made thicker, which will reduce the radiative recombination rate in the well.

On the other hand, decreasing the growth temperature would allow the bismuth content to be higher, with a thinner well to blue-shift the emission wavelength back to 1000-1050 nm. A thinner quantum well would increase the electron and hole wavefunction overlap and increase the radiative recombination rate in the well. However, if the bismuth content is increased above approximately 4.5 % the density of bismuth related defects will likely greatly increase the non-radiative recombination rate.

Therefore, the trade-off between growth temperature, bismuth content, density of localised states, and radiative efficiency in the well should be modelled to find the optimum parameters for the quantum well. The output power of future LEDs could be greatly increased by incorporating the GaAsBi active into an optimised LED structure, featuring a distributed Bragg reflector, strain balancing, a thick current spreading layer, optimal dopant concentrations, and an LED specific contact pattern. Alternatively, the LED could be fabricated as an edge-emitting super-luminescent diode.

For improving the FWHM of the overall emission, since most of the band gap change in GaAsBi occurs in the valence band there is also scope to vary the material in the wells and barriers to achieve stronger electron confinement, enabling transitions between excited states in the wells to obtain a broader emission spectrum. There are a number of approaches which would lead to larger conduction band offsets in the well, e.g. GaAsBi/AlGaAs, InGaAsBi/GaAs, GaAsBiN/GaAs, and GaAsBi/GaAsP. The software written in this work to calculate the bound state energies could be further developed to include these options, with the results used to design future growth runs. It is possible that by combining several of the well and barrier material options the emission wavelength, number of excited state transitions, and the splitting of the excited state transitions from the ground state could be independently tuned to give the broadest possible emission spectrum with a high radiative efficiency. Due to the relatively high uniformity of the quantum well grown in this work, the growth of future MQW devices with different wells thicknesses or bismuth contents should prove highly controllable.